Summer 8-15-2020

Experimental Constraints on Igneous Iron Isotopic Fractionation and Diffusion

Kelsey Brianne Prissel
Washington University in St. Louis

WASHINGTON UNIVERSITY IN ST.LOUIS

Department of Earth and Planetary Sciences

Dissertation Examination Committee:
Michael J. Krawczynski, Chair
Nicolas Dauphas
Robert F. Dymek
Bradley L. Jolliff
Jill D. Pasteris

Experimental Constraints on Igneous Iron Isotopic Fractionation and Diffusion
by
Kelsey Brianne Prissel

A dissertation presented to
The Graduate School
of Washington University in
partial fulfillment of the
requirements for the degree
of Doctor of Philosophy

August 2020
St. Louis, Missouri

Table of Contents

List of Figures

v

List of Tables

Acknowledgments

This dissertation is the culmination of 23 years of formal education, and I would be remiss to not acknowledge every opportunity and person that helped me get to where I am today. As a first-generation Ph.D. student, I didn't really know what this journey would look like, and at this point, it's almost impossible for me to recall that I didn't know what graduate school was until I got to college.

None of this work would have been possible without the assistance of the Earth and Planetary Sciences department and the university. Thank you to all of the faculty and staff members who have shaped my time in graduate school. Brad Jolliff, Jill Pasteris, and Bruce Fegley, thank you for giving me opportunities to be included in your research and teaching, and for writing recommendation letters for fellowship and post-doc applications. I greatly appreciate the feedback and advice I have gotten over the years from many individuals, including Bob Dymek, Randy Korotev, Katharina Lodders, Rita Parai, and Phil Skemer. I can't imagine a better electron microprobe guru than Paul Carpenter; thank you for all of your support, and for the endless stories, donuts, cookies, and coffee. Hélène Couvy, thank you for all of the work you put toward maintaining the lab, without you we would get nothing done! My experiences with the Teaching Center have enriched my time at WashU, and I am especially thankful for Julia Johnson and her help navigating my CIRTL project. I am grateful for the financial support I have received from the McDonnell Center for the Space Sciences Roger B.

many more), outside of the department (especially Chelsey Dunham and Meghan Guild), and the innumerable friends I have made through softball (from little league to college to co-ed slow-pitch).

Of course, I would be nowhere without my family. Thank you to Tabb (and Declan!) for enduring years of secondhand stress. In my darkest times, you have always been the light that pointed me toward my goals and reminded me of my worth. There is not a day that goes by that I do not think about my godson Braxton, whose loss taught me more about life and love than any other. I am grateful for my parents and my grandparents (Mamaw and Papaw), not only for co-signing my undergraduate student loans to make my education possible, but more importantly, for being (along with my dogs Sparkle and Buster) the emotional support that carried me through high school, college, and graduate school. To Mamaw and Papaw, thank you for always leaving the backdoor unlocked when I needed to come home and escape the world. To my sister Haidyn, I am sad that I have missed watching you grow up, having moved out for college when you started kindergarten, and now graduating as you are starting high school(!), but your admiration has inspired me to persevere through the times where I lost sight of why this journey is worthwhile. Mom and Shawn, thank you for your tireless dedication to all of my pursuits; each and every one of my accomplishments has been made possible by the sacrifices you made for me along the way.

<div align="right">Kelsey Brianne Prissel</div>

Washington University in Saint Louis

August 2020

Dedicated to countless "failed" experiments.

Though they are not in this dissertation, they taught me just as much.

ABSTRACT OF THE DISSERTATION

Experimental Constraints on Igneous Iron Isotopic Fractionation and Diffusion

by

Kelsey Brianne Prissel

Doctor of Philosophy in Earth and Planetary Sciences

Washington University in St. Louis, 2020

Assistant Professor Michael J. Krawczynski, Chair

The chapters of this dissertation detail experimental studies that have been conducted in order to determine the diffusivity of iron in the mineral ilmenite ($FeTiO_3$) and the high-temperature behavior of iron isotopes during magma crystallization. The experimental study in Chapter 2 is the first to quantify the rates of cation diffusion in ilmenite. Integrating experimentally determined Fe-Mg and Fe-Mn interdiffusivities with disequilibrium preserved in ilmenite grains from natural volcanic samples, this work has established a new geospeedometry tool with which to estimate the time between magmatic perturbation and eruption on the timescale of hours to months. Chapter 3 investigates the effects of olivine crystallization on high-temperature iron isotopic fractionation over a range of oxygen fugacities and melt titanium compositions. The results demonstrate that there is no resolvable equilibrium fractionation of iron isotopes between olivine and melt at the experimental oxygen fugacities (where iron is mainly Fe^{2+}), nor is there a measurable effect of melt titanium composition on iron isotopic fractionation in the investigated compositional range. These experiments also led to the discovery that iron loss in reducing one-atmosphere gas-mixing experiments occurs not only as loss to the metal wire sample container, but also as evaporative loss, and each mechanism of experimental iron loss has an associated iron isotopic fractionation. In Chapter 4, the equilibrium partitioning of iron and titanium isotopes between ilmenite and

melt was experimentally determined in order to evaluate the role of ilmenite in generating the compositional variability among the lunar mare basalts. The results of the experiments in Chapters 3 and 4 were then incorporated into models of lunar magma ocean crystallization and used to estimate the iron and titanium isotopic compositions of components in mare basalt parent magmas. The iron, titanium, and magnesium isotopic compositions of the lunar mare basalts indicate Fe-Mg interdiffusion has occurred in the Ti-rich component of the mare basalt source regions via subsolidus reaction between ilmenite cumulates and the olivine- and pyroxene-rich lunar mantle. Though additional experimental constraints will be required to fully assess the effects of diffusive isotopic fractionation in ilmenite-bearing rocks, combining the experimental results for Fe-Mg interdiffusion in ilmenite from Chapter 2 with the ilmenite-melt iron isotopic fractionations in Chapter 4 establishes the foundation upon which to build future studies.

Chapter 1

Introduction

The high-temperature chemical behavior of iron is critical to our understanding of the processes involved in planetary formation, differentiation, and volcanism. Iron comprises a substantial portion of planetary reservoirs, existing predominantly as metallic iron (Fe^0) in planetary cores and as Fe^{2+} and Fe^{3+} in the iron-bearing silicates of planetary mantles and crusts. Experimental studies are essential in characterizing the influence of variables, such as temperature, oxygen fugacity, and melt composition, on the geochemical behavior of iron in magmatic systems. The equilibrium partitioning of iron between minerals and melt defines how the major element chemistry of a magma evolves during crystallization and melting. Additionally, diffusion of iron in minerals provides insight into the rates and timescales of dynamic processes occurring in volcanic systems such as melting, heating, mixing, ascent, and eruption. The chapters of this dissertation detail experimental studies that have been conducted in order to determine the diffusivity of iron in the mineral ilmenite ($FeTiO_3$) and the high-temperature behavior of iron isotopes during crystallization.

Though rarely an abundant mineral in its host rocks, the near ubiquitous presence of ilmenite in igneous rocks and the sensitivity of ilmenite composition to temperature and oxygen fugacity make it an important mineral for interpreting the thermal and physical conditions of magmas. The experimental study in Chapter 2 is the first to quantify the rates of cation diffusion in ilmenite. The results of this work indicate that at magmatic temperatures iron diffusion in ilmenite is faster than that in hematite and slower than that in titanomagnetite. Iron diffusion will in part dictate the timescales of equilibration between titanomagnetite and hemo-ilmenite, and this relationship between diffusion rates will be important to consider in geothermometry and oxybarometry using the two oxides, particularly at more oxidizing magmatic conditions. The experimentally determined Fe-Mg and Fe-Mn interdiffusivities allow for the first quantitative interpretation of disequilibrium preserved in ilmenite. Integrating our experimental results with observed chemical zoning in ilmenite grains from natural volcanic samples, we have established a new geospeedometry tool with which to estimate the time between a magmatic perturbation, such as melt recharge, and eruption on the timescale of hours to months.

Chapters 3 and 4 examine the high-temperature, mass-dependent fractionation of stable iron isotopes. The analytical precision of iron isotope measurements has improved by an order of magnitude in the past decade, revealing measurable iron isotopic fractionations present in igneous rocks and minerals. Similar to the major element behavior for iron, the degree of iron isotopic fractionation during magmatic differentiation will depend on factors including temperature, oxidation state, and melt composition. Interpretations of the observed variations in the iron isotopic compositions of igneous rocks have been hindered by the paucity of experimentally determined isotopic fractionations for major rock-forming minerals.

Olivine is an abundant mantle mineral in rocky, differentiated planetary bodies, and is a liquidus phase for a wide range of mafic and ultramafic magma compositions. Chapter 3

investigates the effects of olivine crystallization on high-temperature iron isotopic fractionation over a range of oxygen fugacities and melt titanium compositions. We have combined two independent experimental techniques for determining the equilibrium iron isotopic fractionation between olivine and melt. Our results demonstrate that there is no resolvable equilibrium fractionation of iron isotopes between olivine and melt at the experimental oxygen fugacities (where iron is mainly Fe^{2+}), nor is there a measurable effect of melt titanium composition on iron isotopic fractionation in the investigated compositional range. In providing experimental evidence against equilibrium olivine-melt iron isotopic fractionation at high-temperatures, this work prompts re-interpretation of iron isotopic compositions in olivine-bearing rocks. These experiments also led to the discovery that iron loss in reducing one-atmosphere gas-mixing experiments occurs not only as loss to the metal wire sample container, but also as evaporative loss, and each mechanism of experimental iron loss has an associated iron isotopic fractionation.

In terrestrial igneous systems, the coexistence of Fe^{2+} and Fe^{3+} can promote equilibrium iron isotopic fractionation between minerals and melt. In contrast, lunar mare basalts are generated by melting and crystallization processes in an environment relatively free of Fe^{3+}. Resolvable differences in iron isotopic composition exist among lunar basalts, and this isotopic variability appears coupled to a unique titanium enrichment in lunar magmas that is unparalleled on Earth. Our experimental results from Chapter 3 indicate that neither melt TiO_2 composition nor equilibrium olivine crystallization can explain the observed differences in the iron isotopic composition of the lunar mare basalts.

Ilmenite-bearing cumulates have been previously hypothesized as the main control for both the titanium compositional variability in the lunar mantle and the isotopic distinction observed between the low-Ti and high-Ti mare basalts. In Chapter 4, the equilibrium partitioning of iron and titanium isotopes between ilmenite and melt was experimentally investigated

3

in order to evaluate the role of ilmenite in generating the compositional variability among the lunar mare basalts. The results of the experiments in Chapters 3 and 4 were then incorporated into models of lunar magma ocean crystallization and used to estimate the iron and titanium isotopic compositions of components in mare basalt parent magmas. The titanium isotopic compositional difference between the low- and high-Ti mare basalts was reproduced using the modeled isotopic compositions of lunar magma ocean ilmenite cumulates. However, the difference in iron isotopic composition between the low- and high-Ti mare basalts cannot be attributed solely to products of lunar magma ocean crystallization. Instead, the measured iron and magnesium isotopic compositions of the lunar mare basalts indicate Fe-Mg interdiffusion has occurred in the Ti-rich component of the mare basalt source regions via subsolidus reaction between ilmenite cumulates and the olivine- and pyroxene-rich lunar mantle.

The experimental investigations in Chapters 3 and 4 support models of diffusive fractionation to explain the iron isotopic compositions measured in olivine- and ilmenite-bearing rocks from a variety of igneous environments. At the high temperatures of magmatic processes, equilibrium stable isotopic fractionations between minerals and melt will be small. However, elemental diffusion rates increase with temperature, and thus mass-dependent diffusive fractionation of isotopes may be more pertinent than equilibrium partitioning to the petrologic processes controlling the iron, titanium, and magnesium isotopic compositional variability observed in volcanic rocks. Though additional experimental constraints will be required to fully assess the effects of diffusive isotopic fractionation in ilmenite-bearing rocks, combining the experimental results for Fe-Mg interdiffusion in ilmenite from Chapter 2 with the ilmenite-melt iron isotopic fractionations in Chapter 4 establishes the foundation upon which to build future studies.

Chapter 2

Fe-Mg and Fe-Mn interdiffusion in ilmenite with implications for geospeedometry using oxides

Abstract

The Fe-Mg and Fe-Mn interdiffusion coefficients for ilmenite have been determined as a function of temperature and crystallographic orientation. Diffusion annealing experiments were conducted at 15 kbar between 800°C and 1100°C. For Fe-Mg interdiffusion, each diffusion

couple consisted of an ilmenite polycrystal and an oriented single crystal of geikielite. The activation energy (Q) and pre-exponential factor (D_0) for Fe-Mg diffusion in the ilmenite polycrystal were found to be $Q = 188 \pm 15$ kJ/mol and $logD_0 = -6.0 \pm 0.6$ m^2/s. For the geikielite single crystal, Fe-Mg interdiffusion has $Q = 220 \pm 16$ kJ/mol and $logD_0 = -4.6 \pm 0.7$ m^2/s. Our results indicate that crystallographic orientation did not significantly affect diffusion rates. For Fe-Mn interdiffusion, each diffusion couple consisted of one ilmenite polycrystal and one Mn-bearing ilmenite polycrystal. For Fe-Mn interdiffusion, $Q = 264 \pm 30$ kJ/mol and $logD_0 = -2.9 \pm 1.3$ m^2/s in the ilmenite. We did not find a significant concentration dependence for the Fe-Mg and Fe-Mn interdiffusion coefficients.

Cation diffusion rates were found to be faster in ilmenite than in hematite at temperatures < 1100°C. At oxygen fugacities near the wüstite-magnetite buffer, Fe and Mn diffusion rates are similar for ilmenite and titanomagnetite. We apply these experimentally determined cation diffusion rates to disequilibrium observed in ilmenites from natural volcanic samples in order to estimate the time between perturbation and eruption for the Bishop Tuff, Fish Canyon Tuff, Mt. Unzen, Mt. St. Helens, and kimberlites. When integrated with natural observations of chemically zoned ilmenite and constraints on pre-eruptive temperature and grain size, our experimentally determined diffusivities for ilmenite can be used to estimate a minimum time between magmatic perturbation and eruption on the timescale of hours to months.

2.1   Introduction

Ilmenite is an important and widespread accessory phase present in a variety of igneous rocks ranging in composition from silica-undersaturated kimberlites to high-silica rhyolites. Though rarely an abundant mineral in its host rocks, the near ubiquitous presence of ilmenite

and the sensitivity of ilmenite composition to temperature and oxygen fugacity make it an important mineral for interpreting the thermal and physical conditions of magmas. Ilmenite is a rhombohedral oxide with the end-member composition $Fe^{2+}TiO_3$. Generally, "ilmenite" refers to the layered octahedral atomic structure with formula $A^{2+}B^{4+}O_3$ where A^{2+} and B^{4+} represent charged cations (e.g. Fe^{2+}, Mg^{2+}, Mn^{2+}, Ti^{4+}). The terms "ilmenite" and "hemo-ilmenite" have also been used to refer to compositions represented by the solid solution between ilmenite, $Fe^{2+}TiO_3$, and the isostructural mineral hematite, $(Fe_2^{3+}O_3)$.

Coexisting ilmenite and titanomagnetite (solid solutions of magnetite and ulvöspinel) mineral pairs have been used extensively to infer the pre-eruptive conditions, namely temperature and oxygen fugacity, of magmas beneath volcanic complexes (e.g. Buddington and Lindsley 1964; Pownceby et al. 1987; Bishop 1980; Bacon and Hirschmann 1988; Ghiorso and Evans 2008). However, these methods are based on equilibrium between ilmenite and titanomagnetite, and thus any disequilibrium between the two minerals precludes the use of the oxide compositions in geothermometers or oxybarometers. In practice, the Mg/Mn ratios of coexisting ilmenites and titanomagnetites are used to identify disequilibrium oxide pairs in rapidly cooled volcanic rocks (e.g. Bacon and Hirschmann 1988). Evidence for non-equilibrium in ilmenite also exists as chemical zoning, including but not limited to volcanic rocks from Mt. St. Helens (Rutherford and Devine III 2008), Mt. Unzen (Venezky and Rutherford 1999), kimberlites (Pasteris 1981; Mitchell 1986; Schulze et al. 1995), and the Moon (Taylor et al. 1975).

The preservation of disequilibrium oxide compositions and chemical zoning in ilmenite yield insight into the dynamic processes occurring in ilmenite-bearing volcanic systems such as melting, heating, mixing, ascent, and eruption. Quantifying the rates and timescales of magmatic processes is important to understanding magma transport, differentiation, and mixing prior to eruption. The rates of volcanic processes are often estimated by using experimentally determined diffusion coefficients in diffusion models to match concentration

gradients observed in minerals, particularly for the silicate minerals olivine, feldspar, pyroxene, and quartz (e.g. Costa et al. 2008; Zhang and Cherniak 2010; Till et al. 2015; Shea et al. 2015). Diffusion studies have also been conducted on many oxide minerals, including periclase, spinel, titanomagnetite, and rutile (Van Orman and Crispin 2010, and references therein). In particular, Fe-Mg interdiffusion rates have been well-characterized experimentally for a diversity of major rock-forming minerals including olivine (Chakraborty 1997), pyroxene (Müller et al. 2013), and spinel (Vogt et al. 2015). Despite the common occurrence of ilmenite and its well-studied equilibrium compositions, there has yet to be a quantitative study of the diffusivity of cations (Fe^{2+}, Fe^{3+}, Mg^{2+}, Mn^{2+}, Ti^{4+}) in the ilmenite mineral structure.

Here, we present the first experimentally determined Fe-Mg and Fe-Mn interdiffusivities for ilmenite. With the use of the cation interdiffusion coefficients determined in this study, the compositional profiles preserved in ilmenites can constrain the rates of rapid volcanic processes. We apply these new data to Mg/Mn disequilibrium observed in natural coexisting oxide pairs (ilmenite and titanomagnetite), and to Mg zoning in ilmenite megacrysts found in kimberlites.

2.2 Experimental, analytical, and numerical methods

2.2.1 Experimental approach

Diffusion experiments were conducted in a piston cylinder apparatus at 15 kbar pressure to investigate the diffusivity of Fe^{2+}, Mg^{2+}, and Mn^{2+} in ilmenite solid solutions between 800°C and 1100°C. Synthetic polycrystalline ilmenite was juxtaposed against either an oriented, synthetic geikielite ($MgTiO_3$) crystal or a synthetic polycrystalline Mn-bearing ilmenite in a "diffusion-couple" geometry.

Starting material synthesis and purity. Polycrystalline ilmenites were synthesized by mixing high purity reagent-grade oxides (FeO, MnO, and TiO_2) in stoichiometric proportion (ilmenite, $FeTiO_3$, and Mn-bearing ilmenite, $Fe_{0.95}Mn_{0.05}TiO_3$). Starting materials were produced using two sources of iron: 1) all FeO or 2) a mixture of Fe-metal and Fe_2O_3 (1:1 molar ratio). The iron, manganese, and titanium oxides were mixed under isopropanol in a silicon-nitride ball mill for 3 hours. For mixes with Fe-metal (#001, #007, and #019), the Fe-metal was added after ball mill mixing, and the mixture was ground by hand in an agate mortar until the isopropanol evaporated. The ground starting material was then packed into a graphite capsule (approximately 7 mm depth) and sintered in a piston cylinder apparatus at either 1140°C and 15 kbar or 1165°C and 17.5 kbar for approximately 3 days (Appendix Table A.1). The graphite capsule limits the oxygen fugacity of the experiment to below the graphite-COH buffer producing $Fe^{2+}TiO_3$ with minimal hematite solution (Ulmer and Luth 1991; Médard et al. 2008). Using the empirical relationship determined in Ulmer and Luth (1991) for high-pressure experiments conducted using graphite capsules, we have calculated the upper limit of the oxygen fugacity for our synthesis and diffusion annealing experiments. Relative to the quartz-fayalite-magnetite (QFM) buffer, the upper limit on the oxygen fugacity of the synthesis experiments is QFM−1.2. The upper limit on the oxygen fugacity of our diffusion annealing experiments ranges from QFM−0.4 at 800°C to QFM−1.3 at 1200°C. However, the presence of Fe metal in the ilmenite polycrystals after the synthesis and diffusion annealing experiments indicates the oxygen fugacity conditions of the graphite capsules were more reducing than these estimated upper limits. Sintered polycrystalline ilmenite cylinders were cut into thin, circular wafers, mounted in epoxy, and polished. Geikielite ($MgTiO_3$) single crystals were provided by Jeremy N. Mitchell of Los Alamos National Laboratory, and are described in Mitchell et al. (1998).

The synthetic ilmenite wafers and geikielite were examined for homogeneity by electron microscopy. The synthetic polycrystalline ilmenite aggregates were composed of subhedral crystals $20 - 200$ μm in diameter. Ilmenites synthesized from starting materials containing Fe-metal (mixes #001, #007, and #019) had iron metal present as an accessory phase. Synthetic Mn-bearing ilmenite wafers included minor amounts of ulvöspinel ($FeTi_2O_4$). Thin needles (<2 μm thickness, average 20 μm length) of rutile (TiO_2) were present in the synthetic geikielite single crystals both before and after the experiments (Figure 2.3).

Diffusion annealing experiments. Diffusion-annealing experiments were conducted in a 0.5" piston cylinder apparatus (Boyd and England 1960) in the experimental geochemistry laboratory at Washington University in St. Louis. The polished face of an oriented synthetic geikielite cube was juxtaposed against the polished face of a synthetic polycrystalline ilmenite wafer. The geikielite cubes were prepared by cutting a single crystal of synthetic geikielite into 1 mm thickness wafers, then slicing each wafer into approximately 1 mm edge-length cubes. The cubes were polished either perpendicular or parallel to the c-axis. Orientation of each cube was confirmed using crossed-polarized reflected light. In each Fe-Mg interdiffusion experiment, the geikielite cube was oriented to explore the effect of crystallographic orientation on diffusion. Because the crystals have rhombohedral symmetry, two diffusion directions were investigated: one in which diffusion occurred perpendicular to the c-axis ($\perp$c), and one in which diffusion occurred parallel to the c-axis ($\parallel$c). To investigate Fe-Mn interdiffusion, two synthetic polycrystalline ilmenite wafers, one containing Mn and one initially Mn-free, were juxtaposed so that the polished faces of each wafer were in contact. For each diffusion annealing experiment, the diffusion couple was contained within a graphite capsule and the void spaces of the capsule were filled with graphite powder (Figure 2.1).

Piston cylinder experiments were performed between 800°C and 1100°C at 15 kbar (Table 2.1). Temperature was increased to the desired sample temperature at a rate of 100°C per minute.

Table 2.1: Experimental run details.

Experiment	Ilmenite[a]	Type	Direction[b]	T (°C)	P (kbar)	Time (s)
Fe-Mg $\perp$c						
F032	D007	Fe-Mg	$\perp$c	1200	15	3520
MK24	MK22	Fe-Mg	$\perp$c	1100	15	20820
F111	F055	Fe-Mg	$\perp$c	1100	15	78300
F045	F043	Fe-Mg	$\perp$c	1000	15	80440
F110	F055	Fe-Mg	$\perp$c	1000	15	260340
F119	F116	Fe-Mg	$\perp$c	1000	15	524940
F030	D009	Fe-Mg	$\perp$c	900	15	258320
F053	F049	Fe-Mg	$\perp$c	800	15	522100
Fe-Mg $\parallel$c						
F018	F012	Fe-Mg	$\parallel$c	1100	15	17940
F019	F007	Fe-Mg	$\parallel$c	1000	15	28680
F117	F112	Fe-Mg	$\parallel$c	1000	15	87060
F033	D007	Fe-Mg	$\parallel$c	900	15	252300
F051	F044	Fe-Mg	$\parallel$c	900	15	261930
F118	F116	Fe-Mg	$\parallel$c	900	15	258840
F086	F055	Fe-Mg	$\parallel$c	800	15	517850
Fe-Mn						
F024	F022, F023	Fe-Mn		1100	15	15760
F029	F026, F027	Fe-Mn		1000	15	70390
F031	D008, D009	Fe-Mn		900	15	252730
F028	F026, F027	Fe-Mn		800	15	509590

[a] Ilmenite column indicates the synthesis experiment(s) for the starting polycrystalline ilmenite(s) in each diffusion couple. Run details for synthesis experiments have been provided in Appendix Table A.1.
[b] Direction describes whether the geikielite single crystal was oriented such that the interdiffusion occurred perpendicular to ($\perp$c) or parallel to ($\parallel$c) the c-axis.

Table 2.2: Average profile fitting results from n analytical traverses for each experiment. Reported uncertainty (1σ) was calculated using the two-sided 70% confidence interval student's t multiplier for $n-1$.

Experiment	T (°C)	polycrystal			single crystal		
		ln D (m²/s)	1σ	n	ln D (m²/s)	1σ	n
Fe-Mg $\perp$c							
F032	1200	−29.1	0.4	3	−30.0	0.7	3
MK24	1100	−30.3	0.6	3	−29.1	0.5	3
F111	1100	−30.5	1.0	2	−29.6	0.7	2
F045	1000	−31.7	1.0	2	−31.1	0.7	2
F110	1000	−31.5	0.4	3	−31.1	0.4	3
F119	1000	−31.8	0.5	3	−32.1	0.5	3
F030	900	−33.6	-	1	−33.1	0.8	2
F053	800	−34.7	-	1	−35.5	0.4	3
Fe-Mg $\parallel$c							
F018	1100	−28.7	0.7	2	−29.5	1.0	2
F019	1000	−30.3	0.8	2	−31.3	0.7	2
F117	1000	−31.4	0.6	3	n.d.	n.d.	n.d.
F033	900	−34.4	0.4	4	−33.0	0.3	4
F051	900	−34.9	0.5	4	−32.8	0.3	4
F118	900	−32.2	0.3	3	−32.8	0.4	3
F086	800	−34.1	0.3	3	−35.4	0.5	3
Fe-Mn							
F024	1100	−29.4	1.5	2			
F029	1000	−31.5	0.4	6			
F031	900	−34.4	0.6	4			
F028	800	−35.5	1.3	5			
F158	800	−34.7	0.7	4			
F102	800	−36.8	0.5	4			

n = number of profiles used to determined reported average lnD value and uncertainty. For experiments with only one traverse ($n = 1$), we assigned a 10% error as the standard deviation to be used in the weighted linear regression.
"n.d." indicates a diffusion coefficient was not determined for this sample.
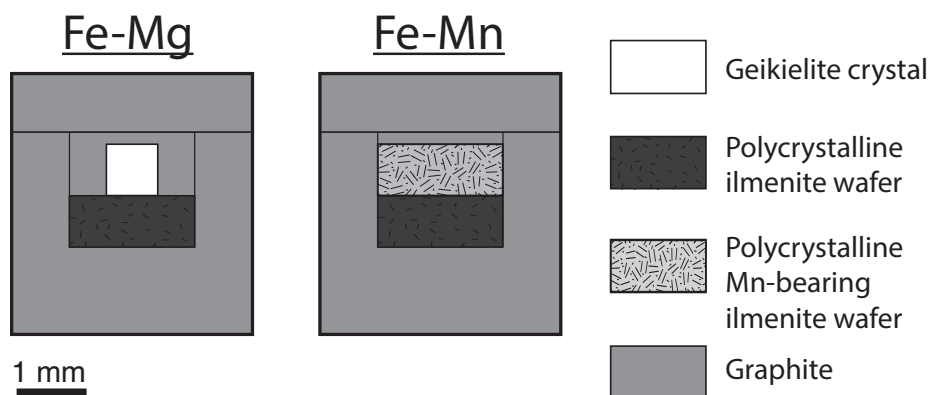
Figure 2.1: Schematic diagram of the experimental diffusion couple geometry. Each ilmenite polycrystal was polished then loaded into a graphite capsule such that the polished face would come into contact with the other half of the diffusion couple (Mn-bearing ilmenite polycrystal or geikielite single crystal). Geikielite single crystals were oriented such that the c-axis was either perpendicular or parallel to the diffusion interface. Graphite powder was used to fill the void space of each capsule and prevent the diffusion couple halves from separating during sample assembly.

Sample temperature was controlled to within $1-2°C$ of the reported temperature throughout the experiment, as monitored by a Eurotherm PID temperature controller. The difference between the Type-C (W-5%Re/W-26%Re) thermocouple reading and sample temperature for the experimental assembly was calibrated using the spinel reaction-progress thermometer (Watson et al. 2002). Experimental pressure was maintained during the experiment by an automatic pressure control system using the hot piston-in technique (Johannes et al. 1971). Experiments were quenched rapidly (approximately 70°C per second) by turning off the power to the apparatus. Experimental run duration was defined as the time between reaching the experimental target temperature and quench. Each experimental capsule was mounted in epoxy and cut perpendicular to the diffusion interface. Then, half of the capsule was mounted in epoxy and the cut face was polished in preparation for electron microprobe analysis.

2.2.2 Analytical methods

Experimental run products were analyzed using a JEOL 8200 electron microprobe at Washington University in St. Louis. Electron microprobe analyses were obtained perpendicularly across the diffusion interface for each experiment. Each quantitative analysis used a 15 kV accelerating potential, 25 nA beam current, and 45 second on-peak counting time. Standardization was performed with a beam diameter of 20 μm on natural and synthetic glass and mineral samples (synthetic Taylor MgO, synthetic Taylor spinel, synthetic Shankland forsterite, synthetic Mn-olivine, synthetic TiO_2, natural Elba Hematite, natural Ilmen Mountains ilmenite NMNH 96189, and natural Kakanui hornblende NMNH 143965). Minimum detection limits were $100 - 300$ ppm (3σ) for all elements. Each linear analytical traverse was positioned to avoid any accessory phases or large cracks in the diffusion couple. Multiple traverses were measured on each experiment in order to assess the consistency of the calculated diffusivities in a single sample. Beam diameter ($1 - 4$ μm) was set equal to half of the point spacing on each traverse to avoid point overlap (i.e., 2 μm beam diameter for 4 μm spacing). Compositional data were reduced using Probe for EPMA software (https://www.probesoftware.com) and then filtered to exclude analyses where the analytical totals were less than 98.5 wt.% or greater than 101.5 wt.%, as well as analyses where the cation total for 3 oxygen atoms were less than 1.98 or greater than 2.02 (ideal ilmenite stoichiometry contains 2 cations per 3 oxygen atoms). Two experiments, F045 and F051, have low analytical totals ($93 - 97$ wt.%), and these are discussed in Section 2.4.3. A detailed discussion of analytical totals is presented in Appendix A.

2.2.3 Numerical analysis of diffusion profiles

Elemental concentration profiles (Fe and Mg or Mn) were used to determine the Fe-Mg or Fe-Mn interdiffusion coefficient for each experiment. Diffusion was modeled as one-dimensional, concentration-independent diffusion in a semi-infinite medium with constant interface concentration (Crank 1975):

$$\frac{C(x,t) - C_{\text{initial}}}{C_{\text{interface}} - C_{\text{initial}}} = erf \frac{x}{2\sqrt{Dt}} \tag{2.1}$$

where D is the interdiffusion coefficient ($\text{m}^2 \text{ s}^{-1}$), $C(x,t)$ is the concentration (mol m^{-3}) at position x (m) after the experimental run time t (s), C_{initial} is the initial concentration on one side of the diffusion couple (e.g., $C_{\text{initial}} = 1$ for mol $MgTiO_3$ in geikielite), and $C_{\text{interface}}$ is the concentration at the diffusion couple interface. This treatment is valid as long as the experimental diffusion profile levels out to the initial concentration in the crystal. In our experiments, the length of the observed concentration profiles on each side of the diffusion interface (<300 μm) is less than the length of the single geikielite crystal or ilmenite polycrystal (>500 μm).

To determine the interdiffusion coefficient for each compositional profile, the diffusion profile was linearized by plotting the inverse of the error function,

$$erf^{-1} \frac{C_{\text{interface}} - C(x,t)}{C_{\text{interface}} - C_{\text{initial}}} \tag{2.2}$$

against position (x) for each half of the diffusion couple. The values for $C_{\text{interface}}$ and C_{initial} were determined from the electron microprobe compositional analyses on each experiment. Then, fitting a straight line to the linearized compositional profile gave the slope, $(4Dt)^{-1/2}$, from which D was calculated for each half of the diffusion couple.
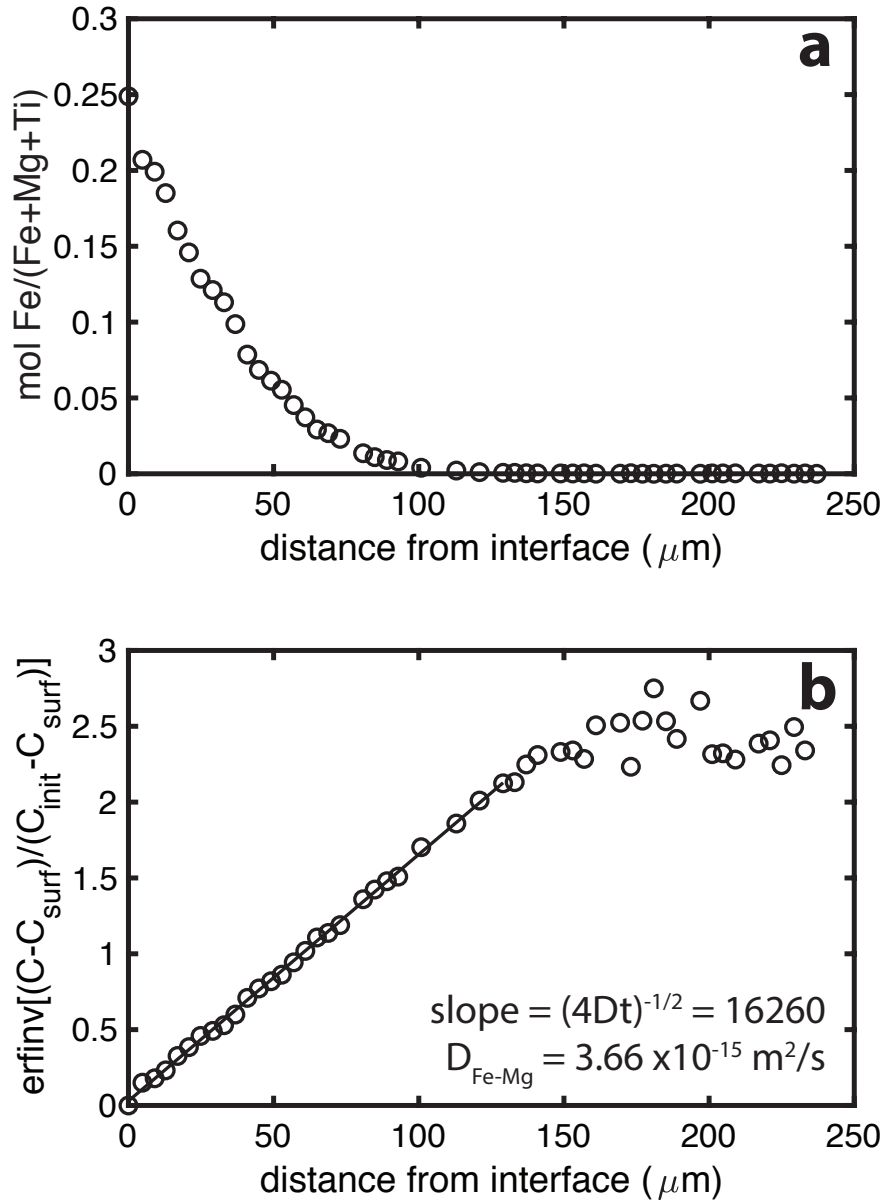
Figure 2.2: a) Analytical traverse taken in the geikielite single crystal from experiment F030 (analysis line 2). The analyses are plotted as Fe mol fraction (mol Fe / (mol Fe + mol Mg + mol Ti). Analytical uncertainty is smaller than the size of the data symbols. b) Inverse error function plot of the profile in (a). The line through the points represents the linear fit from which $D_{\text{Fe-Mg}}$ was determined (as described in Section 2.2.3).

The compositions used for the diffusion profile fitting were the measured Fe and Mn atomic percents (Fe for Fe-Mg interdiffusion, Mn for Fe-Mn interdiffusion), which, unlike using molecular compositions of $FeTiO_3$, avoids any assumption regarding the oxidation state of Fe in each sample. Fits using the molecular compositions, $FeTiO_3$ and $MnTiO_3$, yield similar D values for experiments for which there was no hematite component. Often the two halves of the diffusion couple separated during decompression after the experimental run, resulting in a gap (<35 μm width) along the diffusion interface (Figure 2.3b). Prior to fitting, the x values for the measured diffusion profiles were adjusted by subtracting the gap distance (as measured from back-scattered electron image) so that the compositional profiles measured on each side of the diffusion couple met near the defined diffusion interface, $x = 0$. The position and compositional data for each diffusion profile have been provided in an electronic file available in the data repository at espm.wustl.edu/data (discussed in Appendix A).
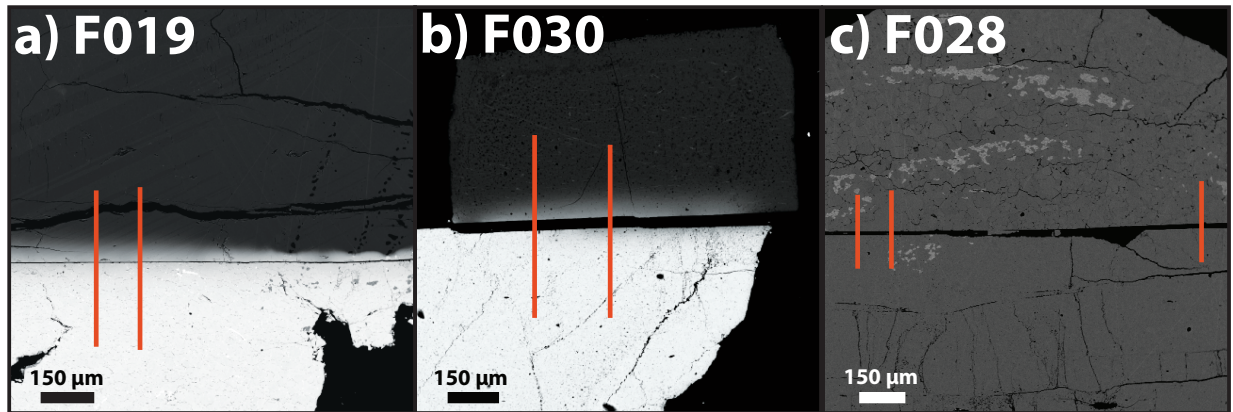
Figure 2.3: Back-scattered electron images for two Fe-Mg interdiffusion experiments (F019, a and F030, b), and one Fe-Mn interdiffusion experiment (F028, c). Each experiment is marked with red lines to indicate the location of the electron microprobe traverses positioned on each sample. For the two Fe-Mg interdiffusion experiments, the dark side of the couple is the geikielite single crystal ($MgTiO_3$) and the bright side of the couple is the ilmenite polycrystal ($FeTiO_3$). a) Cracks form parallel to the diffusion interface during decompression of the experiment. For profiles that go across decompression cracks, we have adjusted the distance from the interface used in the profile fitting by subtracting the width of the crack for analyses taken on the side of the crack away from the interface. b) Often, the two sides of the diffusion couple separate during decompression. Before fitting the profiles, we adjust the profile distances by subtracting the width of the gap. The thin bright phases in the geikielite single crystal are rutile (TiO_2). c) The Mn-bearing ilmenite polycrystal is positioned on the top in this image. The bright gray phase present in both polycrystals, though of greater abundance in the Mn-bearing ilmenite, is ulvöspinel (Fe_2TiO_4).

2.3 Results

The interdiffusion coefficients determined in each experiment are reported in Table 2.2. For each experiment, the reported $D_{\text{Fe-Mg}}$ or $D_{\text{Fe-Mn}}$ is the average value obtained from multiple profiles across the interface in the diffusion couple and the "uncertainty" is defined by the standard deviation of the results from n traverses multiplied by a student's t-value that corresponds to a two-sided 70% confidence interval for $n - 1$ traverses. For experiments with only one traverse ($n = 1$), we assigned a 10% error as the standard deviation to be used in the weighted linear regression. Some profiles exhibit slight asymmetry with respect to the diffusion interface, suggesting there may be a compositional dependence for the interdiffusion coefficients. However, we were not able to quantify this compositional dependence, and if any compositional dependence exists, it is minor.

Ulvöspinel (Fe_2TiO_4) was present as an accessory phase in the polycrystalline sides of the experimental run products, most notably in the Mn-bearing diffusion couples (Figure 2.3c). Additionally, the geikielite in experiment F032 contained minor amounts of qandilite (Mg_2TiO_4). Qandilite has been noted to occur as an accessory phase in the geikielite starting material (Mitchell et al. 1998). We only observed qandilite in this experiment (F032), and we suspect the presence of qandilite has slightly affected the diffusion in the geikielite single crystal. In order to obtain interdiffusion coefficients that best represent diffusion in the ilmenite phase, electron microprobe traverses were positioned in regions of the experimental run product that were free of any accessory phases (Figure 2.3). Thus, the presence or exsolution of accessory phases during the experiment has little effect on the calculated cation diffusion rates.

2.3.1 Time series

An isothermal time series of experiments was conducted at 1000°C to evaluate the repro-
ducibility of the calculated interdiffusion coefficients (Figure 2.4). The time series investigated
Fe-Mg diffusion with the geikielite crystal oriented such that diffusion was perpendicular to
the c-axis. Run durations ranged from 1 to 6 days (Table 2.2). The interdiffusion coefficients
calculated for the ilmenite side of the 1-, 3-, and 6-day experiments are the same within the
estimated uncertainty. Further, the interdiffusion coefficient calculated from the geikielite
side of the 6-day experiment is within the estimated uncertainty of those calculated from
the ilmenite side. The interdiffusion coefficient calculated for the geikielite side of the 1-day
experiment is similar to that calculated from the 3-day experiment. Two additional Fe-Mg
interdiffusion experiments (MK24 and F111) are included in Figure 2.4. These experiments
were both conducted at 1100°C with varied run durations (approximately 6 hours and 1
day, respectively). Again, the results from the ilmenite and geikielite sides are within the
estimated uncertainty for the two time points.

2.3.2 Temperature dependence

The experimentally determined interdiffusion coefficients, D_{Fe-Mg} or D_{Fe-Mn}, for each diffusion
couple type have been fit separately to the Arrhenius equation:

$$lnD = lnD_0 - \frac{Q}{RT} \tag{2.3}$$

where D_0 is the pre-exponential factor (m^2 s^{-1}), Q is the activation energy (J mol^{-1}), R is
the universal gas constant (J mol^{-1} K^{-1}) and T is temperature (K). The activation energy
and pre-exponential factor for each set of experiments was determined by linear regression
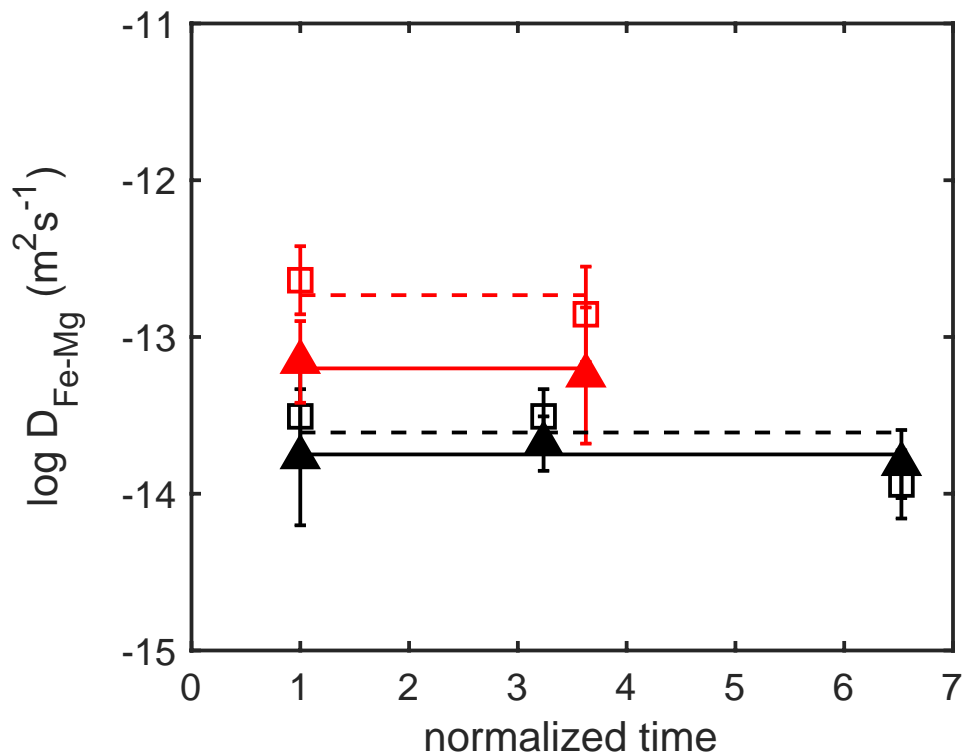
Figure 2.4: Diffusion coefficients determined from time series experiments at 1000°C (black) and 1100°C (red). The results are plotted against the run duration normalized to the duration of the shortest experiment in the time series. Open squares indicate the results from the geikielite single crystal. Closed triangles represent the results obtained from the ilmenite polycrystal. The plotted uncertainty is the 70% confidence interval reported in Table 2.2.

Table 2.3: Experimentally-determined Arrhenius fit parameters and uncertainties. Reported uncertainty (1σ) was calculated from a weighted linear regression of the values reported in Table 2.2. For Fe-Mg interdiffusion, the bold values represent the parameters calculated from a weighted linear regression through the data from both orientations. For Fe-Mn interdiffusion, the bold values represent the parameters determined from the weighted linear regression through data from both sides of the experiment. The bold values have been used to plot the solid lines in Figures 2.5-2.7.

Type	Q (kJ/mol)	log D_0 (m^2/s)
Fe-Mg		
geikielite $\perp$c	224 ± 20	-4.5 ± 0.8
geikielite $\|$c	239 ± 39	-3.6 ± 1.7
	$\mathbf{220 \pm 16}$	$\mathbf{-4.6 \pm 0.7}$
ilmenite	$\mathbf{188 \pm 15}$	$\mathbf{-6.0 \pm 0.6}$
Fe-Mn		
ilmenite	262 ± 30	-3.0 ± 1.2
Mn-ilmenite	241 ± 34	-3.6 ± 1.4
	$\mathbf{264 \pm 30}$	$\mathbf{-2.9 \pm 1.3}$

(Table 2.3). The method of weighted least squares and the uncertainty on the average D from each experiment (reported in Table 2.2) were used to estimate the uncertainty on the calculated activation energy and D_0 for each diffusion couple type (Table 2.3).

Fe-Mg interdiffusion

The difference in the experimental design for the two sets of Fe-Mg interdiffusion experiments was the orientation of the geikielite crystal (with diffusion either perpendicular or parallel to the c-axis). For Fe-Mg interdiffusion experiments, the results from the ilmenite polycrystal side of the diffusion couple are often the same as those from the geikielite single crystal within the estimated uncertainty (Table 2.2). The molar concentration of Ti in the geikielite (approximately $1.00 - 1.02$ Ti cations per 3 oxygens) is slightly higher than that in the ilmenite
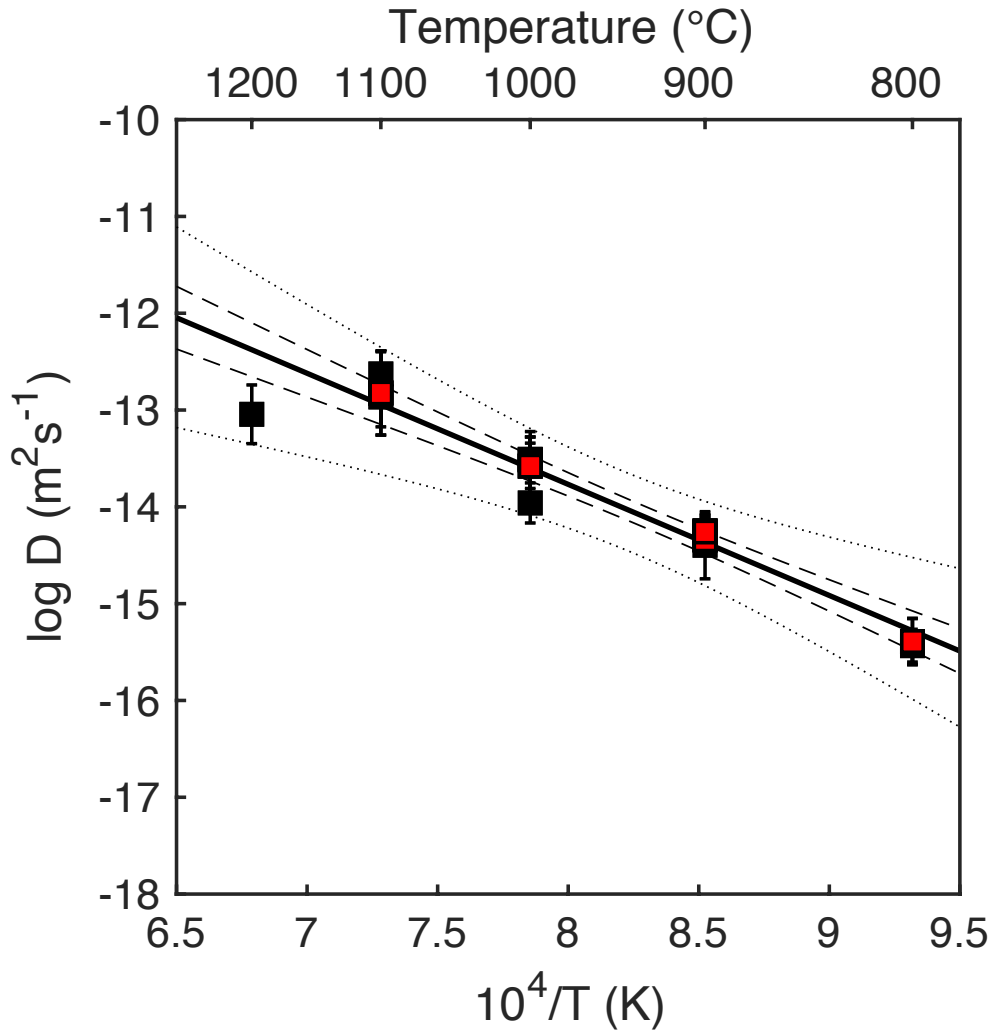
Figure 2.5: Arrhenius plot of results for Fe-Mg interdiffusion in the geikielite single crystal. Each square represents the average interdiffusion coefficient calculated for a given experiment, and the plotted uncertainty is the 70% confidence interval reported in Table 2.2. The black squares are for experiments where the geikielite was oriented such that diffusion occurred perpendicular to the c-axis ($\perp$c), and the red squares are for experiments where the geikielite was oriented such that diffusion occurred parallel to the c-axis ($\parallel$c). The solid line depicts the weighted linear regression through all points (both red and black), and the dashed lines show the uncertainty on this fit (70% confidence interval). The dotted lines depict the uncertainty on the linear fit at the 95% confidence interval.

23
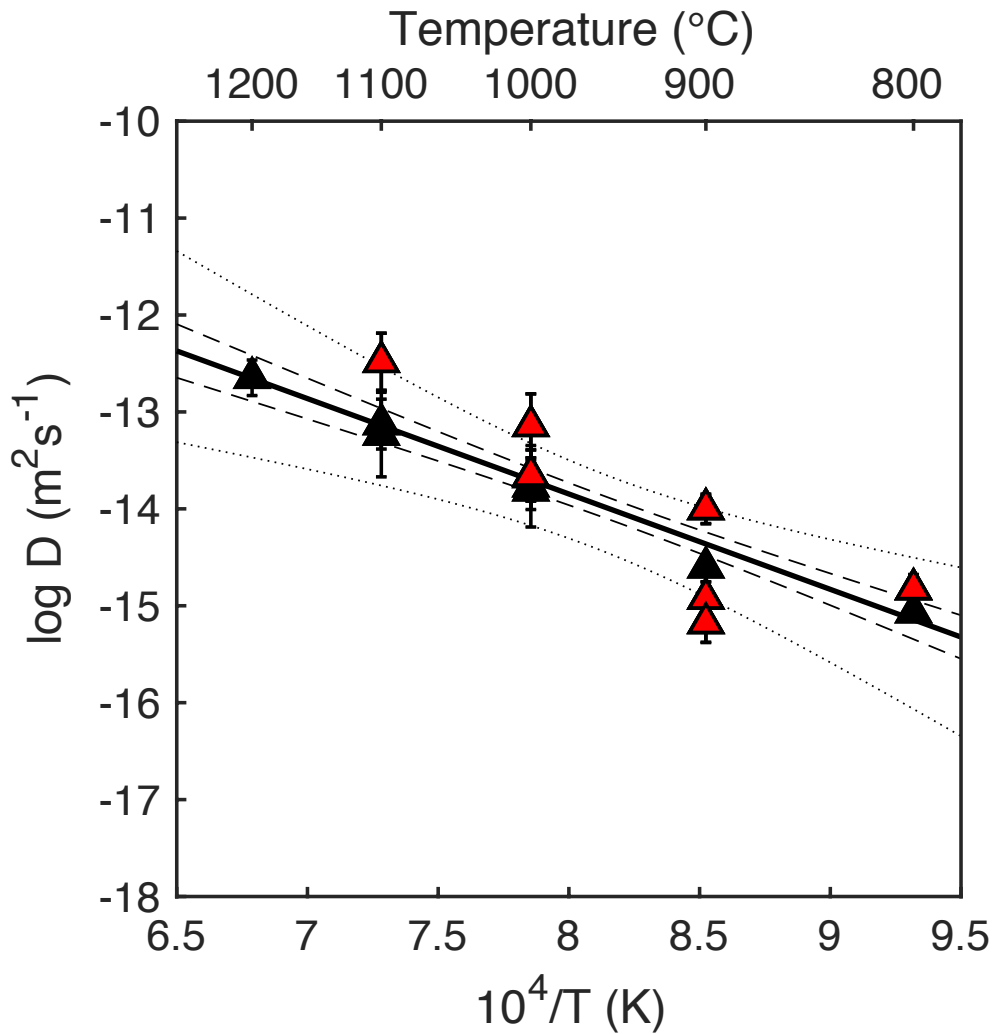
Figure 2.6: Arrhenius plot of results for Fe-Mg interdiffusion in the ilmenite polycrystal. Each triangle represents the average interdiffusion coefficient calculated for a given experiment, and the plotted uncertainty is the 70% confidence interval reported in Table 2.2. The black triangles are for experiments where the geikielite was oriented such that diffusion occurred perpendicular to the c-axis ($\perp$c), and the red triangles are for experiments where the geikielite was oriented such that diffusion occurred parallel to the c-axis ($\parallel$c). The solid line depicts the weighted linear regression through all points (both red and black), and the dashed lines show the uncertainty on this fit (70% confidence interval). The dotted lines depict the uncertainty on the linear fit at the 95% confidence interval.

(approximately $0.98 - 1.00$ Ti cations per 3 oxygens). The Ti excess in the geikielite single crystal results from the method used to synthesize the crystal (Mitchell et al. 1998). Because the geikielite crystal has a higher Ti concentration than the ilmenite polycrystal and the diffusion coefficients might depend on Ti concentration, the two sides of the diffusion couple have been treated separately for the Arrhenius fits. Potential effects of Ti concentration on Fe-Mg interdiffusion are discussed in Section 2.4.3.

The results for Fe-Mg interdiffusion in the geikielite single crystal are similar for the two geikielite orientations, with $Q = 224 \pm 20$ kJ/mol and $logD_0 = -4.5 \pm 0.8$ m^2/s for diffusion perpendicular to the c-axis, and $Q = 239 \pm 39$ kJ/mol and $logD_0 = -3.6 \pm 1.7$ m^2/s for diffusion parallel to the c-axis. Thus, any crystallographic orientation effect on Fe-Mg interdiffusion in the geikielite single crystal was not evident in our results.

For Fe-Mg interdiffusion in the ilmenite polycrystal, we determined that $Q = 188 \pm 15$ kJ/mol and $logD_0 = -6.0 \pm 0.6$ m^2/s. The reported averages and uncertainties were calculated using the diffusion profile fitting results from the ilmenite polycrystals in both sets of Fe-Mg interdiffusion experiments ($\perp$c and $\|$c). Though slight differences exist for the two orientations (Figure 2.6), the calculated temperature dependence for each orientation was the same within uncertainty ($Q = 191 \pm 23$ kJ/mol and $logD_0 = -5.9 \pm 0.9$ m^2/s for experiments where the geikielite was oriented with diffusion perpendicular to the c-axis; $Q = 196 \pm 25$ kJ/mol and $logD_0 = -5.6 \pm 1.1$ m^2/s for experiments where the geikielite was oriented with diffusion parallel to the c-axis). Comparing the results for the temperature dependence of Fe-Mg interdiffusion calculated for ilmenite and geikielite, we find that there is a small yet resolvable difference, with the activation energy for diffusion in the ilmenite polycrystal being lower than that for the geikielite single crystals.
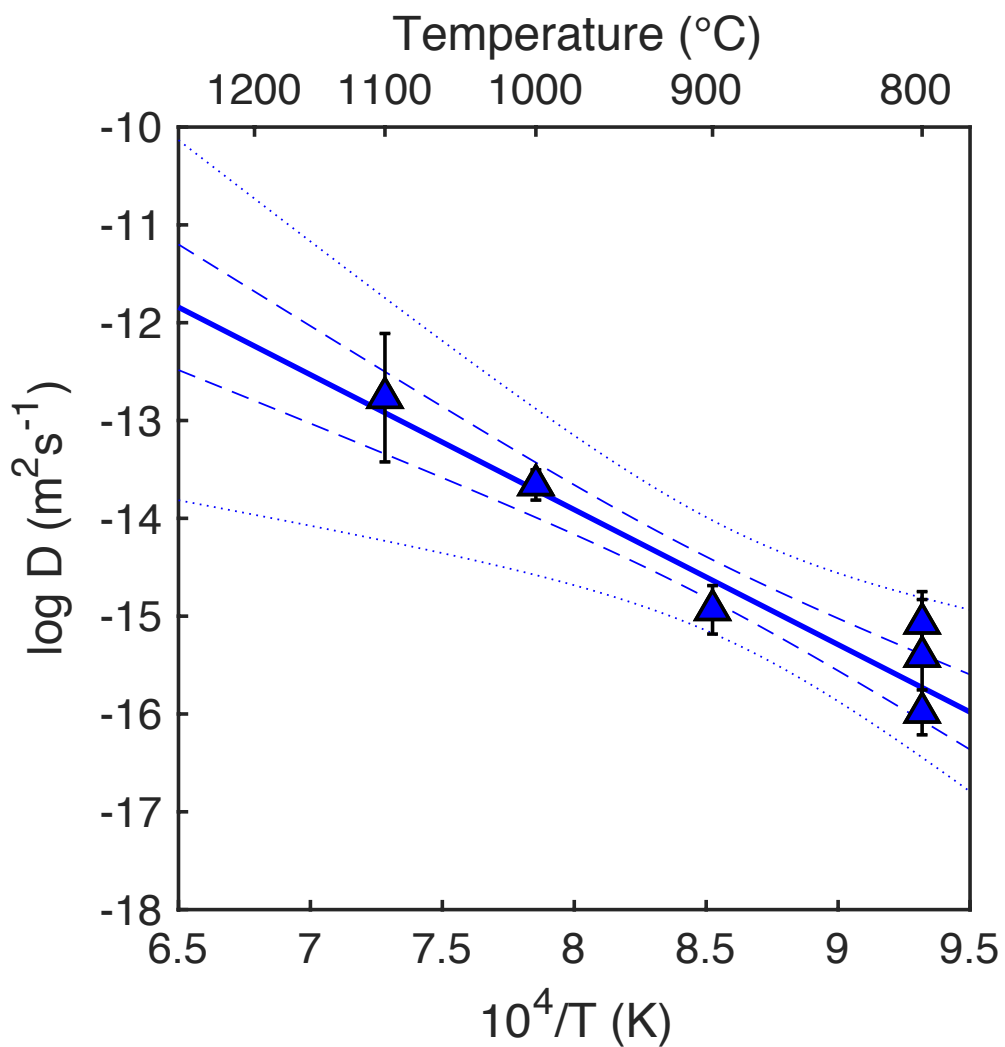
Figure 2.7: Arrhenius plot of results for Fe-Mn interdiffusion in the ilmenite and Mn-ilmenite polycrystals. Each triangle represents the average interdiffusion coefficient calculated from the ilmenite and Mn-bearing ilmenite polycrystals in a given experiment, and the plotted uncertainty is the 70% confidence interval reported in Table 2.2. The solid line depicts the weighted linear regressions through all points, and the dashed lines show the uncertainty on this fit (70% confidence interval). The dotted lines depict the uncertainty on the linear fit at the 95% confidence interval.

Fe-Mn interdiffusion

For Fe-Mn interdiffusion, our experimental results yield $Q = 264 \pm 30$ kJ/mol and $logD_0$ $= -2.9 \pm 1.3$ m^2/s. The reported averages and uncertainties were calculated using the diffusion profile fitting results from both sides of the diffusion couple (ilmenite polycrystal and Mn-bearing ilmenite polycrystal). When treated separately, the results from each side are the same within uncertainty. Manganese is present at low concentrations in the Fe-Mn interdiffusion experiments, and thus behaves as a trace (not major) component. We did not find a Mn concentration dependence for Fe-Mn diffusion.

2.4   Discussion

2.4.1   Comparison to diffusion in hematite

One important distinction between ilmenite and hematite is the oxidation state of Fe, with all Fe^{2+} in pure ilmenite and all Fe^{3+} in pure hematite. Experimental studies of diffusion in hematite indicate that the diffusivity of Fe in hematite decreases with increasing oxygen fugacity (f_{O_2}) (Atkinson and Taylor 1985; Amami et al. 1999; Sabioni et al. 2005). This relationship between diffusion and f_{O_2} suggests that Fe diffusion occurs by a diffusion mechanism involving interstitial sites, rather than a vacancy mechanism. Similar to the equation for cation vacancy formation in magnetite (Aggarwal and Dieckmann 2002), the formation of cation vacancies in ilmenite-hematite solid solution by oxidation of Fe^{2+} to Fe^{3+} can be written as:

$$3\,\text{Fe}^{2+} + \tfrac{3}{4}\,\text{O}_2 \longleftrightarrow 2\,\text{Fe}^{3+} + \text{V}_\text{M} + \tfrac{1}{2}\,\text{Fe}_2\text{O}_3$$

where V_M represents a vacant cation site. This reaction indicates that diffusion through cation vacancies would be faster at higher f_{O_2} because oxygen promotes cation vacancy formation. However, previous studies have determined Fe diffusion in hematite to be slower at higher oxygen fugacities, which indicates that the diffusion of Fe in hematite occurs by cation interstitials rather than cation vacancies (see Section 2.4.3 for additional discussion of diffusion mechanisms).

The activation energies reported from experimental studies of Fe self-diffusion parallel to the c-axis in hematite single crystals range from 510 to 579 kJ/mol for temperatures between 900°C and 1300°C (Sabioni et al. 2005; Amami et al. 1999; Atkinson and Taylor 1985). Atkinson and Taylor (1985) found that the activation energy for Fe diffusion in hematite was lower (174 kJ/mol) at temperatures below 900°C and attributed this change to impurities or point defects, concluding that the high-temperature behavior was more characteristic of pure hematite. Sabioni et al. (2005) found that Fe diffusion in hematite varies as a function of crystallographic orientation, with diffusion perpendicular to the c-axis having an activation energy of 430 kJ/mol. Further, Sabioni et al. (2005) found that between 900°C and 1100°C diffusion perpendicular to the c-axis is slower than diffusion parallel to the c-axis in hematite. These activation energies are approximately double that of Fe-Mg interdiffusion in ilmenite (Section 2.3.2). Because of the difference in activation energies and D_0 for Fe diffusion in hematite and ilmenite, Fe diffusion will be faster in hematite above 1100°C and faster in ilmenite below 1100°C (Figure 2.8).

2.4.2 Comparison to diffusion in magnetite and titanomagnetite

Cation diffusivities in magnetite have been experimentally determined and characterized as a function of temperature, f_{O_2} and composition (Van Orman and Crispin 2010, and references therein). At f_{O_2} near the wüstite-magnetite (WM) buffer, Fe and Mn diffusion in magnetite
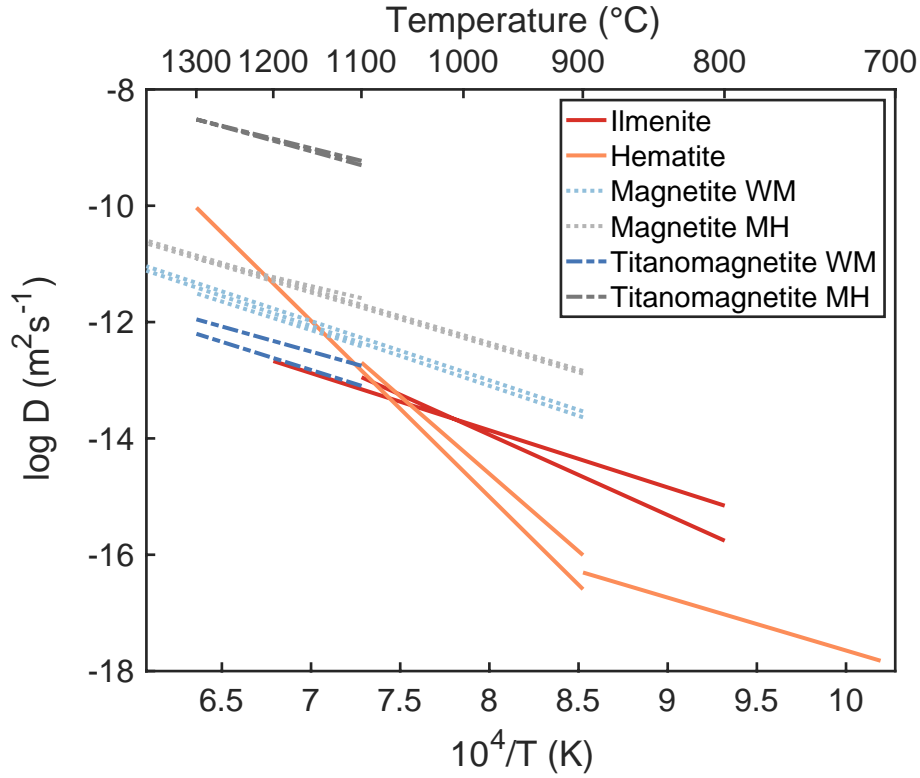
Figure 2.8: Comparison of results for diffusion in ilmenite, hematite, magnetite, and titanomagnetite. For ilmenite, one line represents the average of our reported results for Fe-Mg interdiffusion in ilmenite, and one line represents our reported results for Fe-Mn interdiffusion (bolded values in Table 2.3). For hematite, the Fe diffusivity parallel to the c-axis is plotted using values from Atkinson and Taylor (1985) and Sabioni et al. (2005). For magnetite, the lines represent the literature values for Fe and Mn diffusivity at the wüstite-magnetite (WM) and magnetite-hematite (MH) buffers from Dieckmann and Schmalzried (1977) and Aggarwal and Dieckmann (2002). For titanomagnetite ($X_{Ti} = 0.2$), the lines represent the literature values for Fe and Mn diffusivity at the wüstite-magnetite (WM) and magnetite-hematite (MH) buffers from Aggarwal and Dieckmann (2002).

occurs by a diffusion mechanism involving interstitial sites, similar to diffusion in hematite. In contrast, Fe and Mn diffusion in magnetite dominantly occurs via vacancies at f_{O_2} near the magnetite-hematite buffer. Further, at reducing conditions, cation diffusion rates in magnetite are similar to that in titanomagnetite; however, at more oxidizing conditions diffusion in titanomagnetite is faster than in magnetite because the presence of Ti^{4+} promotes the formation of vacancies.

The activation energies for Fe diffusion in magnetite range from 148 to 230 kJ/mol (Himmel et al. 1953; Izbekov 1958; Ogawa et al. 1968; Dieckmann and Schmalzried 1977; Aggarwal and Dieckmann 2002). Aggarwal and Dieckmann (2002) determined the activation energies for Mn and Ti diffusion in magnetite (Mn, $140 - 188$ kJ/mol; Ti, $208 - 267$ kJ/mol), as well as for Fe and Mn diffusion in titanomagnetite ($X_{Ti} = 0.2$; Fe, $147 - 165$ kJ/mol; Mn, $163 - 185$ kJ/mol). Our experimentally determined activation energy for Fe-Mg in the ilmenite polycrystal (188 ± 15 kJ/mol) is within range of those reported for Fe and Mn diffusion in magnetite and titanomagnetite. The activation energy for Fe-Mg interdiffusion in ilmenite is also similar to that reported for Fe-Mg interdiffusion in synthetic spinel (219 ± 18 kJ/mol Vogt et al. 2015). Our reported activation energy for Fe-Mn interdiffusion in ilmenite (264 ± 30 kJ/mol) is greater than the activation energies reported for Fe and Mn diffusion in magnetite and titanomagnetite, but similar to those reported for Ti diffusion in titanomagnetite. Additionally, the activation energies calculated for Fe-Mg interdiffusion in the geikielite single crystals (224 ± 20 kJ/moland 239 ± 39 kJ/mol) are within range of those reported for Ti diffusion in titanomagnetite.

Coexisting iron-titanium oxides are widely used to estimate pre-eruptive temperatures and oxygen fugacities in volcanic systems (Fish Canyon Tuff, Bishop Tuff, Soufrière Hills, Pinatubo, Mt. Unzen, Mt. St. Helens, Mt. Pelée, and many more). This geothermometer and oxybarometer is based on the exchange of Fe and Ti between coexisting rhombohedral oxide

(ilmenite-hematite solid solution) and spinel (magnetite-ulvöspinel solid solution) phases. Our Fe-Mg and Fe-Mn interdiffusion coefficients were determined between 800°C and 1100°C, which overlaps the range of natural magmatic temperatures relevant to two-oxide equilibration (geothermometer initially calibrated between 600°C to 1000°C, Buddington and Lindsley 1964). Ghiorso and Evans (2008) found that for a database of 730 natural oxide pairs, the estimated oxygen fugacities relative to the nickel-nickel oxide buffer (NNO) fell within NNO±2. For temperatures $600 - 1000$°C this range of oxygen fugacities corresponds to WM+0.5 to WM+7.5. At oxygen fugacities above the wüstite-magnetite buffer, diffusion of Fe and Mn in titanomagnetite is faster than Fe and Mn diffusion in ilmenite and this difference increases with f_{O_2} (Figure 2.8). At temperatures below 1000°C, cation diffusion in ilmenite is faster than diffusion in hematite (Figure 2.8). As f_{O_2} increases, the ilmenite solid solution will become more enriched in the hematite component, and the diffusion rates will decrease. In this way, the cation diffusivities in hemo-ilmenite and titanomagnetite will "diverge" at lower temperature and higher f_{O_2}, and equilibration between the two oxides will be rate limited by diffusion in the rhombohedral oxide.

2.4.3 Potential diffusion mechanisms for Fe, Mg, and Mn in ilmenite

Diffusive exchange of Fe^{2+} and Mg^{2+} or Mn^{2+} cations in ilmenite occurs by a mechanism involving either cation interstitials or cation vacancies. Our experiments were not designed to elucidate the diffusion mechanism, and additional investigation over a range of oxygen fugacities and ilmenite compositions is needed in order to draw strong conclusions. However, here we briefly discuss potential reactions for the formation of cation interstitials and vacancies in ilmenite to provide insight into potential diffusion mechanisms and how diffusivity would vary with composition for each.

Similar to the equation for the formation of cation interstitial defects in hematite (Atkinson and Taylor 1985), the formation of cation interstitials in ilmenite may occur through the reaction:

$$\mathrm{Fe}_{\mathrm{Fe}}^{\times} + 3\,\mathrm{O}_{\mathrm{O}}^{\times} \longleftrightarrow \mathrm{Fe}_{\mathrm{i}}^{\bullet\bullet} + 2\,e' + \tfrac{3}{2}\,\mathrm{O}_2$$
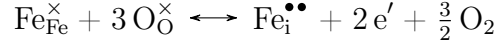
where $\mathrm{Fe}_{\mathrm{Fe}}^{\times}$ denotes Fe residing in a cation site, and $\mathrm{Fe}_{\mathrm{i}}^{\bullet\bullet}$ represents an interstitial Fe with $+2$ charge balanced by two electrons (e'). Here, the interstitial is on the same side of the equation as O_2. Thus, as oxygen fugacity increases, the reaction goes to the left side and the concentration of cation interstitials decreases. Minor oxidation during two of our diffusion annealing experiments may have increased the amount of Fe^{3+} in the ilmenite of those experiments and affected our diffusion results. For experiments F045 and F051, ilmenite analyses with low analytical totals, Ti cation totals <1, and Fe cation totals >1 result from a minor hematite component in the ilmenite (<4 and <2 mol% $\mathrm{Fe}_2\mathrm{O}_3$, respectively). At a given temperature, the calculated Fe-Mg interdiffusion coefficients are lower for experimental ilmenites that contained a minor hematite component (though still within our estimated uncertainty).

Titanium-induced cation vacancies in the geikielite single crystal may explain why diffusion in the geikielite single crystals was faster than in the ilmenite polycrystal and why the results for both geikielite orientations were consistent. Excess Ti in ilmenite would promote the formation of cation vacancies by the reaction:

$$2\,\mathrm{M}_{\mathrm{A}}^{\times} + \mathrm{TiO}_2 \longleftrightarrow \mathrm{Ti}_{\mathrm{A}}^{\bullet\bullet} + \mathrm{V}_{\mathrm{A}}'' + 2\,\mathrm{MO}$$
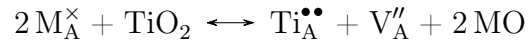
where M in the equation denotes Fe^{2+}, Mg^{2+}, or Mn^{2+} cations. Here, the excess Ti^{4+} resides in A^{2+} sites ($\mathrm{Ti}_{\mathrm{A}}^{\bullet\bullet}$), promoting A-site cation vacancies ($\mathrm{V}_{\mathrm{A}}''$) to maintain charge
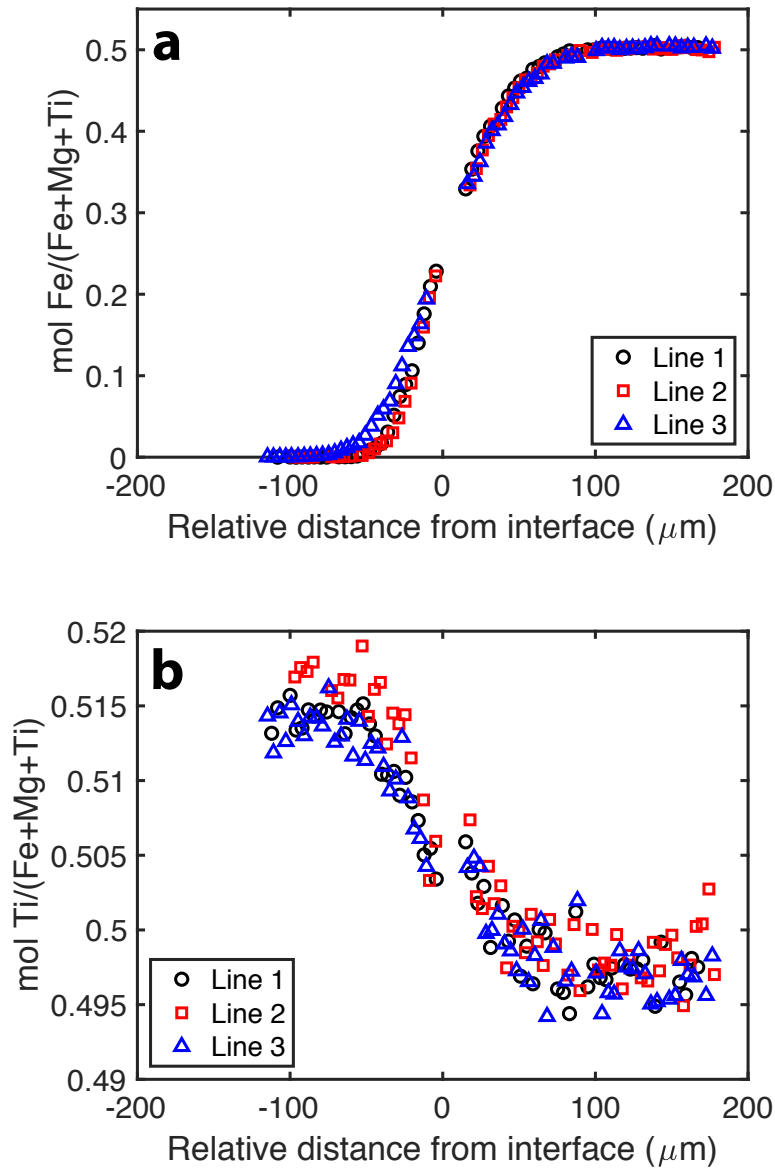
Figure 2.9: Electron microprobe analyses of experiment F032 plotted as a function of distance from the diffusion interface. a) Three Fe concentration profiles for the diffusion couple. b) The observed Ti concentration gradient for each analytical traverse in (a), with greater Ti concentration in the geikielite side of the diffusion couple.

balance. In our diffusion annealing experiments the molar concentration of Ti in the geikielite (approximately $1.00 - 1.02$ Ti cations per 3 oxygens) is higher than that in the ilmenite (approximately $0.98 - 1.00$ Ti cations per 3 oxygens). In many of the Fe-Mg experiments, there is slight zoning in Ti concentrations decreasing from the geikielite across the interface into the ilmenite, suggesting Ti may have diffused from the geikielite single crystal into the ilmenite polycrystal (Figure 2.9). Diffusion involving Ti-induced cation vacancies may explain why the diffusion in the ilmenite polycrystal is slower than that in the geikielite crystal for these experiments. Titanium concentration profiles are not observed for any of the Fe-Mn interdiffusion experiments.

There is potential for grain boundary diffusion to enhance diffusion rates in the ilmenite polycrystal relative to the geikielite single crystal, but we did not observe evidence for this mechanism having a significant effect on our results. Although the ilmenite polycrystals from two experiments conducted at the same temperature ($1000°C$, F019 and F045) exhibit different grain sizes (Appendix Figure A.1), the calculated Fe-Mg interdiffusion coefficients are the same within uncertainty (Table 2.2). Additionally, there were no changes in concentration corresponding to the location of grain boundaries in the electron microprobe traverses on the ilmenite polycrystals from our experiments. Previous comparisons of single crystal and polycrystalline studies for Fe diffusion in hematite have similarly concluded that there is no contribution from rapid grain boundary diffusion (Atkinson and Taylor 1985).

Our experimental results cannot conclusively determine which mechanism is controlling the diffusion of cations in ilmenite, however there are two important observations to consider: (1) the presence of Fe^{3+} in two of the ilmenite polycrystals resulted in decreased diffusivity in the ilmenite compared to the geikielite, and (2) titanium excess in the geikielite single crystals can promote cation vacancy formation and may explain why diffusion in the geikielite is faster than that in the ilmenite.

2.5 Applications

Moving forward we will apply our experimentally determined diffusion rates to natural ilmenite-bearing systems. Coupling our experimentally determined diffusion coefficients with preserved chemical disequilibria in natural ilmenites provides a mechanism by which to constrain the timing of perturbations in magmatic systems. For Fe-Mg interdiffusion we will use an activation energy of 188 kJ/mol and $logD_0$ of -6.0 m^2/s, which is the value obtained from the weighted linear regression through the diffusion results from the polycrystalline ilmenite side of our diffusion couple experiments (Table 2.3). We are using the Arrhenius curve from the ilmenite side of the diffusion couple because the composition of natural ilmenite crystals is more similar to the composition of the ilmenite polycrystal than the geikielite single crystal. For Fe-Mn interdiffusion we will use the parameters determined by the weighted linear regression through data from both sides of the diffusion couple ($Q = 264$ kJ/mol and $logD_0 = -2.9$ m^2/s).

2.5.1 Application to natural disequilibrium oxide pairs

Disequilibrium within an oxide crystal or between pairs is often interpreted to be a result of disturbances in the magmatic plumbing system such as injection of new magma, devolatilization, and decompression (Gardner et al. 1995; Nakamura 1995; Pallister et al. 1996; Venezky and Rutherford 1999; Devine et al. 2003; Blundy et al. 2006; Pallister et al. 2008). These perturbations are potential precursors to eruptions or changes in eruption style, and thus are important to recognize and understand (Wark et al. 2007; Bachmann and Bergantz 2008; Cashman and Sparks 2013).

A test for oxide pair equilibria was developed by Bacon and Hirschmann (1988) from the magnesium and manganese compositions of natural oxide pairs (hemo-ilmenite and titanomagnetite). Natural oxide pair compositions that fall off of this equilibrium line are often not reported. However, they have been found in many eruptive centers, including but not limited to Mt. St. Helens, Mt. Unzen, the Bishop Tuff, and the Fish Canyon Tuff (Ghiorso and Evans 2008). Titanium zoning in natural hemo-ilmenites and titanomagnetites provides additional evidence for oxide disequilibrium in volcanic samples from Mt. Unzen, Mt. St. Helens, Mt. Pinatubo, and Soufrière Hills (Gardner et al. 1995; Nakamura 1995; Pallister et al. 1996; Venezky and Rutherford 1999; Devine et al. 2003; Pallister et al. 2008; Rutherford and Devine III 2008). In practice, oxide pair compositions that do not fall on the empirical line defined by Bacon and Hirschmann (1988) are not used for geothermometry and oxybarometry. However, this oxide pair disequilibrium can instead place constraints on the conditions and timescales of volcanic processes, provided the diffusivities of Mg and Mn are known for both magnetite and ilmenite.

In order to preserve disequilibria in oxides, the time between perturbation and volcanic eruption must be shorter than the rate of mineral equilibration via diffusion. Silicate minerals preserve compositional evidence for temperature perturbations in a magmatic system on time scales that range from months to millions of years (Costa et al. 2008, and references therein). Cation diffusion in Fe-Ti oxides is faster than in silicate minerals, and compositional zoning will be diffusively equilibrated on short time scales (hours to months). Thus, oxide disequilibria record instances where the time between a thermal pulse and eruption is short. Determining the timescales of oxide equilibration can constrain the time between these two events.

Using our experimentally determined Fe-Mn interdiffusivities for ilmenite, we can model the time- and temperature-dependent equilibration of an ilmenite grain as a function of grain
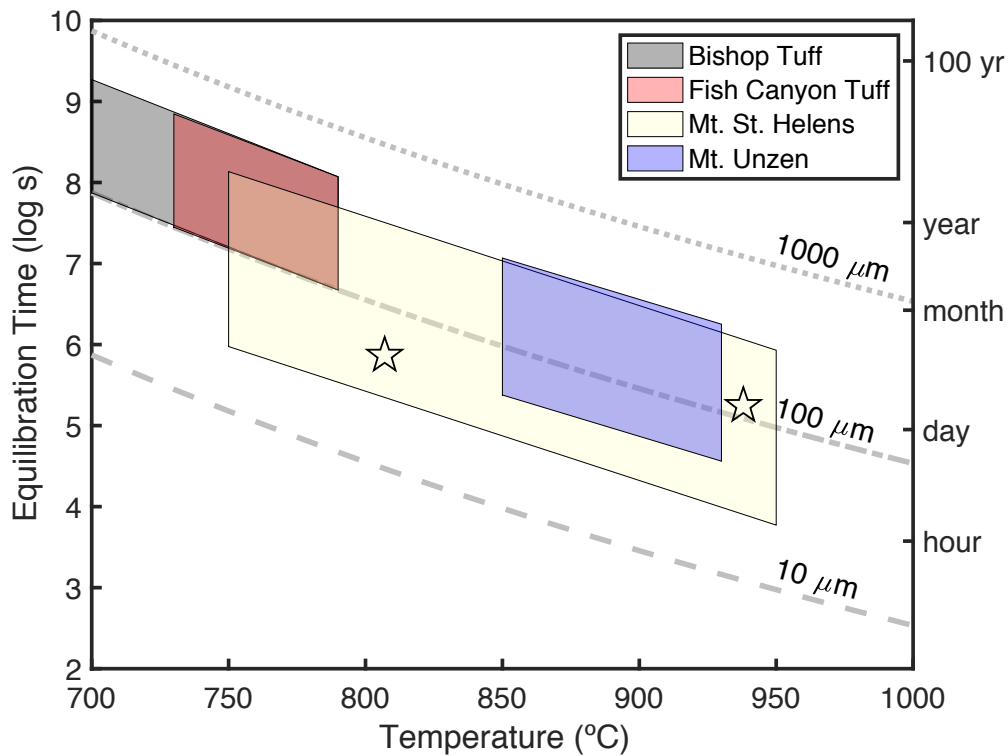
Figure 2.10: Equilibration times for ilmenite grains of a given size, calculated using our results for Fe-Mn interdiffusivity in ilmenite. The dashed lines indicate the time for a grain of a given diameter to equilibrate with respect to Fe and Mn as a function of temperature. The shaded regions were calculated using the characteristic grain sizes and pre-eruptive temperatures for the four volcanic complexes listed. The two stars represent the equilibration times calculated for two zoned ilmenite grains from Pallister et al. (2008).

size. Approximating that the ilmenite grains are spherical, the time it would take an ilmenite grain of a given diameter to equilibrate after a heating or mixing event can be estimated using the following equation from McDougall et al. (1999):

$$f \approx 1 - 6/\pi^2 exp((-\pi^2 Dt)/r^2) \tag{2.4}$$

where f is the fractional approach to equilibrium, D = diffusion coefficient taken at a given temperature (m^2 s^{-1}), r = grain radius (m), and t = the time (s) since the perturbation. This equation is an approximation that applies when $f > \sim 0.85$. In our modeling, we use f = 0.95 as the approximation for complete equilibration because this is within the uncertainty of the Mg/Mn filter.

Disequilibrium between oxide pairs has been observed for each of the volcanic centers discussed below (Johnson and Rutherford 1989; Venezky and Rutherford 1999; Rutherford and Devine III 2008; Bacon and Hirschmann 1988; Hildreth 1979; Whitney and Stormer Jr. 1985; Ghiorso and Evans 2008; Blundy et al. 2006; Pallister et al. 2008). Our experimental data characterizes the interdiffusion of Fe^{2+} and Mn^{2+}, however Fe^{3+} is present in natural volcanic systems. Given a significant Fe_2O_3 component, the ilmenite equilibration rates would likely be slower than those estimated in our calculations.

The reported ilmenite grain sizes for both the Bishop Tuff and the Fish Canyon Tuff range from $100 - 500$ μm (Hildreth 1979; Whitney and Stormer Jr. 1985). The temperature range used for the Bishop Tuff calculation ($700 - 790^\circ$C, Hildreth and Wilson 2007) was estimated using equilibrated Fe-Ti oxide thermometry. The temperature range used for the Fish Canyon Tuff ($730 - 790^\circ$C, Johnson and Rutherford 1989) is the pre-eruptive temperature range deduced from experimental phase equilibrium data. For the Bishop Tuff and Fish Canyon Tuff the reported ilmenite grain sizes and estimated pre-eruptive temperatures suggest the

time between thermal perturbation and eruption is on the order of months to decades (Figure 2.10).

For Mt. Unzen, a pre-eruptive temperature range of $850 - 930°C$ and ilmenite grain size range of $50 - 350$ μm was used for the calculation (Venezky and Rutherford 1999). This temperature range was estimated from a combination of Fe-Ti oxide thermometry and the results of phase equilibrium experiments. For Mt. St. Helens, a temperature range of $750 - 950°C$ and grain size range of $25 - 300$ μm was used in the calculation. These values encompass the temperature ranges estimated from Fe-Ti oxide thermometry for the 1980-1986 and 2004-2006 eruptions and the observed oxide grain sizes (Blundy et al. 2008; Pallister et al. 2008; Rutherford and Devine III 2008).

For ilmenite grains in volcanic samples from Mt. Unzen and Mt. St. Helens, the results of this calculation indicate that ilmenite equilibration times are on the order of hours to months (Figure 2.10). Previously, compositional zoning of Ti in titanomagnetite has been used to estimate the time between thermal perturbation and eruption at Mt. Unzen (e.g., Nakamura 1995; Venezky and Rutherford 1999). These studies indicate that the 1991-1993 Mount Unzen eruption involved continuous replenishment of a dacitic magma source weeks (Venezky and Rutherford 1999) or months (Nakamura 1995) before eruption. At Mt. St. Helens, the pre-eruptive magma-mixing time for the 2004-2006 eruption is estimated to be less than $5 - 8$ weeks from Ti compositional profiles perserved in titanomagnetite (Rutherford and Devine III 2008). Additionally for Mt. St. Helens, an ascent time of 2.6 weeks to 2.5 months has been estimated from the 2004-2006 magma eruption rates (Pallister et al. 2008), whereas an ascent time of $4 - 8$ days has been estimated from the extent of groundmass crystallization in the 1980-1986 eruption products (Geschwind and Rutherford 1995). Our results are consistent with the previous estimates for the timing of magmatic activity at

both volcanoes, and indicate that ilmenite zoning can record processes that occur in hours to months.

Constraints on the pre-eruptive temperature and grain size of zoned ilmenites lowers the uncertainty in the range of estimated equilibration times (Figure 2.10). Given the wide range of temperatures estimated from Fe-Ti oxide thermometry for Mt. St. Helens, it is helpful to focus on specific observations of zoning in ilmenite in order to provide narrow time constraints on a given sample. For example, we have calculated the time it would take to equilibrate two zoned ilmenites reported in Pallister et al. (2008) (results plotted as stars in Figure 2.10). For a zoned ilmenite from the 1980-1986 eruptive products (sample MSH05JV_1_19 in Pallister et al. 2008) with a reported grain size of 120 μm, the grain would equilibrate within 2 days at the reported temperature of 938°C. This result indicates that the cause of chemical zoning occurred less than 2 days prior to eruption. Similarly, the 50 μm zoned ilmenite observed in a sample from the April 1, 2005 eruption (sample SH315-2 in Pallister et al. 2008) would equilibrate within 8.5 days at the reported temperature of 807°C, indicating the zoning formed less than 8.5 days before eruption. While the characteristic equilibration times in Figure 2.10 provide useful time constraints for the volcanic activity at each volcano, these two examples illustrate the utility of our diffusion data when integrated with discrete observations of zoned ilmenites in natural samples.

2.5.2   Application to magnesium zoning in kimberlite megacrysts

Kimberlites are volatile-rich, ultramafic, igneous rocks that contain diamonds and mantle xenoliths. Preservation of diamond through deep magma transport to the surface and ascent of dense mantle xenoliths both require rapid ascent rates. Magma ascent rates for kimberlites have been estimated to reach 30 m/s, which overwhelmingly exceeds the 5 m/s estimate for other xenolith-bearing magmas (Rutherford 2008). Though kimberlites have been extensively

studied, uncertainties still exist regarding kimberlite properties such as source composition, depth, temperature, and oxidation state (e.g., Mitchell 1995; Sparks 2013, and references therein).

Kimberlites contain large (up to 20 cm) megacrysts of garnet, diopside, and ilmenite, referred to as the "megacryst suite". The origin of the megacryst suite has been widely debated; leading theories propose that the megacrysts crystallized at depths of $150-200$ km from a magma that is either proto-kimberlitic or basaltic (Mitchell 1995). There have been many studies on the occurrence, mineralogy, and chemistry of the megacryst suite, particularly with aim to establish the megacryst minerals as an indicator for diamond-bearing kimberlites. However, the timing of megacryst incorporation into the kimberlite magma (i.e., prior to or during ascent) remains unconstrained.

Rapid kimberlite eruption preserves disequilibria between megacrysts and their kimberlitic host matrix in the form of compositional zoning and reaction rims. This disequilibrium is evidence of a perturbation to the megacryst source prior to eruption. Applying diffusion data to the observed disequilibria can help to constrain the timing of this perturbation and address whether the megacrysts are incorporated near the source of the kimberlite magma or during ascent.

The megacryst ilmenites found in kimberlites have characteristically high MgO contents ($5-23$ wt.%) and low ferric iron abundances ($0.2-20$ wt.% Fe_2O_3), making these samples ideal for demonstrating the utility of our Fe^{2+}-Mg^{2+} interdiffusion rates for ilmenite. Additionally, there is widespread evidence for chemical diffusion in the ilmenites of the megacryst suite. One example of this is the preservation of Mg enrichment at the rims of ilmenite grains, yielding diffusion profiles that are on average 100 to 500 μm in length (Mitchell 1986). This

Mg enrichment at the ilmenite rims results from incomplete equilibration between the ilmenite megacrysts and the Mg-rich kimberlitic host magma (Pasteris 1981).

Considering the megacryst suite as an isolated unit that is then sampled by kimberlite magma and brought to the surface, we can use our experimentally determined Fe-Mg interdiffusion rates for ilmenite to determine the timing of megacryst suite incorporation as it relates to kimberlite magma ascent. Specifically, this calculation estimates the duration of Fe-Mg exchange between the ilmenite and kimberlite using the equation

$$t = \frac{x^2}{D_{\text{Fe-Mg}}} \tag{2.5}$$

where t is time (s), $D_{\text{Fe-Mg}}$ is the rate of Fe-Mg interdiffusion calculated as a function of temperature using our experimental results ($\text{m}^2 \text{ s}^{-1}$), and x is the characteristic length of Mg diffusion into the ilmenite (m). For a given ilmenite megacryst, this x corresponds to the distance from the rim at which the Mg concentration in the ilmenite equals the average of the core and rim Mg concentrations. The calculated durations, t, are compared to the estimated kimberlite ascent rates to establish whether the ilmenites were entrained by the kimberlite magma during ascent or whether the diffusive exchange between the kimberlite magma and megacryst ilmenites began prior to eruption.

Using our experimentally determined Fe-Mg interdiffusion rates for ilmenite, we have calculated the time it would take to develop a Mg diffusion profile of a given length in an ilmenite rim (Figure 2.11). Our results from this calculation indicate that the Mg enrichment of ilmenite megacrysts would require ilmenite and kimberlitic magma to be in contact a minimum of hours to weeks depending on the exact temperature. The plotted range of temperatures in Figure 2.11 encompasses both the estimated kimberlite source temperatures ($1350 - 1450°C$, Priestley and McKenzie 2006; Sparks 2013), crystallization temperatures
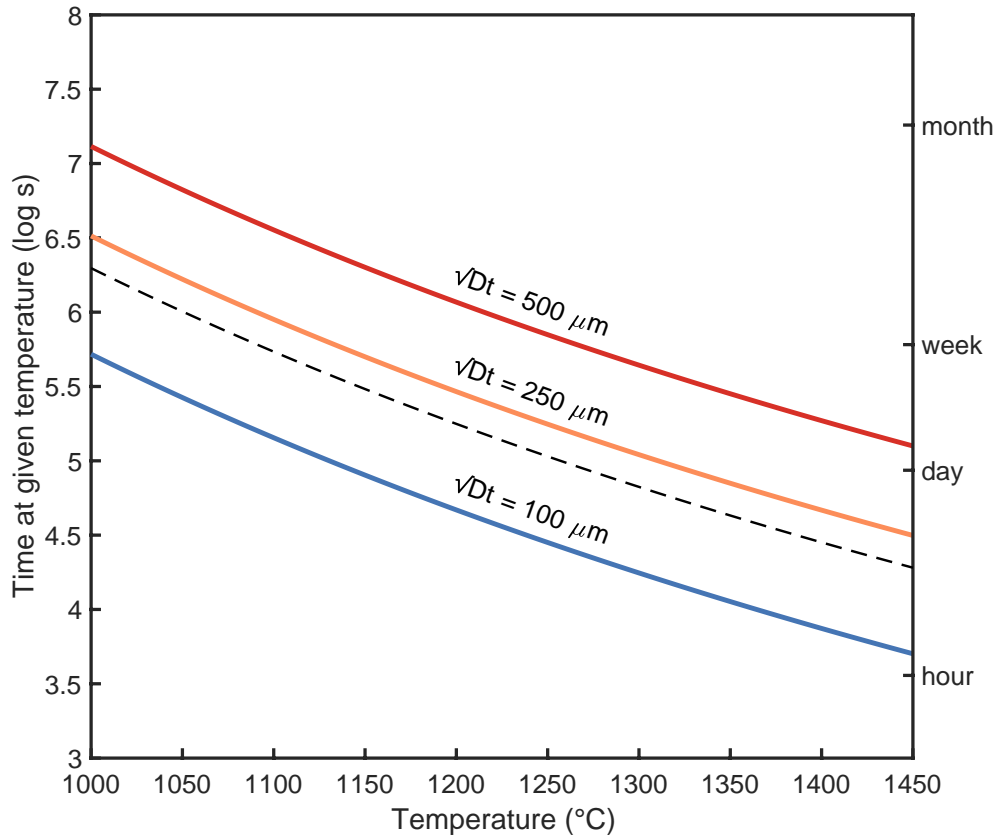
Figure 2.11: Calculated times for Mg-enrichment rims to form by Fe-Mg interdiffusion. Each solid line represents a given length of Mg enrichment at the rim of an ilmenite grain, and indicates the time it would take that enrichment profile to form at a given temperature. The temperature range of the x-axis encompasses the range of estimates for the source temperatures of the host kimberlite magma (Section 2.5.2). The dashed line represents the results calculated from a core-to-rim profile of Mg enrichment measured in a natural ilmenite megacryst by Boctor and Boyd (1980) (Figure 2.12).
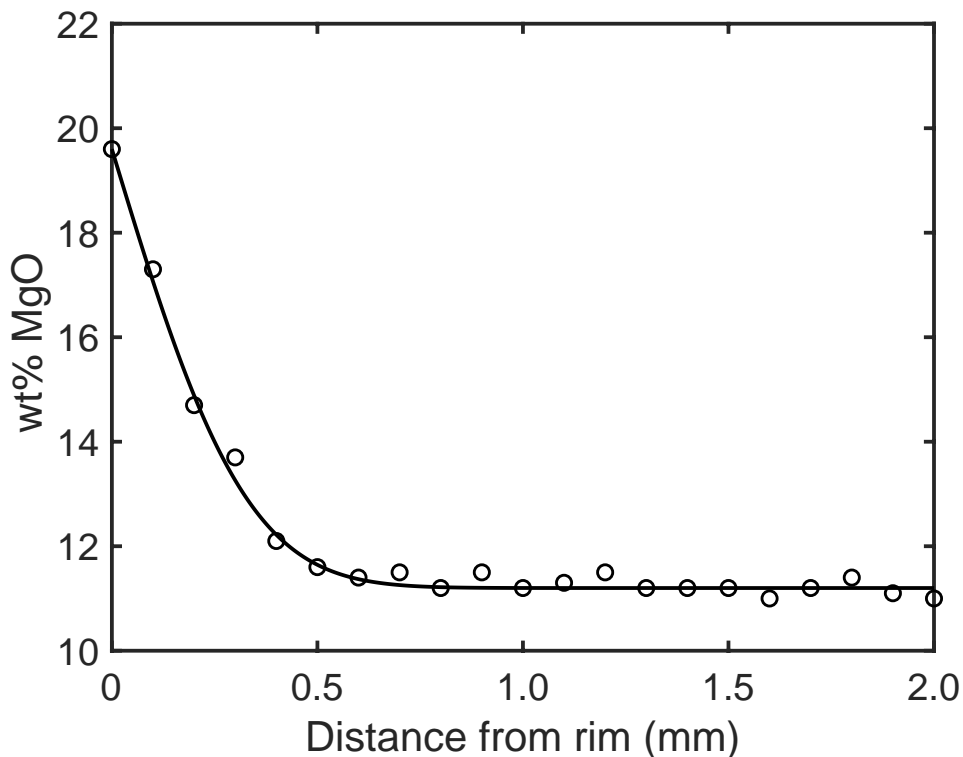
Figure 2.12: Magnesium enrichment profile observed in a natural kimberlitic ilmenite megacryst. The open circles represent the electron microprobe analyses reported in Boctor and Boyd (1980). The solid line depicts our modeled error function fit for the measured profile. The modeled profile was used to calculate the time needed to form the observed Mg-enrichment rim at a given temperature (Figure 2.11).

calculated from olivine-spinel geothermometry ($1030 - 1170°C$, Fedortchouk and Canil 2004), and temperature estimates from models for the ascending magma which consider cooling upon ascent, volatile content, xenolith assimilation, and olivine crystallization ($1050 - 1450°C$ from source to eruption, Kavanagh and Sparks 2009).

In order to provide context for the $\sqrt{Dt}$ distances from the rim in Figure 2.11, we have applied our Fe-Mg interdiffusion results to a core-to-rim profile of Mg enrichment measured in a natural kimberlitic ilmenite megacryst by Boctor and Boyd (1980) (Figure 2.12). Using equation 2.2, we linearized the observed profile, then determined the slope, $(4Dt)^{-1/2}$, from a linear regression through the analytical points. With this slope and our experimentally

44

determined temperature dependence for $D_{\text{Fe-Mg}}$, we calculated the time for the observed Mg-enrichment profile to form by diffusion as a function of temperature (Figure 2.11). The modeled Mg-enrichment profile has been plotted as an error function in Figure 2.12 using equation 2.1.

Consider that the ilmenite megacrysts are sampled from a source depth of 150 km. For magma temperatures greater than $1300°C$, 100 μm rims of Mg enrichment form within hours, suggesting the interaction could take place solely during the rapid ascent stage of kimberlite eruption $(10-30$ m/s$)$. However at these temperatures, the 500 μm rims of Mg enrichment would still require at least a day of interaction with the kimberlite magma. If this interaction occurred only during the ascent stage, this time would roughly translate to kimberlite ascent rates < 2 m/s, which is an order of magnitude slower than previous estimates. This result indicates that either the initial stage of kimberlite magmatic ascent is slow enough to allow for days to weeks of interaction between the kimberlite and megacrysts, or alternatively, that the kimberlite magma and megacrysts are interacting prior to the onset of eruptive ascent.

The initial stage of ascent for xenolith carrying magmas constitutes a majority of the ascent time, and the ascent rates for this stage have been estimated to be between $2.9-16.8$ m/s (Rutherford 2008). If the initial ascent of the kimberlite magma occurs at a rate of 3 m/s, then the ascent time from 150 km would be approximately 14 hours. From our diffusion results, we have determined that an interaction time of 14 hours could produce $100-500$ μm rims of Mg enrichment in an ilmenite grain given a temperature range of $1200-1600°C$. If the 2.9 m/s ascent rate is relevant to the initial stages of kimberlite ascent, then the temperature of the kimberlite host magma can be approximated using the width of the Mg-enrichment rims on the ilmenite megacrysts.

The growth of spinel rims on garnets has previously been used in a similar way to decipher the timing of garnet incorporation into kimberlite magma (Canil and Fedortchouk 1999). However, the reported timescales required to form approximately 25 μm spinel rims on garnet at temperatures between $1000 - 1200°$C are on the order of hours, and at $1400°$C would form within minutes. These timescales indicate that the kelyphitic rims form at either at lower temperatures or shorter timescales than those for the diffusion of Mg into ilmenite megacrysts.

Our experimentally determined cation interdiffusion rates for ilmenite provide a new geospeedometry tool that, when applied to the disequilibrium preserved in kimberlite ilmenite megacrysts, elucidates the processes related to kimberlite magma storage and incorporation of the megacryst suite. It is important to note that in calculating the times to form the observed Mg enrichment at the rims of ilmenite megacrysts we have made consistent assumptions that would result in minimum estimates. All calculations were performed assuming all Fe was present as Fe^{2+}, though in reality Fe^{3+} is present and thus the Fe-Mg interdiffusion rates would be slower. Additionally, grain boundary erosion occurs during ascent and would decrease the profile length (and thus time estimate). Lastly, the formation of perovskite reaction rims on ilmenite megacrysts might also hinder the diffusion of Mg into the ilmenite megacryst. Given these assumptions, it is most likely that the megacryst suite is chemically interacting with the kimberlitic magma prior to the onset of eruptive ascent. This argues for the megacryst suite being present in or near the source region of kimberlitic magmas, rather than being incorporated during ascent like peridotite xenoliths.

2.6 Conclusions

From our experimentally determined Fe-Mg and Fe-Mn interdiffusivities, we find that diffusion in ilmenite is faster than in hematite. Our results indicate that crystallographic orientation did not affect diffusion rates in ilmenite. To apply this data to natural systems, for Fe-Mg interdiffusion we use an activation energy (Q) of 188 kJ/mol and $logD_0$ of -6.0 m^2/s, and for Fe-Mn interdiffusion we use Q = 264 kJ/mol and $logD_0 = -2.9$ m^2/s. Because diffusion in ilmenite is slower than in magnetite, the diffusive exchange between rhombohedral oxide and spinel pairs used in geothermometers and oxybarometers will likely be rate-limited by diffusion in ilmenite-hematite solid solutions. In applying our data to disequilibrium observed in ilmenites from natural volcanic samples, we have estimated the time between perturbation and eruption for the Bishop Tuff, Fish Canyon Tuff, Mt. Unzen, Mt. St. Helens, and kimberlites. In this way, our experimentally determined diffusivities for ilmenite have provided a new tool with which to estimate the timing of volcanic activity.

Acknowledgements

References

Aggarwal, S. and R. Dieckmann (2002). "Point defects and cation tracer diffusion in $(Ti_xFe_{(1-x)})_{3-\delta}O_4$ 1. Non-stoichiometry and point defects." *Physics and Chemistry of Minerals* 29 (10), pp. 695–706.

Amami, B., M. Addou, F. Millot, A. Sabioni, and C. Monty (1999). "Self-diffusion in α-Fe_2O_3 natural single crystals." *Ionics* 5 (5-6), pp. 358–370.

Atkinson, A. and R. Taylor (1985). "Diffusion of ^{55}Fe in Fe_2O_3 single crystals." *Journal of Physics and Chemistry of Solids* 46 (4), pp. 469–475.

Bachmann, O. and G. Bergantz (2008). "The magma reservoirs that feed supereruptions." *Elements* 4 (1), pp. 17–21.

Bacon, C. R. and M. M. Hirschmann (1988). "Mg/Mn partitioning as a test for equilibrium between coexisting Fe-Ti oxides." *American Mineralogist* 73 (1-2), pp. 57–61.

Bishop, F. C. (1980). "The distribution of Fe^{2+} and Mg between coexisting ilmenite and pyroxene with applications to geothermometry." *American Journal of Science* 280 (1), pp. 46–77.

Blundy, J., K. V. Cashman, and K. Berlo (2008). *Evolving magma storage conditions beneath Mount St. Helens inferred from chemical variations in melt inclusions from the 1980-1986 and current (2004-2006) eruptions: Chapter 33 in A volcano rekindled: the renewed eruption of Mount St. Helens, 2004-2006.* Tech. rep. US Geological Survey.

Blundy, J., K. Cashman, and M. Humphreys (2006). "Magma heating by decompression-driven crystallization beneath andesite volcanoes." *Nature* 443 (7107), p. 76.

Boctor, N. Z. and F. Boyd (1980). "Oxide minerals in the Liqhobong kimberlite, Lesotho." *American Mineralogist* 65 (7-8), pp. 631–638.

Boyd, F. and J. England (1960). "Apparatus for phase-equilibrium measurements at pressures up to 50 kilobars and temperatures up to 1750°C." *Journal of Geophysical Research* 65 (2), pp. 741–748.

Buddington, A. and D. Lindsley (1964). "Iron-titanium oxide minerals and synthetic equivalents." *Journal of Petrology* 5 (2), pp. 310–357.

Canil, D. and Y. Fedortchouk (1999). "Garnet dissolution and the emplacement of kimberlites." *Earth and Planetary Science Letters* 167 (3-4), pp. 227–237.

Cashman, K. V. and R. S. J. Sparks (2013). "How volcanoes work: A 25 year perspective." *GSA bulletin* 125 (5-6), pp. 664–690.

Chakraborty, S. (1997). "Rates and mechanisms of Fe-Mg interdiffusion in olivine at 980 °– 1300 °C." *Journal of Geophysical Research: Solid Earth* 102 (B6), pp. 12317–12331.

Costa, F., R. Dohmen, and S. Chakraborty (2008). "Time scales of magmatic processes from modeling the zoning patterns of crystals." *Reviews in Mineralogy and Geochemistry* 69 (1), pp. 545–594.

Crank, J. (1975). *The mathematics of diffusion.* Second Edition. Oxford University Press.

Devine, J., M. Rutherford, G. Norton, and S. Young (2003). "Magma storage region processes inferred from geochemistry of Fe–Ti oxides in andesitic magma, Soufriere Hills Volcano, Montserrat, WI." *Journal of Petrology* 44 (8), pp. 1375–1400.

Dieckmann, R. and H. Schmalzried (1977). "Defects and cation diffusion in magnetite (I)." *Berichte der Bunsengesellschaft für physikalische Chemie* 81 (3), pp. 344–347.

Fedortchouk, Y. and D. Canil (2004). "Intensive variables in kimberlite magmas, Lac de Gras, Canada and implications for diamond survival." *Journal of Petrology* 45 (9), pp. 1725–1745.

Gardner, J. E., S. Carey, M. J. Rutherford, and H. Sigurdsson (1995). "Petrologic diversity in Mount St. Helens dacites during the last 4,000 years: implications for magma mixing." *Contributions to Mineralogy and Petrology* 119 (2-3), pp. 224–238.

Geschwind, C.-H. and M. J. Rutherford (1995). "Crystallization of microlites during magma ascent: the fluid mechanics of 1980–1986 eruptions at Mount St Helens." *Bulletin of Volcanology* 57 (5), pp. 356–370.

Ghiorso, M. S. and B. W. Evans (2008). "Thermodynamics of rhombohedral oxide solid solutions and a revision of the Fe-Ti two-oxide geothermometer and oxygen-barometer." *American Journal of Science* 308 (9), pp. 957–1039.

Hildreth, W. (1979). "The Bishop Tuff: Evidence for the origin of compositional zonation in silicic magma chambers." *Geological Society of America Special Paper* 180, pp. 43–75.

Hildreth, W. and C. J. Wilson (2007). "Compositional zoning of the Bishop Tuff." *Journal of Petrology* 48 (5), pp. 951–999.

Himmel, L., R. Mehl, and C. E. Birchenall (1953). "Self-diffusion of iron in iron oxides and the Wagner theory of oxidation." *JOM* 5 (6), pp. 827–843.

Izbekov, V. (1958). "Diffusion of Fe in magnetite." *Inzh-Fiz Zh* 1, pp. 64–68.

Johannes, W., P. Bell, H. Mao, A. Boettcher, D. Chipman, J. Hays, R. Newton, and F. Seifert (1971). "An interlaboratory comparison of piston-cylinder pressure calibration using the albite-breakdown reaction." *Contributions to Mineralogy and Petrology* 32 (1), pp. 24–38.

Johnson, M. C. and M. J. Rutherford (1989). "Experimental calibration of the aluminum-in-hornblende geobarometer with application to Long Valley caldera (California) volcanic rocks." *Geology* 17 (9), pp. 837–841.

Kavanagh, J. L. and R. S. J. Sparks (2009). "Temperature changes in ascending kimberlite magma." *Earth and Planetary Science Letters* 286 (3-4), pp. 404–413.

McDougall, I., I. Mac Dougall, T. M. Harrison, et al. (1999). *Geochronology and Thermochronology by the $^{40}Ar/^{39}Ar$ Method*. Oxford University Press on Demand.

Médard, E., C. A. McCammon, J. A. Barr, and T. L. Grove (2008). "Oxygen fugacity, temperature reproducibility, and H_2O contents of nominally anhydrous piston-cylinder experiments using graphite capsules." *American Mineralogist* 93 (11-12), pp. 1838–1844.

Mitchell, J. N., N. Yu, K. E. Sickafus, M. A. Nastasi, and K. J. McClellan (1998). "Ion irradiation damage in geikielite ($MgTiO_3$)." *Philosophical Magazine A* 78 (3), pp. 713–725.

Mitchell, R. H. (1986). *Kimberlites: mineralogy, geochemistry, and petrology*. Springer Science & Business Media.

Mitchell, R. H. (1995). *Kimberlites, orangeites, and related rocks*. Springer Science & Business Media.

Müller, T., R. Dohmen, H. Becker, J. H. Ter Heege, and S. Chakraborty (2013). "Fe-Mg interdiffusion rates in clinopyroxene: experimental data and implications for Fe-Mg exchange geothermometers." *Contributions to Mineralogy and Petrology* 166 (6), pp. 1563–1576.

Nakamura, M. (1995). "Continuous mixing of crystal mush and replenished magma in the ongoing Unzen eruption." *Geology* 23 (9), pp. 807–810.

Ogawa, S., T. Nakajima, T. Sasaki, and M. Takahashi (1968). "Ion diffusion and disaccommodation in ferrites." *Japanese Journal of Applied Physics* 7 (8), p. 899.

Pallister, J. S., R. P. Hoblitt, G. P. Meeker, R. J. Knight, and D. F. Siems (1996). "Magma mixing at Mount Pinatubo: petrographic and chemical evidence from the 1991 deposits." *Fire and mud: eruptions and lahars of Mount Pinatubo, Philippines*, pp. 687–731.

Pallister, J. S., C. R. Thornber, K. V. Cashman, M. A. Clynne, H. Lowers, C. W. Mandeville, I. K. Brownfield, and G. P. Meeker (2008). *Petrology of the 2004-2006 Mount St. Helens lava dome–implications for magmatic plumbing and eruption triggering: Chapter 30 in A volcano rekindled: the renewed eruption of Mount St. Helens, 2004-2006*. Tech. rep. US Geological Survey.

Pasteris, J. D. (1981). "The significance of groundmass ilmenite and megacryst ilmenite in kimberlites." *Contributions to Mineralogy and Petrology* 75 (4), pp. 315–325.

Pownceby, M. I., V. J. Wall, and H. S. C. O'Neill (1987). "Fe-Mn partitioning between garnet and ilmenite: experimental calibration and applications." *Contributions to Mineralogy and Petrology* 97 (1), pp. 116–126.

Priestley, K. and D. McKenzie (2006). "The thermal structure of the lithosphere from shear wave velocities." *Earth and Planetary Science Letters* 244 (1-2), pp. 285–301.

Rutherford, M. J. (2008). "Magma ascent rates." *Reviews in Mineralogy and Geochemistry* 69 (1), pp. 241–271.

Rutherford, M. J. and J. D. Devine III (2008). *Magmatic conditions and processes in the storage zone of the 2004-2006 Mount St. Helens dacite: Chapter 31 in A volcano rekindled: the renewed eruption of Mount St. Helens, 2004-2006*. Tech. rep. US Geological Survey.

Sabioni, A., A.-M. Huntz, A. Daniel, and W. Macedo (2005). "Measurement of iron self-diffusion in hematite single crystals by secondary ion-mass spectrometry (SIMS) and comparison with cation self-diffusion in corundum-structure oxides." *Philosophical Magazine* 85 (31), pp. 3643–3658.

Schulze, D. J., P. F. Anderson, B. C. Hearn Jr, and C. M. Hetman (1995). "Origin and significance of ilmenite megacrysts and macrocrysts from kimberlite." *International Geology Review* 37 (9), pp. 780–812.

Shea, T., F. Costa, D. Krimer, and J. E. Hammer (2015). "Accuracy of timescales retrieved from diffusion modeling in olivine: A 3D perspective." *American Mineralogist* 100 (10), pp. 2026–2042.

Sparks, R. (2013). "Kimberlite volcanism." *Annual Review of Earth and Planetary Sciences* 41, pp. 497–528.

Taylor, L. A., D. Uhlmann, R. Hopper, and K. Misra (1975). "Absolute cooling rates of lunar rocks-Theory and application." *Lunar and Planetary Science Conference Proceedings*. Vol. 6, pp. 181–191.

Till, C. B., J. A. Vazquez, and J. W. Boyce (2015). "Months between rejuvenation and volcanic eruption at Yellowstone caldera, Wyoming." *Geology* 43 (8), pp. 695–698.

Ulmer, P. and R. W. Luth (1991). "The graphite-COH fluid equilibrium in P, T, f_{O_2} space." *Contributions to Mineralogy and Petrology* 106 (3), pp. 265–272.

Van Orman, J. A. and K. L. Crispin (2010). "Diffusion in oxides." *Reviews in Mineralogy and Geochemistry* 72 (1), pp. 757–825.

Venezky, D. Y. and M. J. Rutherford (1999). "Petrology and Fe–Ti oxide reequilibration of the 1991 Mount Unzen mixed magma." *Journal of Volcanology and Geothermal Research* 89 (1-4), pp. 213–230.

Vogt, K., R. Dohmen, and S. Chakraborty (2015). "Fe-Mg diffusion in spinel: New experimental data and a point defect model." *American Mineralogist* 100 (10), pp. 2112–2122.

Wark, D., W. Hildreth, F. Spear, D. Cherniak, and E. Watson (2007). "Pre-eruption recharge of the Bishop magma system." *Geology* 35 (3), pp. 235–238.

Watson, E., D. Wark, J. Price, and J. Van Orman (2002). "Mapping the thermal structure of solid-media pressure assemblies." *Contributions to Mineralogy and Petrology* 142 (6), pp. 640–652.

Whitney, J. A. and J. C. Stormer Jr. (1985). "Mineralogy, petrology, and magmatic conditions from the Fish Canyon Tuff, central San Juan volcanic field, Colorado." *Journal of Petrology* 26 (3), pp. 726–762.

Zhang, Y. and D. J. Cherniak (2010). "Diffusion in minerals and melts." *Reviews in Mineralogy and Geochemistry* 72 (1).

Chapter 3

Experimentally determined effects of olivine crystallization and melt titanium content on iron isotopic fractionation in planetary basalts

Abstract

Olivine is the most abundant mantle mineral at depths relevant to oceanic crust production through melting. It is also a liquidus phase for a wide range of mafic and ultramafic magma compositions. We have experimentally investigated the effects of olivine crystallization and melt composition on the fractionation of Fe isotopes in igneous systems. To test whether there is a melt compositional control on Fe isotopic fractionation, we have conducted nuclear resonant inelastic X-ray scattering (NRIXS) measurements on a suite of synthetic glasses ranging from 0.4 to 16.3 wt.% TiO_2. The resulting force constants are similar to those of the reduced (f_{O_2} = IW) terrestrial basalt, andesite, and dacite glasses reported by Dauphas et al. (2014), indicating that there is no measurable effect of titanium composition on Fe isotopic fractionation in the investigated compositional range. We have also conducted olivine crystallization experiments and analyzed the Fe isotopic composition of the experimental olivines and glasses using solution MC-ICPMS. Olivine and glass separates from a given experimental charge have the same iron isotopic composition within error. This result is robust in both the high-Ti glass (Apollo 14 black) and low-Ti glass (Apollo 14 VLT) compositions, and at the two oxygen fugacities investigated (IW−1, IW+2). Additionally, we have determined that Fe loss in reducing one-atmosphere gas-mixing experiments occurs not only as loss to the Re wire container, but also as evaporative loss, and each mechanism of experimental Fe loss has an associated Fe isotopic fractionation.

We apply our results to interpreting Fe isotopic variations in the lunar mare basalts and lunar dunite 72415-8. Our experimental results indicate that neither melt TiO_2 composition nor equilibrium olivine crystallization can explain the observed difference in the iron isotopic composition of the lunar mare basalts. Additionally, equilibrium iron isotopic fractionation between olivine and melt cannot account for the "light" iron isotopic composition of lunar

dunite 72415-8, unless the melt from which it is crystallizing was already enriched in light iron isotopes. Our results support models of diffusive fractionation to explain the light iron isotopic compositions measured in olivine from a variety of rock types and reduced ($f_{O_2} =$ IW-1 to IW$+2$) igneous environments (e.g., lunar dunite and basalts, terrestrial peridotites and basalts, martian shergottites).

3.1   Introduction

Analytical developments over the past decade have revealed that igneous rocks and minerals display variations in the isotopic composition of non-traditional stable isotope systems (i.e., not C, H, N, O, S; Teng et al. 2017, and references therein). The degree of mass-dependent fractionation between stable isotopes has been attributed to factors such as oxidation state, bonding environment, and volatility. While early studies focused on low-temperature stable isotopic fractionation, a growing number of studies have revealed measurable isotopic fractionations present in high temperature igneous systems (e.g., Beard and Johnson 2004; Poitrasson et al. 2004; Weyer et al. 2005; Williams et al. 2005; Teng et al. 2008, and subsequent studies). Interpretations of these variations are often hampered by the paucity of equilibrium fractionation factors between coexisting phases, which limits quantitative modeling of the relevant igneous processes.

High-temperature stable isotopic fractionations have been used to elucidate planetary-scale processes, such as the formation of the Moon, as well as smaller scale processes, such as the differentiation of magma. In particular, high-precision studies of stable isotopes have resolved isotopic differences between terrestrial and lunar samples for certain elements (e.g., Wang and Jacobsen 2016). However, for many isotopic systems, it is difficult to tell whether the Earth and Moon have different isotopic compositions because the processes of magmatic

differentiation, including lunar magma ocean crystallization and later magma generation and crystallization, have imparted stable isotopic variations to lunar rocks that need to be understood and disentangled before a claim can be made regarding the bulk composition of the Earth or Moon. The increased precision of modern isotope analyses has resolved a "dichotomy" present between the bulk stable isotopic compositions of the low-Ti and high-Ti mare basalts on the Moon (Figure 3.1). Specifically, this dichotomy has been observed for Fe (Wiesli et al. 2003; Poitrasson et al. 2004; Weyer et al. 2005; Craddock et al. 2010; Liu et al. 2010; Sossi and Moynier 2017), with high-Ti mare basalts being isotopically "heavy" compared to low-Ti basalts ($\delta^{56}Fe_{high-Ti} > \delta^{56}Fe_{low-Ti}$). The dichotomy was also observed for Mg ($\delta^{26}Mg_{high-Ti} < \delta^{26}Mg_{low-Ti}$; Sedaghatpour et al. 2013), Li ($\delta^{7}Li_{high-Ti} > \delta^{7}Li_{low-Ti}$; Day et al. 2016), and Ti ($\delta^{49}Ti_{high-Ti} > \delta^{49}Ti_{low-Ti}$; Millet et al. 2016). Though the difference in stable isotopic compositions between the high- and low-Ti basalts is well documented analytically, the petrologic processes responsible for the lunar isotopic dichotomy remain elusive.

Despite increasing evidence for high-temperature isotopic fractionation in igneous rocks (e.g., Dauphas and Rouxel 2006; Dauphas et al. 2017), there is a paucity of experimental studies of isotopic fractionation during magmatic differentiation of mafic compositions. The iron isotopic compositions of igneous rocks have been extensively studied, and the documented isotopic variations in igneous rocks are caused by a combination of partial melting (e.g., Williams et al. 2005; Weyer and Ionov 2007; Dauphas et al. 2009a; Dauphas et al. 2014; Williams and Bizimis 2014), equilibrium and fractional crystallization (e.g., Teng et al. 2008; Dauphas et al. 2014; Roskosz et al. 2015), and diffusive fractionation (e.g., Dauphas and Rouxel 2006; Sio et al. 2013; Oeser et al. 2015; Sio and Dauphas 2016; Collinet et al. 2017). Experimental studies of equilibrium Fe isotope partitioning at high temperature have investigated metal-silicate systems, fayalite-magnetite fractionation, as well as Fe isotopic fractionation between evolved
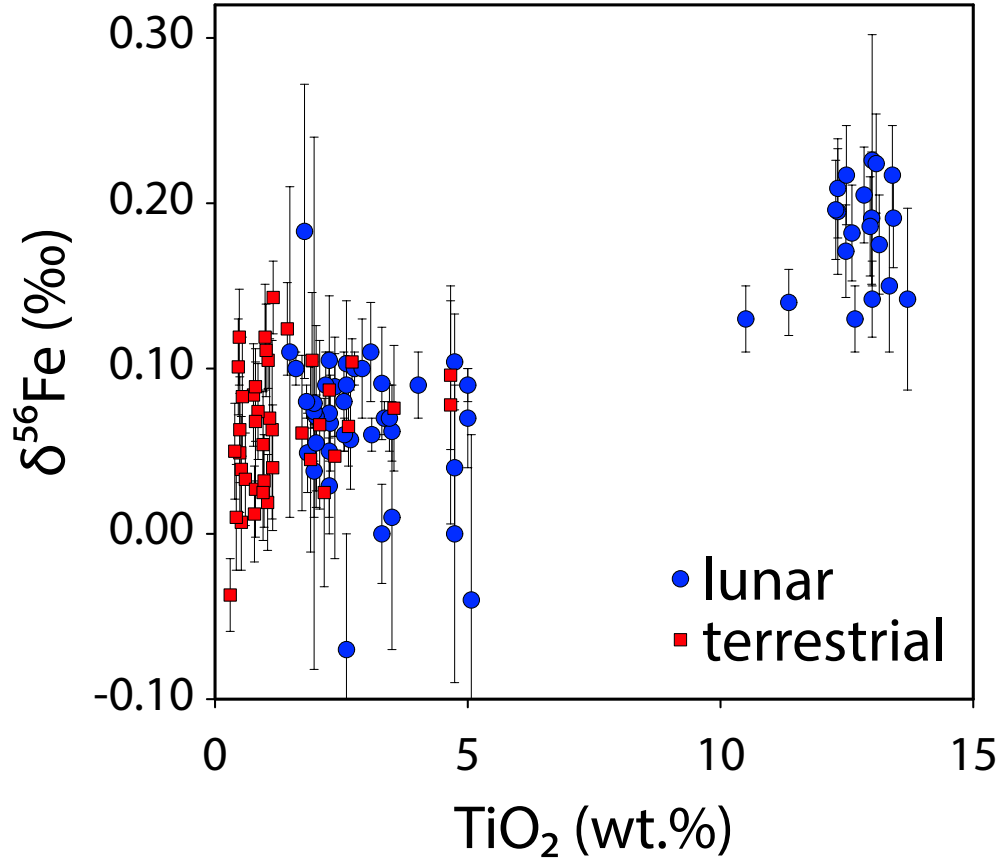
Figure 3.1: Iron isotopic compositions plotted as a function of TiO_2. Red points represent terrestrial basalts and andesites, and blue points represent lunar basalts. The terrestrial suite is similar in Fe isotopic composition to the low-Ti basalts, however high-Ti basalts have greater $\delta^{56}Fe$ values. The observed fractionation between low- and high-Ti lunar mare basalts appears to be bi-modal, although it is uncertain if this modality is due to sampling bias, as basalts with intermediate Ti concentrations have not been frequently measured. Compositions and isotope measurement errors (95% confidence interval) are from Wiesli et al. 2003; Poitrasson et al. 2004; Weyer et al. 2005; Teng et al. 2008; Dauphas et al. 2009b; Schuessler et al. 2009; Craddock et al. 2010; Liu et al. 2010; Wang et al. 2015; Sossi and Moynier 2017.

rhyolitic compositions and sulfides (e.g., Schuessler et al. 2007; Shahar et al. 2008; Poitrasson et al. 2009). Additionally, Dauphas et al. (2014) investigated the Fe bonding structure in a suite of terrestrial volcanic glass compositions ranging from basalt to rhyolite, concluding that Fe isotopic composition is influenced by the redox state of iron and the silica content of the melt.

Evidence for mineralogical, compositional, and redox controls on Fe isotope partitioning in igneous rocks highlights the importance of experimentally quantifying mineral-melt fractionations for major rock-forming minerals. Olivine is a ubiquitous mineral on rocky, differentiated planetary bodies. Even a small ($< 0.1‰$) olivine-melt Fe isotopic fractionation could significantly fractionate the Fe isotopes in mantle reservoirs during planetary differentiation; for example, an olivine-melt fractionation $\delta^{56}\text{Fe}_{\text{olivine}}$ - $\delta^{56}\text{Fe}_{\text{melt}} = -0.05‰$ would increase the $\delta^{56}\text{Fe}$ of a magma ocean by $0.1‰$ after 50% fractional crystallization of olivine. The measured iron isotopic compositions of olivine separates are often used to interpret olivine-melt fractionations (e.g., Williams et al. 2005; Wang et al. 2015). Yet, naturally occurring minerals have complex crystallization-cooling histories, and inferring an equilibrium fractionation factor from such measurements is fraught with difficulties. The use of natural samples to determine olivine-melt equilibrium iron isotopic fractionations is complicated by diffusion-driven, kinetic iron isotopic fractionations (e.g., Teng et al. 2008; Teng et al. 2011; Sio et al. 2013). In terrestrial igneous rocks, both Fe^{2+} and Fe^{3+} coexist, which can cause equilibrium isotopic fractionation between melt and olivine (i.e., Teng et al. 2008; Dauphas et al. 2009a). Redox-driven fractionation on Earth may obscure the existence of equilibrium iron isotopic fractionation between olivine and Fe^{2+} in silicate melt. On the other hand, large Fe isotopic fractionations exist among lunar basalts in an environment relatively free of Fe^{3+}. The absence of Fe^{3+} on the Moon supports mechanisms of mineral fractionation, melt composition, and/or diffusive re-equilibration as cause for the observed iron isotopic variation

between the low- and high-Ti mare basalts. The iron isotopic fractionations associated with these equilibrium and kinetic processes need to be well-characterized in order to distinguish the effects of each process on the resulting iron isotopic compositions of igneous rocks.

To investigate the effects of melt composition and olivine crystallization on Fe isotopic fractionation, we have experimentally determined the olivine-melt equilibrium partitioning of Fe isotopes for a compositional suite of synthetic lunar volcanic glasses. We have implemented a dual approach, combining independent techniques (MC-ICPMS and NRIXS) for determining equilibrium Fe isotopic fractionations between high temperature phases. In focusing our experimental study on compositions and oxygen fugacities relevant for lunar differentiation, we investigated Fe isotopic fractionation in the case where Fe^{3+} is of negligible abundance. Furthermore, in experimentally examining the Fe isotope dichotomy between high-Ti and low-Ti lunar mare basalts, we have examined whether the bulk titanium content of a melt exhibits a compositional control on the resulting Fe isotope signature of the basalt.

3.2 Methods

We have investigated the equilibrium fractionation of Fe isotopes between olivine and melt using two independent techniques. To determine the melt compositional control on Fe isotopic fractionation between lunar melts and olivine, we have conducted nuclear resonant inelastic X-ray scattering (NRIXS) measurements on a suite of synthetic glasses ranging from 0.4 to 16.3 wt.% TiO_2. To evaluate the magnitude of iron isotopic fractionation at equilibrium between olivine and melt, we have conducted olivine crystallization experiments and analyzed the Fe isotopic composition of the experimental olivines and glasses using solution MC-ICPMS. Direct olivine crystallization experiments were conducted using two bulk compositions: a synthetic glass similar to Apollo 14 VLT (very low Ti), and a synthetic Apollo 14 black glass

Table 3.1: Reference lunar volcanic glass compositions from Delano (1986).

Composition	SiO$_2$	TiO$_2$	Al$_2$O$_3$	Cr$_2$O$_3$	FeO	MnO	MgO	CaO	Na$_2$O	K$_2$O
Apollo 14 VLT	46.00	0.55	9.30	0.58	18.20	0.21	15.90	9.24	0.11	0.07
Apollo 16 Green	43.90	0.39	7.83	0.39	21.90	0.24	16.90	8.44	-	-
Apollo 14 Yellow	40.80	4.58	6.16	0.41	24.70	0.30	14.80	7.74	0.42	0.10
Apollo 17 Orange	39.40	8.63	6.21	0.67	22.20	0.28	14.70	7.53	0.41	0.04
Apollo 14 Black	34.00	16.40	4.60	0.92	24.50	0.31	13.30	6.90	0.23	0.16

(Table 3.1). Both of these compositions have olivine as a liquidus phase at one atmosphere pressure.

In comparing the results of both the NRIXS and direct crystallization experimental methods, we have determined the effect of equilibrium olivine crystallization and melt titanium content on Fe isotopic fractionation during high-temperature igneous processes. Additionally, the reducing experimental run conditions minimize Fe^{3+} content in the olivine and glass, making our results directly applicable to lunar oxygen fugacity conditions (IW-2 to IW$+1$; Sato 1973).

3.2.1 Starting materials

For the NRIXS measurements, synthetic lunar ultramafic volcanic glass compositions were prepared from oxide powders to match the Apollo 16 green (0.39 wt.% TiO$_2$), Apollo 14 yellow (4.58 wt.% TiO$_2$), Apollo 17 orange (8.63 wt.% TiO$_2$), and Apollo 14 black (16.4 wt.% TiO$_2$) glass compositions given in Delano (1986) (Table 3.1). These glasses were chosen to span the range of TiO$_2$ content in the picritic lunar glass suite. Sodium and potassium were added to the mixtures as carbonates (Na$_2$CO$_3$, K$_2$CO$_3$), calcium was added as CaSiO$_3$, and all other components were added as single element oxides. In order to perform the NRIXS measurements, which are only sensitive to the Mössbauer isotope ^{57}Fe, ^{57}Fe-enriched Fe$_2$O$_3$

powder (96.64% ^{57}Fe, Cambridge Isotopes) was used. Oxides were mixed by hand under isopropanol in an agate mortar and pestle for 20 minutes.

For the olivine crystallization experiments, the starting materials were prepared to be similar in composition to the synthetic Apollo 14 VLT (green) and Apollo 14 black glasses in Delano (1986) (Table 3.1). Calcium was added as $CaCO_3$ for the green glass, and $CaTiO_3$ for the black glass. Compositions used for the olivine crystallization experiments contained natural Fe isotope abundances and were mixed without the addition of Cr, Na, or K. Oxides, silicates, carbonates, and titanates were mixed under isopropanol in a silicon-nitride ball mill for 3 hours. Polyvinyl alcohol was added as a binding agent to the starting material mixtures for both the NRIXS and olivine crystallization techniques. Once dry, 75 mg aliquots of each mixture were pressed into cylindrical pellets of 4 mm diameter and 2 mm height in preparation to be melted in the gas-mixing furnace. Great care was exercised to ensure that no cross-contamination took place between the experiments involving enrichment in ^{57}Fe and those with natural Fe isotopic abundances. However, select experiments did exhibit slight enrichments in ^{57}Fe (detailed in Appendix B). By focusing on δ^{56}Fe, we minimize any potential effects of ^{57}Fe contamination.

3.2.2   Experimental methods

Lunar volcanic glass syntheses and olivine crystallization experiments were conducted in vertical gas-mixing furnaces at Washington University in St. Louis. Sample pellets were fused to rhenium loops and hung by a Pt wire thread in the furnace hot spot for the run duration. Experimental samples were then quenched rapidly by melting the Pt hanging wire and dropping the sample from within the furnace into a beaker of deionized water. The ^{57}Fe-doped glass syntheses were conducted for approximately 3 hours at 1400°C and an oxygen fugacity corresponding to the iron-wüstite buffer (Table 3.2). Olivine crystallization

61
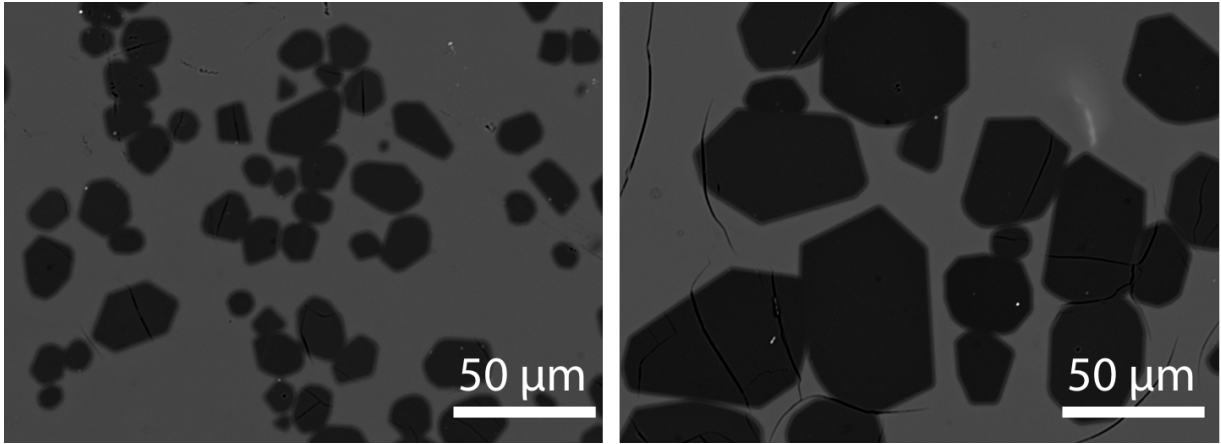
Figure 3.2: Back-scattered electron image of two olivine crystallization experiments. Both experiments were conducted at f_{O_2} = IW+2. Experiment durations were 1 day (left) and 4 days (right). Experimental olivine crystals (dark gray) in the 4-day experiment ($\sim$50 μm diameter) are larger than those grown in the 1-day experiment ($\sim$20 μm). Additionally, the olivine grains are compositionally homogenous, i.e., there is no visible Fe zoning within the grains at the $\pm$0.5 wt.% FeO level.

experiments were conducted at f_{O_2} values of IW$-$1 and IW+2 for durations of 6 hours, 1 day, and 4 days (Table 3.2). The temperatures for the olivine crystallization experiments ranged from 1262 to 1269°C, with $\pm$1°C variation during a given experimental run (Table 3.2). These temperatures were optimal for producing low modal abundances ($10-20$ wt.%) of large olivine crystals.

All experimental run products were synthesized at oxygen fugacities that bracket the oxygen conditions inferred for the Moon. These reducing conditions minimize the presence of Fe^{3+}, which has been demonstrated to affect Fe isotope partitioning (e.g., Dauphas et al. 2014). A controlled flow of H_2 and CO_2 gases buffered the oxygen fugacity throughout each experiment. The fugacity was monitored with a Ca-doped zirconia oxygen probe using air as the reference gas. The f_{O_2} was found to vary between 0.01 to 0.15 log units (1σ standard deviation) during a given experiment (Table 3.2).

Table 3.2: Experimental run conditions and products.

Experiment	Composition	Mix[a]	Time (hr)	T (°C)	$\log_{10} f_{O_2}$	Δ IW	Phases (mode)	Olivine K_D[b]	% Fe loss/gain[c]
NRIXS [57]Fe-doped glasses									
J020	Apollo 16 Green	#14	2.9	1400	−9.7	0.0	gl (100)	-	−3.5
J021	Apollo 14 Yellow	#15	3.6	1399	−9.8	−0.1	gl (100)	-	−6.7
J022	Apollo 14 Black	#17	2.6	1400	−9.8	−0.1	gl (100)	-	−2.1
J023	Apollo 17 Orange	#16	2.8	1400	−9.7	0.0	gl (100)	-	−2.4
Green IW−1 Series									
J017	Apollo 14 VLT	#10	5.9	1266	−12.2	−1.1	gl (81) + ol (19)	0.32	−4.6
J019	Apollo 14 VLT	#10	23.4	1266	−12.2	−1.1	gl (82) + ol (18)	0.34	−5.4
J040	Apollo 14 VLT	#29	96.2	1262	−12.1	−1.0	gl (83) + ol (17)	0.34	−17.9
H056	Apollo 14 VLT	#29	96.4	1266	−12.2	−1.0	-	-	-
Black IW−1 Series									
H042	Apollo 14 Black	#11	6.0	1266	−12.1	−1.0	gl (90) + ol (10)	0.24	−3.4
H025	Apollo 14 Black	#5	22.4	1265	−11.1	0.1	gl (90) + ol (10)	0.24	−5.7
H057	Apollo 14 Black	#28	92.9	1263	−12.1	−1.0	gl (92) + ol (8)	0.26	−17.9
H043	Apollo 14 Black	#11	96.0	1266	−12.2	−1.0	-	-	-
H055	Apollo 14 Black	#28	94.1	1267	−12.1	−1.0	-	-	-
Green IW+2 series									
J009	Apollo 14 VLT	#10	5.5	1269	−9.2	1.9	gl (83) + ol (17)	0.32	0.3
H031	Apollo 14 VLT	#10	24.1	1266	−9.2	2.0	gl (83) + ol (17)	0.32	−1.9
J007	Apollo 14 VLT	#10	96.0	1268	−9.2	1.9	gl (84) + ol (16)	0.32	−8.4
H030	Apollo 14 VLT	#10	96.0	1265	−9.1	2.0	-	-	-
Black IW+2 series									
H039	Apollo 14 Black	#11	6.3	1265	−9.2	2.0	gl (92) + ol (8)	0.23	−4.2
H038	Apollo 14 Black	#11	24.2	1266	−9.1	2.0	gl (91) + ol (9)	0.23	−6.0
H037	Apollo 14 Black	#11	96.3	1266	−9.1	2.0	gl (91) + ol (9)	0.24	−8.8
J012	Apollo 14 Black	#11	96.3	1266	−9.1	2.0	-	-	-

[a] For mixes #5, #10, and #11, FeO was added as a mixture of Fe metal sponge and Fe_2O_3 powder. All other mixes were prepared with only Fe_2O_3.

[b] K_D represents the olivine-melt Fe-Mg exchange coefficient calculated by $(X_{Fe}^{ol} \times X_{Mg}^{melt}) / (X_{Fe}^{melt} \times X_{Mg}^{ol})$.

[c] % Fe loss/gain is estimated using the FeO content of the starting composition and the FeO content of the sample (calculated from the phase compositions and modal abundances).
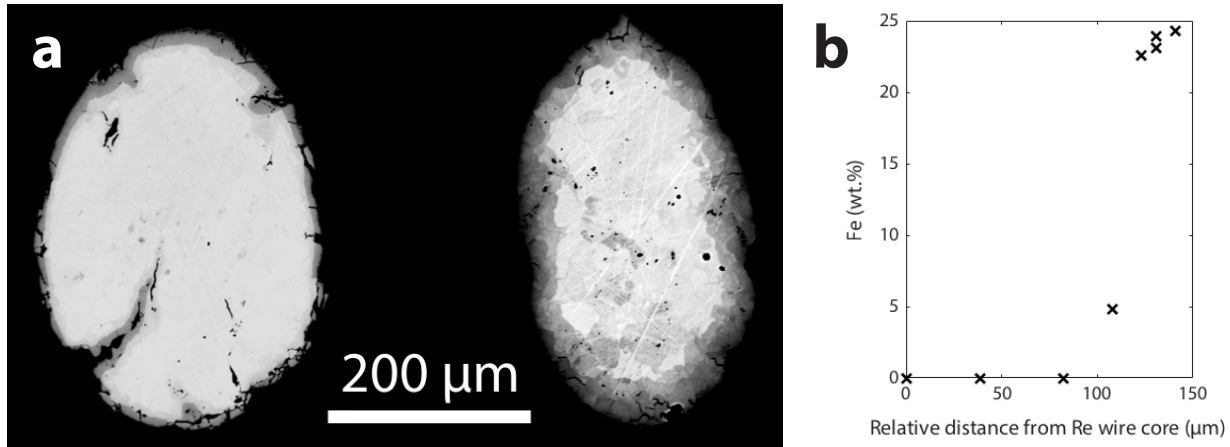
Figure 3.3: a) Back-scattered electron image of two Re wires. The wires were mounted in epoxy post-experiment and polished to create a measureable cross section. Both wires were used in experiments conducted at $f_{O_2} = \mathrm{IW}-1$. Experiment durations were 6 hours (left) and 4 days (right). Experimental Fe loss to the Re wire increases with time, producing a thicker Fe-enriched layer (dark gray) while the core of the Re wire remains Fe-free (light gray). b) Electron microprobe core-to-rim Fe (wt.%) profile in a Re wire from a 4-day experiment conducted at $f_{O_2} = \mathrm{IW}-1$.

Long experimental run durations aided in crystal growth, allowing for clean mechanical separation of olivine grains for MC-ICPMS work. Olivine grains from our four-day experiments exhibited a range in grain diameter from 20 to 100 μm, compared to the 5 to 50 μm grain diameter range for the one-day experiments (Figure 3.2). However, Fe loss from an experimental charge increases with increased run duration (Table 3.2, Figure 3.3a). Thus, a four-day run duration was deemed optimal for the olivine crystallization experiments needed to minimize Fe loss from the experiment, while providing experimental olivines large enough to hand-separate for MC-ICPMS measurements. To ensure that clean olivine and glass could be retrieved for MC-ICPMS work, olivine and glass were separated from the four-day experiments. Quantitative analysis of the Fe loss in these experiments is presented in Section 3.4.1.

64

3.2.3 Approach to equilibrium

The experimentally produced olivines are compositionally homogenous and do not exhibit compositional zoning within the grains (Figure 3.2), and electron microprobe compositional analyses show low standard deviations amongst all analyzed grains in a given sample (Table 3.3). Mineral-liquid Fe-Mg exchange coefficients ($K_D^{Fe\text{-}Mg}$, Table 3.2) for our olivine-bearing experiments are a function of melt Ti content ($0.32-0.34$ for 0.06 wt.% TiO_2; $0.23-0.26$ for 18 wt.% TiO_2) and are consistent with the results of Krawczynski and Grove (2012). In addition, a time series of experiments was conducted for each experimental starting composition (Apollo 14 VLT green glass, Apollo 14 black glass) at each experimental oxygen fugacity ($IW-1$, $IW+2$) in order to evaluate the effect of experimental Fe loss on the olivine-melt equilibrium. Experimental iron loss increases with increased run duration and decreased oxygen fugacity (Table 3.2). Thus, the lowest oxygen fugacity ($f_{O_2} = IW-1$) experiments experienced significant (up to 18%) Fe loss during the four-day experiments (see discussion in Section 3.4.1). Despite the increased Fe loss, the mineral-liquid Fe-Mg exchange coefficients for the four-day experiments are the same as those calculated for the shorter duration experiments (Table 3.2), indicating that olivine-melt equilibrium was maintained.

3.2.4 Analytical methods

Electron microprobe analysis

Experimental run products were analyzed for major element abundances using the JEOL JXA-8200 electron microprobe at Washington University in St. Louis. Standardization was performed with a beam diameter of 20 μm on natural and synthetic glass and mineral samples. We used the mean atomic number (MAN) method (Donovan et al. 2016) for wavelength

Table 3.3: Electron microprobe analyses of experimental run products in oxide weight percent.

Experiment	Phase	n[a]	SiO₂	s.d.	TiO₂	s.d.	Al₂O₃	s.d.	Cr₂O₃	s.d.	FeO	s.d.	MnO	s.d.	MgO	s.d.	CaO	s.d.	Na₂O	s.d.	K₂O	s.d.	Total
NRIXS ⁵⁷Fe-doped glasses																							
J020	glass	17	44.69	0.18	0.40	0.02	7.95	0.04	0.41	0.01	21.02	0.12	0.19	0.02	16.19	0.07	8.18	0.04	0.04	0.01	0.011	0.003	99.08
J021	glass	15	41.17	0.18	4.39	0.04	5.55	0.06	0.57	0.01	23.02	0.13	0.28	0.02	14.21	0.08	7.35	0.04	0.18	0.01	0.039	0.006	96.75
J022	glass	13	33.95	0.12	16.27	0.11	4.65	0.03	0.77	0.02	23.71	0.08	0.16	0.01	12.85	0.09	6.61	0.03	0.08	0.01	0.019	0.004	99.07
J023	glass	13	40.17	0.13	8.69	0.07	6.00	0.03	0.26	0.01	21.67	0.15	0.36	0.02	14.42	0.07	7.31	0.05	0.16	0.01	0.021	0.005	99.05
Green IW−1 Series																							
J017	glass	11	47.85	0.18	0.64	0.03	11.51	0.33			16.80	0.27	0.16	0.02	10.51	0.27	11.37	0.38					98.83
	olivine	17	38.98	0.34	b.d.		0.05	0.05			20.36	0.86	0.15	0.02	40.05	0.76	0.33	0.07					99.91
J019	glass	14	48.08	0.18	0.62	0.02	11.55	0.05			16.55	0.11	0.15	0.01	10.65	0.10	11.39	0.04					98.99
	olivine	20	38.73	0.67	b.d.		0.31	1.18			20.80	0.15	0.14	0.02	39.84	0.55	0.35	0.05					100.17
J040	glass	19	49.28	0.21	0.67	0.02	11.46	0.06			14.37	0.13	0.21	0.02	11.27	0.04	11.61	0.04					98.87
	olivine	16	39.47	0.24	b.d.		0.03	0.01			18.13	0.21	0.21	0.02	41.99	0.31	0.29	0.01					100.11
Black IW−1 Series																							
H042	glass	16	33.43	0.24	18.13	0.20	5.18	0.04			23.86	0.21	0.27	0.02	10.36	0.09	7.50	0.03					98.74
	olivine	19	38.24	0.44	0.65	0.78	0.05	0.05			21.59	0.38	0.19	0.02	39.07	0.48	0.21	0.03					100.00
H025	glass	18	34.08	0.35	18.08	0.16	5.29	0.07			23.32	0.15	0.28	0.02	10.64	0.20	7.54	0.08					99.22
	olivine	7	39.14	0.24	0.16	0.04	b.d.				21.28	0.09	0.20	0.02	40.01	0.37	0.17	0.02					100.96
H057	glass	13	35.65	0.11	18.35	0.08	5.40	0.05			20.19	0.13	0.35	0.03	11.34	0.06	7.59	0.04					98.86
	olivine	24	39.14	0.16	0.21	0.05	0.02	0.01			18.90	0.18	0.25	0.02	41.58	0.21	0.15	0.01					100.24
Green IW+2 series																							
J009	glass	15	47.40	0.40	0.64	0.02	11.20	0.20			17.86	0.22	0.20	0.02	10.81	0.20	11.09	0.07					99.20
	olivine	13	38.74	0.48	b.d.		0.06	0.08			20.86	0.41	0.19	0.02	39.77	0.60	0.39	0.02					100.01
H031	glass	18	47.67	0.29	0.65	0.02	11.44	0.09			17.46	0.14	0.19	0.02	10.88	0.10	11.06	0.05					99.35
	olivine	7	39.04	0.19	b.d.		0.04	0.01			20.53	0.17	0.19	0.02	39.98	0.25	0.36	0.02					100.13
J007	glass	19	48.64	0.24	0.65	0.02	11.38	0.14			16.27	0.20	0.20	0.01	11.23	0.15	11.19	0.08					99.56
	olivine	10	39.54	0.08	b.d.		0.04	0.01			19.47	0.46	0.19	0.01	41.43	0.40	0.33	0.02					101.00
Black IW+2 series																							
H039	glass	13	33.72	0.26	17.64	0.07	5.14	0.03			23.73	0.13	0.31	0.02	10.84	0.09	7.45	0.04					98.83
	olivine	12	38.80	0.26	0.30	0.16	0.05	0.06			20.67	0.25	0.24	0.02	40.79	0.52	0.23	0.05					101.08
H038	glass	11	33.83	0.12	17.93	0.10	5.17	0.03			23.27	0.16	0.31	0.02	10.75	0.06	7.56	0.02					98.82
	olivine	13	38.90	0.27	0.15	0.03	0.03	0.01			20.62	0.17	0.24	0.03	40.93	0.17	0.20	0.01					101.07
H037	glass	13	34.18	0.13	18.02	0.07	5.23	0.03			22.54	0.10	0.32	0.02	10.93	0.04	7.59	0.04					98.82
	olivine	15	38.57	0.45	0.12	0.02	0.02	0.01			20.31	0.17	0.25	0.02	40.93	0.43	0.20	0.01					100.40

[a] Compositions are reported as an average of *n* analyses. Oxide measurements are reported with 1σ standard deviation in the adjacent "s.d." column.
b.d. indicates that the measured composition was below detection limit.
Cr₂O₃, Na₂O, and K₂O were not measured in the olivine crystallization experiments.

dispersive spectrometer background correction and measured the following elements: Si, Al, Ti, Cr, Fe, Mn, Mg, Ca, Na, K. Each quantitative analysis used a 15 kV accelerating potential and 25 nA beam current. Glass compositions were analyzed with a 20 μm beam diameter, and olivine compositions were analyzed with a focused beam ($\sim$1 μm diameter). Each compositional data point was reduced using *Probe for EPMA* software. Averages of the analyzed glass and olivine compositions are reported in Table 3.3. Only analyses with totals $98.5 - 101.5$ weight percent (wt.%) are included in the reported averages (with the exception of experiment J021, for which the analytical totals were on average 96.75 wt.% likely due to incomplete degassing of the carbonates in the starting material). Olivine analyses were filtered to include only those with olivine stoichiometry (cation total between $2.98 - 3.02$ for 4 oxygen atoms). The same calibration was used for the compositional analysis of the experimental wires, with pure Re, Fe, and Pt metal samples added as analytical standards. The Re experiment wires were analyzed from core to rim with a 2 μm beam diameter.

Nuclear Resonant Inelastic X-ray Scattering Spectroscopy (NRIXS) methods

Nuclear resonant inelastic X-ray scattering spectroscopy (NRIXS) was used to probe the excitation modes of iron atoms and derive quantities needed to calculate equilibrium fractionation factors. From the phonon excitation probability function, $S(E)$, or the partial phonon density of states, $g(E)$, (itself derived from S), the force constant for the iron sublattice can be extracted (e.g., Dauphas et al. 2012; Dauphas et al. 2014; Liu et al. 2017) (also see Polyakov et al. 2007, for a different approach based on the kinetic energy). Assuming that the bonds are harmonic and given the high temperatures involved in magmatic processes, the reduced partition function ratio, or β-factor is calculated as a function of temperature from the mean force constant of the iron bonds, $\langle F \rangle$ in N/m (the higher order terms needed to calculate iron β-factors at low temperature are given in Table 3.4):

$$1000 \ln \beta = 2904 \frac{\langle F \rangle}{T^2} \tag{3.1}$$

At a given temperature, the equilibrium stable isotopic fractionation factor (e.g., $\alpha_{\text{mineral-melt}}$) between two phases is related to the β-factor and Fe isotopic composition (δ^{56}Fe) for each phase through:

$$1000 \ln \alpha_{\text{mineral-melt}} = \delta^{56} Fe_{\text{mineral}} - \delta^{56} Fe_{\text{melt}} = 1000 \ln \beta_{\text{mineral}} - 1000 \ln \beta_{\text{melt}} \tag{3.2}$$

Using the measured force constants for synthetic lunar glasses and olivine (Dauphas et al. 2014), the equilibrium fractionation factor between olivine and melt can be theoretically determined using equation 3.2, assuming that the iron force constant in the glass is not significantly different from that of a melt of the same composition.

Multicollector-Inductively Coupled Plasma Mass Spectrometry (MC-ICPMS) methods

The quenched experimental samples were crushed, and then individual phases were hand separated for Fe isotopic analysis with a Thermo Scientific Neptune MC-ICPMS in the Origins Lab at the University of Chicago. The instrument was upgraded in the course of its life by addition of an OnToolBooster Jet pump, bringing it to specifications on par with the Neptune Plus model. Olivine grains were hand-picked from the experimental samples under an optical microscope using cross-polarized light to distinguish the birefringent olivines from the isotropic glass. Separated olivine grains ranged between 30 and 100 μm in diameter and

contained minor amounts of glass, present as thin layers on the edge of the grains. Glass separates were approximately 50-150 μm in diameter, and the transparency of the glass allowed for separation of glass pieces that were free of olivine grains.

Olivine and glass separates were then dissolved for MC-ICPMS analysis. The starting material powders, used experiment wires, and "total samples" (experimental sample left after minor glass and olivine separate removal) were also dissolved and measured to aid in interpretation of the measured isotopic compositions (see Section 3.4.1). Following the routine sample dissolution protocol of the Origins Lab (e.g., Dauphas et al. 2009b; Craddock and Dauphas 2011), we digested 10-40 mg of each sample through hot-plate acid dissolution with mixtures of concentrated HF-HNO_3-$HClO_4$ and HCl-HNO_3-$HClO_4$. An additional dissolution step using aqua regia (3:1 ratio of HCl-HNO_3) was used for the starting material powders, Re wires, and "total samples". This step was repeated three times to ensure all of the Fe had been dissolved from the samples. However, a white residue (rich in TiO_2 and Al_2O_3), remained after two weeks of dissolution for the starting material powders and "total samples". Analysis of the white residues by electron dispersive spectroscopy confirmed that there was no Fe present, indicating that the dissolution effectively removed all Fe from the samples despite the remaining white residue. After the heated dissolution steps, each sample was dried out (the samples with visible residues were centrifugated and the supernatants were used), then dissolved in 6M HCl in preparation for Fe column chemistry.

The sample solutions were purified for Fe through column chemistry following the routine methods of the Origins Lab at the University of Chicago (e.g., Dauphas et al. 2004; Dauphas and Rouxel 2006; Dauphas et al. 2009b). The iron isotopic compositions of the sample solutions were measured using the standard-bracketing method of Dauphas et al. (2009b), and are reported as δ^{56}Fe relative to IRMM-524, whose isotopic composition is identical to IRMM-014 (Craddock and Dauphas 2011).

Table 3.4: Mean force constants for synthetic lunar volcanic glass suite.

| Sample | $\langle F \rangle$ (N/m) | $1000ln\beta = A/T^2 + B/T^4 + C/T^6$ (T in K) | | |
		A ($\times10^5$)	B ($\times10^9$)	C ($\times10^{13}$)
Apollo 16 Green (J020)	189 ± 9	5.36 ± 0.26	-4.29 ± 0.68	12.34 ± 3.60
Apollo 14 Yellow (J021)	195 ± 12	5.55 ± 0.34	-4.87 ± 0.99	16.20 ± 5.57
Apollo 17 Orange (J023)	203 ± 11	5.79 ± 0.32	-4.90 ± 0.79	13.24 ± 3.81
Apollo 14 Black (J022)	191 ± 11	5.45 ± 0.31	-4.35 ± 0.74	11.48 ± 3.45
Fo_{82} Olivine[a]	197 ± 10	5.61 ± 0.28	-2.59 ± 0.44	3.04 ± 1.14

[a] Olivine force constant data from Dauphas et al. (2014).

3.3 Results

Here we report experimentally determined mean force constants of iron bonds in synthetic glass samples and iron isotopic compositions of synthetic olivine and glass separates. Iron isotopic fractionation factors determined from the force constants and iron isotopic compositions demonstrate an absence of resolvable iron isotopic fractionation during olivine crystallization in reducing ($f_{O_2} =$ IW-1 to IW$+2$) conditions.

3.3.1 NRIXS results

The force constants calculated from NRIXS spectra on our synthetic lunar glasses show that within error, the lunar glasses have the same force constant, averaging to a value of 195 ± 22 N/m (Table 3.4). This similarity in force constants over the 0.4 – 16.3 wt.% TiO_2 range of our synthetic glasses suggests that Fe isotopic fractionation is not a function of melt Ti content (Figure 3.4). Further, the mean force constants of our synthetic suite of lunar glasses are similar to the force constants generated for reduced ($f_{O_2} =$ IW) terrestrial basalts (197 ± 8 N/m) in Dauphas et al. (2014). The force constants from the synthetic lunar glasses are
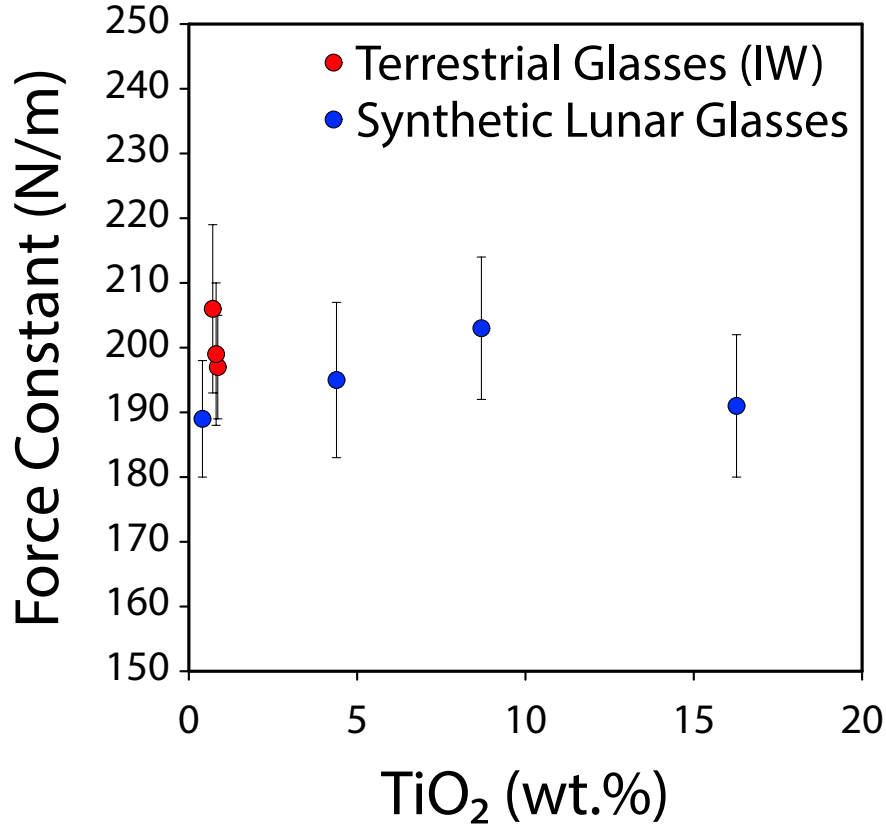
Figure 3.4: Force constants from a suite of melt compositions plotted as a function of TiO_2 content. Red points represent the reduced (f_{O_2} = IW) terrestrial basalt, andesite, and dacite glasses from Dauphas et al. (2014), and blue points represent the synthetic lunar volcanic glass compositions measured in this work. There is no correlation between force constants and TiO_2 content within the investigated $0.4 - 16.3$ wt.% TiO_2 compositional range.

also similar to the previously determined iron force constant for olivine (Fo_{86}, Fe^{3+} absent) of 197 ± 10 N/m (Dauphas et al. 2014).

3.3.2 Olivine crystallization experiments

The measured Fe isotopic compositions of the experimental glass and olivine separates indicate that there is no measurable fractionation between olivine and glass (Table 3.5). The isotopic difference between the starting material, experiment wire, and olivine and glass separates can be explained by the fractionation of Fe isotopes during experimental Fe loss to the Re

wire and through evaporation (Section 3.4.1). The iron isotopic composition of the starting material powders (Table 3.5) is controlled by both the iron isotopic composition of Fe_2O_3 (used in all starting compositions) and Fe metal sponge (used only in starting compositions #010 and #011) (Appendix Table B.1). To further illustrate the isotopic relationship among all experimental parts, the measured Fe isotopic compositions have been plotted in Figure 3.5. For each experiment, the olivine Fe isotopic composition is indistinguishable from that of the glass. The measured compositions thus indicate that olivine does not significantly fractionate iron isotopes when crystallizing from lunar melt compositions at lunar-like f_{O_2}.

Table 3.5: Iron isotopic compositions for each experiment. Reported values (‰) are the weighted averages and weighted errors (95% confidence interval) of multiple measurements.

Sample	Starting Composition	f_{O_2}	Starting Material				Experiment Wire					"Total Sample"				Glass				Olivine			
			δ^{56}Fe	2σ	δ^{57}Fe	2σ	μg Fe	δ^{56}Fe	2σ	δ^{57}Fe	2σ	δ^{56}Fe	2σ	δ^{57}Fe	2σ	δ^{56}Fe	2σ	δ^{57}Fe	2σ	δ^{56}Fe	2σ	δ^{57}Fe	2σ
H056	Apollo 14 VLT (#029)	IW−1	0.26	0.04	0.38	0.06	434	0.13	0.04	0.37	0.06	0.65	0.04	1.01	0.06	0.60	0.04	0.93	0.06	0.60	0.04	0.96	0.06
H043	Apollo 14 Black (#011)	IW−1	0.06	0.02	0.08	0.05	924	0.06	0.03	0.08	0.07	0.28	0.04	0.46	0.06	0.27	0.03	0.43	0.07	0.28	0.03	0.46	0.07
H055	Apollo 14 Black (#028)	IW−1	0.32	0.04	0.44	0.06	722	0.42	0.04	0.67	0.06	0.57	0.04	0.89	0.06	0.54	0.04	0.88	0.06	0.54	0.04	1.04	0.06
H030	Apollo 14 VLT (#010)	IW+2	0.00	0.03	0.01	0.05	39	−0.53	0.05	−0.80	0.08	0.13	0.04	0.18	0.07	0.11	0.03	0.16	0.04	0.12	0.03	0.19	0.04
J012	Apollo 14 Black (#011)	IW+2	0.06	0.02	0.08	0.05	42	−0.37	0.05	−0.56	0.08	0.08	0.03	0.11	0.05	0.11	0.02	0.15	0.04	0.10	0.03	0.15	0.05

For N measurements and i = 1,....N, the weighted averages and weighted errors are calculated from the iron isotopic composition and standard deviation on each measurement (i) using the following equations: $w_i = 1/\sigma_i^2$, $\sigma_{\text{average}} = 1/\sqrt{\Sigma w_i}$, $\delta^{56}\text{Fe}_{\text{average}} = \Sigma(w_i \delta^{56}\text{Fe}_i)/\Sigma w_i$
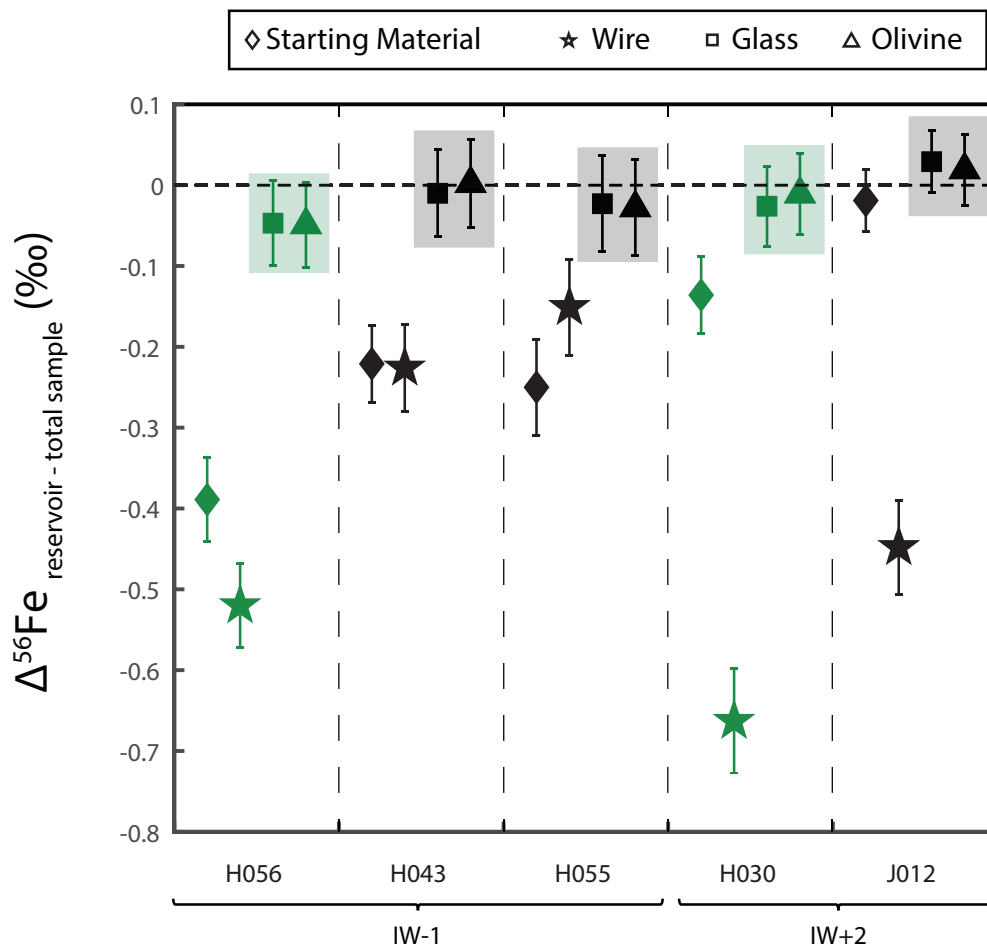
Figure 3.5: Iron isotopic compositions for each experiment part from Table 3.5 reported as $\Delta^{56}\text{Fe}_{\text{part} - \text{total sample}}$ $\left(\delta^{56}\text{Fe}_{\text{part}} - \delta^{56}\text{Fe}_{\text{total sample}} \right)$. Error bars represent 95% confidence interval. Green symbols indicate a synthetic green glass starting composition, and black symbols indicate a synthetic black glass starting composition. Olivine and glass pairs from a given experiment are highlighted.

3.4 Discussion

3.4.1 Quantitative analysis of experiment iron loss

The four-day olivine crystallization experiments experienced up to 18% total Fe loss (Table 3.2). We estimated the amount of total Fe loss using a mass balance of the measured phase compositions and the bulk starting composition of the experiment (Krawczynski and Olive 2011). A rhenium wire was used in all of the experiments to minimize the diffusive Fe loss to the metal loop at reduced oxygen fugacities (Borisov and Jones 1999). The experimental runs at $f_{O_2} = $ IW+2 experienced less Fe loss than those at $f_{O_2} = $ IW−1 (9% vs. 18% Fe loss, Table 3.2). The total amount of iron lost from our experiments under reducing conditions is consistent with the estimated loss in experiments ran at similar conditions by Borisov and Jones (1999). Electron microprobe analyses of the Re wires after completion of the experiments (Figure 3.3b, Appendix Table B.2) yield Fe concentrations within the range of those measured in Re wires from Borisov and Jones (1999). The Re wire is always enriched in the light isotopes of iron, which is consistent with the fact that transport through the wire is diffusive, and light isotopes of iron diffuse faster than heavier ones (Mullen 1961; Roskosz et al. 2006; Dauphas 2007; Richter et al. 2009; Van Orman and Krawczynski 2015). However, the Fe mass balance between the wire and sample cannot account for all of the sample Fe loss.

To account for the effect of Fe loss on the measured Fe isotopic compositions of the samples, we measured the Fe isotopic compositions of the bulk starting material, experiment wire, and the sample material remaining after olivine and glass separates were removed (Table 3.5). Owing to their similar Fe isotopic compositions, removal of minor olivine and glass fractions from the sample did not change the bulk isotopic composition of the remaining

sample material (un-separated glass and olivine, hereafter referred to as "total sample"). For each of the olivine crystallization experiments, the isotopic compositions (δ^{56}Fe) of the total sample were higher than that for the bulk starting material. Open system behavior of Fe and isotopic fractionation between the bulk starting material and the total sample can be explained by Fe loss to the Re wire and evaporative Fe loss in the gas-mixing furnace. Using the measured iron isotopic compositions of the bulk starting material, experiment wire, and the total sample, we were able to quantify the mass of Fe lost and the associated Fe isotopic fractionation for both mechanisms of Fe loss occurring during an experimental run.

The incorporation of Fe into Re wire during the experiment induced some Fe isotopic fractionation, with the wire having a lighter iron isotopic composition than the total sample (Table 3.5, Figure 3.5). Roskosz et al. (2006) demonstrated that experimental iron loss to Pt wires fractionates iron isotopes. In that study, kinetic fractionation of Fe isotopes produced an isotopically light Pt wire (relative to the experimental sample) in short duration experiments. In longer duration experiments, Fe isotopes equilibrated between the Pt wire and experimental charge producing an isotopically heavier Pt wire, which presumably represented the equilibrium partitioning of stable Fe isotopes between Pt and melt. Similar to the Pt wire results of Roskosz et al. (2006), the Re wires from our experiments are isotopically lighter than the experimental samples. This is most likely associated with diffusive transport of iron, as it is well-documented in a variety of systems that light isotopes diffuse faster than heavier ones (e.g., Richter et al. 2009; Van Orman and Krawczynski 2015), resulting in light isotope enrichment in the reservoir that experiences net Fe gain (i.e., the Re wire) relative to the source (i.e., the silicate melt). Owing to this kinetic fractionation, iron isotopes are more fractionated between the Re wire and total sample in the experiments that experienced less iron loss (f_{O_2} = IW+2). That is, as more Fe diffuses into the Re wire, the fractionation between the wire and the sample decreases. Only one sample (H055) has a Re wire iron

isotopic composition that is heavier than the iron isotopic composition of the bulk starting material, but the wire is still isotopically lighter than the glass. Owing to the presence of a thin glass coating on the H055 wire, it is possible that a minor amount of experimental glass was dissolved along with the wire during preparation for iron isotope measurement. This would result in a measured iron isotopic composition for the wire that is heavier than the iron isotopic composition of the wire without glass.

Although loss of Fe to the Re wire fractionates Fe isotopes and produces a heavier Fe isotopic composition for the total sample relative to the bulk starting material, the total amount of Fe incorporated into the wire cannot account for the magnitude of Fe isotopic fractionation between the two, nor the bulk Fe loss. Similar to Fe loss to the Re wire, evaporative Fe loss would preferentially deplete the experiments in lighter Fe isotopes, resulting in greater δ^{56}Fe for the olivine, glass, and total sample compared to the bulk starting material.

To assess the extent of both evaporative Fe loss and Fe loss to the Re wire, we calculated an isotopic mass balance of the measured experiment parts (starting material, wire, and total sample) and, by difference, the Fe that evaporated during the experiment. For example, using the isotopic measurements (Table 3.5) for each part of experiment H056 we can estimate a δ^{56}Fe for the Fe lost by evaporation:

$$\delta^{56}Fe_{\text{starting material}} = \sum_i X_{Fe}^i \times \delta^{56}Fe_i \qquad (3.3)$$

where i denotes a reservoir of the experiment (wire, total sample, gas), where X_{Fe} represents the mass fraction of the initial Fe present in each reservoir, δ^{56}Fe$_{\text{starting material}}$, δ^{56}Fe$_{\text{total sample}}$, δ^{56}Fe$_{\text{wire}}$ are measured values, and δ^{56}Fe$_{\text{gas}}$, X_{Fe}^{wire}, $X_{Fe}^{\text{total sample}}$, X_{Fe}^{gas} can then be calculated

from mass balance constraints (results presented in Figure 3.6 and Figure 3.7). $X_{Fe}^{\text{total sample}}$ is equivalent to one minus the percent total Fe loss estimated from mass balance of the measured phases and the experimental starting composition (Krawczynski and Olive, 2011). For H056, which experienced 18% total Fe loss, $X_{Fe}^{\text{total sample}} = 0.82$ (Figure 3.7). X_{Fe}^{wire} is calculated using the ICP-MS Fe concentration measurement of the dissolved wire (μg, Table 3.5) and the estimated mass of Fe in the starting material (75 mg pellet, wt.% FeO for starting composition, Table 3.1). For H056, $X_{Fe}^{\text{wire}} = 0.04$. Following this, X_{Fe}^{gas} can be calculated assuming $X_{Fe}^{\text{total sample}} + X_{Fe}^{\text{wire}} + X_{Fe}^{\text{gas}} = 1$. Thus, for H056, $X_{Fe}^{\text{gas}} = 0.14$. From this calculation, we conclude that 14% of the initial Fe in the starting material was lost by evaporation during the experiment.

The last unknown of equation 3.3 is the "iron isotopic composition" of the Fe lost through evaporation ($\delta^{56}\text{Fe}_{\text{gas}}$), or rather the net isotopic fractionation that resulted from the evaporation. To estimate the evaporative fractionation, we solve equation 3.3 for $\delta^{56}\text{Fe}_{\text{gas}}$ using the X_{Fe} values calculated above (Figure 3.7) and the measured $\delta^{56}\text{Fe}$ values for the experiment parts (Table 3.5). For H056, the resulting isotopic composition associated with the evaporated gas is $\delta^{56}\text{Fe}_{\text{gas}} = -2.01\text{‰}$, and the bulk isotopic fractionation factor is $\alpha_{\text{experiment-vapor}} = 1.0028$. Our estimates of the evaporative isotopic fractionation based on the mass balance of our measured experimental run products (bulk $\alpha_{\text{experiment-vapor}}$) range from 1.0002 to 1.0028, with the smallest fractionation between experiment and vapor (1.0002) existing for experiment J012, the high-Ti (black glass) composition conducted at IW+2. The experiment-vapor fractionation in our gas-mixing furnace experiments is smaller than that in a vacuum furnace because the Fe vapor pressure is higher, which dampens the isotopic fractionation (Richter et al. 2002; Richter 2004; Dauphas and Rouxel 2006; Richter et al. 2007; Richter et al. 2009; Dauphas et al. 2015). Most likely, the evaporative Fe loss proceeded through a Rayleigh distillation. Using the $\alpha_{\text{experiment-vapor}}$ calculated for each experiment, we have modeled the change
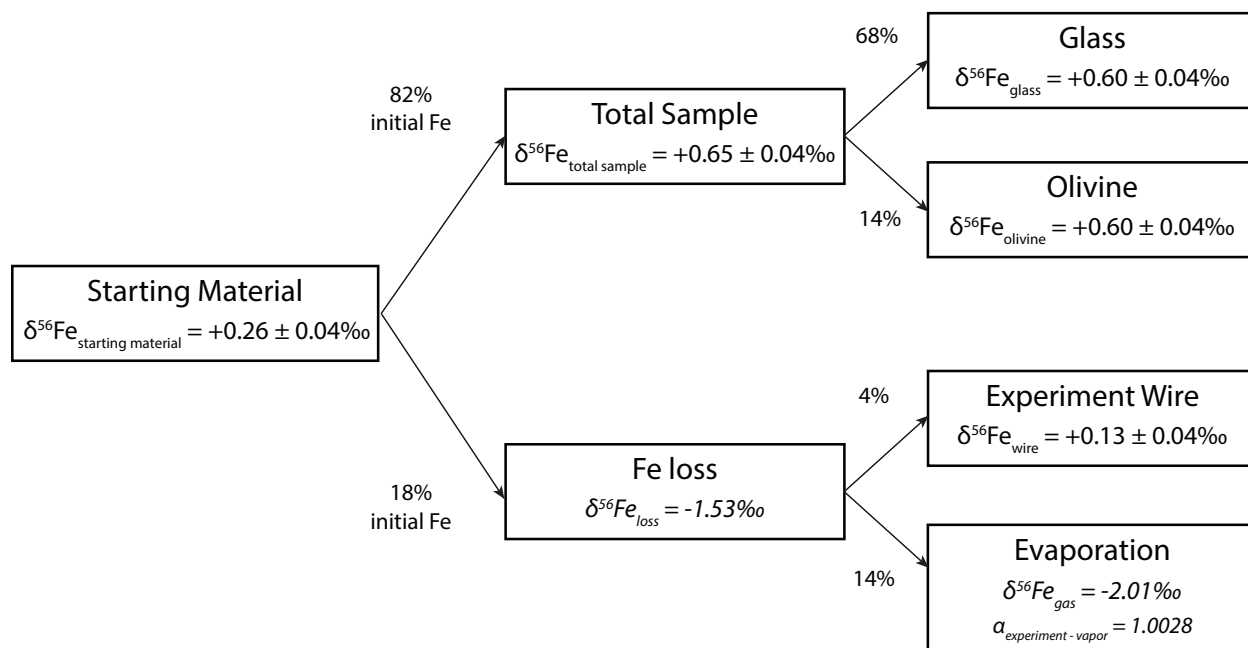
Figure 3.6: A schematic diagram illustrating the Fe mass and isotope distributions detailed in Section 3.4.1 for experiment H056. The labeled percent values at each branch represent the percent of the initial Fe attributed to a given experiment reservoir. Measured iron isotopic compositions of each experiment reservoir are mass balanced to explain the effect of Fe loss on the iron isotopic composition of the total sample. Iron isotopic compositions and fractionations in italics indicate calculated (not measured) values. Percent initial Fe for olivine and glass separates is calculated using the olivine and glass proportions given in Table 3.2 (83% glass, 17% olivine for H056) and the calculated percent initial Fe for the total sample ($X_{Fe}^{\text{total sample}} = 1 - X_{Fe}^{\text{loss}}$). A similar calculation was performed for each experiment using the measured iron isotopic compositions for all the experiment reservoirs (starting material, olivine, glass, total sample, experiment wire).
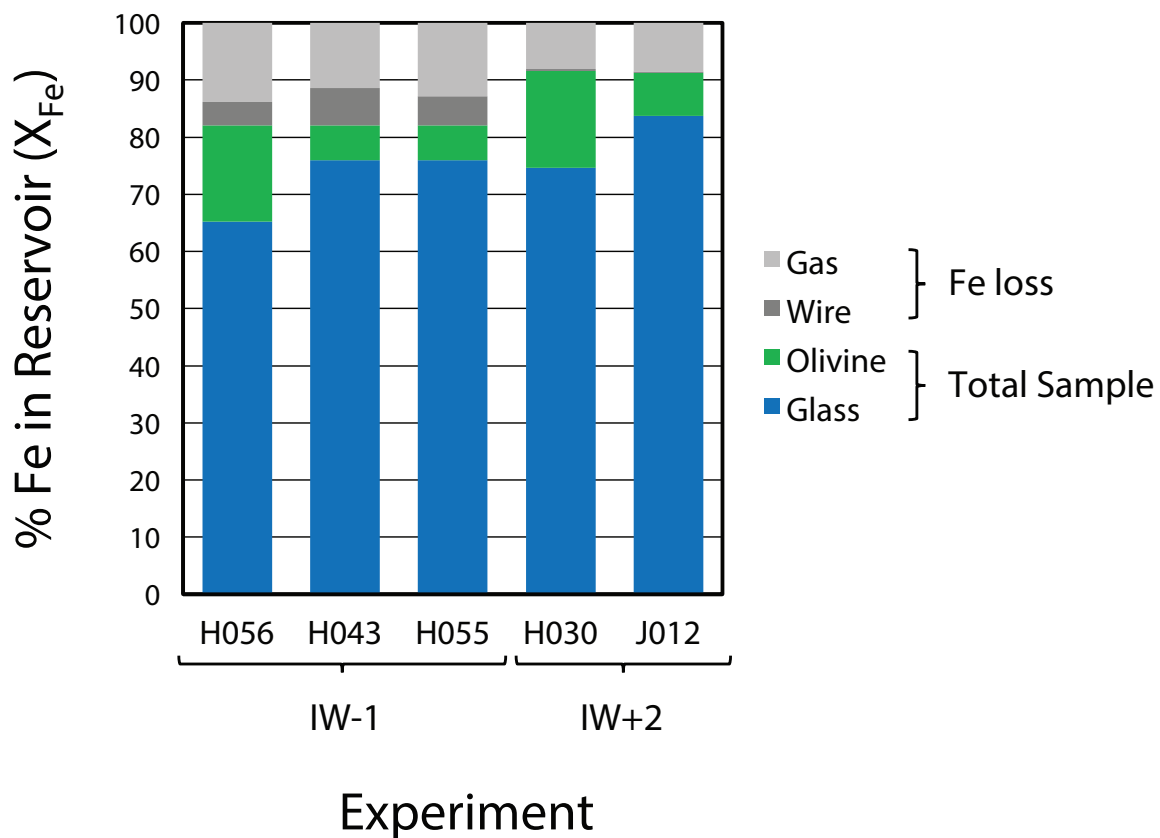
Figure 3.7: A stacked bar graph indicating the X_{Fe} calculated for each Fe reservoir for each experiment. The bracketed labels below the experiment names indicate the oxygen fugacity of the experiment (IW$-$1 or IW$+$2). Additionally, the legend identifies which reservoirs constitute Fe loss (wire, gas) and "total sample" Fe (olivine, glass).

in the iron isotopic composition of the experimental sample as iron is lost by evaporation (Figure 3.8).

For experiments conducted at f_{O_2} = IW-1, on average 5% of the Fe starting material was lost to the Re wire (average $X_{Fe}^{\text{wire}} = 0.05$), while this value is negligible at IW$+2$ (Figure 3.7). Additionally, 13% of the Fe starting material was lost via evaporation at IW-1 (average $X_{Fe}^{\text{gas}} = 0.13$), whereas 8% of the starting material Fe was lost by evaporation at IW$+2$ (average $X_{Fe}^{\text{gas}} = 0.08$). In one-atmosphere gas-mixing furnace experiments, Fe loss has generally been considered as loss to the container (e.g., Re or Pt wire), while volatile element loss (e.g., Na, K) has been attributed to vaporization (Corrigan and Gibb 1979; Donaldson and Gibb 1979; Grove 1981; Borisov and Jones 1999). Our results indicate that at IW-1, ~75% of the estimated Fe loss occurred via evaporation, and only 25% of the Fe loss can be attributed through loss to the Re wire. At IW$+2$, the estimated Fe loss is due to ~95% evaporative loss and ~5% loss to the Re wire.

To further assess the potential for evaporative isotopic fractionation at our experimental run conditions, we have calculated the evaporative flux of Fe (J_{Fe}) from the sample using the Hertz-Knudsen equation:

$$J_{Fe} = \frac{\alpha_{Fe}(P_{Fe}^v - P_{Fe}^a)}{\sqrt{2\pi M_{Fe}RT}} \tag{3.4}$$

in which J is the evaporative flux in moles cm^{-2} s^{-1}, α is the evaporation coefficient, M is molecular weight, P^v is equilibrium vapor pressure for the element considered, P^a is the ambient pressure for the element considered, R is the universal gas constant (J mol^{-1} K^{-1}), and T is temperature (K). Following the methods outlined in Fedkin et al. (2006), we calculated the equilibrium vapor pressure of Fe assuming both Fe and FeO species exist in the gas, and the only contribution of Fe to the furnace gas atmosphere is from the experimental
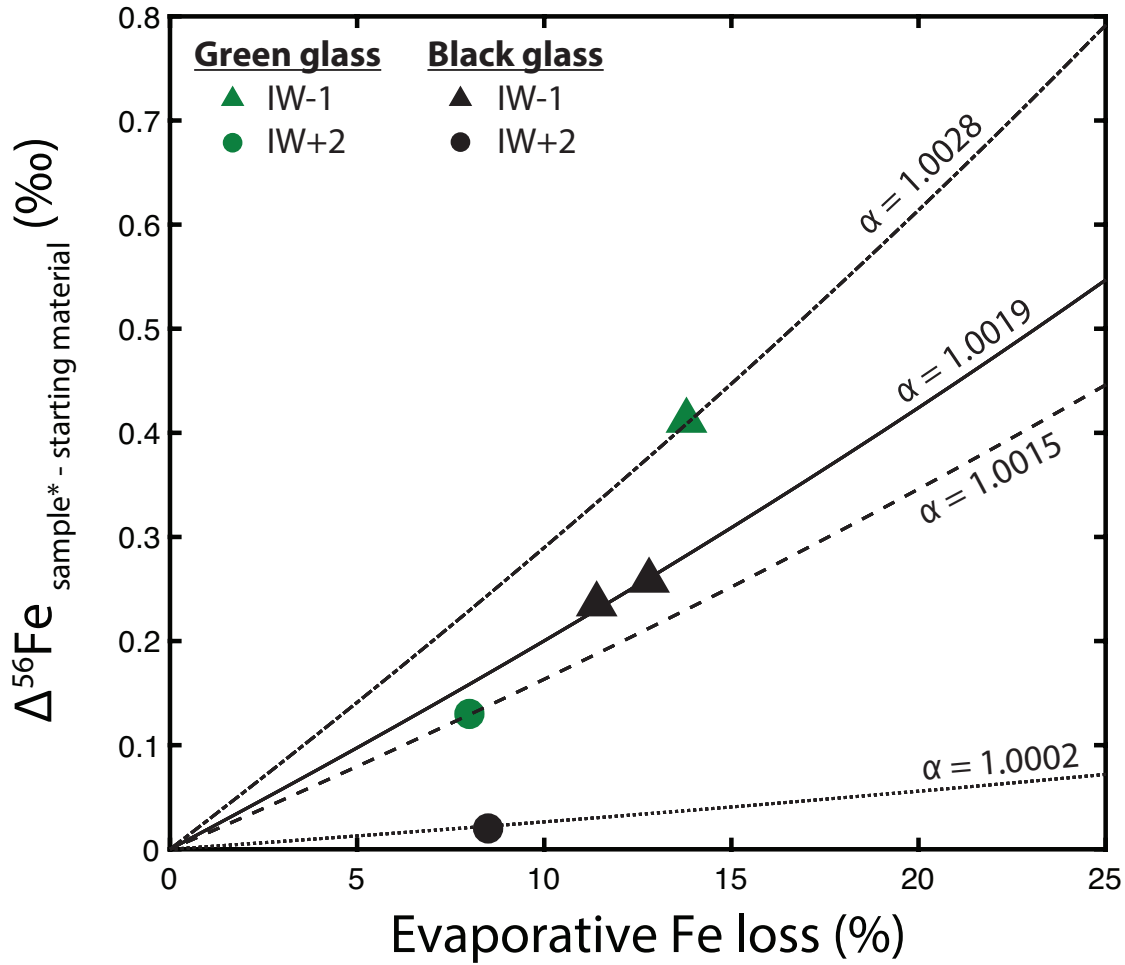
Figure 3.8: The iron isotopic evolution of an experimental sample as evaporative Fe loss proceeds through Rayleigh distillation, as calculated using $\alpha_{\text{experiment-vapor}}$ for each experiment. The iron isotopic composition is reported as $\Delta^{56}\text{Fe}_{\text{sample*-starting material}}$ ($\delta^{56}\text{Fe}_{\text{sample*}} - \delta^{56}\text{Fe}_{\text{starting material}}$) using $\delta^{56}\text{Fe}_{\text{starting material}}$ from Table 3.5. $\delta^{56}\text{Fe}_{\text{sample*}}$ represents the iron isotopic composition of the "total sample" after accounting for the iron isotopic fractionation associated with Fe loss to the Re wire (Section 3.4.1, Figures 3.6, 3.7). This correction was performed to isolate the effect of evaporation on the heavy iron isotopic enrichment that occurs during the experiment, however both losses (to wire, to vapor) would occur simultaneously throughout the experiment. Green symbols indicate a synthetic green glass starting composition, and black symbols indicate a synthetic black glass starting composition. The shape of the symbols reflects the f_{O_2} of each experiment as indicated in the legend. Each modeled line is labeled with the corresponding $\alpha_{\text{experiment-vapor}}$ used in the Rayleigh distillation equation.

sample:

$$P_{Fe}^v = P_{Fe}^{\text{sample}} = P_{FeO} + P_{Fe} \qquad (3.5)$$

The partial pressures of the gases evaporated from the molten experimental sample are then calculated from the volatilization reactions:

$$FeO_{(l)} \rightarrow FeO_{(g)} \qquad (3.6)$$

$$FeO_{(l)} \rightarrow Fe_{(g)} + \frac{1}{2}O_{2(g)} \qquad (3.7)$$

The equilibrium constants, k, for reactions 3.6 and 3.7 are constructed from the thermodynamic data in the JANAF tables (Chase 1996) and used to calculate the equilibrium vapor pressure of Fe:

$$P_{Fe}^{\text{sample}} = k_6 a_{FeO} + \frac{k_7 a_{FeO}}{\sqrt{f_{O_2}}} \qquad (3.8)$$

where a_{FeO} is the activity of FeO in the molten experimental sample, and f_{O_2} is the oxygen fugacity of the experiment. We used the rhyolite-MELTS code (Ghiorso and Sack 1995; Asimow and Ghiorso 1998; Gualda et al. 2012) to calculate the activity of FeO in the silicate liquid for each experimental starting composition at the experimental temperature and oxygen fugacity. Using equation 3.8, we calculate P_{Fe}^{sample}, which is then used to calculate the evaporative flux, J_{Fe}, from equation 3.4. Assuming the gas flow in our furnace is efficient in removing any Fe gas that is released into the furnace from the sample, we set the ambient vapor pressure of Fe (Pa) equal to 0. Then, the only unknown needed to solve for

the evaporative flux (J_{Fe}) using equation 3.4 is the Fe evaporation coefficient (α_{Fe}). The evaporation coefficients we used in equation 3.4 to calculate evaporative Fe loss that matches the estimated evaporative Fe loss from our samples are $\alpha_{Fe} = 2.5 \times 10^{-3}$ at IW−1, and $\alpha_{Fe} = 6.3 \times 10^{-2}$ at IW+2 (see Appendix B for additional detail).

Through isotopic measurement and mass balance calculations of our experiments, we have demonstrated that isotopic fractionation during evaporation and loss to the experimental container are essential considerations for experimental studies of isotope partitioning. Despite this open system behavior, the olivine and glass phases were always in equilibrium, as diffusion in the melt is fast (at 1265°C, anhydrous basaltic melt $D_{Fe} \sim 10^{-11}$ m^2/s; Zhang et al. 2010), and $10 - 50$ μm diameter olivine grains would diffusively equilibrate at the experimental run temperature and duration. For example, at experimental conditions of 1265°C and IW+2, a 50 μm olivine grain would equilibrate with respect to Fe and Mg in approximately 50 hours (McDougall and Harrison 1999; Dohmen and Chakraborty 2007). The olivine and glass separates showed deviation from the starting material, but had identical isotopic composition to that of the "total sample" which diffusively maintained equilibrium. Thus, the measured Fe isotopic compositions of the olivine and glass can accurately be compared to interpret the olivine-melt Fe isotopic fractionation during olivine crystallization.

3.4.2 Factors controlling iron isotopic fractionation on the Moon

We have applied our results to test whether the lunar iron isotope "dichotomy" observed between the high- and low-Ti basalts can be explained by olivine crystallization or melt titanium content.

From our complementary NRIXS and olivine crystallization experiments, we have concluded that any equilibrium fractionation of iron isotopes between olivine and melt at lunar-like

oxygen fugacities is not resolvable within analytical uncertainties. Olivine-melt Fe isotopic fractionation factors for the lunar volcanic glasses were determined from our measured force constants on the glass suite and the olivine NRIXS results from Dauphas et al. (2014) (Figure 3.9). Our result from the MC-ICPMS olivine crystallization study is consistent with the Fe isotopic fractionation factors predicted by the NRIXS measurements on olivine (Dauphas et al. 2014) and the suite of lunar volcanic glasses (this study), in that there is not a resolvable iron isotopic fractionation. Some major element variations in lunar mare basalts can be attributed to differences in source compositions having experienced varying degrees of olivine fractionation (Shearer et al. 2006, and references therein). Additionally, extensive crystallization of the lunar magma ocean involving significant fractionation of olivine has been previously hypothesized as a mechanism for generating the isotopically heavy source regions for the high-Ti basalts (Wang et al. 2015). However, because olivine does not fractionate iron isotopes to a measureable extent, varying degrees of equilibrium olivine crystallization can be eliminated as a potential mechanism for generating the mare basalt iron isotope dichotomy. The fractionation of phases other than olivine, such as clinopyroxene and ilmenite, are likely more important in interpreting both the major element and isotopic compositions of the lunar mare basalt suites.

Both of our experimental approaches indicate that the difference in melt titanium content between low-Ti and high-Ti mare basalts cannot explain the observed iron isotope dichotomy. Partitioning of Fe into olivine has been shown to be a function of Ti content (Longhi et al. 1978; Xirouchakis et al. 2001; Krawczynski and Grove 2012). Titanium influences the coordination environment of Fe^{2+} in silicate melt by forming Fe-Ti complexes, and as a result, Fe is preferentially incorporated into the melt relative to olivine (Krawczynski and Grove 2012). However Fe isotope partitioning does not appear to correlate with melt titanium content, as demonstrated by our NRIXS force constant measurements (Table 3.4, Figure
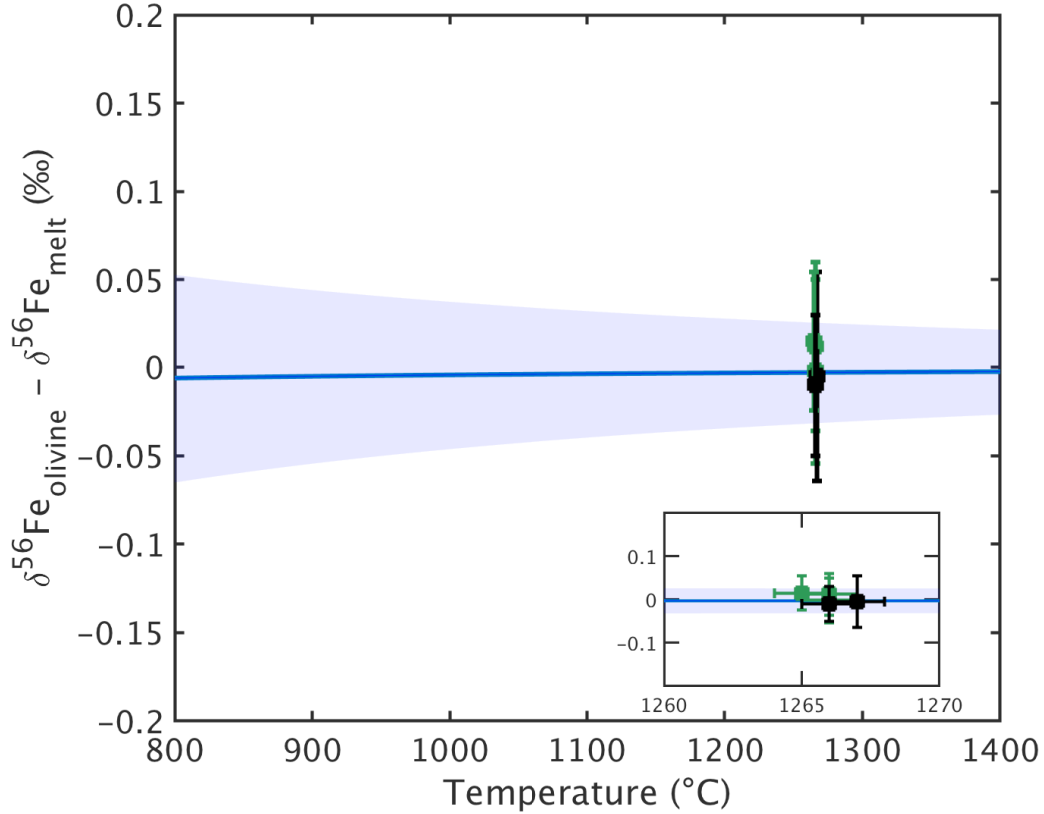
Figure 3.9: Equilibrium mineral-melt fractionation of iron isotopes for olivine plotted as a function of temperature. The blue line represents the difference between the average beta factor calculated from the NRIXS mean force constants for our synthetic lunar glasses and the beta factor for olivine (Fo_{82}) from Dauphas et al. (2014). The blue shading represents the error associated with the calculated beta factors. The difference between the iron isotopic compositions of olivine and glass separates in each crystallization experiment (Table 3.5) are plotted with the associated measurement errors (95% confidence interval). Green symbols indicate a synthetic green glass starting composition, and black symbols indicate a synthetic black glass starting composition. The inset in the bottom right is the same data plotted in the main figure, with the x-axis expanded on the experiment run temperatures. There is no resolvable difference between olivine and the synthetic lunar glass suite under equilibrium conditions, as evidenced by our experimental results from both the NRIXS and ICPMS approaches.

3.4) and our olivine crystallization experiments from both the low-Ti and high-Ti glass compositions. Within the investigated range of titanium content, the average coordination number of Fe^{2+} does not vary enough to influence the NRIXS force constants. Though the major element partitioning of Fe into olivine is affected by Fe^{2+}-Ti complexes in silicate melt, we conclude that the isotopic partitioning of Fe is not affected by melt titanium content. In contrast, Dauphas et al. (2014) demonstrated that melt compositional parameters such as silica content and the redox state of iron (i.e., Fe^{3+} content) influence the Fe bonding structure, and consequently, the iron isotopic composition, in a suite of terrestrial volcanic glass compositions ranging from basalt to rhyolite.

3.4.3 Iron isotopic composition of lunar dunite 72415

Olivines from lunar dunite 72415 are considerably lighter than the mare basalts ($\delta^{56}Fe_{dunite} = -0.35 \pm 0.20$‰, Wang et al. 2015; Sossi and Moynier 2017). These values, if representative of equilibrium fractionation from a parent melt isotopically similar to the mare basalts ($\delta^{56}Fe$ = 0‰ to +0.2‰), differ from the predicted Fe isotopic fractionation of this study. The absence of resolvable equilibrium iron isotopic fractionation between olivine and lunar melts in our experiments supports a non-equilibrium model for generating the light iron isotopic composition of the lunar dunite.

As Fe begins to diffuse into olivine, the isotopes of Fe with lighter mass will be preferentially enriched, creating a "light" iron isotopic composition (Teng et al. 2008; Dauphas et al. 2010; Teng et al. 2011; Sio et al. 2013; Sio and Dauphas 2017). The lunar dunite is highly magnesian ($Fo_{84} - Fo_{89}$, Dymek et al. 1975), and any Fe that diffuses into the olivine will greatly affect the mass balance of Fe isotopes in the dunite. Diffusive iron isotopic fractionation modeling that reproduces the observed Fe-Mg zoning profiles in lunar dunite olivine grains, can produce iron isotope signatures as low as $\delta^{56}Fe = -0.21$‰ and -0.3‰ (Wang et al. 2015). Further,

kinetic isotopic fractionation models of Fe-Mg interdiffusion and olivine crystallization (Teng et al. 2008; Teng et al. 2011; Sio et al. 2013; Oeser et al. 2015; Collinet et al. 2017; Sio and Dauphas 2017) reproduce isotopic fractionations as large as 1‰ observed in olivine grains.

Models of lunar dunite (72415-72418) petrogenesis detail the potential petrologic processes involved in generating a kinetic origin for the isotopically light dunite signature. Early petrologic investigations of the lunar dunite identified it as an early lunar magma ocean cumulate (e.g., Dymek et al. 1975). In contrast, Ryder (1992) concluded that the lunar dunite crystallized at shallow depths less than 1 km. The early lunar magma ocean cumulate hypothesis was invoked by Wang et al. (2015) to explain the isotopically light iron isotopic compositions of the dunite. If the lunar dunite is an early lunar magma ocean cumulate, then, assuming equilibrium conditions, the composition from which the dunite is crystallizing must already be isotopically light; δ^{56}Fe$= -0.35 \pm 0.20$‰.

One way an isotopically light dunite source composition could potentially be generated is by an early core formation and metal-silicate partitioning. Experimental and analytical studies of metal-silicate iron isotope partitioning have suggested that metal is isotopically heavier (Δ^{56}Fe$_{\text{metal-silicate}} \approx +0.1$‰) than coexisting silicate (Poitrasson et al. 2005; Shahar et al. 2015; Elardo and Shahar 2017). However, a number of investigations (e.g., Schuessler et al. 2007; Poitrasson et al. 2009; Hin et al. 2012; Shahar et al. 2016; Liu et al. 2017) have concluded that no significant iron isotopic fractionation occurs between metal and silicate in equilibrium. The disagreement results from the significant differences in starting compositions, phases, capsule materials, and experimental conditions between studies. Assuming an equilibrium iron isotopic fractionation did exist between metal and silicate, if the dunite source were once deep enough to be in isotopic equilibrium with the lunar core, it would have a relatively light iron isotopic composition. However, the estimates for the bulk mantle iron isotopic composition of the Moon after core formation (e.g., minimum δ^{56}Fe$= -0.15$‰; Elardo and

Shahar 2017), still cannot explain the magnitude of light iron isotopic compositions measured in the lunar dunite by equilibrium metal-silicate fractionation alone.

Another alternative method of generating isotopically light olivine in the lunar dunite is partial melting. Iron isotope studies of terrestrial peridotites, which are the residues of partial melting and depletion, show a correlation between iron isotopic compositions and depletion, becoming lighter at higher extents of partial melting (Williams et al. 2005; Weyer and Ionov 2007; Williams et al. 2009; Williams and Bizimis 2014). It is possible that the iron isotopic composition of the lunar dunite is a result of partial melting, however the existing models of lunar dunite petrogenesis (i.e., Dymek et al. 1975; Ryder 1992; Shearer et al. 2015) identify the dunite as being of cumulate origin, not an ultra-depleted residue of partial melting.

Considering the potential models for lunar dunite petrogenesis, kinetic fractionation via Fe-Mg interdiffusion seems likely to have occurred, and this mechanism could easily explain the light Fe isotopic compositions measured in the lunar dunite olivines. Regardless of whether the lunar dunite is a deep magma ocean cumulate (Dymek et al. 1975) or shallow cumulate (Ryder 1992; Shearer et al. 2015), the Mg-rich nature of the dunite ensures it would have interacted with a higher Fe/Mg melt before and/or during its ascent to the lunar surface/sub-surface. In this way, iron diffusion into the dunite is a plausible occurrence during every proposed model of dunite formation. Iron diffusion into the Fe-poor olivine of the lunar dunite would decrease the δ^{56}Fe composition, producing the negative δ^{56}Fe values measured by both Wang et al. (2015) and Sossi and Moynier (2017).

3.4.4 Considerations for high-temperature iron isotopic fractiona-tion on Earth and Mars

The results of our olivine crystallization experiments indicate that the absence of a measureable equilibrium iron isotopic fractionation between olivine and melt is robust over $f_{O_2} = \text{IW}-1$ to IW+2 in both the low-Ti (green glass) and high-Ti (black glass) compositions. Thus, we can apply our results for the synthetic lunar glass compositions to olivine-bearing systems on Earth and Mars with a similar range in oxygen fugacity, keeping in mind that there could be melt compositional controls in addition to that of TiO_2 determined in this work.

Estimations for the oxygen fugacity of Earth's upper mantle from spinel peridotites lie within QFM±2 (IW+1.5 to IW+5.5 at magmatic temperatures), with select abyssal peridotites and peridotite massifs extending to QFM−3 (∼IW+0.5) (Frost and McCammon 2008, and references therein). Garnet peridotites are more reducing than spinel peridotites, with the majority of f_{O_2} estimations falling between IW−1 and IW+2 (Frost and McCammon 2008). Additionally, the oxygen fugacity of martian basalts is estimated to be QFM−3 to QFM−1 (∼IW to IW+3) (Herd et al. 2002). Considering these estimates of magmatic oxygen fugacity, the IW−1 to IW+2 range of our experiments is relevant to garnet peridotites, as well as the most reduced spinel peridotites and martian basalts.

Iron isotopic compositions of terrestrial peridotites are $\delta^{56}\text{Fe}= -0.1‰$ to $+0.15‰$ (Dauphas et al. 2017). The range of peridotite iron isotopic compositions are considered to be a result of melt extraction based on the correlation between iron isotopic composition and depletion, with iron isotopic compositions of residues becoming lighter at higher extents of partial melting (Williams et al. 2005; Weyer and Ionov 2007; Williams et al. 2009; Williams and Bizimis 2014). Alternatively, the heavy isotopic enrichment in the melt relative to the residue may be a result of Fe^{3+} in the melt (Dauphas et al. 2009a; Dauphas et al. 2014).

For instance, the difference between the iron isotopic compositions of spinel and garnet peridotites has been attributed to the contrasting behavior of Fe^{3+} during melting (Williams et al. 2005). Experimental determinations of mineral-melt iron isotopic fractionations for additional minerals (i.e., pyroxene, spinel) are needed in order to fully model the evolution of iron isotopic compositions during partial melting, as there exists experimental evidence for equilibrium iron isotopic fractionation between spinel and olivine (Shahar et al. 2008; Roskosz et al. 2015).

3.5 Conclusion

Olivine separates are often enriched in lighter iron isotopes relative to coexisting minerals and the bulk rock (e.g., terrestrial peridotites, Beard and Johnson 2004; Poitrasson et al. 2004; Williams et al. 2005; terrestrial basalts, Teng et al. 2008; Teng et al. 2011; Sio et al. 2013; lunar basalts, Poitrasson et al. 2004; Wang et al. 2012; Wang et al. 2015; martian basalts, Collinet et al. 2017). Considering the olivine-melt fractionation results presented in this work, the only known mechanism capable of fractionating iron isotopes to a measureable degree is diffusive fractionation (Dauphas et al. 2010; Teng et al. 2011; Sio et al. 2013; Oeser et al. 2015; Sio and Dauphas 2016; Collinet et al. 2017). Thus, the olivine grains enriched in light Fe isotopes in mafic rocks are not a result of primary igneous crystallization, but rather a diffusive fractionation, potentially related to re-equilibration (Teng et al. 2011; Sio et al. 2013; Oeser et al. 2015) or simultaneous Fe diffusion and crystal growth (Sio and Dauphas 2016; Collinet et al. 2017). A diffusive fractionation mechanism is further supported by existing isotopic disequilibrium between coexisting mineral pairs in peridotite samples (Beard and Johnson 2004; Roskosz et al. 2015). This disequilibrium in peridotites has been hypothesized as a result of multiple phases of melt extraction, melt percolation, melt-rock reaction, or metasomatism (Beard and Johnson 2004; Williams et al. 2005; Macris et al. 2015; Roskosz et al. 2015; Zhao

et al. 2017). If the light iron isotopic compositions of terrestrial peridotites can conclusively be attributed to metasomatism, then the light iron isotopic composition of the lunar dunite (discussed in Section 3.4.3) may also be a result of metasomatism, as metasomatism has been invoked to explain chemical trends and petrographic textures observed in the lunar dunite (Shearer et al. 2015).

Acknowledgements

References

Asimow, P. D. and M. S. Ghiorso (1998). "Algorithmic Modifications Extending MELTS to Calculate Subsolidus Phase Relations." *American Mineralogist* 83, pp. 1127–1131.

Beard, B. L. and C. M. Johnson (2004). "Inter-mineral Fe isotope variations in mantle-derived rocks and implications for the Fe geochemical cycle." *Geochimica et Cosmochimica Acta* 68 (22), pp. 4727–4743. ISSN: 0016-7037.

Borisov, A. and J. H. Jones (1999). "An evaluation of Re, as an alternative to Pt, for the 1 bar loop technique: An experimental study at 1400 °C." *American Mineralogist* 84 (10), pp. 1528–1534.

Chase, M. W. (1996). "NIST-JANAF Thermochemical Tables for the Bromine Oxides." *Journal of Physical and Chemical Reference Data* 25 (4), p. 1069.

Collinet, M., B. Charlier, O. Namur, M. Oeser, E. Médard, and S. Weyer (2017). "Crystallization history of enriched shergottites from Fe and Mg isotope fractionation in olivine megacrysts." *Geochimica et Cosmochimica Acta* 207, pp. 277–297.

Corrigan, G. and F. G. Gibb (1979). "The loss of Fe and Na from a basaltic melt during experiments using wire-loop method." *Mineralogical Magazine* 43, pp. 121–126.

Craddock, P. R., N. Dauphas, and R. Clayton (2010). "Mineralogical control on iron isotopic fractionation during lunar differentiation and magmatism." *Lunar and Planetary Science Conference*. Vol. 41, p. 1230.

Craddock, P. R. and N. Dauphas (2011). "Iron Isotopic Compositions of Geologic Reference Materials and Chondrites." *Geostandards and Geoanalytical Research* 35 (1), pp. 101–123.

Dauphas, N., F. Z. Teng, and N. T. Arndt (2010). "Magnesium and iron isotope in 2.7 Ga Alexo komatiites: mantle signatures, no evidence for Soret diffusion, and identification of diffusive transport in zoned olivine." *Geochimica et Cosmochimica Acta* 74 (11), pp. 3274–3291.

Dauphas, N. (2007). "Diffusion-driven kinetic isotope effect of Fe and Ni during formation of Widmanstätten pattern." *Meteoritics and Planetary Science* (42), pp. 1597–1613.

Dauphas, N., P. R. Craddock, P. D. Asimow, V. C. Bennett, A. P. Nutman, and D. Ohnenstetter (2009a). "Iron isotopes may reveal the redox conditions of mantle melting from Archean to Present." *Earth and Planetary Science Letters* 288, pp. 255–267.

Dauphas, N., P. E. Janney, R. A. Mendybaev, M. Wadhwa, F. M. Richter, A. M. Davis, M. van Zuilen, R. Hines, and C. N. Foley (2004). "Chromatographic separation and multicollection-ICPMS analysis of iron. Investigating mass-dependent and -independent isotope effects." *Anal Chem* 76 (19), pp. 5855–63. ISSN: 0003-2700 (Print) 0003-2700.

Dauphas, N., S. G. John, and O. Rouxel (2017). "Iron Isotope Systematics." *Reviews in Mineralogy and Geochemistry* 82, pp. 415–510.

Dauphas, N., F. Poitrasson, C. Burkhardt, H. Kobayashi, and K. Kurosawa (2015). "Planetary and meteoritic Mg/Si and δ^{30}Si variations inherited from solar nebular chemistry." *Earth and Planetary Science Letters* (427), pp. 236–248.

Dauphas, N., A. Pourmand, and F.-Z. Teng (2009b). "Routine isotopic analysis of iron by HR-MC-ICPMS: how precise and how accurate?" *Chemical Geology* 267, pp. 175–184.

Dauphas, N., M. Roskosz, E. E. Alp, D. Golden, C. K. Sio, F. L. Tissot, M. Y. Hu, J. Zhao, L. Gao, and R. Morris (2012). "A general moment NRIXS approach to the determination of equilibrium Fe isotopic fractionation factors: Application to goethite and jarosite." *Geochimica et Cosmochimica Acta* 94, pp. 254–275.

Dauphas, N., M. Roskosz, E. E. Alp, D. Neuville, M. Y. Hu, C. K. Sio, F. L. Tissot, J. Zhao, L. Tissandier, E. Médard, and C. Cordier (2014). "Magma redox and structural controls on iron isotope variations in Earth's mantle and crust." *Earth and Planetary Science Letters* 398, pp. 127–140.

Dauphas, N. and O. Rouxel (2006). "Mass spectrometry and natural variations of iron isotopes." *Mass Spectrom Rev* 25 (4), pp. 515–50. ISSN: 0277-7037 (Print) 0277-7037.

Day, J. M., L. Qiu, R. Ash, W. McDonough, F.-Z. Teng, R. L. Rudnick, and L. A. Taylor (2016). "Evidence for high-temperature fractionation of lithium isotopes during differentiation of the Moon." *Meteoritics and Planetary Science* 51, pp. 1046–1062.

Delano, J. W. (1986). "Pristine Lunar Glasses: Criteria, Data, and Implications." *Journal of Geophysical Research* 91 (B4), pp. D201–D213.

Dohmen, R. and S. Chakraborty (2007). "Fe-Mg diffusion in olivine II: point defect chemistry, change of diffusion mechanisms and a model for calculation of diffusion coefficients in natural olivine." *Phys Chem Minerals* 34, pp. 409–430.

Donaldson, C. H. and F. G. Gibb (1979). "Changes in sample compostion during experiments using 'wire-loop' technique." *Mineralogical Magazine* 43, pp. 115–119.

Donovan, J. J., J. W. Singer, and J. T. Armstrong (2016). "A new EPMA method for fast trace element analysis in simple matrices." *American Mineralogist* 101 (8), pp. 1839–1853.

Dymek, R. F., A. L. Albee, and A. A. Chodos (1975). "Comparative petrology of lunar cumulate rocks of possible primary origin: Dunite 72415, troctolite 76535, norite 78235, and anorthosite 62237." *Proceedings of the Lunar Science Conference 6th*, pp. 301–341.

Elardo, S. M. and A. Shahar (2017). "Non-chondritic iron isotope ratios in planetary mantles as a result of core formation." *Nature Geoscience* 10, pp. 317–321.

Fedkin, A., L. Grossman, and M. S. Ghiorso (2006). "Vapor pressures and evaporation coefficients for melts of ferromagnesian chondrule-like compositions." *Geochimica et Cosmochimica Acta* 70, pp. 206–223.

Frost, D. J. and C. A. McCammon (2008). "The Redox State of Earth's Mantle." *Annu. Rev. Earth Planet. Sci.* 36, pp. 389–420.

Ghiorso, M. S. and R. O. Sack (1995). "Chemical Mass Transfer in Magmatic Processes. IV. A Revised and Internally Consistent Thermodynamic Model for the Interpolation and Extrapolation of Liquid-Solid Equilibria in Magmatic Systems at Elevated Temperatures and Pressures." *Contributions to Mineralogy and Petrology* 119, pp. 197–212.

Grove, T. L. (1981). "Use of FePt Alloys to Eliminate the Iron Loss Problem in 1 Atmosphere Gas Mixing Experiments: Theoretical and Practical Considerations." *Contributions to Mineralogy and Petrology* 78, pp. 298–304.

Gualda, G., M. S. Ghiorso, R. Lemons, and T. Carley (2012). "Rhyolite-MELTS: A modified calibration of MELTS optimized for silica-rich, fluid-bearing magmatic systems." *Journal of Petrology* 53, pp. 875–890.

Herd, C. D., L. E. Borg, J. H. Jones, and J. J. Papike (2002). "Oxygen fugacity and geochemical variations in the martian basalts: Implications for martian basalt petrogenesis and the oxidation state of the upper mantle of Mars." *Geochimica et Cosmochimica Acta* 66 (11), pp. 2025–2036.

Hin, R. C., M. W. Schmidt, and B. Bourdon (2012). "Experimental evidence for the absence of iron isotope fractionation between metal and silicate liquids at 1 GPa and 1250-1300 °C and its cosmochemical consequences." *Geochimica et Cosmochimica Acta* 93, pp. 164–181.

Krawczynski, M. J. and T. L. Grove (2012). "Experimental investigation of the influence of oxygen fugacity on the source depths for high titanium lunar ultramafic magmas." *Geochimica et Cosmochimica Acta* 79, pp. 1–19.

Krawczynski, M. J. and J. L. Olive (2011). "A new fitting algorithm for petrological mass-balance problems." *AGU Fall Meeting Abstracts.* Vol. 1, p. 2613.

Liu, J., N. Dauphas, M. Roskosz, M. Y. Hu, H. Yang, W. Bi, J. Zhao, E. E. Alp, J. Y. Hu, and J.-F. Lin (2017). "Iron isotopic fractionation between silicate mantle and metallic core at high pressure." *Nat Commun* 8, p. 14377. ISSN: 2041-1723.

Liu, Y., M. J. Spicuzza, P. R. Craddock, J. M. Day, J. W. Valley, N. Dauphas, and L. A. Taylor (2010). "Oxygen and iron isotope constraints on near-surface fractionation effects and the composition of lunar mare basalt source regions." *Geochimica et Cosmochimica Acta* 74, pp. 6249–6262.

Longhi, J., D. Walker, and J. Hays (1978). "The distribution of Fe and Mg between olivine and lunar basaltic liquids." *Geochimica et Cosmochimica Acta* 42, pp. 1545–1558.

Macris, C. A., C. E. Manning, and E. D. Young (2015). "Crystal chemical constraints on inter-mineral Fe isotope fractionation and implications for Fe isotope disequilibrium in San Carlos mantle xenoliths." *Geochimica et Cosmochimica Acta* 154, pp. 168–185.

McDougall, I. and T. M. Harrison (1999). *Geochronology and thermochronology by the 40Ar/39Ar method.* Second Edition. New York, NY: Oxford University Press.

Millet, M., N. Dauphas, N. D. Greber, K. Burton, C. Dale, B. Debret, C. Macpherson, G. Nowell, and H. M. Williams (2016). "Titanium stable isotope investigation of magmatic processes on the Earth and Moon." *Earth and Planetary Science Letters* 449, pp. 197–205.

Mullen, J. (1961). "Isotope effect in intermetallic diffusion." *Physical Review* (121), pp. 1649–1658.

Oeser, M., R. Dohmen, I. Horn, S. Schuth, and S. Weyer (2015). "Processes and time scales of magmatic evolution as revealed by Fe-Mg chemical and isotopic zoning in natural olivines." *Geochimica et Cosmochimica Acta* 154, pp. 130–150.

Poitrasson, F., A. N. Halliday, D.-C. Lee, S. Levasseur, and N. Teutsch (2004). "Iron isotope differences between Earth, Moon, Mars and Vesta as possible records of contrasted accretion mechanisms." *Earth and Planetary Science Letters* 223, pp. 253–266.

Poitrasson, F., S. Levasseur, and N. Teutsch (2005). "Significance of iron isotope mineral fractionation in pallasites and iron meteorites for the core-mantle differentiation of terrestrial planets." *Earth and Planetary Science Letters* 234, pp. 151–164.

Poitrasson, F., M. Roskosz, and A. Corgne (2009). "No iron isotope fractionation between molten alloys and silicate melt to 2000 degrees C and 7.7 GPa: Experimental evidence and implications for planetary differentiation and accretion." *Earth and Planetary Science Letters* 278, pp. 376–385.

Polyakov, V. B., R. Clayton, J. Horita, and S. D. Mineev (2007). "Equilibrium iron isotope fractionation factors of minerals: Reevaluation from the data of nuclear inelastic resonant X-ray scattering and Mössbauer spectroscopy." *Geochimica et Cosmochimica Acta* 71, pp. 3833–3846.

Richter, F. M. (2004). "Timescales determining the degree of kinetic isotope fractionation by evaporation and condensation." *Geochimica et Cosmochimica Acta* 68, pp. 4971–4992.

Richter, F. M., N. Dauphas, and F.-Z. Teng (2009). "Non-traditional fractionation of non-traditional isotopes: Evaporation, chemical diffusion and Soret diffusion." *Chemical Geology* 258, pp. 92–103.

Richter, F. M., A. M. Davis, D. S. Ebel, and A. Hashimoto (2002). "Elemental and isotopic fractionation of Type B calcium-, aluminum-rich inclusions: experiments, theoretical considerations, and constraints on their thermal evolution." *Geochimica et Cosmochimica Acta* 66, pp. 521–540.

Richter, F. M., P. E. Janney, R. A. Mendybaev, A. M. Davis, and M. Wadhwa (2007). "Elemental and isotopic fractionation of Type B CAI-like liquids by evaporation." *Geochimica et Cosmochimica Acta* 71, pp. 5544–5564.

Roskosz, M., B. Luais, H. C. Watson, M. J. Toplis, C. M. Alexander, and B. O. Mysen (2006). "Experimental quantification of the fractionation of Fe isotopes during metal segregation from a silicate melt." *Earth and Planetary Science Letters* 248, pp. 851–867.

Roskosz, M., C. K. I. Sio, N. Dauphas, B. Wenli, F. L. Tissot, M. Y. Hu, J. Zhao, and E. E. Alp (2015). "Spinel-olivine-pyroxene equilibrium iron isotopic fractionation and applications to natural peridotites." *Geochimica et Cosmochimica Acta* 169, pp. 184–199.

Ryder, G. (1992). "Chemical Variation and Zoning of Olivine in Lunar Dunite 72415: Near-Surface Accumulation." *Proceedings of Lunar and Planetary Science* 22, pp. 373–380.

Sato, M. (1973). "Oxygen fugacity values of Apollo 12, 14, and 15 lunary samples and reduced state of lunar magmas." *Lunar and Planetary Science Conference Proceedings* 4, pp. 1061–1079.

Schuessler, J. A., R. Schoenberg, H. Behrens, and F. von Blanckenburg (2007). "The experimental calibration of the iron isotope fractionation factor between pyrrhotite and peralkaline rhyolitic melt." *Geochimica et Cosmochimica Acta* 71, pp. 417–433.

Schuessler, J. A., R. Schoenberg, and O. Sigmarsson (2009). "Iron and lithium isotope systematics of the Hekla volcano, Iceland - Evidence for Fe isotope fractionation during magma differentiation." *Chemical Geology* 258, pp. 78–91.

Sedaghatpour, F., F.-Z. Teng, Y. Liu, D. Sears, and L. A. Taylor (2013). "Magnesium isotopic composition of the Moon." *Geochimica et Cosmochimica Acta* 120, pp. 1–16.

Shahar, A., V. J. Hillgren, M. F. Horan, J. Mesa-Garcia, L. A. Kaufman, and T. D. Mock (2015). "Sulfur-controlled iron isotope fractionation experiments of core formation in planetary bodies." *Geochimica et Cosmochimica Acta* 150, pp. 253–264.

Shahar, A., E. Schauble, R. Caracas, A. Gleason, M. Reagan, Y. Xiao, J. Shu, and W. Mao (2016). "Pressure-dependent isotopic composition of iron alloys." *Science* 352, pp. 580–582.

Shahar, A., E. Young, and C. Manning (2008). "Equilibrium high-temperature Fe isotope fractionation between fayalite and magnetite: An experimental calibration." *Earth and Planetary Science Letters* 268, pp. 330–338.

Shearer, C. K., S. M. Elardo, N. E. Petro, L. E. Borg, and F. M. McCubbin (2015). "Origin of the lunar highlands Mg-suite: An integrate petrology, geochemistry, chronology, and remote sensing perspective." *American Mineralogist* 100, pp. 294–325.

Shearer, C. K. et al. (2006). "Thermal and Magmatic Evolution of the Moon." *Reviews in Mineralogy and Geochemistry* 60, pp. 365–518.

Sio, C. K. I. and N. Dauphas (2016). "Thermal and crystallization histories of magmatic bodies by Monte Carlo inversion of Mg-Fe isotopic profiles in olivine." *Geology*.

Sio, C. K. I. and N. Dauphas (2017). "Thermal and crystallization histories of magmatic bodies by Monte Carlo inversion of Mg-Fe isotopic profiles in olivine." *Geology* 45 (1), pp. 67–70.

Sio, C. K. I., N. Dauphas, F.-Z. Teng, M. Chaussidon, R. T. Helz, and M. Roskosz (2013). "Discerning crystal growth from diffusion profiles in zoned olivine by in situ Mg-Fe isotopic analyses." *Geochimica et Cosmochimica Acta* 123, pp. 302–321.

Sossi, P. A. and F. Moynier (2017). "Chemical and isotopic kinship of iron in the Earth and Moon deduced from the lunar Mg-Suite." *Earth and Planetary Science Letters* 471, pp. 125–135.

Teng, F.-Z., N. Dauphas, and R. T. Helz (2008). "Iron Isotope Fractionation During Magmatic Differentiation in Kilauea Iki Lava Lake." *Science* 320, pp. 1620–1622.

Teng, F.-Z., N. Dauphas, R. T. Helz, S. Gao, and S. Huang (2011). "Diffusion-driven magnesium and iron isotope fractionation in Hawaiian olivine." *Earth and Planetary Science Letters* 308, pp. 317–324.

Teng, F.-Z., N. Dauphas, and J. M. Watkins (2017). *Non-Traditional Stable Isotopes*. Vol. 82. Reviews in Mineralogy and Geochemistry.

Van Orman, J. A. and M. J. Krawczynski (2015). "Theoretical constraints on the isotope effect for diffusion in minerals." *Geochimica et Cosmochimica Acta* 164, pp. 365–381.

Wang, K. and S. B. Jacobsen (2016). "Potassium isotopic evidence for a high-energy giant impact origin of the Moon." *Nature* 538, pp. 487–490.

Wang, K., S. B. Jacobsen, F. Sedaghatpour, H. Chen, and R. L. Korotev (2015). "The earliest Lunar Magma Ocean differentiation recorded in Fe isotopes." *Earth and Planetary Science Letters* 430, pp. 202–208.

Wang, K., F. Moynier, N. Dauphas, J.-A. Barrat, P. R. Craddock, and C. K. Sio (2012). "Iron isotope fractionation in planetary crusts." *Geochimica et Cosmochimica Acta* 89, pp. 31–45.

Weyer, S., A. D. Anbar, G. P. Brey, C. Münker, K. Mezger, and A. B. Woodland (2005). "Iron isotope fractionation during planetary differentiation." *Earth and Planetary Science Letters* 240, pp. 251–264.

Weyer, S. and D. Ionov (2007). "Partial melting and melt percolation: The message from Fe isotopes." *Earth and Planetary Science Letters* 259, pp. 119–133.

Wiesli, R. A., B. L. Beard, L. A. Taylor, and C. M. Johnson (2003). "Space weathering processes on airless bodies: Fe isotope fractionation in the lunar regolith." *Earth and Planetary Science Letters* 216, pp. 457–465.

Williams, H. M. and M. Bizimis (2014). "Iron isotope tracing of mantle heterogeneity within the source regions of oceanic basalts." *Earth and Planetary Science Letters* 404, pp. 396–407.

Williams, H. M., S. G. Nielsen, C. Renac, W. L. Griffin, S. Y. O'Reilly, C. A. McCammon, N. Pearson, F. Viljoen, J. C. Alt, and A. N. Halliday (2009). "Fractionation of oxygen and iron isotopes by partial melting processes: Implications for the interpretation of stable isotopes signatures in mafic rocks." *Earth and Planetary Science Letters* 283, pp. 156–166.

Williams, H. M., A. H. Peslier, C. A. McCammon, A. N. Halliday, S. Levasseur, N. Teutsch, and J.-P. Burg (2005). "Systematic iron isotope variations in mantle rocks and minerals: The effects of partial melting and oxygen fugacity." *Earth and Planetary Science Letters* 235, pp. 435–452.

Xirouchakis, D., M. M. Hirschmann, and J. A. Simpson (2001). "The effect of titanium on the silica content and on mineral-liquid partitioning of mantle-equilibrated melts." *Geochimica et Cosmochimica Acta* 65, pp. 2201–2217.

Zhang, Y., H. Ni, and Y. Chen (2010). "Diffusion in Silicate Melts." *Reviews in Mineralogy and Geochemistry* 72, pp. 311–408.

Zhao, X., Z. Zhang, S. Huang, Y. Liu, X. Li, and H. Zhang (2017). "Coupled extremely light Ca and Fe isotopes in peridotites." *Geochimica et Cosmochimica Acta* 208, pp. 368–380.

Chapter 4

Importance of ilmenite crystallization and subsolidus reaction for iron, titanium, and magnesium isotopic variability in lunar mare basalts

Abstract

The equilibrium partitioning of Fe and Ti isotopes between ilmenite and melt was experimentally investigated in order to evaluate the role of ilmenite in generating the isotopic compositional variability among the lunar mare basalts. Ilmenite crystallization experiments were conducted using two bulk compositions: an ilmenite-saturated basaltic andesite, and an ilmenite-saturated Apollo 14 black glass, and the Fe and Ti isotopic compositions of the experimental ilmenites and glass (quenched melt) were analyzed using solution MC-ICPMS.

Additionally, nuclear resonant inelastic X-ray scattering (NRIXS) measurements on synthetic ilmenite were conducted and compared to previous NRIXS measurements on synthetic lunar glasses in order to derive temperature-dependent ilmenite-melt Fe isotopic fractionations. The experimentally determined ilmenite-melt fractionations (Δ^{56}Fe$_{\text{ilmenite-melt}} = -0.05 \pm 0.02\text{‰}$ and Δ^{49}Ti$_{\text{ilmenite-melt}} = -0.09 \pm 0.03\text{‰}$ at 1100°C) have been incorporated into a lunar magma ocean crystallization model that was developed to track the major element and isotopic compositional evolution of lunar magma ocean cumulates and residual liquid. In a three-component mixing model for mare basalt parent magmas, the Ti isotopic compositional difference between the low- and high-Ti mare basalts was reproduced using the modeled Ti isotopic compositions of lunar magma ocean ilmenite cumulates. However, the difference in Fe isotopic composition between the low- and high-Ti mare basalts cannot be attributed solely to products of lunar magma ocean crystallization. Instead, the Fe and Mg isotopic compositions of the lunar mare basalts indicate Fe-Mg interdiffusion has occurred in the Ti-rich component of the mare basalt source regions via subsolidus reaction between ilmenite cumulates and the olivine- and pyroxene-rich lunar mantle.

4.1 Introduction

As demonstrated by the compositional variability observed among lunar volcanic samples, the lunar mantle is heterogeneous, particularly with respect to titanium. Lunar mare basalts and ultramafic volcanic glasses, which represent melts of the lunar interior, are characterized by low- and high-Ti suites. High-titanium mare basalts and volcanic glasses have compositions with $10-15$ wt.% TiO$_2$ and greater, whereas a majority of terrestrial basalts contain less than 2 wt.% TiO$_2$ (Figure 4.1, Basaltic Volcanism Study Project 1981). The distinctive titanium enrichment in lunar magmas indicates that the nature of the mantle and melt generation processes on the Moon differs from that on Earth.
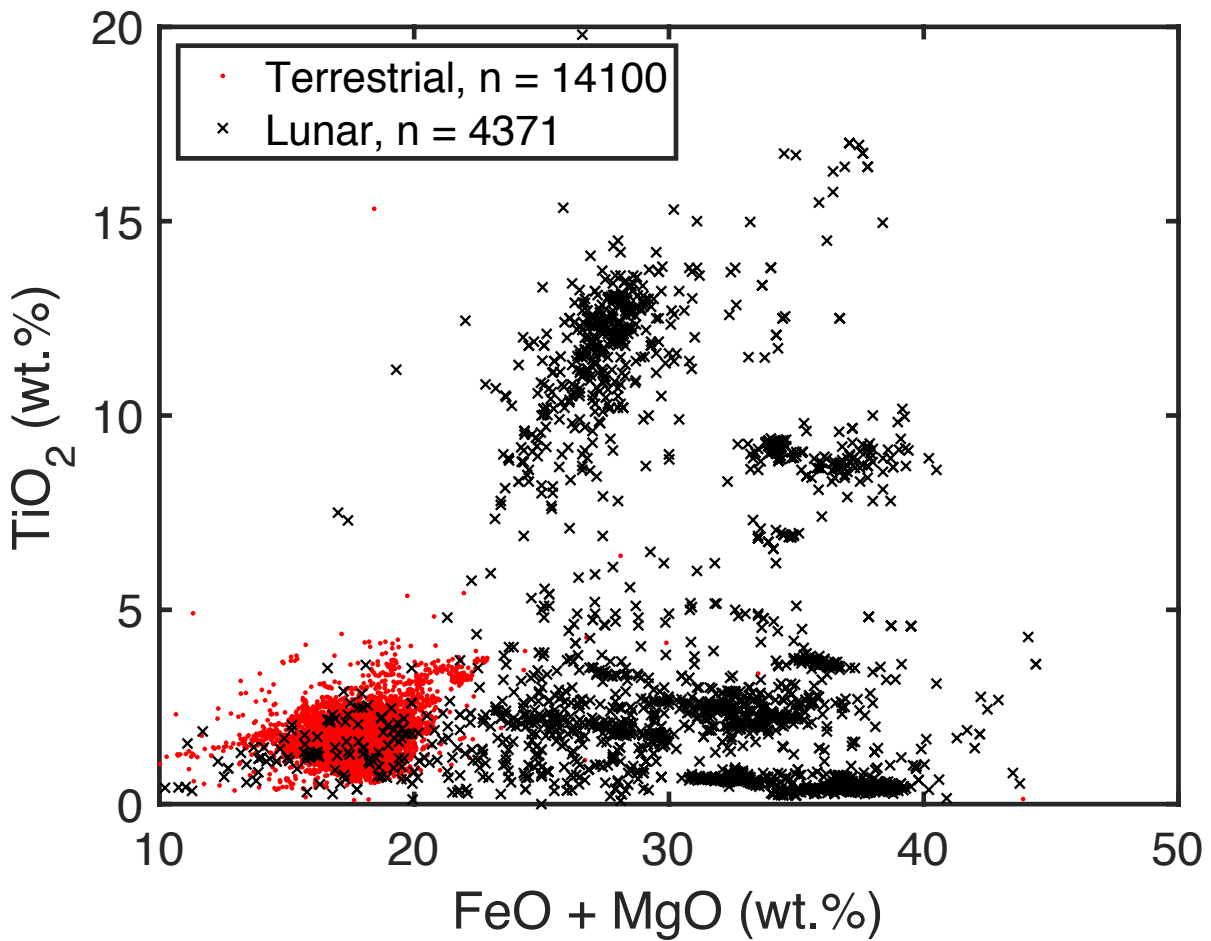
Figure 4.1: Compositional variations between terrestrial mid-ocean ridge basalts (red dots) and lunar mare basalts and volcanic glasses (black x's). Terrestrial data (14,100 samples) were downloaded from the PetDB Database (www.earthchem.org/petdb) on June 24, 2019 using the following parameters: tectonic setting = spreading center and rock classification = basalt. Lunar data (4,371 samples) were downloaded from the database compiled by Clive Neal (www3.nd.edu/∼cneal/Lunar-L/Mare-Basalt-Database.xls).

The mantle source regions for the mare basalts are thought to be comprised of products and chemical gradients related to the crystallization of a lunar magma ocean (e.g., Walker et al. 1975; Snyder et al. 1992). In general, there are three important compositional components in the mare basalt sources related to the products of a lunar magma ocean: ultramafic cumulates, high-titanium ilmenite-bearing cumulates, and a potassium-, rare earth element-, and phosphorus-rich component (KREEP). Models of lunar magma ocean crystallization begin with estimates for a bulk Moon composition magma and precipitate olivine and orthopyroxene as the sole phases for more than 50% of crystallization (e.g., Snyder et al. 1992; Elkins-Tanton et al. 2011; Elardo et al. 2011). Though the relative mineral proportions are model dependent, these "ultramafic cumulates" are characterized by a mixture of olivine and orthopyroxene and likely make up the majority of the lunar mantle. In the late stages of lunar magma ocean crystallization after approximately 90% of the original magma has solidified, ilmenite, an Fe-Ti oxide, begins to crystallize, producing ilmenite-bearing cumulates. The KREEP component in the mare basalt sources is considered to be related to the residual liquid that remains toward the end of magma ocean solidification, as this component is enriched in incompatible elements that would not have partitioned strongly into the earlier crystallizing minerals olivine, orthopyroxene, clinopyroxene, ilmenite, and plagioclase. Of the three main compositional components in the mare basalt sources, the ilmenite-bearing cumulates are most important in understanding the titanium variation between the source regions for the low- and high-Ti basalts.

Though ilmenite-bearing lunar magma ocean cumulates have often been invoked as the source of titanium enrichment in the lunar mantle, questions remain regarding the abundance and location of ilmenite in the lunar interior, as well as the processes responsible for incorporating ilmenite into the mantle sources for mare basalt magmas. The onset of ilmenite crystallization in the lunar magma ocean will dictate at which point ilmenite-bearing cumulates are formed

and will in part determine the modal abundance of ilmenite in the lunar mantle. Recent experimental studies of lunar magma ocean crystallization have provided improved constraints on when ilmenite precipitates and in what proportion relative to co-crystallizing minerals (Lin et al. 2017a; Lin et al. 2017b; Charlier et al. 2018; Rapp and Draper 2018; Lin et al. 2019). Minerals less dense than the residual lunar magma ocean liquid from which they crystallize, such as plagioclase, are expected to float toward the lunar surface and aggregate to form a crust. In contrast, an ilmenite-rich cumulate layer is hypothesized to sink through the lunar mantle due to the relatively high density of ilmenite (Hess and Parmentier 1995). The feasibility and extent of ilmenite-bearing cumulate downwelling involves numerous geodynamic considerations (e.g., timing relative to magma ocean solidification, rheology of the lunar mantle, thickness of the ilmenite-bearing layer, proportion of ilmenite in the cumulate layer) (Zhao et al. 2019; Li et al. 2019). In addition to lunar magma ocean processes, the mechanisms involved in the re-melting of ilmenite-bearing cumulates and ascent of dense high-Ti magmas to the lunar surface are important in establishing the location and distribution of ilmenite-rich regions within the lunar mantle (Wagner and Grove 1997; Van Orman and Grove 2000; Vander Kaaden et al. 2015; Mallik et al. 2019).

High-precision, non-traditional stable isotope analyses of lunar samples have recently provided new compositional constraints to consider when modeling the heterogeneity of the lunar mare basalt sources. Resolvable differences in iron, titanium, and magnesium isotopic compositions exist between the low-Ti and high-Ti mare basalts (Figure 4.2). For iron and titanium, the high-Ti mare basalts are isotopically "heavy" compared to low-Ti basalts ($\delta^{56}\text{Fe}_{\text{high-Ti}}$ > $\delta^{56}\text{Fe}_{\text{low-Ti}}$ and $\delta^{49}\text{Ti}_{\text{high-Ti}}$ > $\delta^{49}\text{Ti}_{\text{low-Ti}}$; Wiesli et al. 2003; Poitrasson et al. 2004; Weyer et al. 2005; Craddock et al. 2010; Liu et al. 2010; Millet et al. 2016; Sossi and Moynier 2017; Poitrasson et al. 2019). In contrast for magnesium, high-Ti mare basalts are isotopically "light"

relative to low-Ti basalts ($\delta^{26}\text{Mg}_{\text{high-Ti}} < \delta^{26}\text{Mg}_{\text{low-Ti}}$; Sedaghatpour et al. 2013; Sedaghatpour and Jacobsen 2019).

Ilmenite has been hypothesized as the main control for the isotopic distinction observed between the low- and high-Ti mare basalts. Previous studies have concluded that the heavy Fe, heavy Ti, and light Mg isotopic compositions of the high-Ti mare basalts were inherited from ilmenite-bearing lunar magma ocean cumulates (Weyer et al. 2005; Liu et al. 2010; Craddock et al. 2010; Sedaghatpour et al. 2013; Wang et al. 2015; Sedaghatpour and Jacobsen 2019).

In order to evaluate the role of ilmenite in generating the isotopic compositional variability among the mare basalts, the isotopic composition of the ilmenite-bearing lunar magma ocean cumulates as well as any isotopic fractionation that occurs during ilmenite crystallization or melting must be identified. To this aim, we have experimentally investigated the equilibrium partitioning of Fe and Ti isotopes between ilmenite and melt. We have developed a lunar magma ocean crystallization model that for the first time incorporates isotopic, minor element, and major element compositions in a coherent, fully mass-balanced way. Combining our ilmenite-melt isotopic fractionations with models of lunar magma ocean crystallization and mare basalt petrogenesis, we have quantified to what extent ilmenite-bearing cumulates can account for the Fe, Ti, and Mg isotopic compositions of the lunar mare basalts.
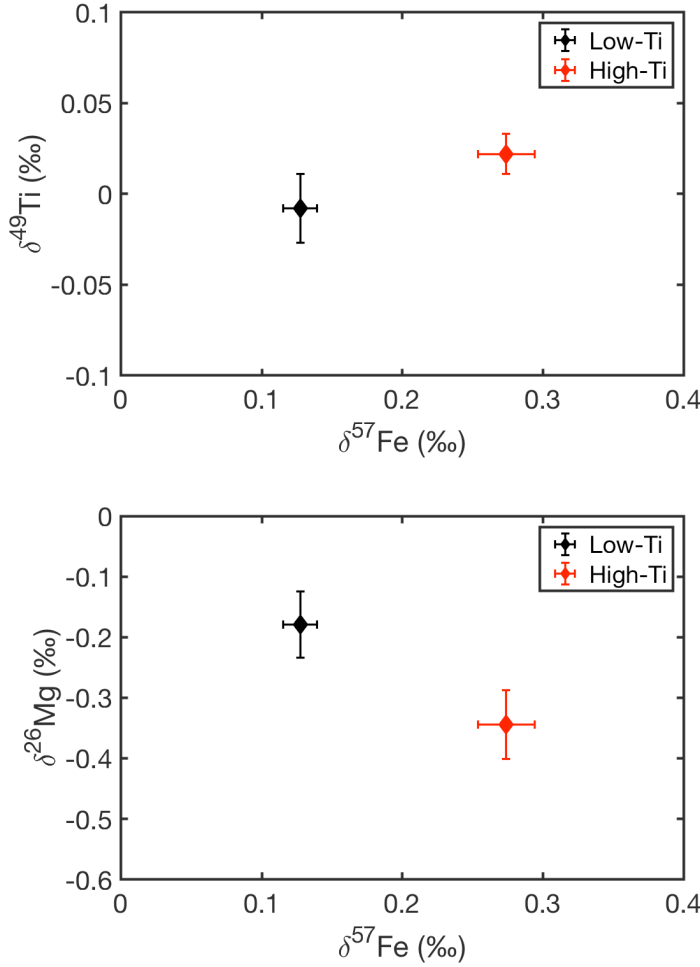
Figure 4.2: Average iron, magnesium, and titanium isotopic compositions of low- and high-Ti lunar mare basalts. Isotopic fractionation is observed between the low- and high-Ti lunar mare basalts for all three elements. There appears to be a negative correlation between Fe and Mg isotopic compositions and a positive correlation between Fe and Ti isotopic compositions. For Fe, the plotted values and error bars represent previously reported averages and 2 SE (two standard error) uncertainties, respectively, for the low-Ti (n = 27) and high-Ti (n = 25) mare basalts (Poitrasson et al. 2019). For Mg, the averages and 2 SE uncertainties (low-Ti n = 14, high-Ti n = 15) have been calculated from the data reported in Sedaghatpour et al. (2013) and Sedaghatpour and Jacobsen (2019). For Ti, the average and 2 SE uncertainty has been calculated for the high-Ti basalts (n = 5) from the data reported in Millet et al. (2016). Because the Ti isotopic compositions of the low-Ti basalts (n = 3) were identical, the error bars on the low-Ti average instead represent the largest analytical uncertainty (95% confidence interval) reported for the three measurements.

4.2 Experimental calibration

4.2.1 Starting materials

Ilmenite crystallization experiments were conducted using two bulk compositions: an ilmenite-saturated basaltic andesite, and an ilmenite-saturated Apollo 14 black glass (Table 4.1). The two starting compositions were chosen such that ilmenite would be the only Fe-bearing phase crystallized during the experiment. Both starting materials were synthesized from a combination of oxide, carbonate, and titanate powders that were mixed under isopropanol in a silicon-nitride ball mill for 3 hours. Calcium was added as $CaCO_3$ for the basaltic andesite, and $CaTiO_3$ for the Apollo 14 black glass. Polyvinyl alcohol was added as a binding agent to the basaltic andesite starting material, and once dry, 75 mg aliquots were pressed into cylindrical pellets of 4 mm diameter and 2 mm height. The sample pellets were fused to rhenium wire loops in preparation for the gas-mixing furnace.

4.2.2 Ilmenite-saturated basaltic andesite

One starting composition, "ilmenite-saturated basaltic andesite", was determined by adding additional TiO_2 to an evolved lunar basalt composition in order to stabilize ilmenite as a liquidus phase. Ilmenite crystallization experiments on the basaltic andesite composition were

Table 4.1: Starting material compositions for ilmenite crystallization experiments reported in oxide weight percent.

Composition	Mix	SiO_2	TiO_2	Al_2O_3	FeO	MnO	MgO	CaO
ilm-saturated basaltic andesite	#38	53.7	7.2	10.9	18.9	0.2	1.1	8.0
ilm-saturated Apollo 14 black glass	#48	23.7	28.8	5.4	33.1	0.4	5.3	3.2

conducted in one-atmosphere vertical gas-mixing furnaces at Washington University in St. Louis. The experiments were conducted for durations of 3-8 days (Table 4.2). A controlled flow of H_2 and CO_2 gases buffered the oxygen fugacity at approximately one log unit above iron-wüstite ($f_{O_2} = $ IW+1) throughout each experiment. The fugacity was monitored with a Ca-doped zirconia oxygen probe using air as the reference gas. Starting material pellets were fused to rhenium loops and hung by a Pt wire thread in the furnace hot spot for the run duration. The reported run duration in Table 4.2 reflects the time between sample insertion and sample quench. Experimental samples were quenched rapidly by melting the Pt hanging wire and dropping the sample from within the furnace into a beaker of deionized water.

We conducted a series of experiments in order to determine a cooling sequence that would crystallize ilmenite grains suitable for hand-picking for isotopic analysis. Each sample was inserted into the furnace at the starting temperature (T_{start}) and remained at that temperature for either 3 hours (experiments J045, H062, H063, J046) or 24 hours (experiments J047 and J109). The temperature of the furnace was then decreased to the final sample temperature (T_{final}) at a programmed cooling rate (see Table 4.2). Experiments H062 and J046 had an additional 24-hour dwell at 1123°C in between T_{start} and T_{final}. The programmed cooling sequence promotes the nucleation of crystals, and slower cooling rates allow for more euhedral crystal growth (Hammer 2006). We determined that a final temperature of approximately 1098° was necessary in order to crystallize a proportion of ilmenite sufficient for hand-picking and isotopic isotopic analysis. Additionally, the ilmenite grains from the experiments cooled at 1°C/hr were thinner and more elongate than those in the experiments cooled at 0.5°C/hr. Therefore, experiments J047 and J109, which cooled at a rate of 0.5°C/hr and equilibrated at the final sample temperature for 2-3 days, were selected for isotopic analysis.

The experimental run products for the basaltic andesite composition contain glass, ilmenite, quartz, and plagioclase (Figure 4.3). Ilmenite is present as euhedral grains that range from
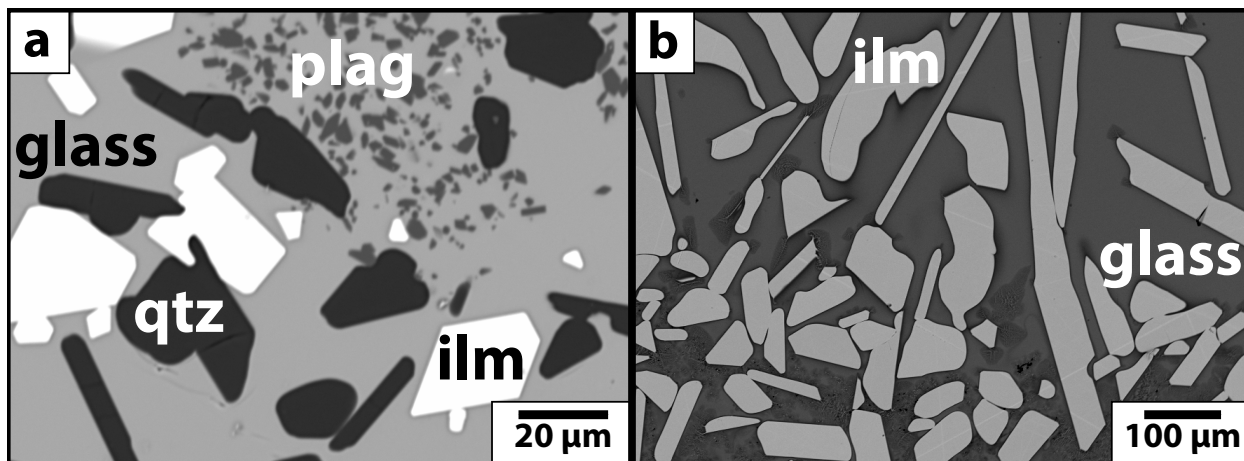
Figure 4.3: Back-scattered electron image of two ilmenite crystallization experiments. a) Ilmenite-saturated basaltic andesite experiment J047 contains ilmenite (white, blocky crystals), quartz (dark gray, rounded crystals), plagioclase (medium gray, small crystals), and glass (bright gray matrix). b) Ilmenite-saturated Apollo 14 black glass experiment F131 contains ilmenite (bright gray crystals) and glass (gray matrix). Additionally, regions of quench crystals (dark gray) are observed toward the bottom of the capsule (bottom of image).

10 to 40 μm in diameter. Quartz is present as subhedral, occasionally elongate grains that range from 10 to 60 μm in diameter. Plagioclase is present throughout the sample as patches of < 10 μm grains.

4.2.3 Ilmenite-saturated Apollo 14 black glass

The second starting composition, "ilmenite-saturated Apollo 14 black glass", was chosen in order to conduct experiments in which ilmenite was the only crystallizing phase. Ilmenite and glass separation for isotopic analysis was made easier by having ilmenite as the sole crystalline phase (without co-existing plagioclase or quartz).

We determined the starting composition for the ilmenite-only experiments by experimentally saturating an Apollo 14 black glass composition with synthetic ilmenite. To do this, we began with a mixture of oxide and titanate powders that was prepared to be similar in composition to Apollo 14 black glass (Delano 1986). We synthesized an ilmenite powder by

110

Table 4.2: Run conditions and products for one-atmosphere gas-mixing furnace experiments conducted on the ilmenite-saturated basaltic andesite composition (Mix #38, Table 4.1). T_{start} reports the temperature of the furnace when the sample was inserted. T_{final} is the temperature at which the experiment equilibrated after the furnace was decreased from T_{start} at the reported cooling rate.

Experiment	T_{start} (°C)	T_{final} (°C)	Cooling rate (°C/hr)	Time (hr)[a]	Phases (mode)	$\log_{10} f_{O_2}$	Δ IW	% Fe loss[b]
J045	1177	1122	1.0	65	glass + quartz	−12.1	+0.8	
H062	1179	1098	1.0	144	glass (55) + quartz (21) + plag (16) + ilm (8)	−12.6	+0.7	7.8
H063	1149	1099	1.0	92	glass + quartz + plag + ilm	−12.6	+0.7	
J046	1178	1098	1.0	192	glass + quartz + plag + ilm	−12.5	+0.8	
J047	1122	1098	0.5	147	glass (55) + quartz (23) + plag (15) + ilm (7)	−12.6	+0.8	5.2
J109	1120	1097	0.5	116	glass (54) + quartz (22) + plag (17) + ilm (7)	−12.5	+0.9	4.4

[a] Reported time reflects the time elapsed between sample insertion and sample quench.
[b] Percent Fe loss was estimated using the FeO content of the starting composition and the FeO content of the sample (calculated from the phase compositions and modal abundances).
The major element compositions of the phases in experiments J045, H063, and J046 were not analyzed, and thus there are no quantitative results for phase abundance or Fe loss to report.

mixing Fe sponge, Fe_2O_3, and TiO_2 in stochiometric proportions ($FeTiO_3$). Then, we loaded the synthetic black glass and ilmenite starting materials into a graphite capsule in a 2:1 mass ratio. The sample was heated to 1420°C in a piston cylinder assembly at 10 kbar pressure for 24.1 hours. The experimental run products were analyzed for major element composition using the electron microprobe. The average composition of the quenched melt near the ilmenite-black glass interface was chosen as the target composition for our ilmenite-saturated Apollo 14 black glass starting material (Table 4.1, Section 4.2.1).

Experiments on the ilmenite-saturated Apollo 14 black glass composition were conducted in a piston cylinder at Washington University in St. Louis. For each experiment, the starting material was packed into a graphite capsule with $4 - 4.5$ mm height and approximately 0.75 mm wall thickness. The use of a graphite sample capsule promotes experimental oxygen fugacities at which minimal Fe^{3+} exists in the mineral and glass phases (Médard et al. 2008). Piston cylinder experiments were performed at 10 kbar pressure (Table 4.3). Experimental pressure was maintained during the experiment by an automatic pressure control system using the hot piston-in technique (Johannes et al. 1971). Sample temperature was 1350°C and controlled to within $1 - 3$°C of the reported temperature throughout the experiment, as monitored by a Eurotherm PID temperature controller. The offset between the thermocouple reading and sample temperature for the experimental assembly was calibrated using the spinel reaction-progress thermometer (Watson et al. 2002). Experiments were rapidly quenched by turning off the power to the apparatus. The reported experimental run durations (Table 4.2) reflect the time between reaching the experimental target temperature and quench. After the experiment, the sample capsule was cut in half and mounted in epoxy, then the cut face was polished in preparation for electron microprobe analysis.

The phase assemblage for the ilmenite-saturated Apollo 14 black glass experiments consists of ilmenite and glass (Figure 4.3). Ilmenite is present as subhedral grains that range from 20

Table 4.3: Run conditions and products for piston cylinder experiments conducted on the ilmenite-saturated Apollo 14 black glass composition (Mix #48, Table 4.1).

Experiment	P (kbar)	T (°C)	Time (hr)	Phases (mode)	% Fe loss[a]
F127	10	1400	3.0	glass	
F126	10	1300	4.3	glass + ilm	
F128	10	1350	20.7	glass + ilm	
F131	10	1350	13.7	glass (74) + ilm (26)	−0.1
F143	10	1350	15.2	glass (82) + ilm (18)	0.0

[a] Percent Fe loss was estimated using the FeO content of the starting composition and the FeO content of the sample (calculated from the phase compositions and modal abundances). A negative value indicates Fe gain.
The major element compositions of the phases in experiments F126, F127, and F128 were not analyzed, and thus there are no quantitative results for phase abundance or Fe loss to report.

to 200 μm in diameter, with elongate ilmenite grains extending up to 500 μm in length. In addition to ilmenite and glass, patches of thin silicate crystals are present toward the top of the experiment capsule (closest to the thermocouple). The dendritic texture of the silicate crystals suggests they precipitated during quench. Additional experiments were conducted at 1400°C and 1300°C. The experiment at 1400°C (F127) did not crystallize ilmenite, and the experiment at 1300°C (F126) had a higher proportion of ilmenite crystals than those conducted at 1350°C. Though experiments F131 and F143 were conducted at the same temperature and pressure, the estimated phase abundances for ilmenite and glass differ by approximately 10% (Table 4.3). We observed a slight decrease (0.3%) in the average output power supplied to the apparatus during the last 4 hours of experiment F131; this change may explain the higher proportion of ilmenite in F131, as a decrease in output power would lower the sample temperature.

4.2.4 Electron microprobe analysis

Synthetic minerals and glasses from both sets of ilmenite crystallization experiments were analyzed for major element abundances using the JEOL JXA-8200 at Washington University

in St. Louis. Standardization was performed with a beam diameter of 20 μm on natural and synthetic glass and mineral samples (synthetic Shankland forsterite, synthetic Mn-olivine, synthetic TiO_2, natural Ilmen Mountains ilmenite NMNH 96189, natural anorthite NMNH 137041, natural wollastonite, and natural Kakanui hornblende NMNH 143965). We used the mean atomic number (MAN) method (Donovan et al. 2016) for wavelength dispersive spectrometer background correction and measured the following elements: Si, Al, Ti, Fe, Mn, Mg, Ca. Each quantitative analysis used a 15 kV accelerating potential and 25 nA beam current.

Glass compositions were analyzed with a 30 μm beam diameter for experiment F131, 10 μm beam diameter for experiments J047 and F143, and 5 μm beam diameter for experiment J109. Ilmenite compositions were analyzed with a 10 μm beam diameter for experiment F131, 2 μm beam diameter for experiment J109, and ~1 μm beam diameter for experiments J047 and F143. Quartz was analyzed with a 2 μm beam diameter. Plagioclase was analyzed with ~1 μm beam diameter. Compositional data were reduced using Probe for EPMA software (https://www.probesoftware.com) and then filtered to exclude analyses where the analytical totals were less than 98.5 wt.% or greater than 101.5 wt.%. This threshold was expanded to include totals greater than 97 wt.% for J047 glass analyses, and totals less than 103 wt.% for quartz and plagioclase analyses on experiment J109. Ilmenite analyses for experiments J047 and J109 were filtered to include only those where the cation total for 3 oxygen atoms was greater than 1.98 and less than 2.02 (ideal ilmenite stoichiometry contains 2 cations per 3 oxygen atoms). For experiments F131 and F143, ilmenite analyses contained 1.96-1.98 cations per 3 oxygen atoms. Averages of the analyzed glass and mineral compositions are reported in Table 4.4.

Table 4.4: Electron microprobe analyses of experimental run products in oxide weight percent.

Experiment	Phase	n[a]	SiO$_2$	s.d.	TiO$_2$	s.d.	Al$_2$O$_3$	s.d.	FeO	s.d.	MnO	s.d.	MgO	s.d.	CaO	s.d.	Total
Ilmenite-saturated basaltic andesite																	
J047	glass	13	43.86	0.34	6.42	0.06	9.93	0.03	26.51	0.19	0.45	0.02	1.88	0.01	8.71	0.03	97.76
	ilmenite	18	b.d.		52.43	0.33	0.29	0.03	44.23	0.33	0.50	0.04	1.77	0.19	0.21	0.06	99.43
	quartz	7	98.06	0.70	0.59	0.04	0.15	0.03	0.54	0.06	0.03	0.01	b.d.		0.09	0.01	99.46
	plagioclase	8	43.43	0.68	0.22	0.13	35.30	0.54	1.27	0.47	0.03	0.02	0.10	0.03	19.40	0.23	99.75
J109	glass	17	45.32	0.38	6.36	0.08	9.90	0.10	26.54	0.19	0.44	0.02	1.94	0.03	9.00	0.03	99.49
	ilmenite	15	0.23	0.10	52.21	0.68	0.31	0.04	44.62	0.21	0.52	0.02	1.80	0.06	0.26	0.12	99.95
	quartz	8	100.83	0.66	0.60	0.04	0.21	0.12	0.53	0.10	b.d.		b.d.		0.11	0.04	102.3
	plagioclase	10	44.61	0.27	0.73	0.86	34.02	3.32	3.13	3.12	0.06	0.05	0.23	0.21	18.61	1.40	101.4
Ilmenite-saturated Apollo 14 black glass																	
F131	glass	61	32.62	0.69	17.58	0.87	7.21	0.16	31.22	0.44	0.37	0.02	5.68	0.18	4.67	0.11	99.34
	ilmenite	44	b.d.		56.37	0.15	0.78	0.02	38.45	0.18	0.29	0.02	4.96	0.03	0.03	0.01	100.9
F143	glass	26	29.28	0.65	21.14	0.71	6.53	0.15	31.68	0.41	0.36	0.02	5.74	0.25	4.34	0.11	99.05
	ilmenite	23	b.d.		57.38	0.23	0.85	0.02	37.03	0.23	0.28	0.02	5.11	0.04	0.05	0.02	100.7

[a] Compositions are reported as an average of *n* analyses. Oxide measurements are reported with 1σ standard deviation in the adjacent "s.d." column.

b.d. indicates that the measured composition was below detection limit.

4.2.5 Sample dissolution and Multicollector-Inductively Coupled Plasma Mass Spectrometry (MC-ICPMS) methods

In order to determine the Fe isotopic fractionation factor between ilmenite and melt, we hand-separated ilmenite and glass (quenched melt) from the experimental run products and measured the Fe isotopic composition of each phase using solution MC-ICPMS. For each basaltic andesite experiment, the quenched experimental sample was crushed, select sample chips were mounted for electron microprobe analysis, and the rest of the material remained for isotopic analysis. For each Apollo 14 black glass experiment, half of the experiment capsule was mounted for electron microprobe analysis, and then after analysis was recovered from the mount and combined with the other half of the sample for isotopic analysis. Each of the experiments was ground using a mortar and pestle, and the material was sieved to < 63 μm. Opaque ilmenite grains were hand-picked from the experimental samples under an optical microscope. The transparency of the glass allowed for separation of glass pieces that were free of crystals.

Ilmenite and glass separates were then dissolved in acid, purified for Fe through column chemistry, and analyzed for Fe and Ti isotopic composition using the Thermo Scientific Neptune MC-ICPMS in the Origins Lab at the University of Chicago. The starting material powders, experiment wires, and "total samples" (experimental sample left after glass and ilmenite separate removal) were also dissolved and measured to aid in interpretation of the measured isotopic compositions. We began each sample digestion with a heated acid dissolution using a 2:1 mixture of concentrated $HF-HNO_3$ on a hot-plate set to 120°C. The second dissolution step was performed using aqua regia (3:1 ratio of $HCl-HNO_3$). High-pressure Parr Bombs were used for the next digestion step following a protocol similar to Craddock and Dauphas (2011). Each sample was loaded into a 6 ml Savillex PFA vial with

2.5 mL HF and 0.5 mL HNO$_3$. The sample vial was heated inside a 45 mL Parr Bomb at 170°C for 3 days. After the bomb digestion step, each sample was dried out and then dissolved in 500 μL of 6M HCl (with the exception of the digested starting material powders, which instead used 1 mL 6M HCl). Sample solutions were split in half, with 250 μL of each solution being used for Fe isotopic measurement and the remaining 250 μL of each sample solution being reserved for Ti isotopic measurement.

The sample solutions were purified for Fe through column chemistry following the routine methods of the Origins Lab at the University of Chicago (e.g., Dauphas et al. 2004; Dauphas and Rouxel 2006; Dauphas et al. 2009b). The iron isotopic compositions of the sample solutions were measured using the standard-bracketing method of Dauphas et al. (2009b), and are reported in Table 4.5 as δ^{56}Fe relative to IRMM-524, whose isotopic composition is identical to IRMM-014 (Craddock and Dauphas 2011).

We have also measured the Ti isotopic compositions of the experimental run products for one of the ilmenite crystallization experiments (J047). For Ti isotopic measurement, a titanium double spike (^{47}Ti$-^{49}$Ti) was added to each dissolved sample in a 48:52 spike-to-sample ratio based on the mass of titanium in the sample (Millet and Dauphas 2014). The samples were then prepared for Ti isotopic measurement through ion-exchange chromatography following the Origins Lab protocols previously described in Millet et al. (2016), Greber et al. (2017), and Johnson et al. (2019). Titanium isotopes were measured on a MC-ICPMS bracketed with standards that were doped with the same double spike mixture as the sample. The ^{48}Ti concentrations were matched within $\pm10\%$ of the sample Ti concentration. Following a block of 5 samples, a clean blank solution was measured for on-peak baseline correction. The titanium isotopic compositions are reported as δ^{49}Ti relative to the Origins Laboratory Ti reference material (OL-Ti, Millet and Dauphas 2014) (Table 4.6). Reported uncertainties (95% confidence interval) on the Ti isotopic compositions were determined using the methods

Table 4.5: Iron isotopic compositions for each experiment. Reported values (‰) are the weighted averages and weighted errors (95% confidence interval) of multiple measurements.

Sample	Starting Composition (Mix)	Starting Material				Glass				Ilmenite				Total Sample					Experiment Wire			
		δ^{56}Fe	2σ	δ^{57}Fe	2σ	δ^{56}Fe	2σ	δ^{57}Fe	2σ	δ^{56}Fe	2σ	δ^{57}Fe	2σ	δ^{56}Fe	2σ	δ^{57}Fe	2σ	μg Fe	δ^{56}Fe	2σ	δ^{57}Fe	2σ
J047	basaltic andesite (#38)	0.256	0.039	0.385	0.059	0.254	0.030	2.680	0.050	0.317	0.030	2.854	0.050	0.317	0.032	2.894	0.046	7.8	0.062	0.043	2.659	0.065
F131	Apollo 14 black glass (#48)	0.267	0.027	0.376	0.039	0.280	0.023	0.425	0.033	0.238	0.022	0.342	0.032	0.304	0.031	0.468	0.043					

For N measurements and i = 1,...N, the weighted averages and weighted errors are calculated from the iron isotopic composition and standard deviation on each measurement (i) using the following equations: $w_i = 1/\sigma_i^2$; $\sigma_{average} = 1/\sqrt{\Sigma w_i}$, $\delta^{56}Fe_{average} = \Sigma(w_i \delta^{56}Fe_i)/\Sigma w_i$

Table 4.6: Titanium isotopic compositions for experiment J047. Reported uncertainties are 95% confidence interval.

Sample	δ^{49}Ti (‰)	n[a]
Starting Material	-0.144 ± 0.018	9
Glass	-0.140 ± 0.024	6
Ilmenite	-0.228 ± 0.021	9
Total Sample	-0.168 ± 0.013	9

[a] Number of repeated sample measurements.

described in Dauphas et al. (2009b) and incorporate both the measurement uncertainty and the long-term external reproducibility of the instrument. Basalt geostandard BHVO-2 was processed simultaneously with the experimental samples, and the measured Ti isotopic composition (δ^{49}Ti$= +0.019 \pm 0.009$‰) is in agreement with previously reported values (δ^{49}Ti$= +0.020 \pm 0.006$‰, Millet et al. 2016, and δ^{49}Ti$= +0.021 \pm 0.020$‰ Millet and Dauphas 2014).

4.2.6 Nuclear resonant inelastic X-ray scattering spectroscopy (NRIXS) approach for iron isotopes

In addition to the ilmenite crystallization experiments, we synthesized ilmenite for nuclear resonant inelastic X-ray scattering spectroscopy (NRIXS) measurement in order to derive quantities needed for calculating equilibrium iron isotopic fractionation factors involving ilmenite. The starting material for the ilmenite synthesis was created using a stoichiometric mixture (1:2) of ^{57}Fe$_2$O$_3$ and TiO$_2$ powders. In order to perform the NRIXS measurements, which are only sensitive to the Mössbauer isotope ^{57}Fe, ^{57}Fe-enriched Fe$_2$O$_3$ powder (96.64% ^{57}Fe, Cambridge Isotopes) was used. The oxide powders were mixed by hand with isopropanol in an agate mortar and pestle for 2 hours. Two ^{57}Fe-doped ilmenite syntheses were conducted.

One synthesis was conducted at Case Western Reserve University in a one atmosphere box furnace at 1201°C for 122.1 hours. For this synthesis, the starting material was placed in a small SiO_2 glass tube, then vacuum sealed in a larger SiO_2 glass tube. The second ^{57}Fe-doped ilmenite synthesis was conducted at Washington University in St. Louis in a piston cylinder at 15 kbar and 1140°C for 65.7 hours. The sample starting material was loaded into a 7.89 mm tall graphite capsule with 0.75 mm wall thickness. The NRIXS results for the one-atmosphere synthesis are reported here. Forthcoming NRIXS measurements on the ilmenite synthesized using the piston cylinder will determine whether these reported results are robust.

From the phonon excitation probability function, $S(E)$, or the partial phonon density of states, $g(E)$, itself derived from S, the force constant for the iron sublattice can be extracted (e.g., Dauphas et al. 2012; Dauphas et al. 2014; Liu et al. 2017). The force constant calculated from the NRIXS spectra on our synthetic ilmenite is 156 ± 10 N/m. Given the high temperatures involved in magmatic processes, and assuming that the bonds are harmonic, the reduced partition function ratio, or β-factor, is calculated as a function of temperature from the mean force constant of the iron bonds, $\langle F \rangle$ in N/m.

$$1000 \ln \beta = 2904 \frac{\langle F \rangle}{T^2} \tag{4.1}$$

At a given temperature, the equilibrium stable isotopic fractionation factor ($\alpha_{\text{mineral-melt}}$) between two phases is related to the β-factor and Fe isotopic composition (δ^{56}Fe) for each phase through:

$$1000 \ln \alpha_{\text{mineral-melt}} = \delta^{56}Fe_{\text{mineral}} - \delta^{56}Fe_{\text{melt}} = 1000 \ln \beta_{\text{mineral}} - 1000 \ln \beta_{\text{melt}} \tag{4.2}$$

The equilibrium iron isotopic fractionation between ilmenite and lunar melts can be calculated as a function of temperature using equations 4.1 and 4.2, the force constant for ilmenite

reported in this work (156 ± 10 N/m), and the force constants previously reported for a suite of synthetic lunar volcanic glasses (Prissel et al. 2018). The fractionation between ilmenite and synthetic Apollo 16 green glass ($\langle F \rangle = 189 \pm 9$ N/m, Prissel et al. 2018) is reported for 1100°C and 1350°C in Table 4.7.

4.2.7 Ilmenite-melt isotopic fractionation

The measured Fe isotopic compositions of the experimental glass and ilmenite separates define an ilmenite-melt iron isotopic fractionation for each experiment (Table 4.7). The results from our ilmenite crystallization experiments are contradictory, with one set indicating that ilmenite is isotopically heavier than the co-existing glass ($\delta^{56}\text{Fe}_{\text{ilmenite}} > \delta^{56}\text{Fe}_{\text{glass}}$), and the other indicating that ilmenite is lighter ($\delta^{56}\text{Fe}_{\text{ilmenite}} < \delta^{56}\text{Fe}_{\text{glass}}$). This difference may be attributed to factors such as the composition of the melt and ilmenite or the experimental oxygen fugacity. We have conducted replicate experiments (J109 and F143) in order to test whether the two starting compositions yield different ilmenite-melt fractionation factors. Forthcoming isotopic measurements of experiments J109 and F143 will conclude whether the results for experiments J047 and F131 reported here are robust. (Additionally, experiment J047 contains excess ^{57}Fe, likely from contamination of the initial starting material pellet prior to the experiment. While this does not explain the difference in δ^{56}Fe between the two ilmenite crystallization experiments, the contamination is another reason to repeat this experiment.) The ilmenite-melt iron isotopic fractionation derived from the Apollo 14 black glass ilmenite crystallization experiment agrees with the fractionation calculated from the NRIXS approach, and thus, for our modeling purposes we will use these fractionations, with ilmenite being isotopically lighter than the melt (Table 4.7). Further, our results are consistent with previously reported ilmenite-melt Fe isotopic fractionations deduced from experimental studies ($\delta^{56}\text{Fe}_{\text{ilmenite}} - \delta^{56}\text{Fe}_{\text{melt}} = -0.013$‰, Sossi and O'Neill 2017), but differ

Table 4.7: Comparison of the ilmenite-melt Fe isotopic fractionations experimentally determined in this work. For each method, the reported uncertainty on the ilmenite-melt fractionation was calculated from the reported measurement uncertainties on ilmenite and glass.

Method	T (°C)	$\Delta^{56}\mathbf{Fe_{ilmenite\text{-}melt}}$ (‰)	$\Delta^{57}\mathbf{Fe_{ilmenite\text{-}melt}}$ (‰)
Ilmenite crystallization (J047)	1098	$+0.06 \pm 0.04$	–
Ilmenite crystallization (F131)	1350	-0.04 ± 0.03	-0.08 ± 0.05
NRIXS[a]	1350	-0.04 ± 0.01	
	1100	-0.05 ± 0.02	

[a] NRIXS fractionations have been calculated at the given temperatures using the force constant for ilmenite reported in this work and the force constant for a synthetic Apollo 16 green glass reported in Prissel et al. (2018).
$\Delta^{57}Fe_{ilmenite\text{-}melt}$ is not reported for experiment J047 because this experiment contained excess ^{57}Fe due to sample contamination.

from those inferred from measured Fe isotopic compositions of natural mineral separates (i.e., $\delta^{56}Fe_{ilmenite} - \delta^{56}Fe_{melt} = +0.20‰$, Craddock and Dauphas 2011; Wang et al. 2015).

In comparing the Ti isotopic compositions of our synthetic glass and ilmenite (Table 4.6), we have determined an ilmenite-melt Ti isotopic fractionation of $\Delta^{49}Ti_{ilmenite\text{-}melt} = -0.09 \pm 0.03$. Previously, Millet et al. (2016) defined a temperature-dependent oxide-melt isotopic fractionation $\Delta^{49}Ti_{oxide\text{-}melt} = -0.23 \times \frac{10^6}{T^2}$. Calculating the $\Delta^{49}Ti_{oxide\text{-}melt}$ fractionation for the experimental temperature of 1098°C yields $\Delta^{49}Ti_{oxide\text{-}melt} = -0.12‰$, and this is within the estimated uncertainty of our experimentally determined fractionation. Our experimentally determined ilmenite-melt Ti isotopic fraction is also within range of that predicted from the temperature and melt SiO_2 composition of our experiment (Deng et al. 2019; Johnson et al. 2019).

All of our experiments have been conducted at oxygen fugacities relevant to the oxygen conditions inferred for the Moon. These reducing conditions minimize the presence of Fe^{3+}, which has been demonstrated to affect Fe isotope partitioning (Teng et al. 2008; Dauphas

et al. 2009a; Dauphas et al. 2014). Moving forward, we have incorporated our experimentally determined Fe and Ti isotopic fractionations between ilmenite and melt into models of lunar magma ocean crystallization.

4.3   Lunar magma ocean crystallization

We have developed a lunar magma ocean (LMO) crystallization model that tracks both the major element chemistry and the isotopic composition of the minerals precipitating from the LMO and the residual LMO liquid. The onset of ilmenite crystallization and ilmenite-melt isotopic fractionation are the most important considerations for modeling the isotopic composition of the ilmenite-bearing lunar magma ocean cumulates. Experimental studies of lunar magma ocean crystallization have determined that ilmenite begins crystallizing near 88-98% LMO solidification (Lin et al. 2017a; Lin et al. 2017b; Charlier et al. 2018; Rapp and Draper 2018; Lin et al. 2019). These results are consistent with previous theoretical estimates for ilmenite saturation in the LMO (87-95% LMO solidification, Snyder et al. 1992; Elkins-Tanton et al. 2011), and the experimental mineral assemblages provide improved constraints on the major element evolution of the LMO with which to calibrate our model.

Our model begins with a given bulk composition for the lunar magma ocean (Table 4.8) and crystallizes according to the mineral phases and proportions determined by recent experimental studies (Figure 4.4). For each crystallization sequence, the published synthetic

Table 4.8: Major element composition of bulk silicate Moon as defined in each lunar magma ocean model.

	SiO_2	TiO_2	Al_2O_3	Cr_2O_3	FeO	MnO	MgO	CaO	Na_2O	K_2O	P_2O_5
Lin et al. (2017a, 2017b, 2019)	45.49	0.52	4.50		10.50		35.74	3.23			
Charlier et al. (2018)	46.10	0.17	3.93	0.50	7.62	0.13	38.30	3.18	0.05	0.01	0.02
Rapp and Draper (2018)	45.90	0.15	4.15	0.50	8.15	0.12	38.40	2.95	0.10	0.01	0.01
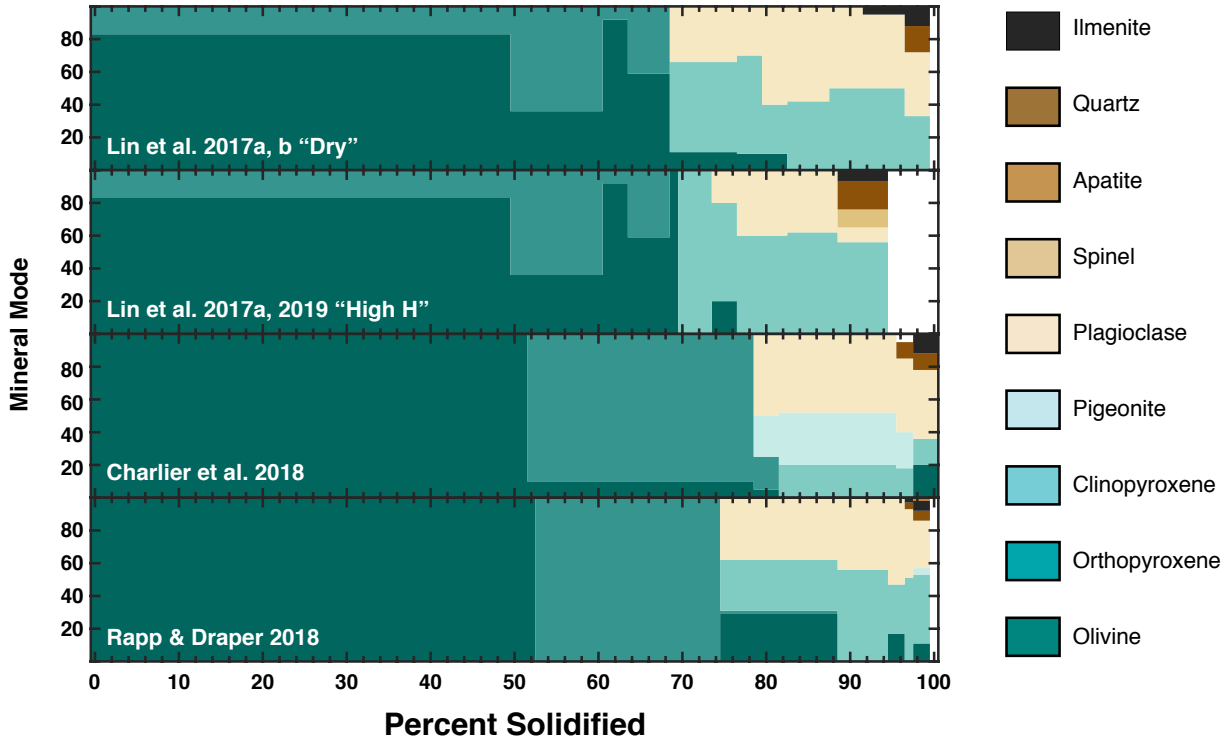
Figure 4.4: Solidified lunar magma ocean phase assemblages determined by previous experimental studies (Lin et al. 2017a; Lin et al. 2017b; Charlier et al. 2018; Rapp and Draper 2018; Lin et al. 2019). For the Lin et al. models (top two bar charts): "Dry" summarizes the experimental results on a nominally anhydrous starting composition, while "High H" reflects an initial 3150 ppm H_2O in the starting lunar magma ocean composition. Charlier et al. (2018) results are those from experiments on the lunar primitive upper mantle (LPUM) composition (Table 4.8).

mineral and glass compositions define the mineral-melt partitioning, $D_{mineral\text{-}melt}$, for SiO_2, TiO_2, Al_2O_3, Cr_2O_3, FeO, MnO, MgO, CaO, Na_2O, K_2O, and P_2O_5 in each mineral phase. Each experimental model has been treated in a separate iteration such that the major element behavior is internally consistent for each model and the major element composition of the liquid evolves similarly to that observed for the melt compositions of the experiments (Figure 4.5). As we are most interested in the compositional effects of ilmenite crystallization, only the experimental crystallization sequences that reach ilmenite saturation have been included here.

At each calculation step, our model uses the published LMO models to determine what minerals will be crystallizing, and what the proportion of each mineral will be in the solid crystallized at that step. The concentration of element i in a given mineral is defined as

$$C^i_{\text{mineral}} = D^i_{\text{mineral-melt}} \times C^i_{\text{melt}}$$

The bulk composition of the instantaneous solid at a given crystallization step, C^i_s, is calculated from the mass proportion of each mineral phase crystallized, X_n, and the concentration of element i in each phase n, C^i_n.

$$C^i_s = \sum_{n=1}^{n}(X_n \times C^i_n)$$

The new liquid, $C^i_{l,1}$ is calculated from the initial composition of the liquid at a given step, $C^i_{l,0}$, the mass fraction of solid crystallized in that step, X^i_s, and the composition of the bulk solid.

$$C^i_{l,1} = C^i_{l,0} - X^i_s \times C^i_s$$

4.3.1   Isotopic constraints

Our model is capable of tracking the isotopic compositional evolution for any of the eleven elements included in the starting composition provided there are constraints on the initial isotopic composition of the lunar magma ocean and isotopic mineral-melt fractionations for that element. Previous attempts to characterize the isotopic compositional evolution of the lunar magma ocean liquid and cumulates have been hampered by a lack of experimentally determined mineral-melt fractionations, particularly for ilmenite. Experimental and
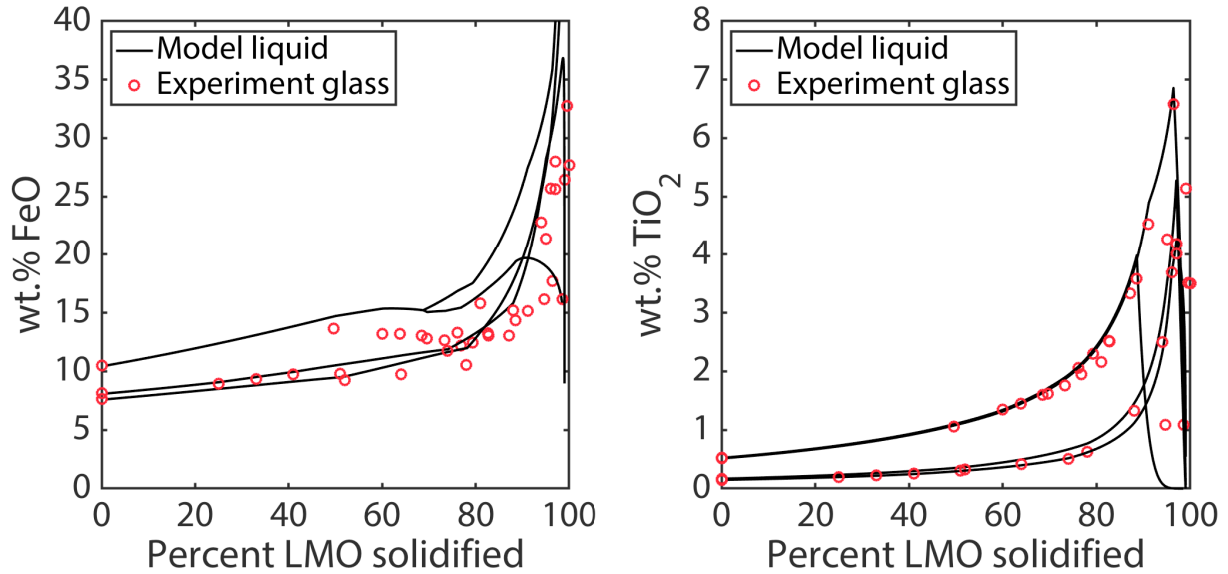
Figure 4.5: Modeled evolution of the lunar magma ocean FeO and TiO$_2$ liquid compositions (black lines). Red circles represent the reported glass compositions for the lunar magma ocean experiments used to calibrate the major element evolution of our models (Lin et al. 2017a; Lin et al. 2017b; Charlier et al. 2018; Rapp and Draper 2018; Lin et al. 2019).

theoretical studies have indicated that the Fe isotopic composition of ilmenite would either be lighter than the melt (this work) or indistinguishable from that of the melt (Poitrasson et al. 2004; Poitrasson 2007; Sossi and O'Neill 2017). Alternatively, previous estimates for ilmenite-melt isotopic fractionations based on the measured isotopic compositions of lunar ilmenite separates have suggested that, relative to co-existing minerals and melt, ilmenite would be heavier in Fe isotopes and lighter in Mg isotopes (Craddock et al. 2010; Wang et al. 2015; Sedaghatpour et al. 2013). For Ti isotopes, natural sample studies and first-principles calculations have concluded that ilmenite is isotopically lighter than the melt (Millet et al. 2016; Greber et al. 2017; Deng et al. 2019; Johnson et al. 2019; Wang et al. 2020), and this is consistent with our experimental results. Here we have focused on modeling the evolution of the Fe and Ti isotopic compositions using our experimentally-calibrated ilmenite-melt isotopic fractionations.

Estimates for the bulk silicate Moon isotopic composition define the initial isotopic compositions of the LMO liquid (δ^{56}Fe $= +0.063 \pm 0.023$‰, Poitrasson et al. 2019; δ^{49}Ti $= -0.003 \pm 0.014$‰, Millet et al. 2016). The subsequent crystallization calculation is outlined for Fe isotopes below. We calculate the isotopic composition of the liquid, δ^{56}Fe$_l$, and each cumulate mineral, δ^{56}Fe$_{mineral}$, during LMO crystallization using mineral-melt isotopic fractionations, $\alpha_{mineral\text{-}melt}$, and the following equation:

$$\delta^{56}\text{Fe}_{mineral} = \alpha_{mineral\text{-}melt} \times (\delta^{56}\text{Fe}_l + 1000) - 1000$$

The bulk iron isotopic composition of the instantaneous solid at a given crystallization step, δ^{56}Fe$_s$, is calculated by mass balance using the concentration of Fe and the Fe isotopic composition of each mineral phase, n, crystallized.

$$\delta^{56}\text{Fe}_s = \sum_{n=1}^{n} (\frac{C_n^{Fe}}{C_s^{Fe}} \times \delta^{56}\text{Fe}_n)$$

The Fe isotopic composition of the solid crystallized at each step, and the moles of Fe in the solid and liquid, $[Fe]_s$ and $[Fe]_l$, are used to determine the Fe isotopic composition of the remaining liquid

$$\delta^{56}\text{Fe}_{l,1} = \frac{[Fe]_l \times \delta^{56}\text{Fe}_{l,0} - [Fe]_s \times \delta^{56}\text{Fe}_s}{[Fe]_l - [Fe]_s}$$

For the Fe and Ti isotope modeling presented in this work, we have only imposed a mineral-melt isotopic fractionation for ilmenite. Previous investigations have concluded that olivine and pyroxene crystallization at lunar oxygen fugacities would not significantly fractionate iron isotopes (δ^{56}Fe$_{melt} - \delta^{56}$Fe$_{mineral} < 0.02$‰, Sossi and O'Neill 2017; Prissel et al. 2018). The ilmenite-melt isotopic fractionations used in our model (Table 4.9) have been selected based

Table 4.9: Initial Fe and Ti isotopic compositions of the lunar magma ocean and ilmenite-melt isotopic fractionations used in crystallization models.

Element	Initial composition (‰)	$\alpha_{\text{ilmenite-melt}}$
Fe	$\delta^{56}\text{Fe}= 0.063$[a]	0.99994
Ti	$\delta^{49}\text{Ti}= -0.003$[b]	0.99991

[a] Poitrasson et al. (2019)
[b] Millet et al. (2016)

on our experimental results (Section 4.2.7). For Ti isotopes, the ilmenite-melt fractionation has been set equal to that determined from our ilmenite crystallization experiment. For Fe isotopes, the ilmenite-melt fractionation has been calculated at 1000°C using the force constant for ilmenite reported in this work and the force constant for a synthetic Apollo 16 green glass reported in Prissel et al. (2018). A temperature of 1000°C was chosen in order to extend to the coldest temperatures of the previously published lunar magma ocean crystallization experiments. Mass-dependent isotopic fractionations are larger at lower temperatures, and thus the calculated fractionation, $\Delta^{56}\text{Fe}_{\text{ilmenite-melt}} = -0.06 \pm 0.02‰$, represents a maximum fractionation between ilmenite and melt during ilmenite crystallization from the lunar magma ocean.

4.3.2 Model results

In the case that ilmenite is isotopically lighter than the melt, ilmenite fractionation during the lunar magma ocean drives the melt and subsequently crystallizing ilmenite toward heavier isotopic compositions (Figure 4.6). Our modeling results indicate that the first ilmenites to crystallize from the lunar magma ocean would have Fe isotopic composition $\delta^{56}\text{Fe} = 0.00‰$ and Ti isotopic composition $\delta^{49}\text{Ti} = -0.093‰$. Toward the end of lunar magma ocean crystallization, the fractionation of Fe and Ti isotopes by ilmenite leads to progressively heavier Fe and Ti isotopic compositions for both the ilmenite cumulates and the residual

liquid. This isotopic enrichment can result in ilmenite with δ^{56}Fe $= +0.093$‰ and δ^{49}Ti $= +0.96$‰, and a residual liquid with δ^{56}Fe $= +0.152$‰ and δ^{49}Ti $= +1.07$‰. It is important to note that most of the ilmenite crystallized from the lunar magma ocean will have isotopic compositions toward the lower end of this modeled compositional range, as the heaviest ilmenites will only constitute a small fraction of the total ilmenite crystallized.
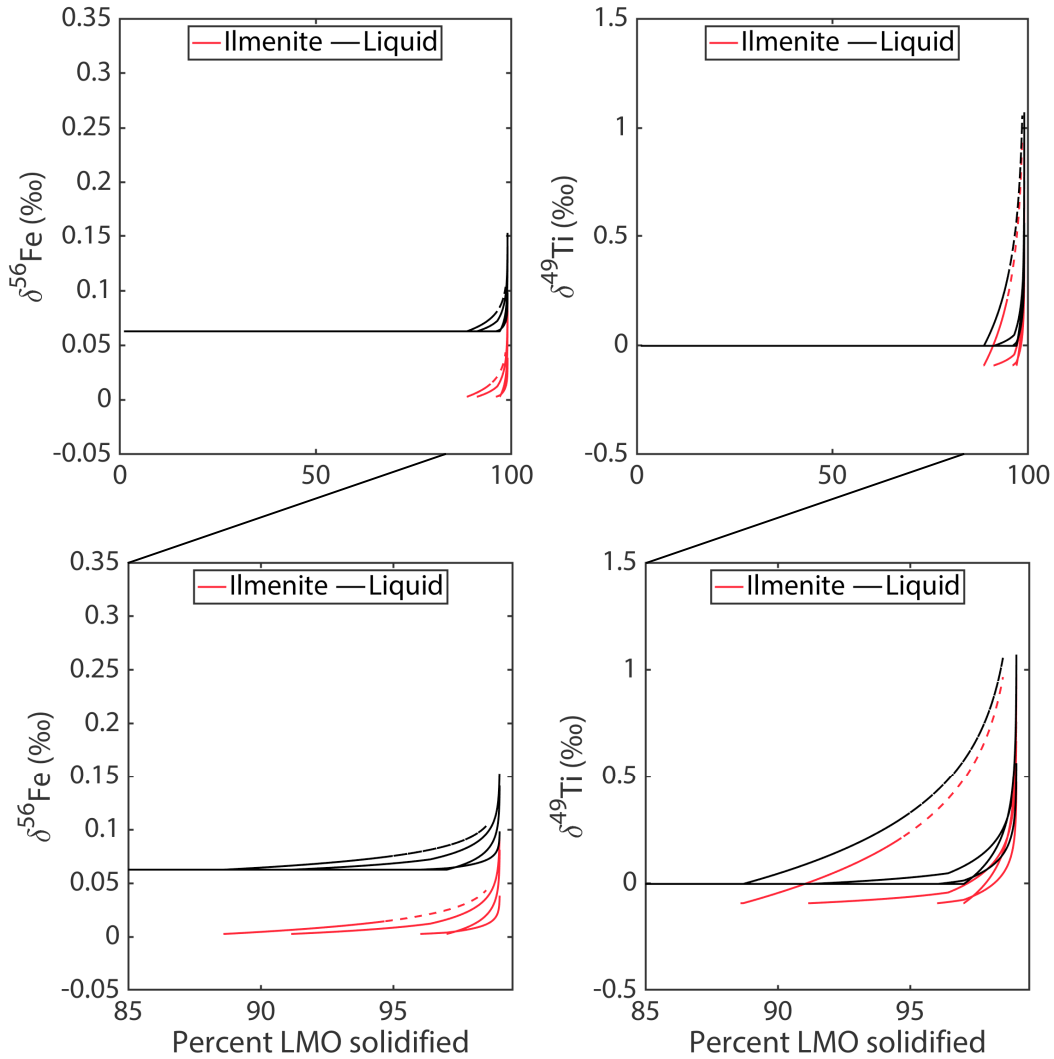
Figure 4.6: Model results for the iron and titanium isotopic compositional evolution of the lunar magma ocean liquid and ilmenite cumulates. The isotopic compositions of the LMO liquid (black) and ilmenite (red) are plotted as a function of percent LMO solidified for each experimental crystallization sequence (see Figure 4.4). In these models, ilmenite is the only mineral that has been assigned a mineral-melt isotopic fractionation. Because of this, the isotopic composition of the lunar magma ocean liquid does not begin to deviate from the initial starting composition until the onset of ilmenite crystallization in each model. The bottom row of figures highlights the isotopic evolution in the last 15% of lunar magma ocean crystallization. The two dashed lines in each figure pane represent an extrapolation of the Lin et al. (2019) "High H" crystallization sequence, which ends at 94.7 percent solidified.

4.4 Mare basalt isotopic mixing model

In conjunction with our LMO crystallization model, we have developed a multi-component mixing model for the isotopic compositions of the mare basalts. For each mare basalt type, the major element composition of the parent magma is defined using a previously reported parental melt composition (Table 4.10).

We have modeled the mare basalt parent magmas as a mixture of ilmenite, a potassium-, rare earth element-, and phosphorus-rich (KREEP) component, and a third additional component (here referred to as "component X"), the composition of which varies with each mare basalt type. The major element composition of the ilmenite is defined as the average composition of our synthetic ilmenites in experiment F131 (Table 4.4). We have assigned the composition of the KREEP component to be that of KREEP basalt 15386 (Vaniman and Papike 1980). This KREEP basalt has been used to approximate the KREEP component in previous mare basalt mixing models (e.g., Dickinson et al. 1985; Shervais et al. 1985; Neal et al. 1988). Component X encompasses the compositional components of the mare basalt parental melts that would not be represented by ilmenite or KREEP, and this would consist predominantly of olivine, pyroxene, and plagioclase. Though we are using KREEP basalt 15386 to define an endmember composition in our mixing models, it is important to note that the KREEP basalt itself is a mixture of components that may not be equally distributed throughout the lunar mantle.

The proportion of KREEP component in each mare basalt type has been calculated from the K_2O composition of the parental melts (Table 4.10). We assume all of the K_2O in the mare basalt parent magma is sourced from the KREEP component, and thus the calculated proportion represents a maximum proportion of KREEP, as any K_2O in the other two components would decrease this estimate. After accounting for the proportion of KREEP

Table 4.10: Major element compositions of mare basalt parental magmas.

Mare Basalt Type	SiO_2	TiO_2	Al_2O_3	Cr_2O_3	FeO	MnO	MgO	CaO	Na_2O	K_2O	P_2O_5
Apollo 11 low-K[a]	39.6	11.1	9.5	0.47	19.1	0.28	8.1	11.1	0.36	0.05	
Apollo 11 high-K[b]	42.8	10.2	8.0	0.29	20.0	0.25	8.0	10.0	0.50	0.26	
Apollo 17 A[c]	37.9	13.0	8.9	0.41	19.6	0.24	9.5	10.0	0.42	0.07	
Apollo 17 B[c]	36.9	14.2	8.9	0.43	20.5	0.26	9.0	9.4	0.41	0.04	
Apollo 17 C[d]	38.5	12.3	8.7	0.61	18.5	0.26	9.7	10.1		0.07	
Apollo 12[e]	45.0	2.9	8.6	0.38	21.0	0.28	11.6	9.4	0.23	0.06	0.07
Apollo 15[f]	44.3	2.3	8.5	0.68	22.7	0.31	11.5	9.4	0.28	0.05	0.08

[a] Apollo 11 high-Ti, low-K basalt (Type B3) parent magma composition as estimated from sample 10045 (Snyder et al. 1992).

[b] Apollo 11 high-Ti, high-K basalt composition from sample 10085, experimentally proven to be a candidate for the single magma that recreates the variability observed in this sample suite (Beaty et al. 1979; Grove and Beaty 1980; Meyer 2005).

[c] Apollo 17 high-Ti basalt parent magma compositions as defined by the most MgO- and TiO_2-rich, fine grained samples: Type A= 71555, Type B= 71066 (Murali et al. 1977; Warner et al. 1979; Neal et al. 1990).

[d] Apollo 17 high-Ti basalt (Type C) parent magma composition as estimated from the average composition of samples 74245, 74275, and 74247 (Snyder et al. 1992).

[e] Apollo 12 low-Ti basalt parent magma composition as defined by sample 12009 (Green et al. 1971; Meyer 2005).

[f] Apollo 15 low-Ti basalt parent magma as defined by the most olivine- and Mg-rich sample, 15622 (Chappell and Green 1973; Meyer 2005).

in the parent melt composition, we assume any remaining TiO_2 in the parent melt can be attributed to the ilmenite component of our mixing model. Similarly, this calculation method results in a maximum proportion of ilmenite, as any TiO_2 in component X would decrease the estimated ilmenite proportion. Then, the estimated proportions of the KREEP and ilmenite components (Table 4.11) determine the proportion and composition of component X for each parent melt composition (Table 4.12).

4.4.1 Isotopic composition of ilmenite component in mare basalt parent magmas

We have determined the isotopic composition of the ilmenite component in the mare basalt parent magmas using the estimated mixing proportions for each component and previously

Table 4.11: Estimated proportions of the three mixing components for each parent melt composition.

Mare Basalt Type	KREEP	Ilmenite	Component X
Apollo 11 low-K	0.07	0.17	0.76
Apollo 11 high-K	0.39	0.14	0.47
Apollo 17 A	0.10	0.20	0.71
Apollo 17 B	0.06	0.22	0.72
Apollo 17 C	0.10	0.19	0.71
Apollo 12	0.10	0.04	0.86
Apollo 15	0.07	0.03	0.89

Table 4.12: Calculated major element compositions of mixing component X for each mare basalt parent magma. Given that all K_2O and TiO_2 in the parent magma has been attributed to the KREEP and ilmenite component, respectively, neither of these elements is present in component X. The major element composition of the KREEP component used in the mixing calculation has also been included for reference.

Mare Basalt Type	SiO_2	TiO_2	Al_2O_3	Cr_2O_3	FeO	MnO	MgO	CaO	Na_2O	K_2O	P_2O_5
Apollo 11 low-K	49.1	*0*	11.5	0.61	14.9	0.37	8.9	14.2	0.42	*0*	
Apollo 11 high-K	51.1	*0*	4.9	0.34	21.2	0.42	8.9	13.9	0.48	*0*	
Apollo 17 A	48.6	*0*	11.0	0.56	14.5	0.34	11.2	13.4	0.51	*0*	
Apollo 17 B	48.9	*0*	11.6	0.59	14.8	0.36	10.5	12.8	0.52	*0*	
Apollo 17 C	49.5	*0*	10.7	0.86	13.6	0.36	11.6	13.6		*0*	
Apollo 12	47.1	*0*	8.4	0.41	21.4	0.31	12.4	10.0	0.19	*0*	0.00
Apollo 15	45.5	*0*	8.3	0.74	23.1	0.34	12.0	9.7	0.25	*0*	0.03
KREEP basalt[a]	50.8	2.2	14.8	0.35	10.6	0.16	8.2	9.7	0.73	0.67	0.70

[a] Major element composition of KREEP basalt 15386 used to define KREEP component in mixing model (Vaniman and Papike 1980).
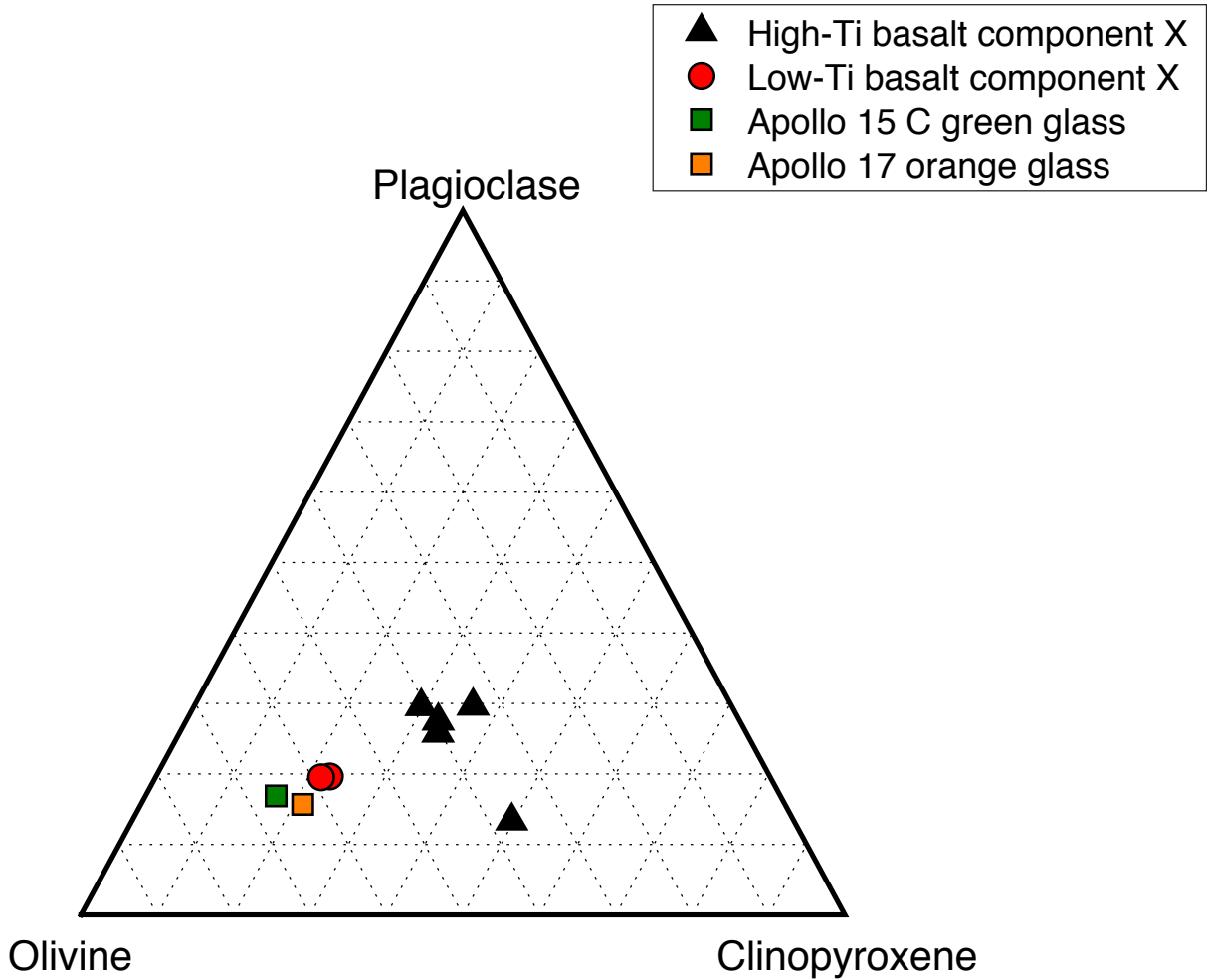
Figure 4.7: Mixing component X compositions plotted in a clinopyroxene-olivine-plagioclase pseudo-ternary diagram using the projection scheme of Tormey et al. (1987). Estimated compositions for component X in the low-Ti mare basalts (red circles) have more olivine normative compositions than those estimated for the high-Ti mare basalts (black triangles). In this projection, the lunar volcanic glasses (Apollo 15 C green and Apollo 17 orange, Delano 1986) are similar to the component X compositions estimated for the low-Ti mare basalts. Dashed lines denote 10 mol% intervals for the ternary components.

published mare basalt isotopic compositions (Table 4.13). For each mare basalt sample, we use the component proportions calculated for the parent magma of its corresponding basalt type (Table 4.11). For the mixing calculation described here, we have assumed that the mare basalt isotopic compositions are representative of the parent magma isotopic compositions. However, shallow petrogenetic processes such as fractional crystallization or partial melting may also influence the mare basalt isotopic compositions, resulting in elemental and isotopic fractionation from the parent magma compositions.

In order to determine the isotopic composition of the ilmenite component, we have calculated an isotopic mass balance for each mare basalt sample using the following equation:

$$\delta^i_{\text{sample}} = X^i_{\text{KP}}\delta^i_{\text{KP}} + X^i_{\text{ilm}}\delta^i_{\text{ilm}} + X^i_{\text{comp x}}\delta^i_{\text{comp x}} \qquad (4.3)$$

where δ^i represents the isotopic composition of element i and X represents the mass fraction of element i for a given component (KP = KREEP, ilm = ilmenite, comp x = component X) calculated from the composition and estimated proportion of each component.

Isotopic compositions have been assigned to the KREEP component and component X (Table 4.13). The Fe and Mg isotopic compositions of the KREEP component are those of KREEP basalt sample 15386 (Poitrasson et al. 2019; Sedaghatpour and Jacobsen 2019). Because the Ti isotopic composition has not been measured for sample 15386, we have instead used the Ti isotopic composition of a KREEP-rich impact melt breccia for our calculation (Greber et al. 2017). Component X primarily consists of Fe- and Mg-rich silicates (olivine, pyroxene) and relatively Fe- and Mg-poor plagioclase (Figure 4.7). The Fe and Mg isotopic composition of component X will be dictated by the isotopic composition of the ultramafic phases. Olivine and pyroxene cumulates from lunar magma ocean crystallization are expected to comprise a majority of the lunar mantle, and these cumulates are likely the main contributors of Fe

Table 4.13: Measured iron, titanium, and magnesium isotopic compositions and the calculated isotopic composition of the ilmenite mixing component for each mare basalt sample.

Sample	Sample Type	Sample Composition[a] (‰)			Ilmenite Component (‰)		
		δ^{56}Fe	δ^{49}Ti	δ^{26}Mg	δ^{56}Fe	δ^{49}Ti	δ^{26}Mg
70017	High-Ti, B	0.21	0.015	−0.25	0.36	0.012	−0.15
70215	High-Ti, B2	0.17	0.033	−0.37	0.29	0.030	−1.05
75075	High-Ti, B1	0.22	0.018	−0.69	0.39	0.015	−3.36
72155	High-Ti, A	0.21	0.023		0.38	0.018	
70035	High-Ti, A	0.14		−0.55	0.23		−2.60
74275	High-Ti, C	0.18		−0.42	0.31		−1.66
71539	High-Ti, A	0.21		−0.23	0.39		0.06
75015	High-Ti, A	0.21		−0.25	0.39		−0.11
74255	High-Ti, C	0.18		−0.25	0.32		−0.10
10044	High-Ti, Low-K	0.24		−0.42	0.50		−1.51
10049	High-Ti, High-K	0.11		−0.18	0.19		0.86
15016	Low-Ti, olivine	0.07	−0.008	−0.09	0.10	−0.036	10.5
12002	Low-Ti, olivine	0.09		−0.39	0.35		−6.47
12005	Low Ti, ilmenite	0.10		−0.12	0.46		6.85
12051	Low Ti, ilmenite	0.10		−0.16	0.51		4.91
12021	Low-Ti, pigeonite	0.07		−0.18	0.12		3.93
12052	Low-Ti, pigeonite	0.07		−0.09	0.12		8.31
15058	Low-Ti, pigeonite	0.10		−0.16	0.62		6.22
15075	Low-Ti, pigeonite	0.05		−0.15	−0.18		6.84
15475	Low-Ti, pigeonite	0.04		−0.12	−0.36		8.69
15499	Low-Ti, pigeonite	0.08		−0.12	0.31		8.69
12063	Low-Ti, ilmenite	0.09		−0.22	0.35		1.99
15555	Low-Ti, olivine	0.06		−0.67	0.01		−25.2
12009	Low-Ti, olivine	0.05	−0.008		−0.17	−0.036	
12011	Low-Ti, pigeonite	0.07		−0.11	0.07		7.34
12038	Low-Ti, feldspathic	0.08		−0.24	0.22		0.97
15386	KREEP basalt	0.11	0.330[b]	−0.35			
	Component X[c]	0.06	−0.003	−0.26			

[a] Data sources for sample isotopic compositions: Fe, Weyer et al. 2005; Liu et al. 2010; Sossi and O'Neill 2017; Poitrasson et al. 2019; Ti, Millet et al. 2016; Greber et al. 2017; Mg, Sedaghatpour et al. 2013; Sedaghatpour and Jacobsen 2019.

[b] The Ti isotopic composition used in the mixing model for KREEP basalt 15386 is that of SaU 169 KREEPy impact melt breccia (Greber et al. 2017).

[c] Previous estimates for bulk silicate Moon isotopic composition assigned to component X in the mixing model (Fe, Poitrasson et al. 2019; Ti, Millet et al. 2016; Mg, Sedaghatpour et al. 2013).

and Mg to component X. Because olivine and orthopyroxene will not fractionate Fe and Mg isotopes to a measurable extent during equilibrium crystallization or melting (Teng et al. 2010; Sossi and O'Neill 2017; Prissel et al. 2018), component X can be approximated as having bulk silicate Moon Fe and Mg isotopic composition (Sedaghatpour et al. 2013; Poitrasson et al. 2019).

The isotopic composition of the ilmenite component is then calculated using:

$$\delta^i_{\text{ilm}} = (\delta^i_{\text{sample}} - X^i_{\text{KP}}\delta^i_{\text{KP}} - X^i_{\text{comp x}}\delta^i_{\text{comp x}})/X^i_{\text{ilm}} \tag{4.4}$$

The isotopic mixing calculations for the mare basalts indicate that the ilmenite component would have the isotopic composition δ^{56}Fe$= -0.36$‰ to $+0.62$‰, δ^{49}Ti$= -0.036$‰ to $+0.030$‰, and δ^{26}Mg$= -25.2$‰ to $+10.5$‰ (Table 4.13). The isotopic compositions of the ilmenites crystallizing from our lunar magma ocean models (Figure 4.6) match the estimated Ti isotopic composition of the ilmenite component, but not the estimated Fe isotopic composition (Figure 4.8).

Previous models for the isotopic composition of the ilmenite-bearing lunar magma ocean cumulates that incorporated a light fractionation for ilmenite did not replicate the enrichment in heavy Fe and Ti isotopes observed in the high-Ti mare basalts, and instead invoked additional processes, such as partial melting, in order to explain the magnitude of Fe and Ti isotopic fractionation (Millet et al. 2016; Greber et al. 2017; Sossi and O'Neill 2017). Though the KREEP component constitutes a small fraction of the mare basalt parent magma (Table 4.11), combining the heavy Ti isotopic composition of the KREEP component with the Ti isotopic composition of the lunar magma ocean ilmenites reproduces the Ti isotopic compositions of the high-Ti mare basalts. Though the Ti isotopic composition assigned to the KREEP component (δ^{49}Ti$= +0.33$‰) is significantly heavier than that of the high-Ti
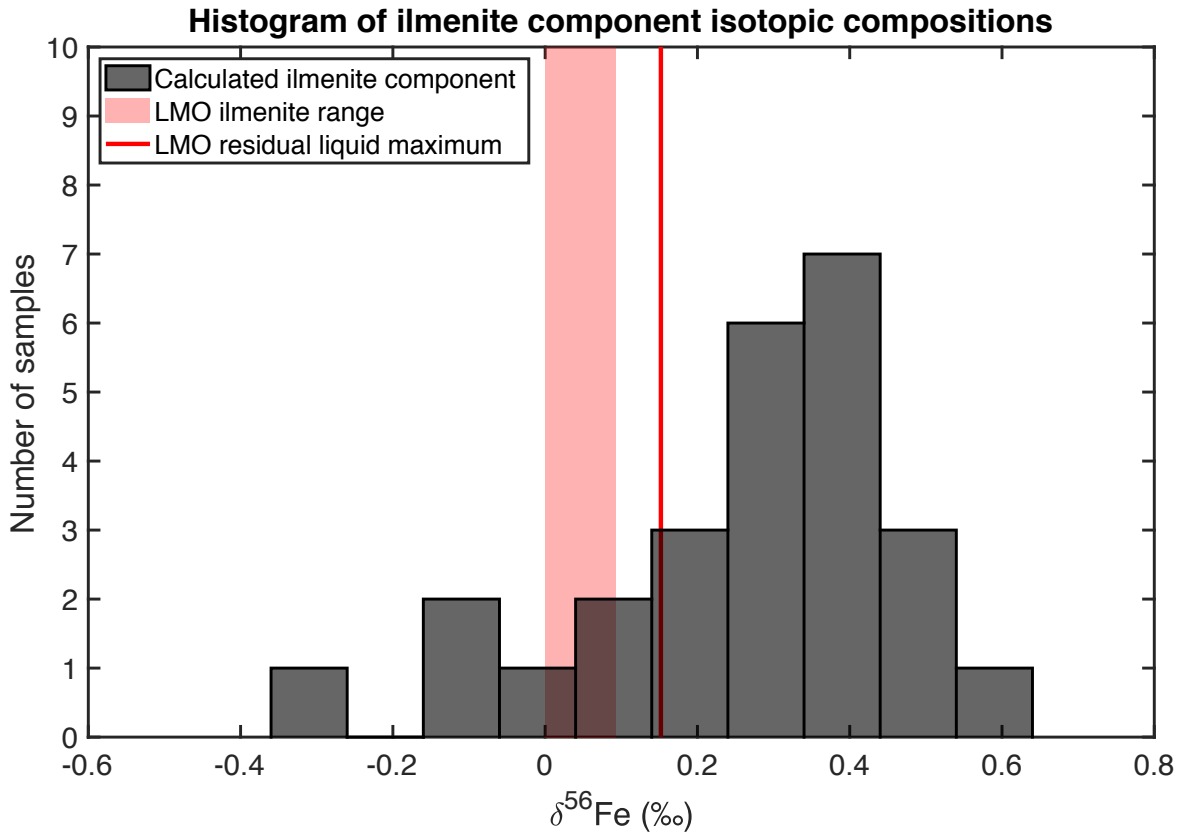
Figure 4.8: Comparison of the estimated iron isotopic compositions of the ilmenite component in mare basalt parent magmas and the lunar magma ocean model ilmenites. Iron isotopic compositions of the ilmenite component in mare basalt samples (n = 26, Table 4.13) are plotted as a histogram in black. The red shaded region highlights the iron isotopic compositional range for the ilmenites crystallized from our lunar magma ocean models (Figure 4.6). Most of the estimated isotopic compositions for the ilmenite component are heavier than the ilmenites crystallized from our LMO models. The heaviest iron isotopic composition of our modeled residual LMO liquid is plotted as a red line for reference.

basalts, this value is reasonable considering our lunar magma ocean models in which the residual LMO liquid thought to be related to KREEP gets enriched up to $\delta^{49}\text{Ti}= +1.07‰$.

Consistent with previous works, our model indicates that the Fe isotopic enrichment of the high-Ti basalts cannot be explained solely by ilmenite crystallization in the lunar magma ocean. Though the late-stage ilmenites and residual liquids get progressively heavier in Fe isotopic composition as the LMO crystallizes, the magnitude of this enrichment is not enough to match the high-Ti basalt iron isotopic compositions. In calculations that use the heaviest residual liquid from our LMO models ($\delta^{56}\text{Fe}= +0.152‰$) instead of the Fe isotopic composition of sample 15836 ($\delta^{56}\text{Fe}= +0.11‰$), the estimated iron isotopic compositions for the ilmenite component are still heavier than those of the ilmenites crystallizing from the lunar magma ocean. Importantly, our mixing calculations have been designed such that the estimated iron isotopic compositions of the ilmenite component are minimum values. We have assigned all the K_2O to the KREEP component, but potassium may also be sourced from the ilmenite or component X. An additional source for potassium would decrease the calculated proportion of KREEP component in the mare basalt parent magma, resulting in a heavier estimated Fe isotopic composition for the ilmenite component. Similarly, if component X is Ti-bearing, the estimated proportion of the ilmenite in the mare basalt parent magma would decrease, and thus the ilmenite Fe isotopic compositions would need to be heavier than those reported (Table 4.13) in order to explain the Fe isotopic compositions of the high-Ti basalts.

4.5 Implications for mare basalt petrogenesis

Our modeling has shown that the difference in Ti isotopic composition between the low- and high-Ti lunar mare basalts can be explained by the proportion of the ilmenite and KREEP components in their parental melts (Section 4.4.1). However, these models are not

able to account for the difference in Fe isotopic compositions between the two basalt suites. Specifically, the estimated Fe isotopic composition for the ilmenite (or Ti-bearing) component of the high-Ti mare basalts is heavier than the modeled Fe isotopic compositions of lunar magma ocean ilmenite cumulates and residual liquids (Figure 4.8).

Partial melting of ilmenite is not a viable mechanism for generating the heavy Fe isotopic compositions of the high-Ti mare basalt parent magmas because this process would also fractionate Ti isotopes. The equilibrium ilmenite-melt isotopic fractionations determined in this work indicate that ilmenite would be isotopically lighter than co-existing melt. Partial melting of ilmenite in the mare basalt source regions would produce melts enriched in heavy Fe and Ti isotopes relative to the residue, provided ilmenite was not exhausted from the source (Millet et al. 2016; Greber et al. 2017; Sossi and O'Neill 2017). However, the melting process would lead to fractionation for both Fe and Ti isotopes, and our experimentally determined ilmenite-melt isotopic fractionations reveal that the magnitude of titanium isotopic fractionation would be greater than that for iron.

Two observations are critical in determining the origin of the heavy iron isotopic compositions of the mare basalts: 1) the Fe isotopic difference appears to be linked to the Ti major element compositional variability, and 2) there is a negative correlation between the Fe and Mg isotopic compositions of the mare basalts (Figure 4.2). This relationship between Fe and Mg isotopic compositions suggests that diffusive exchange of Fe and Mg contributes to the isotopic signature of the high-Ti component in the mare basalt parental melts. Diffusion of Mg into this component would produce lighter Mg isotopic compositions, and conversely, diffusion of Fe out of this component would lead to heavier Fe isotopic compositions (e.g., Dauphas et al. 2010; Teng et al. 2011; Van Orman and Krawczynski 2015). Additionally, the magnitude of diffusive isotopic fractionation would depend on the concentrations of Fe and Mg in the high-Ti component.

A potential method for inducing Fe-Mg interdiffusion in the high-Ti component of the mare basalt parent magmas is the chemical reaction between ilmenite-bearing lunar magma ocean cumulates and a lunar mantle comprised predominantly of olivine and pyroxene. Toward the end of lunar magma ocean crystallization, ilmenite-bearing cumulates are hypothesized to sink into the lunar mantle because these late-stage cumulates are more dense than the underlying cumulates consisting mainly of silicate minerals (e.g., Hess and Parmentier 1995). Ilmenite in contact with an olivine and orthopyroxene cumulate can produce the Fe-Ti oxide mineral armalcolite via the subsolidus reaction

$$2\,\mathrm{FeTiO_3} + \mathrm{MgSiO_3} \longrightarrow (\mathrm{Mg,Fe})_2\mathrm{SiO_4} + (\mathrm{Mg,Fe})\mathrm{Ti_2O_5}$$

at depths less than 280 km in the lunar mantle (Thacker et al. 2009). As this chemical reaction progresses from left to right, Fe diffuses out of the oxide phase and into the silicate phase, and conversely, Mg diffuses out of the silicate phase and into the oxide phase. This Fe-Mg interdiffusion would produce heavier Fe isotopic compositions and lighter Mg isotopic compositions in the Fe-Ti oxide phase. At the onset of the reaction, the magnitude of Mg isotopic fractionation in the oxide would be greater than that of the Fe isotopic fractionation because the ilmenite begins with a composition that is nearly pure ilmenite ($\mathrm{FeTiO_3}$). Titanium is not being diffusively exchanged in this reaction; therefore there would not be an associated Ti isotopic fractionation. Negative correlations have been previously observed for the measured Fe and Mg isotopic compositions of natural ilmenites sampled from terrestrial mafic intrusions (Chen et al. 2018; Tian et al. 2019). In these studies, the relationship between Fe and Mg isotopic compositions was attributed to diffusive isotopic fractionation involving subsolidus Fe-Mg exchange between ilmenite and silicate minerals. Experimental investigations of the lunar mare basalts have concluded that the generation of high-Ti mare basalt parent magmas involves chemical reaction between a high-Ti component and mafic cumulates (e.g., Van Orman and Grove 2000; Mallik et al. 2019). If Fe-Mg interdiffusion

between ilmenite and olivine-, pyroxene-rich lunar magma ocean cumulates produced the heavy Fe isotopic composition of the high-Ti component in the mare basalt parental melts, then a complementary ultramafic component with a relatively light Fe isotopic composition may also exist in the lunar mantle. Interestingly, the measured iron isotopic compositions of lunar dunite 72415, the sample thought to be most representative of the ultramafic lunar magma ocean cumulates (e.g., Dymek et al. 1975), are consistently the lightest Fe isotopic compositions measured for any lunar sample (δ^{56}Fe$= -0.4 \pm 0.1$‰, Wang et al. 2015; Sossi and Moynier 2017; Poitrasson et al. 2019).

4.6   Conclusions

1. We have experimentally investigated the equilibrium partitioning of Fe and Ti isotopes between ilmenite and melt in order to evaluate the role of ilmenite in generating the isotopic compositional variability among the lunar mare basalts. Our experimentally determined ilmenite-melt isotopic fractionations for Fe and Ti indicate that ilmenite would be isotopically lighter than co-existing melt (Δ^{56}Fe$_{\text{ilmenite-melt}} = -0.05 \pm 0.02$‰ and Δ^{49}Ti$_{\text{ilmenite-melt}} = -0.09 \pm 0.03$‰ at 1100°C).

2. We have incorporated our Fe and Ti ilmenite-melt isotopic fractionations into models of lunar magma ocean crystallization, and in doing so have estimated the Fe and Ti isotopic compositions of the LMO ilmenite cumulates and residual liquid. In a three-component mixing model for the major element and isotopic compositions of mare basalt parent magmas, the Ti isotopic compositions of ilmenites crystallizing from the lunar magma ocean reproduce the Ti isotopic compositional differences between the low- and high-Ti mare basalt suites. However, the difference between the Fe isotopic compositions of the low- and high-Ti basalts cannot be explained by the Fe isotopic composition of the modeled lunar magma ocean ilmenites and residual liquid.

3. The negative correlation between the Fe and Mg isotopic compositions of the low- and high-Ti mare basalts indicates that Fe-Mg interdiffusion has occurred in the Ti-rich component of the mare basalt parental melts. Diffusive exchange of Fe and Mg via subsolidus reaction between ilmenite cumulates and the olivine- and pyroxene-rich lunar mantle at depths less than 280 km can explain the observed correlations between the measured Fe, Ti, and Mg isotopic compositions of the low- and high-Ti mare basalts.

References

Basaltic Volcanism Study Project (1981). *Basaltic Volcanism on the Terrestrial Planets.* Pergamon Press, Inc.

Beaty, D., S. Hill, A. Albee, M.-S. Ma, and R. Schmitt (1979). "The petrology and chemistry of basaltic fragments from the Apollo 11 soil, part I." *Lunar and Planetary Science Conference Proceedings.* Vol. 10, pp. 41–75.

Chappell, B. and D. Green (1973). "Chemical compositions and petrogenetic relationships in Apollo 15 mare basalts." *Earth and Planetary Science Letters* 18 (2), pp. 237–246.

Charlier, B., T. L. Grove, O. Namur, and F. Holtz (2018). "Crystallization of the lunar magma ocean and the primordial mantle-crust differentiation of the Moon." *Geochimica et Cosmochimica Acta* 234, pp. 50–69.

Chen, L.-M., F.-Z. Teng, X.-Y. Song, R.-Z. Hu, S.-Y. Yu, D. Zhu, and J. Kang (2018). "Magnesium isotopic evidence for chemical disequilibrium among cumulus minerals in layered mafic intrusion." *Earth and Planetary Science Letters* 487, pp. 74–83.

Craddock, P. R., N. Dauphas, and R. Clayton (2010). "Mineralogical control on iron isotopic fractionation during lunar differentiation and magmatism." *Lunar and Planetary Science Conference.* Vol. 41, p. 1230.

Craddock, P. R. and N. Dauphas (2011). "Iron Isotopic Compositions of Geologic Reference Materials and Chondrites." *Geostandards and Geoanalytical Research* 35 (1), pp. 101–123.

Dauphas, N., F. Z. Teng, and N. T. Arndt (2010). "Magnesium and iron isotope in 2.7 Ga Alexo komatiites: mantle signatures, no evidence for Soret diffusion, and identification of diffusive transport in zoned olivine." *Geochimica et Cosmochimica Acta* 74 (11), pp. 3274–3291.

Dauphas, N., P. R. Craddock, P. D. Asimow, V. C. Bennett, A. P. Nutman, and D. Ohnenstetter (2009a). "Iron isotopes may reveal the redox conditions of mantle melting from Archean to Present." *Earth and Planetary Science Letters* 288, pp. 255–267.

Dauphas, N., P. E. Janney, R. A. Mendybaev, M. Wadhwa, F. M. Richter, A. M. Davis, M. van Zuilen, R. Hines, and C. N. Foley (2004). "Chromatographic separation and multicollection-ICPMS analysis of iron. Investigating mass-dependent and -independent isotope effects." *Anal Chem* 76 (19), pp. 5855–63. ISSN: 0003-2700 (Print) 0003-2700.

Dauphas, N., A. Pourmand, and F.-Z. Teng (2009b). "Routine isotopic analysis of iron by HR-MC-ICPMS: how precise and how accurate?" *Chemical Geology* 267, pp. 175–184.

Dauphas, N., M. Roskosz, E. E. Alp, D. Golden, C. K. Sio, F. L. Tissot, M. Y. Hu, J. Zhao, L. Gao, and R. Morris (2012). "A general moment NRIXS approach to the determination of equilibrium Fe isotopic fractionation factors: Application to goethite and jarosite." *Geochimica et Cosmochimica Acta* 94, pp. 254–275.

Dauphas, N., M. Roskosz, E. E. Alp, D. Neuville, M. Y. Hu, C. K. Sio, F. L. Tissot, J. Zhao, L. Tissandier, E. Médard, and C. Cordier (2014). "Magma redox and structural controls on iron isotope variations in Earth's mantle and crust." *Earth and Planetary Science Letters* 398, pp. 127–140.

Dauphas, N. and O. Rouxel (2006). "Mass spectrometry and natural variations of iron isotopes." *Mass Spectrom Rev* 25 (4), pp. 515–50. ISSN: 0277-7037 (Print) 0277-7037.

Delano, J. W. (1986). "Pristine Lunar Glasses: Criteria, Data, and Implications." *Journal of Geophysical Research* 91 (B4), pp. D201–D213.

Deng, Z., M. Chaussidon, P. Savage, F. Robert, R. Pik, and F. Moynier (2019). "Titanium isotopes as a tracer for the plume or island arc affinity of felsic rocks." *Proceedings of the National Academy of Sciences* 116 (4), pp. 1132–1135.

Dickinson, T., G. Taylor, K. Keil, R. A. Schmitt, S. Hughes, and M. Smith (1985). "Apollo 14 aluminous mare basalts and their possible relationship to KREEP." *Journal of Geophysical Research: Solid Earth* 90 (S02), pp. C365–C374.

Donovan, J. J., J. W. Singer, and J. T. Armstrong (2016). "A new EPMA method for fast trace element analysis in simple matrices." *American Mineralogist* 101 (8), pp. 1839–1853.

Dymek, R. F., A. L. Albee, and A. A. Chodos (1975). "Comparative petrology of lunar cumulate rocks of possible primary origin: Dunite 72415, troctolite 76535, norite 78235, and anorthosite 62237." *Proceedings of the Lunar Science Conference 6th*, pp. 301–341.

Elardo, S. M., D. S. Draper, and C. K. Shearer Jr (2011). "Lunar Magma Ocean crystallization revisited: Bulk composition, early cumulate mineralogy, and the source regions of the highlands Mg-suite." *Geochimica et Cosmochimica Acta* 75 (11), pp. 3024–3045.

Elkins-Tanton, L. T., S. Burgess, and Q.-Z. Yin (2011). "The lunar magma ocean: Reconciling the solidification process with lunar petrology and geochronology." *Earth and Planetary Science Letters* 304 (3-4), pp. 326–336.

Greber, N. D., N. Dauphas, I. S. Puchtel, B. A. Hofmann, and N. T. Arndt (2017). "Titanium stable isotopic variations in chondrites, achondrites and lunar rocks." *Geochimica et cosmochimica acta* 213, pp. 534–552.

Green, D., A. Ringwood, N. Ware, W. Hibberson, A. Major, and E. Kiss (1971). "Experimental petrology and petrogenesis of Apollo 12 basalts." *Lunar and Planetary Science Conference Proceedings.* Vol. 2, p. 601.

Grove, T. and D. Beaty (1980). "Classification, experimental petrology and possible volcanic histories of the Apollo 11 high-K basalts." *Lunar and Planetary Science Conference Proceedings.* Vol. 11, pp. 149–177.

Hammer, J. E. (2006). "Influence of f_{O_2} and cooling rate on the kinetics and energetics of Fe-rich basalt crystallization." *Earth and Planetary Science Letters* 248 (3-4), pp. 618–637.

Hess, P. C. and E. Parmentier (1995). "A model for the thermal and chemical evolution of the Moon's interior: Implications for the onset of mare volcanism." *Earth and Planetary Science Letters* 134 (3-4), pp. 501–514.

Johannes, W., P. Bell, H. Mao, A. Boettcher, D. Chipman, J. Hays, R. Newton, and F. Seifert (1971). "An interlaboratory comparison of piston-cylinder pressure calibration using the albite-breakdown reaction." *Contributions to Mineralogy and Petrology* 32 (1), pp. 24–38.

Johnson, A. C., S. M. Aarons, N. Dauphas, N. X. Nie, H. Zeng, R. T. Helz, S. J. Romaniello, and A. D. Anbar (2019). "Titanium isotopic fractionation in Kilauea Iki lava lake driven by oxide crystallization." *Geochimica et Cosmochimica Acta* 264, pp. 180–190.

Li, H., N. Zhang, Y. Liang, B. Wu, N. J. Dygert, J. Huang, and E. Parmentier (2019). "Lunar cumulate mantle overturn: A model constrained by ilmenite rheology." *Journal of Geophysical Research: Planets* 124 (5), pp. 1357–1378.

Lin, Y., H. Hui, X. Xia, S. Shang, and W. van Westrenen (2019). "Experimental constraints on the solidification of a hydrous lunar magma ocean." *Meteoritics & Planetary Science.*

Lin, Y., E. J. Tronche, E. S. Steenstra, and W. van Westrenen (2017a). "Evidence for an early wet Moon from experimental crystallization of the lunar magma ocean." *Nature Geoscience* 10 (1), pp. 14–18.

Lin, Y., E. J. Tronche, E. S. Steenstra, and W. van Westrenen (2017b). "Experimental constraints on the solidification of a nominally dry lunar magma ocean." *Earth and Planetary Science Letters* 471, pp. 104–116.

Liu, J., N. Dauphas, M. Roskosz, M. Y. Hu, H. Yang, W. Bi, J. Zhao, E. E. Alp, J. Y. Hu, and J.-F. Lin (2017). "Iron isotopic fractionation between silicate mantle and metallic core at high pressure." *Nat Commun* 8, p. 14377. ISSN: 2041-1723.

Liu, Y., M. J. Spicuzza, P. R. Craddock, J. M. Day, J. W. Valley, N. Dauphas, and L. A. Taylor (2010). "Oxygen and iron isotope constraints on near-surface fractionation effects and the composition of lunar mare basalt source regions." *Geochimica et Cosmochimica Acta* 74, pp. 6249–6262.

Mallik, A., T. Ejaz, S. Shcheka, and G. Garapic (2019). "A petrologic study on the effect of mantle overturn: Implications for evolution of the lunar interior." *Geochimica et Cosmochimica Acta* 250, pp. 238–250.

Médard, E., C. A. McCammon, J. A. Barr, and T. L. Grove (2008). "Oxygen fugacity, temperature reproducibility, and H_2O contents of nominally anhydrous piston-cylinder experiments using graphite capsules." *American Mineralogist* 93 (11-12), pp. 1838–1844.

Meyer, C. (2005). "Lunar sample compendium."

Millet, M., N. Dauphas, N. D. Greber, K. Burton, C. Dale, B. Debret, C. Macpherson, G. Nowell, and H. M. Williams (2016). "Titanium stable isotope investigation of magmatic processes on the Earth and Moon." *Earth and Planetary Science Letters* 449, pp. 197–205.

Millet, M.-A. and N. Dauphas (2014). "Ultra-precise titanium stable isotope measurements by double-spike high resolution MC-ICP-MS." *Journal of Analytical Atomic Spectrometry* 29 (8), pp. 1444–1458.

Murali, A., M.-S. Ma, J. Laul, and R. Schmitt (1977). "Chemical Composition of Breccias, Feldspathic Basalt and Anorthosites from Apollo 15 (15308, 15359, 15382 and 15362), Apollo 16 (60618 and 65785), Apollo 17 (72435, 72536, 72559, 72735, 72738, 78526 and 78527), and Luna 20 (22012 and 22013)." *Lunar and Planetary Science Conference*. Vol. 8.

Neal, C. R., L. A. Taylor, S. S. Hughes, and R. A. Schmitt (1990). "The significance of fractional crystallization in the petrogenesis of Apollo 17 Type A and B high-Ti basalts." *Geochimica et Cosmochimica Acta* 54 (6), pp. 1817–1833.

Neal, C. R., L. A. Taylor, and M. M. Lindstrom (1988). "Apollo 14 mare basalt petrogenesis-Assimilation of KREEP-like components by a fractionating magma." *Lunar and Planetary Science Conference Proceedings*. Vol. 18, pp. 139–153.

Poitrasson, F. (2007). "Does planetary differentiation really fractionate iron isotopes?" *Earth and Planetary Science Letters* 256 (3-4), pp. 484–492.

Poitrasson, F., A. N. Halliday, D.-C. Lee, S. Levasseur, and N. Teutsch (2004). "Iron isotope differences between Earth, Moon, Mars and Vesta as possible records of contrasted accretion mechanisms." *Earth and Planetary Science Letters* 223, pp. 253–266.

Poitrasson, F., T. Zambardi, T. Magna, and C. R. Neal (2019). "A reassessment of the iron isotope composition of the Moon and its implications for the accretion and differentiation of terrestrial planets." *Geochimica et Cosmochimica Acta* 267, pp. 257–274.

Prissel, K. B., M. J. Krawczynski, N. X. Nie, N. Dauphas, H. Couvy, M. Y. Hu, E. E. Alp, and M. Roskosz (2018). "Experimentally determined effects of olivine crystallization and melt titanium content on iron isotopic fractionation in planetary basalts." *Geochimica et Cosmochimica Acta* 238, pp. 580–598.

Rapp, J. and D. Draper (2018). "Fractional crystallization of the lunar magma ocean: Updating the dominant paradigm." *Meteoritics & Planetary Science* 53 (7), pp. 1432–1455.

Sedaghatpour, F. and S. B. Jacobsen (2019). "Magnesium stable isotopes support the lunar magma ocean cumulate remelting model for mare basalts." *Proceedings of the National Academy of Sciences* 116 (1), pp. 73–78.

Sedaghatpour, F., F.-Z. Teng, Y. Liu, D. Sears, and L. A. Taylor (2013). "Magnesium isotopic composition of the Moon." *Geochimica et Cosmochimica Acta* 120, pp. 1–16.

Shervais, J. W., L. A. Taylor, and M. M. Lindstrom (1985). "Apollo 14 mare basalts: Petrology and geochemistry of clasts from consortium breccia 14321." *Journal of Geophysical Research: Solid Earth* 90 (S02), pp. C375–C395.

Snyder, G. A., L. A. Taylor, and C. R. Neal (1992). "A chemical model for generating the sources of mare basalts: Combined equilibrium and fractional crystallization of the lunar magmasphere." *Geochimica et Cosmochimica Acta* 56 (10), pp. 3809–3823.

Sossi, P. A. and F. Moynier (2017). "Chemical and isotopic kinship of iron in the Earth and Moon deduced from the lunar Mg-Suite." *Earth and Planetary Science Letters* 471, pp. 125–135.

Sossi, P. A. and H. S. C. O'Neill (2017). "The effect of bonding environment on iron isotope fractionation between minerals at high temperature." *Geochimica et Cosmochimica Acta* 196, pp. 121–143.

Teng, F.-Z., N. Dauphas, and R. T. Helz (2008). "Iron Isotope Fractionation During Magmatic Differentiation in Kilauea Iki Lava Lake." *Science* 320, pp. 1620–1622.

Teng, F.-Z., N. Dauphas, R. T. Helz, S. Gao, and S. Huang (2011). "Diffusion-driven magnesium and iron isotope fractionation in Hawaiian olivine." *Earth and Planetary Science Letters* 308, pp. 317–324.

Teng, F.-Z., W.-Y. Li, S. Ke, B. Marty, N. Dauphas, S. Huang, F.-Y. Wu, and A. Pourmand (2010). "Magnesium isotopic composition of the Earth and chondrites." *Geochimica et Cosmochimica Acta* 74 (14), pp. 4150–4166.

Thacker, C., Y. Liang, Q. Peng, and P. Hess (2009). "The stability and major element partitioning of ilmenite and armalcolite during lunar cumulate mantle overturn." *Geochimica et Cosmochimica Acta* 73 (3), pp. 820–836.

Tian, H.-C., C. Zhang, F.-Z. Teng, Y.-J. Long, S.-G. Li, Y. He, S. Ke, X.-Y. Chen, and W. Yang (2019). "Diffusion-driven extreme Mg and Fe isotope fractionation in Panzhihua ilmenite: Implications for the origin of mafic intrusion." *Geochimica et Cosmochimica Acta*.

Tormey, D., T. Grove, and W. Bryan (1987). "Experimental petrology of normal MORB near the Kane Fracture Zone: 22–25 N, mid-Atlantic ridge." *Contributions to Mineralogy and Petrology* 96 (2), pp. 121–139.

Van Orman, J. A. and T. L. Grove (2000). "Origin of lunar high-titanium ultramafic glasses: Constraints from phase relations and dissolution kinetics of clinopyroxene-ilmenite cumulates." *Meteoritics & Planetary Science* 35 (4), pp. 783–794.

Van Orman, J. A. and M. J. Krawczynski (2015). "Theoretical constraints on the isotope effect for diffusion in minerals." *Geochimica et Cosmochimica Acta* 164, pp. 365–381.

Vander Kaaden, K. E., C. B. Agee, and F. M. McCubbin (2015). "Density and compressibility of the molten lunar picritic glasses: Implications for the roles of Ti and Fe in the structures of silicate melts." *Geochimica et Cosmochimica Acta* 149, pp. 1–20.

Vaniman, D. and J. Papike (1980). "Lunar highland melt rocks-Chemistry, petrology and silicate mineralogy." *Lunar Highlands Crust*, pp. 271–337.

Wagner, T. and T. Grove (1997). "Experimental constraints on the origin of lunar high-Ti ultramafic glasses." *Geochimica et Cosmochimica Acta* 61 (6), pp. 1315–1327.

Walker, D., J. Longhi, E. M. Stolper, T. L. Grove, and J. F. Hays (1975). "Origin of titaniferous lunar basalts." *Geochimica et Cosmochimica Acta* 39 (9), pp. 1219–1235.

Wang, K., S. B. Jacobsen, F. Sedaghatpour, H. Chen, and R. L. Korotev (2015). "The earliest Lunar Magma Ocean differentiation recorded in Fe isotopes." *Earth and Planetary Science Letters* 430, pp. 202–208.

Wang, W., S. Huang, F. Huang, X. Zhao, and Z. Wu (2020). "Equilibrium inter-mineral titanium isotope fractionation: Implication for high-temperature titanium isotope geochemistry." *Geochimica et Cosmochimica Acta* 269, pp. 540–553.

Warner, R. D., G. J. Taylor, G. H. Conrad, H. R. Northrop, S. Barker, K. Keil, M.-S. Ma, and R. Schmitt (1979). "Apollo 17 high-Ti mare basalts-New bulk compositional data, magma types, and petrogenesis." *Lunar and Planetary Science Conference Proceedings*. Vol. 10, pp. 225–247.

Watson, E., D. Wark, J. Price, and J. Van Orman (2002). "Mapping the thermal structure of solid-media pressure assemblies." *Contributions to Mineralogy and Petrology* 142 (6), pp. 640–652.

Weyer, S., A. D. Anbar, G. P. Brey, C. Münker, K. Mezger, and A. B. Woodland (2005). "Iron isotope fractionation during planetary differentiation." *Earth and Planetary Science Letters* 240, pp. 251–264.

Wiesli, R. A., B. L. Beard, L. A. Taylor, and C. M. Johnson (2003). "Space weathering processes on airless bodies: Fe isotope fractionation in the lunar regolith." *Earth and Planetary Science Letters* 216, pp. 457–465.

Zhao, Y., J. De Vries, A. van den Berg, M. Jacobs, and W. van Westrenen (2019). "The participation of ilmenite-bearing cumulates in lunar mantle overturn." *Earth and Planetary Science Letters* 511, pp. 1–11.

Appendix A

Appendix to Chapter 2

Compiled electron microprobe data for all diffusion couple experiments   The electron microprobe analyses for each experiment are available as an electronic file ("compiled-probe-data.xlsx") in the online repository at espm.wustl.edu/data. This file contains the electron microprobe and position data for each traverse used to calculate the Fe-Mg (or Fe-Mn) interdiffusivity reported for each experiment. There is a tab for each experiment, labeled with the experiment name. Additionally, the Fe-Mn interdiffusion experiments include "(Mn)" on the tab after the experiment name.

On the spreadsheet for each tab are the analytical results from different traverses labeled "line 1", "line 2", etc. The analyses are reported as element weight percent (wt.%) excluding oxygen, and the analytical totals are reported in the "Total" column for each line. Entries labeled "b.d." indicate that the measured composition was below detection limit. These reported analyses have already been filtered to exclude analyses where the analytical totals were less than 98.5 wt.% or greater than 101.5 wt.%, as well as analyses where the cation total for 3 oxygen atoms were less than 1.98 or greater than 2.02 (ideal ilmenite stoichiometry contains 2 cations

per 3 oxygen atoms). In cases where the aforementioned wt.% total threshold eliminated a majority of the analyses for at least one side of the diffusion couple, this threshold was slightly expanded. For experiment F053, analytical totals greater than 98.0 wt.% and less than 102.0 wt.% were included. For experiment F086, analytical totals greater than 98.0 wt.% were included. For experiment F119, line 1 includes analytical totals < 104.0 wt.% and line 2 includes analytical totals < 106.0 wt.% (unlike F119 line 3, these lines were positioned close to the edges of the geikielite crystal and this likely affected the analytical totals). Two experiments, F045 and F051, have significantly low analytical totals. For F051, totals greater than 95.0 wt.% were included. For F045, totals greater than 94.0 wt.% were included. The low analytical totals for these experiments reflect a minor Fe^{3+} component in the ilmenite sides of the diffusion couples.

Accompanying the element wt.% data for each profile is the "relative distance from interface (μm)" column. This reports the relative distance (one side negative, one side positive) from the diffusion interface after corrections have been applied for any gap between the two sides of the diffusion couple and decompression cracks.

For the diffusion profile fitting, each wt.% element was converted to moles of that element, and then the mole fraction for each element was determined by dividing the moles of an element by the sum of the moles of Fe, Mg, Mn (if included), and Ti. The mole fraction for Fe (or Mn) and the values reported for the distance from the interface were then used for the diffusion profile fits.

In a few cases, data for only one side of the couple has been reported because there was an issue in fitting the profile taken on the unreported side. For traverses F053 line 2, F053 line 3, and F030 line 2, the ilmenite polycrystal material near the diffusion interface plucked during polishing, and thus the analytical profile did not fully capture the change in composition

[152]

near the interface. The line 1 analyses of the Mn-bearing ilmenite side in experiment F028 were affected by the presence of ulvöspinel. For experiment F117, the geikielite side of the diffusion couple was not fully recovered from the experiment capsule.

Table A.1: Experimental run conditions for ilmenite polycrystal syntheses.

Experiment	Starting Material[a]	T (°C)	P (kbar)	Time (s)	Fe[b]	Assembly[c]
F007	#001	1165	17.5	257640	Fe metal + Fe_2O_3	MgO sleeve
F011	#007	1165	17.5	339840	Fe metal + Fe_2O_3	pyrophyllite sleeve
F012	#007	1165	17.5	260340	Fe metal + Fe_2O_3	pyrophyllite sleeve
F022	#007	1165	17.5	252840	Fe metal + Fe_2O_3	MgO sleeve
F023	#019 (Mn)	1165	17.5	423180	Fe metal + Fe_2O_3	MgO sleeve
F026	#022 (Mn)	1140	15.0	269220	FeO	MgO sleeve
F027	#021	1140	15.0	329040	FeO	pyrophyllite sleeve
D007	#021	1140	15.0	254340	FeO	pyrophyllite sleeve
D008	#022 (Mn)	1140	15.0	238920	FeO	MgO sleeve
D009	#021	1140	15.0	427920	FeO	MgO sleeve
F041	#021	1140	15.0	247200	FeO	MgO sleeve
F043	#021	1140	15.0	263160	FeO	MgO sleeve
F044	#021	1140	15.0	258720	FeO	MgO sleeve
F049	#021	1140	15.0	255660	FeO	MgO sleeve
F055	#021	1140	15.0	323340	FeO	MgO sleeve
F112	#021	1140	15.0	252660	FeO	MgO sleeve
F116	#021	1140	15.0	261240	FeO	MgO sleeve
MK22	MK_mix	1125	17.5	334680	FeO	MgO sleeve

[a] The "Starting Material" column identifies the powdered mixture used for the synthesis, and Mn-bearing ilmenite mixtures are denoted with "(Mn)".

[b] The "Fe" column indicates whether Fe was added to the starting material as a mixture of Fe metal and Fe_2O_3 or as all FeO.

[c] The "Assembly" column indicates the sleeve material used to hold the graphite capsule (either MgO or pyrophyllite).
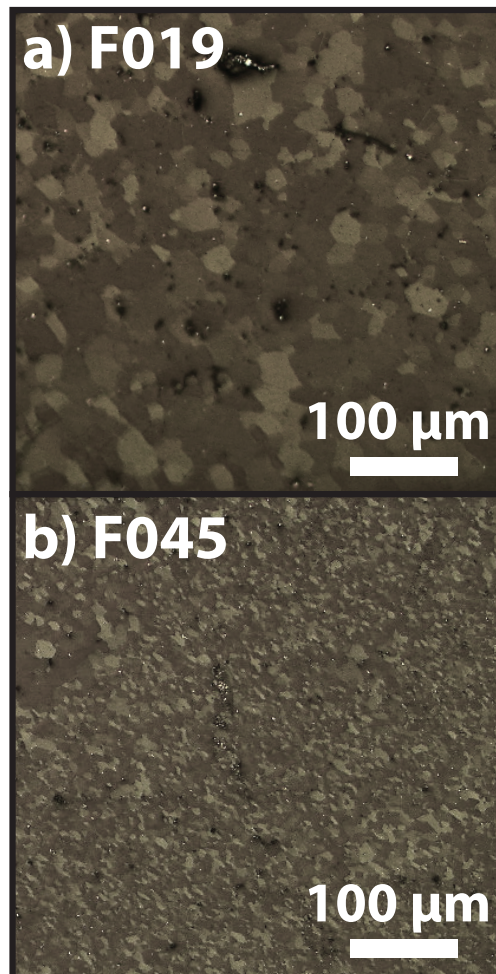
Figure A.1: Cross-polarized reflected light images of two ilmenite polycrystals from diffusion annealing experiments conducted at 1000°C. The grain size of the ilmenite polycrystal in experiment F019 (a) is an order of magnitude larger than that in experiment F045 (b). Despite the difference in grain size, the calculated Fe-Mg interdiffusion coefficients for the two experiments are the same within uncertainty, suggesting grain boundary diffusion did not significantly contribute to the observed cation diffusion.
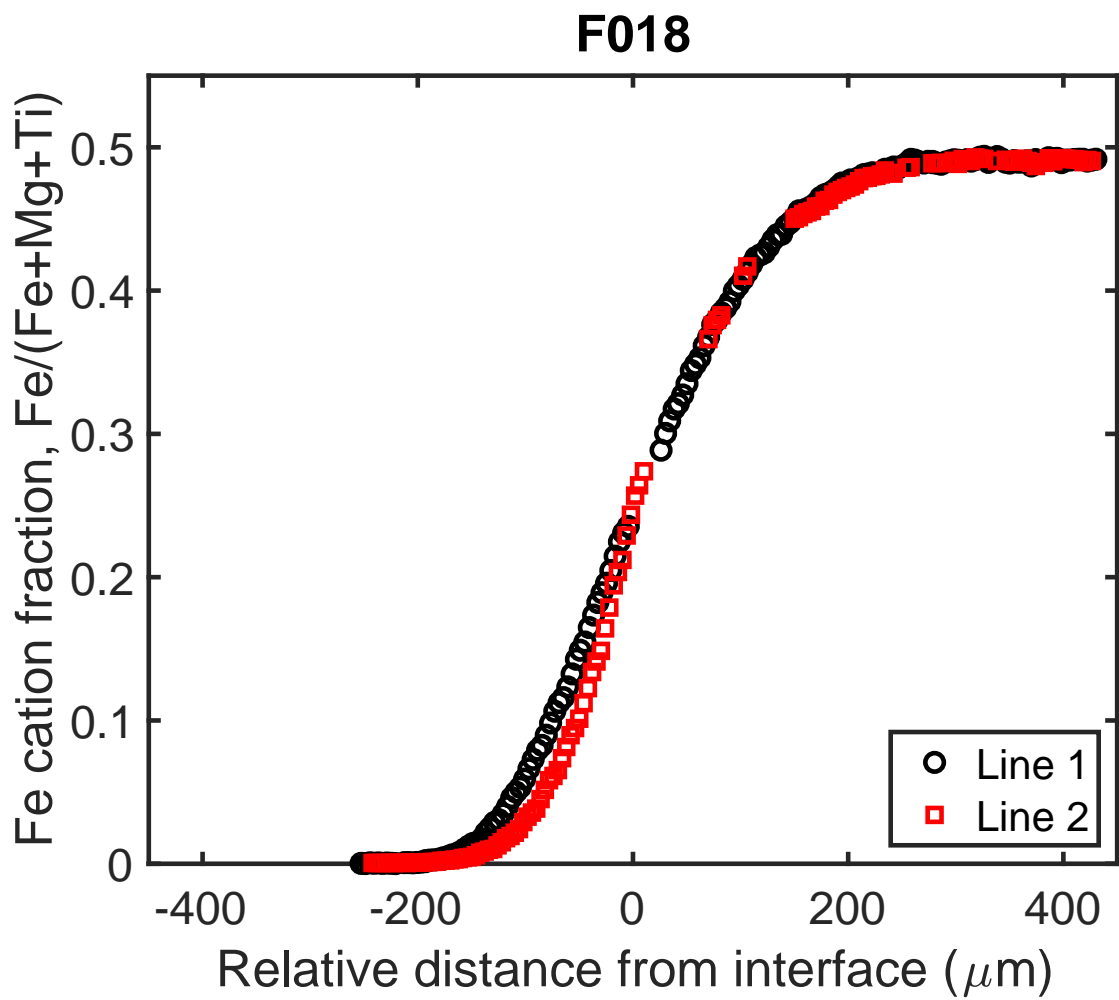
Figure A.2: Electron microprobe analyses of experiment F018.
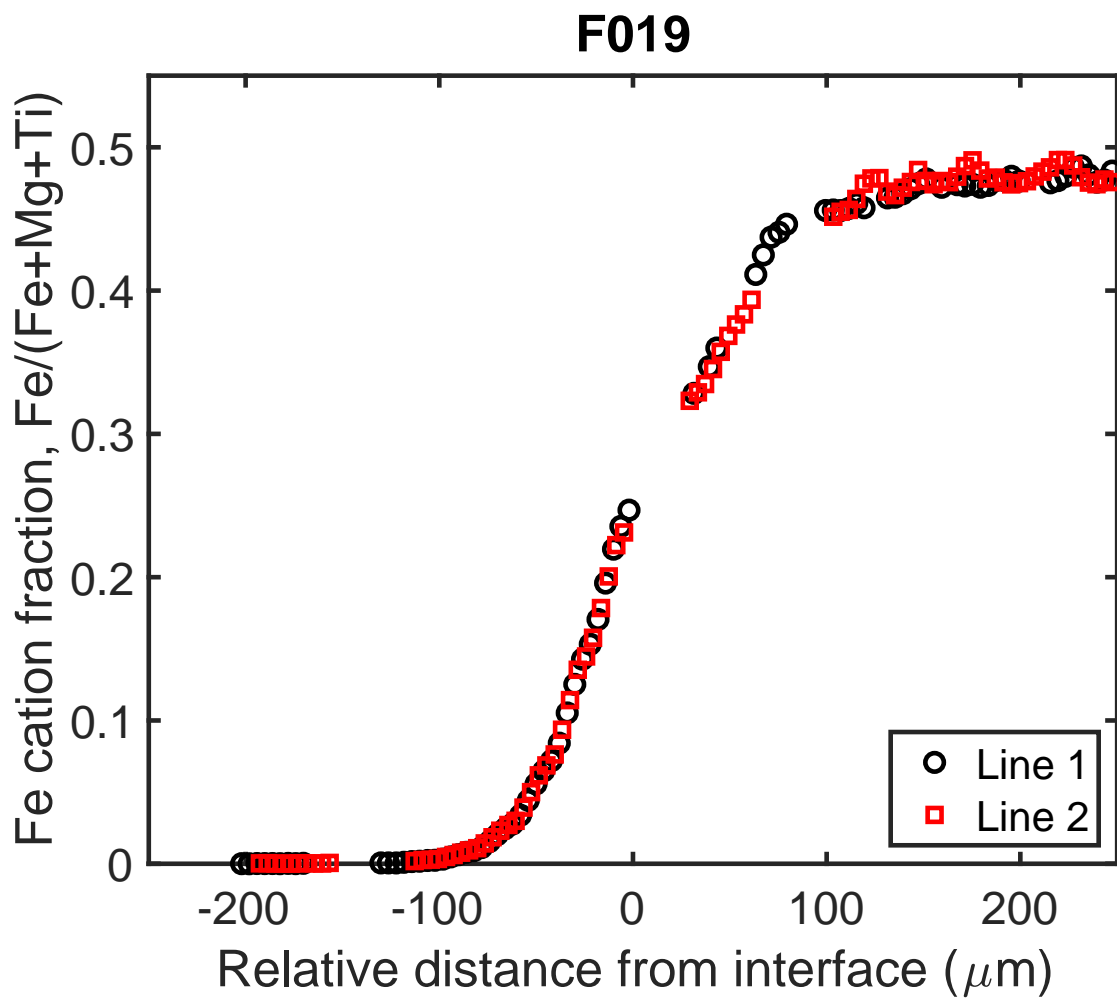
Figure A.3: Electron microprobe analyses of experiment F019.
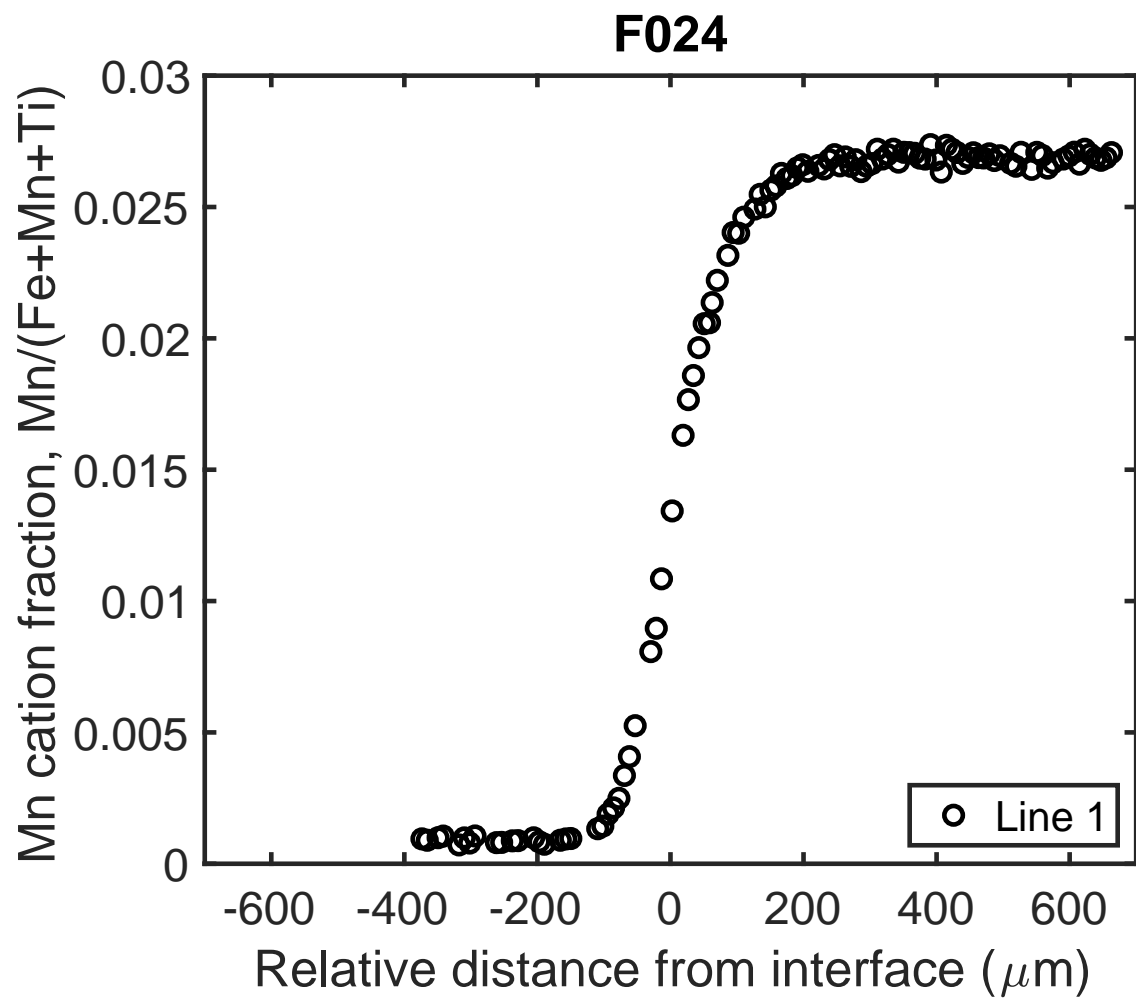
Figure A.4: Electron microprobe analyses of experiment F024.
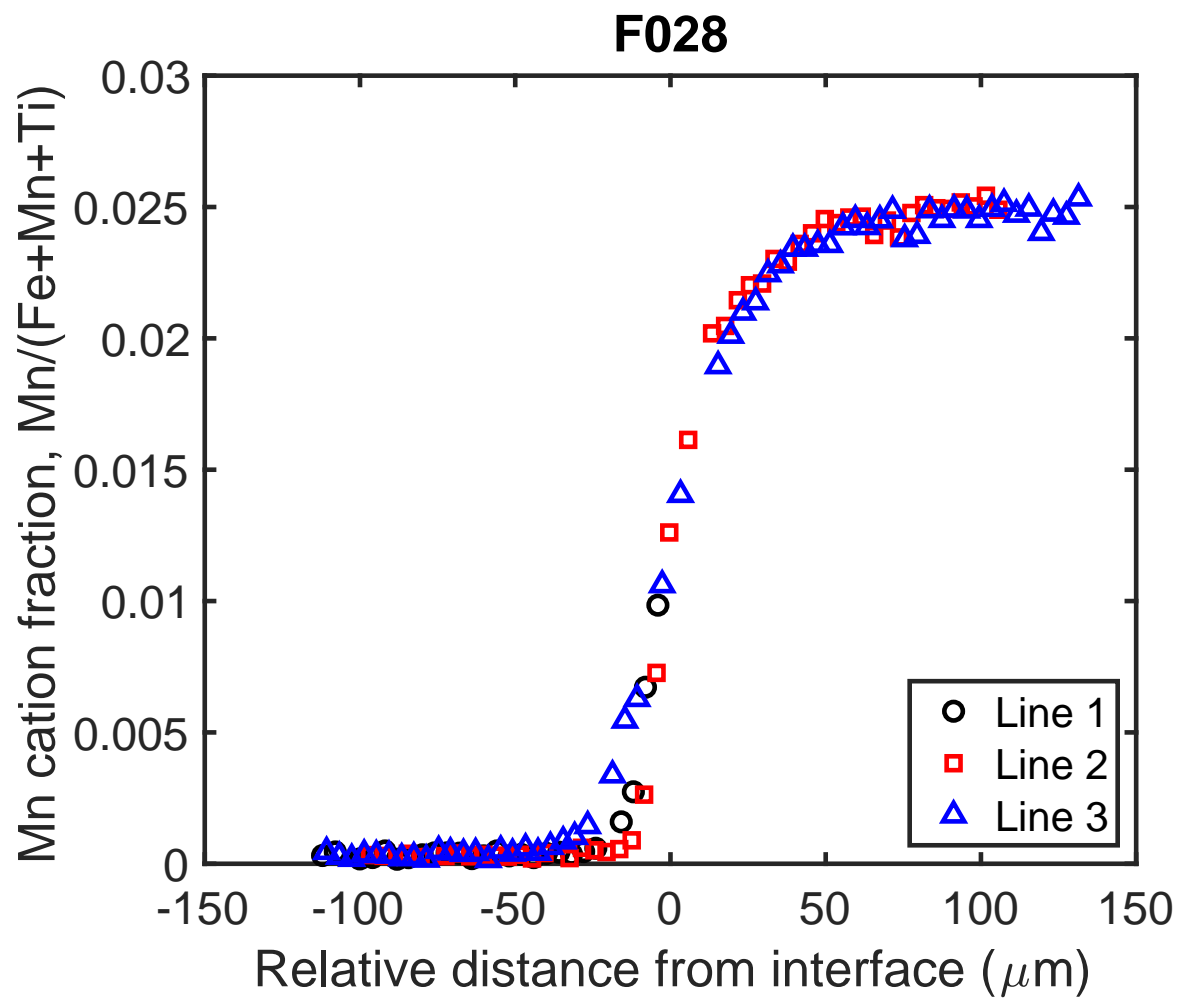
Figure A.5: Electron microprobe analyses of experiment F028.
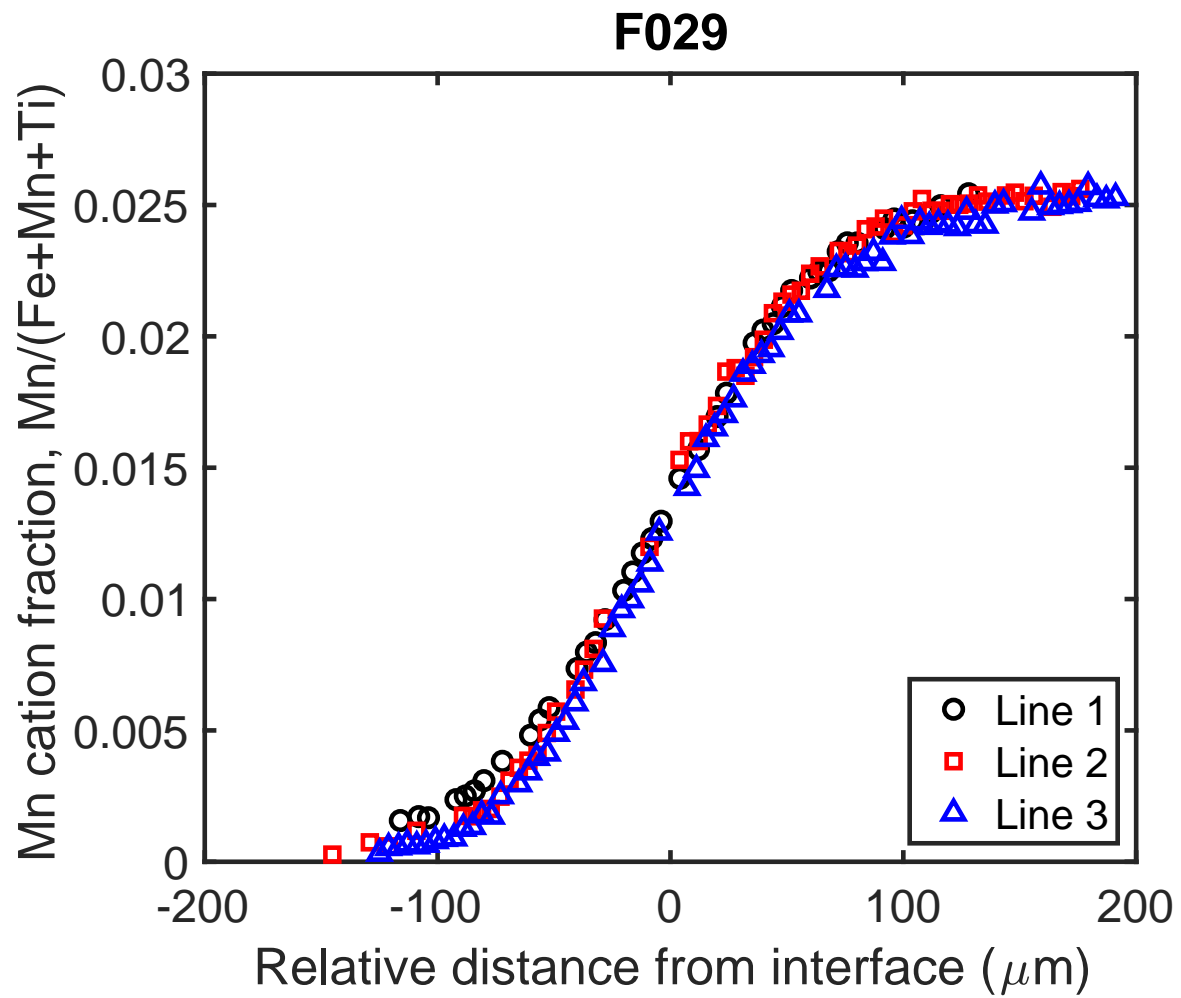
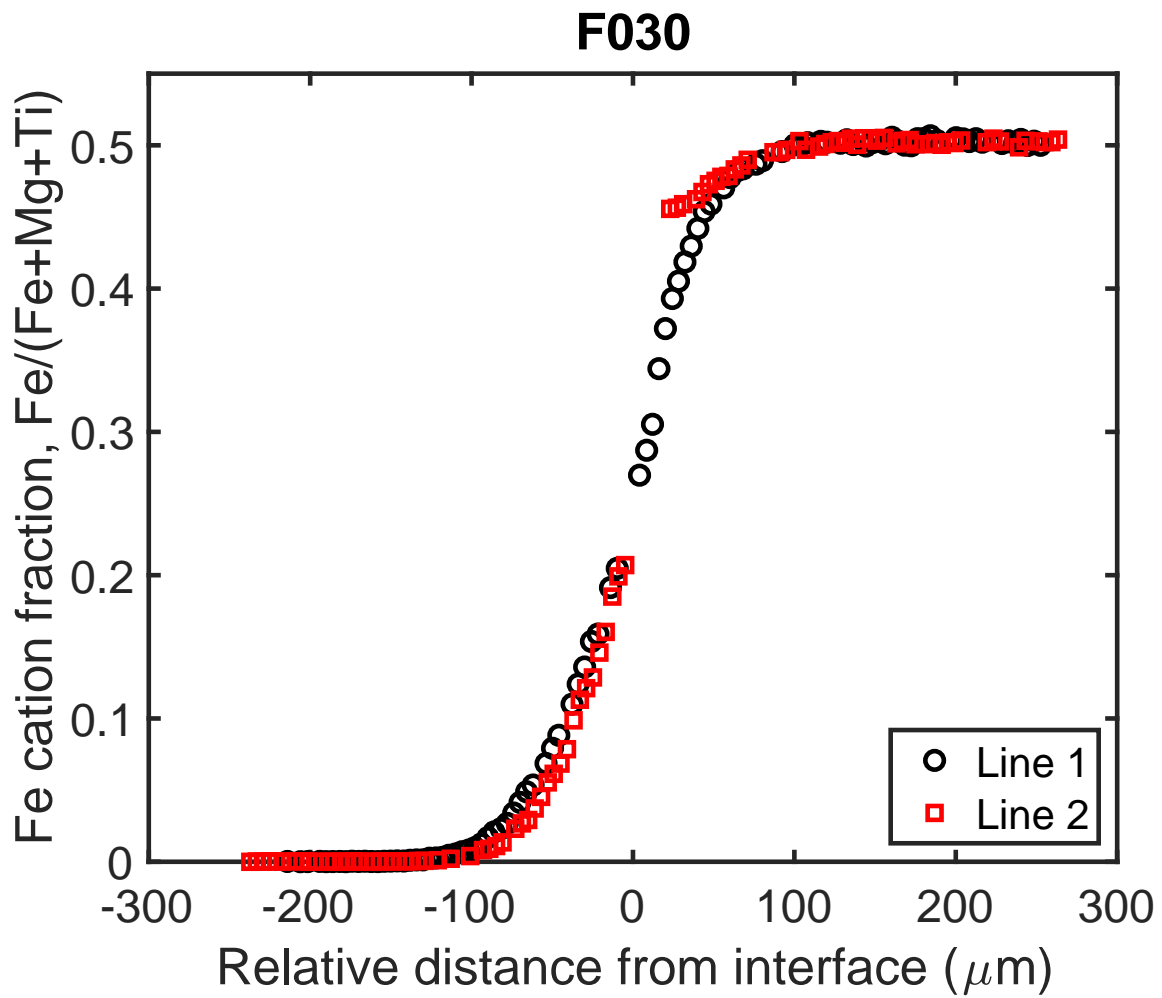Figure A.6: Electron microprobe analyses of experiment F029.

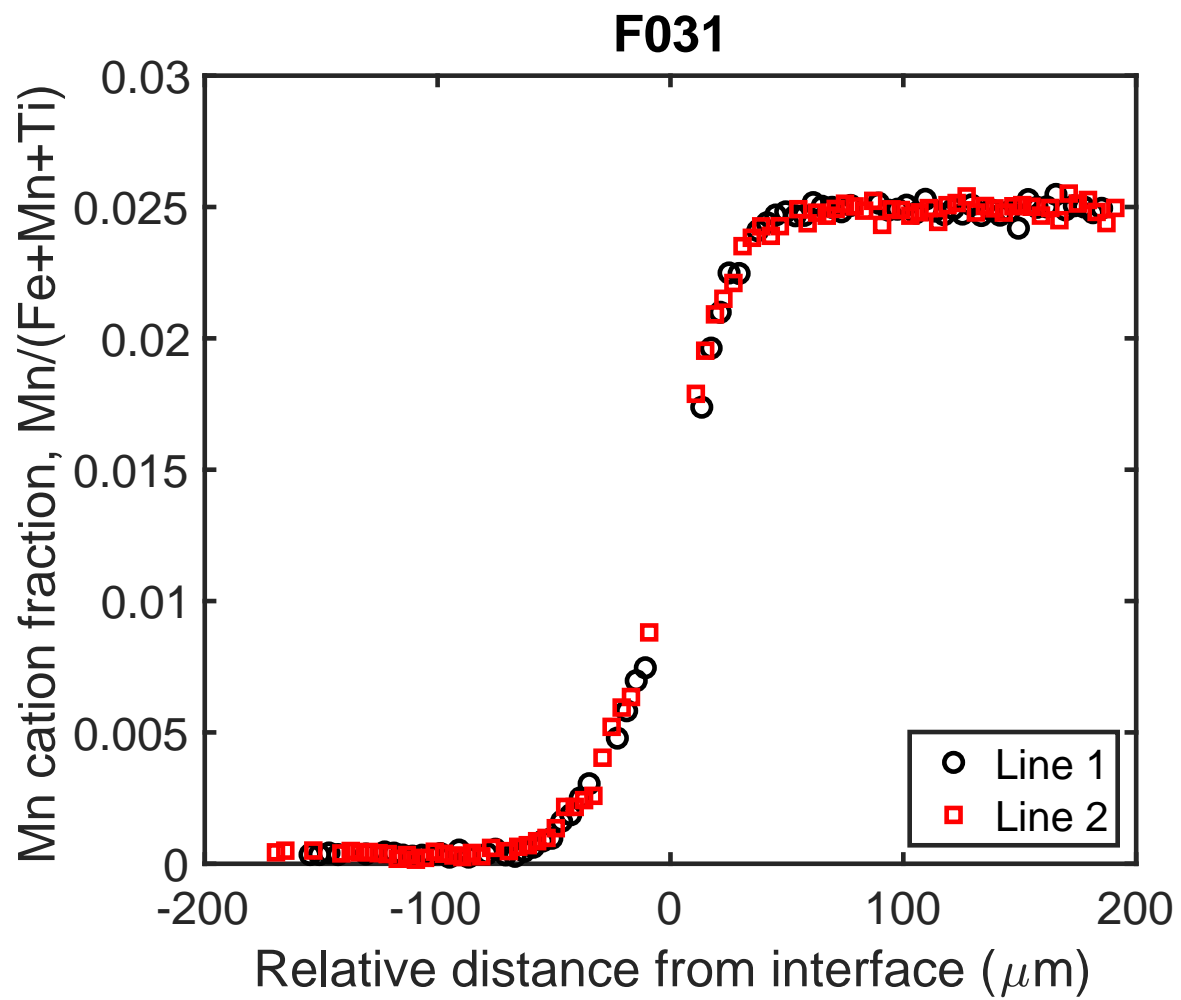Figure A.7: Electron microprobe analyses of experiment F030.

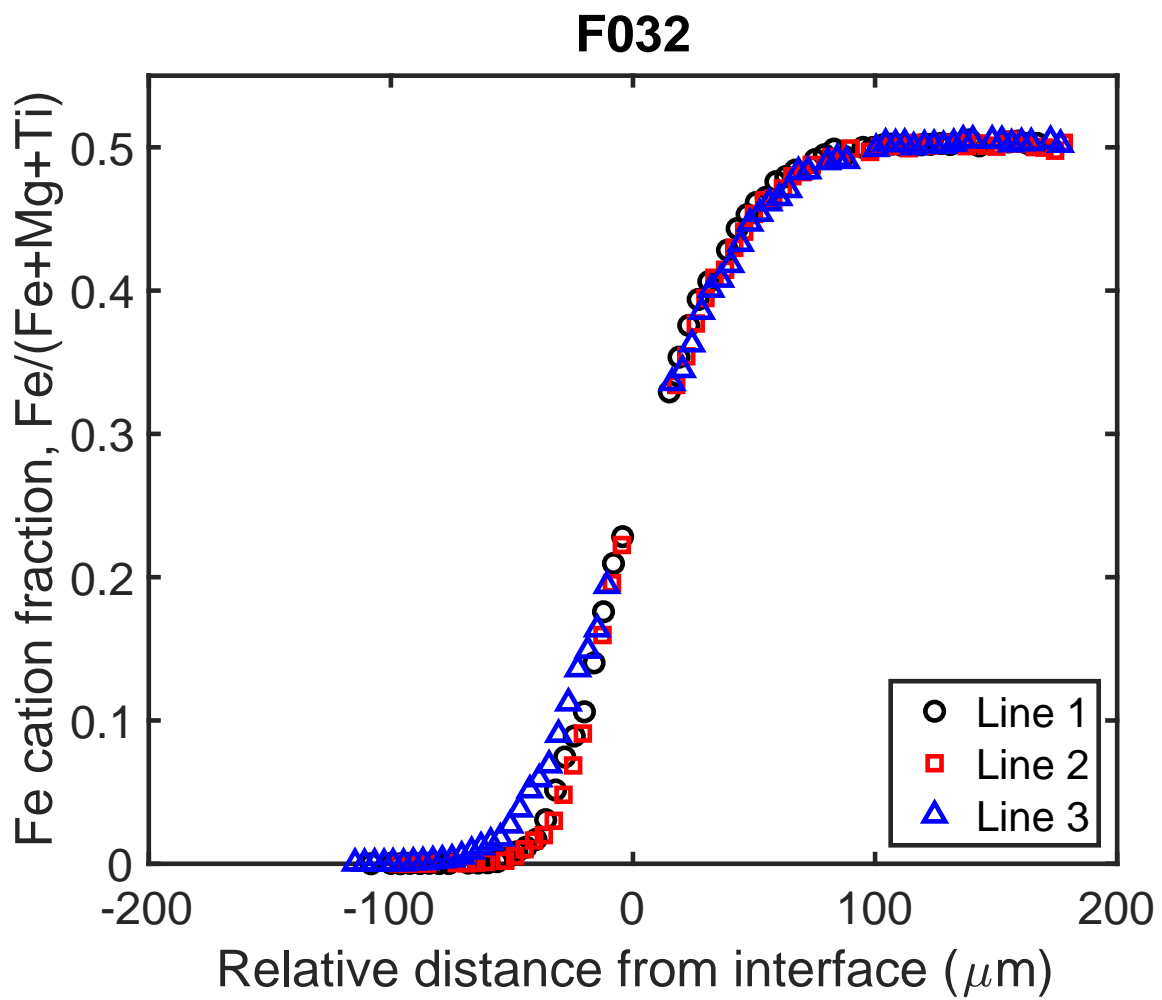Figure A.8: Electron microprobe analyses of experiment F031.

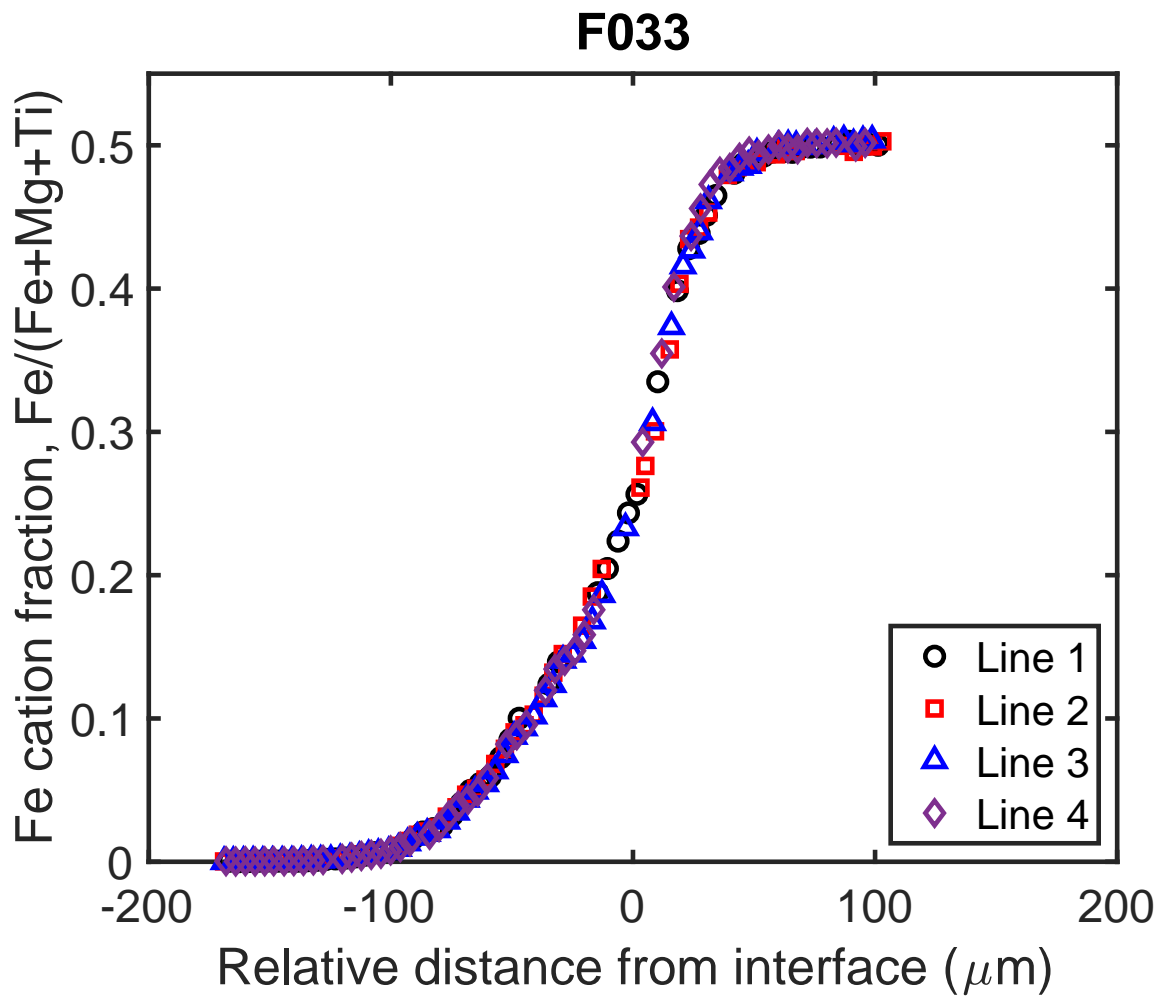Figure A.9: Electron microprobe analyses of experiment F032.

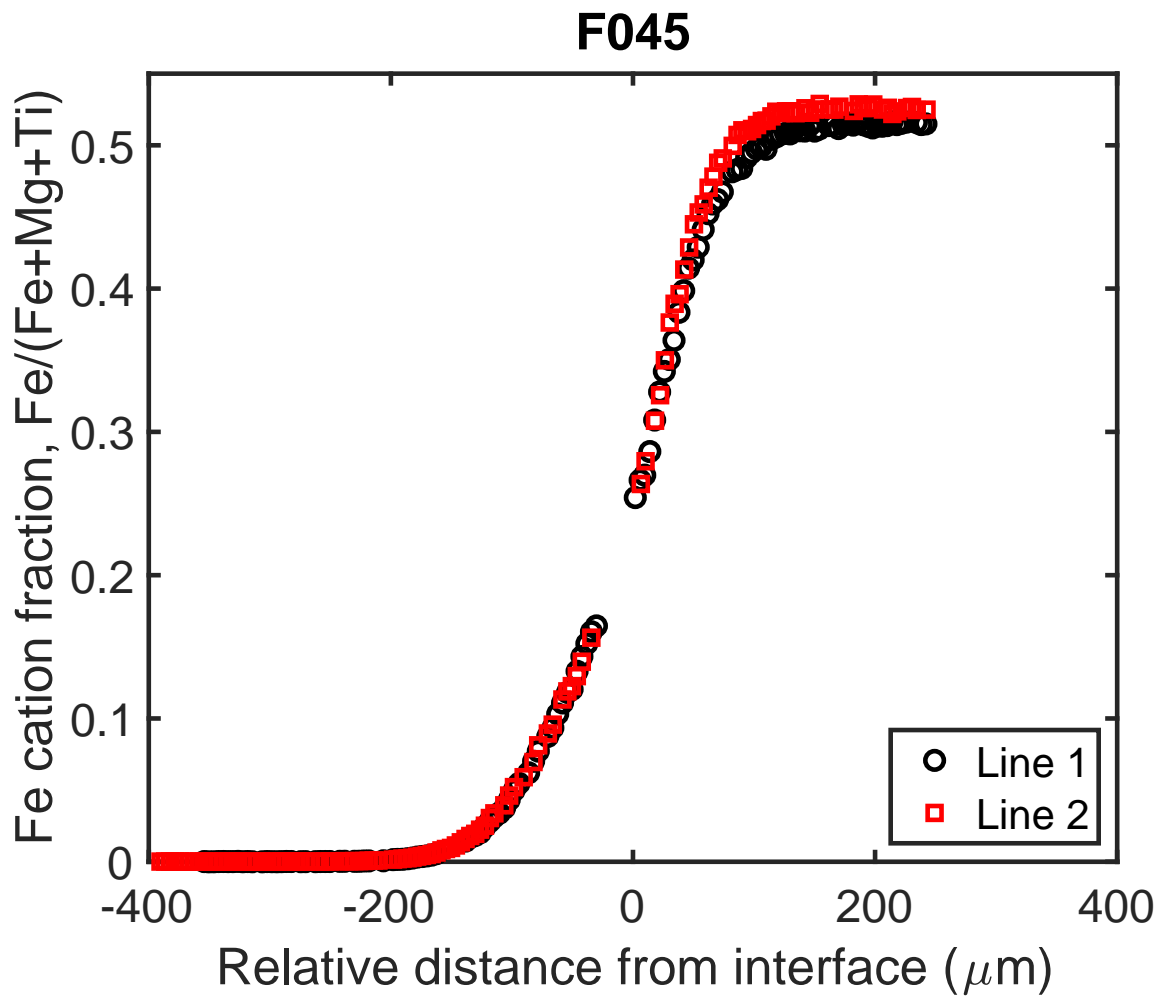Figure A.10: Electron microprobe analyses of experiment F033.

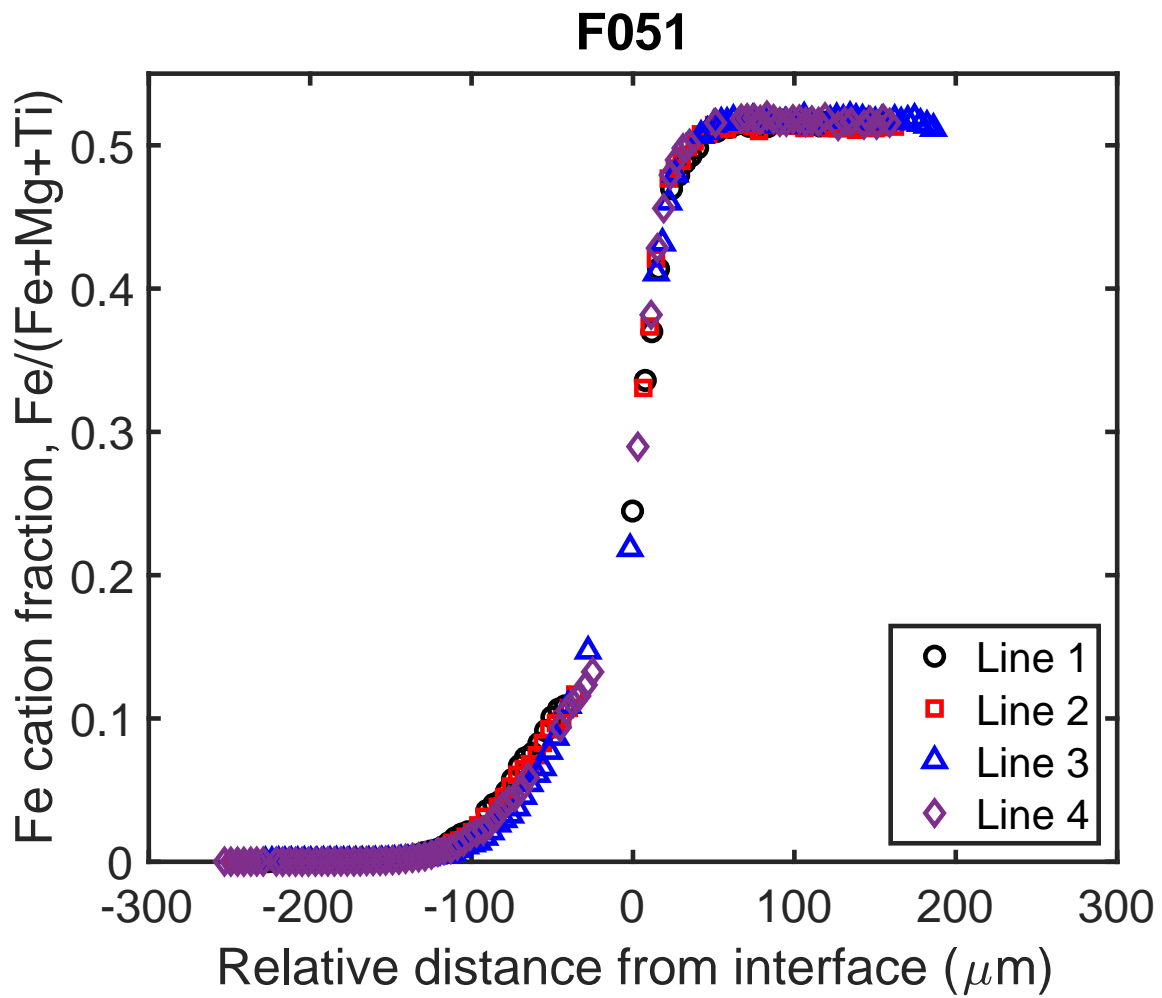Figure A.11: Electron microprobe analyses of experiment F045.

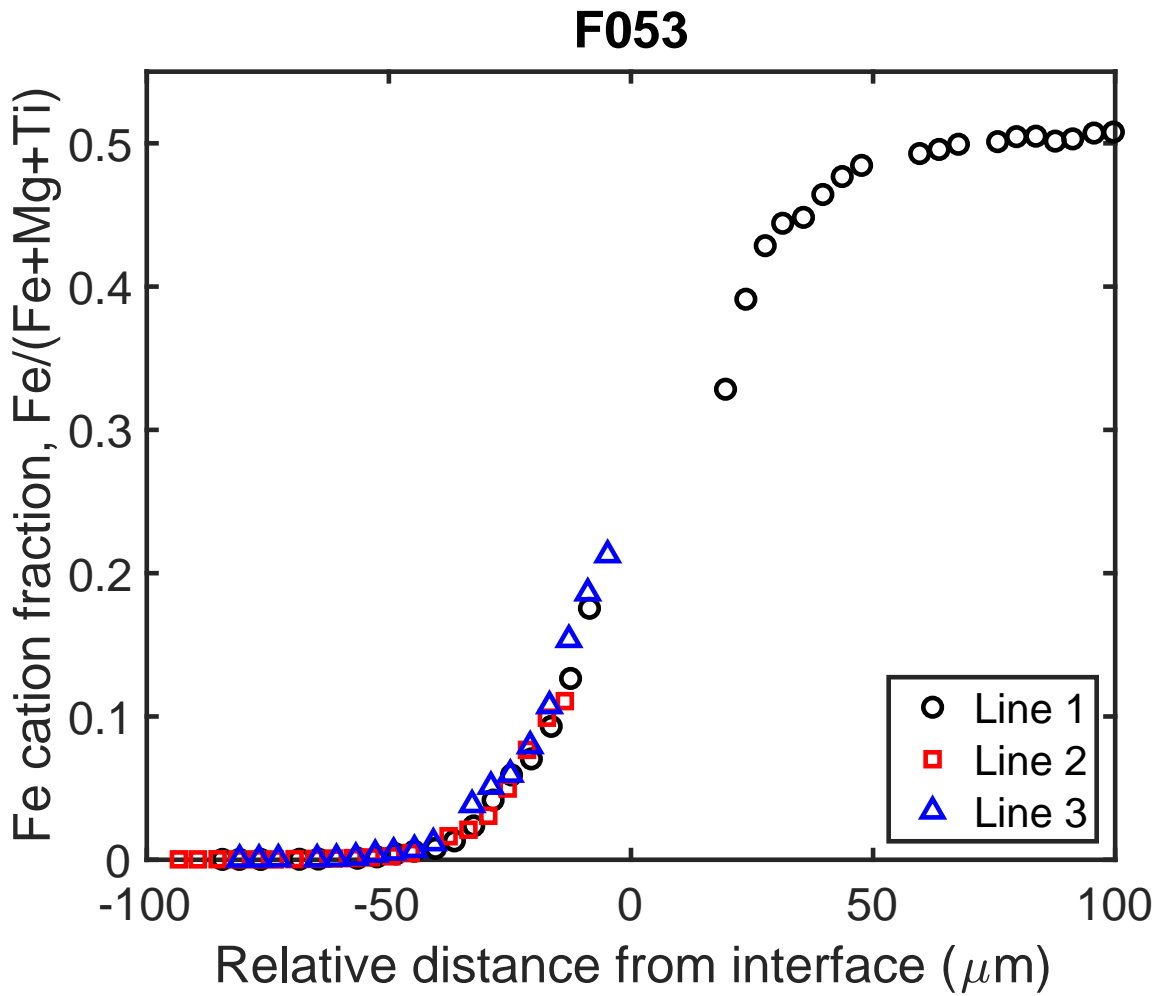Figure A.12: Electron microprobe analyses of experiment F051.

Figure A.13: Electron microprobe analyses of experiment F053.

Figure A.14: Electron microprobe analyses of experiment F086.

Figure A.15: Electron microprobe analyses of experiment F110.

Figure A.16: Electron microprobe analyses of experiment F111.
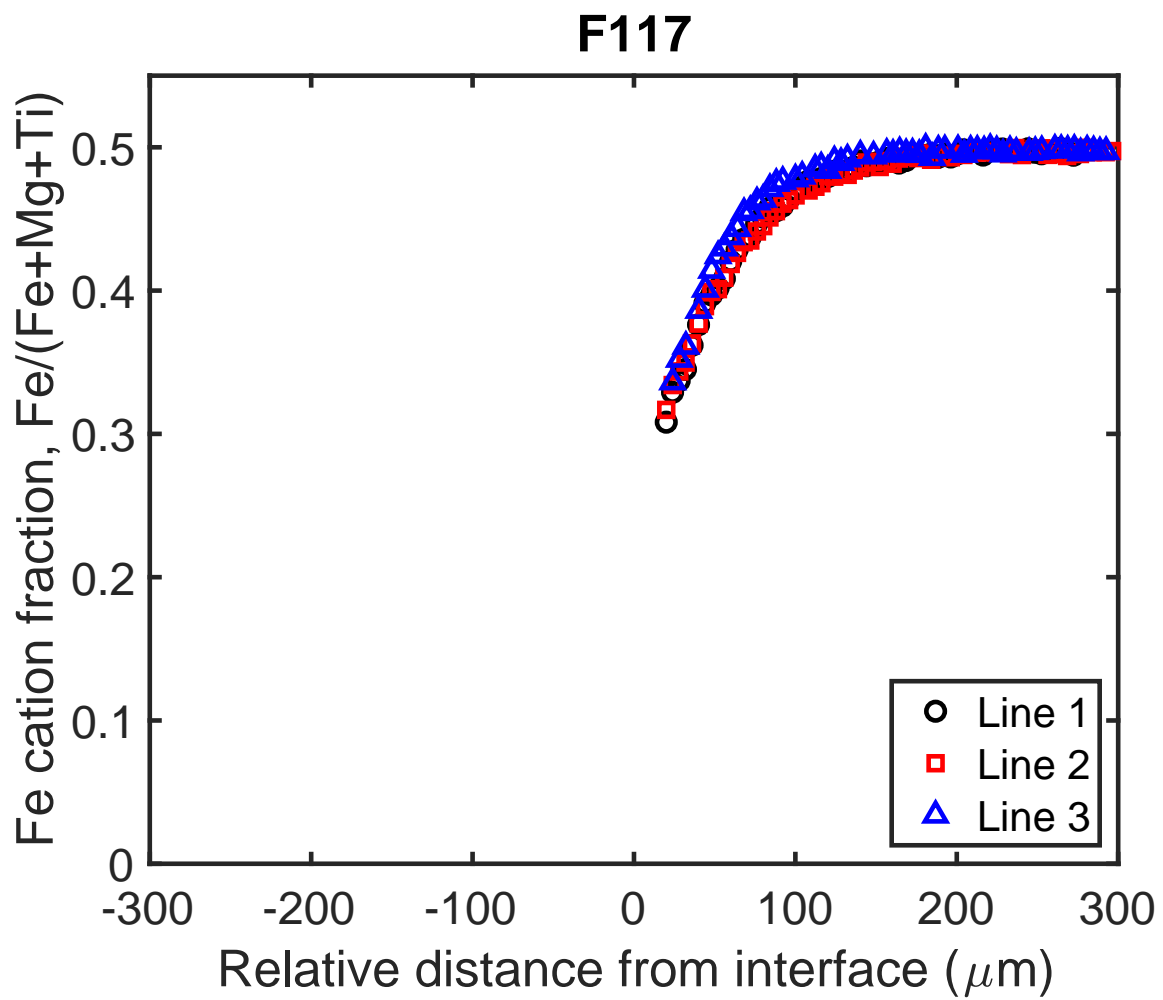
Figure A.17: Electron microprobe analyses of experiment F117.
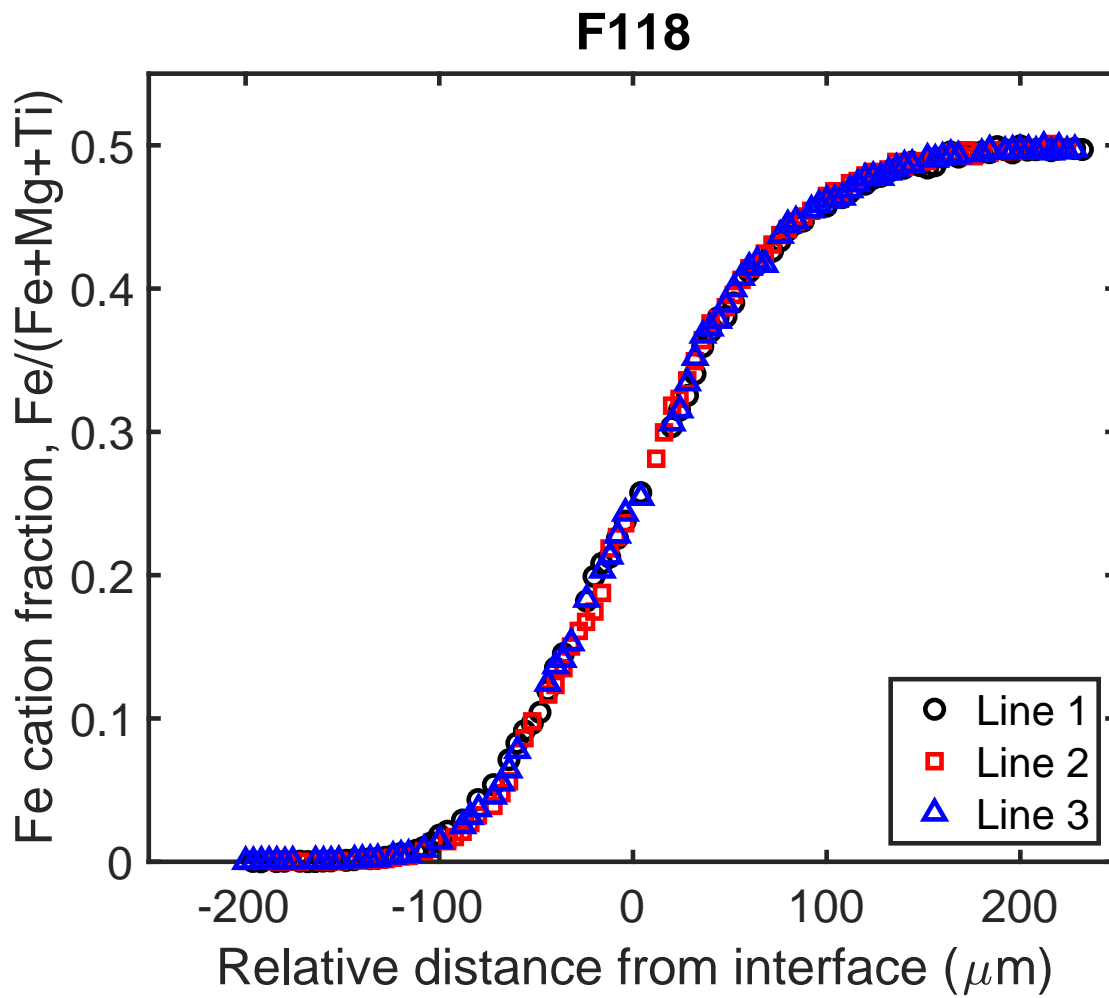
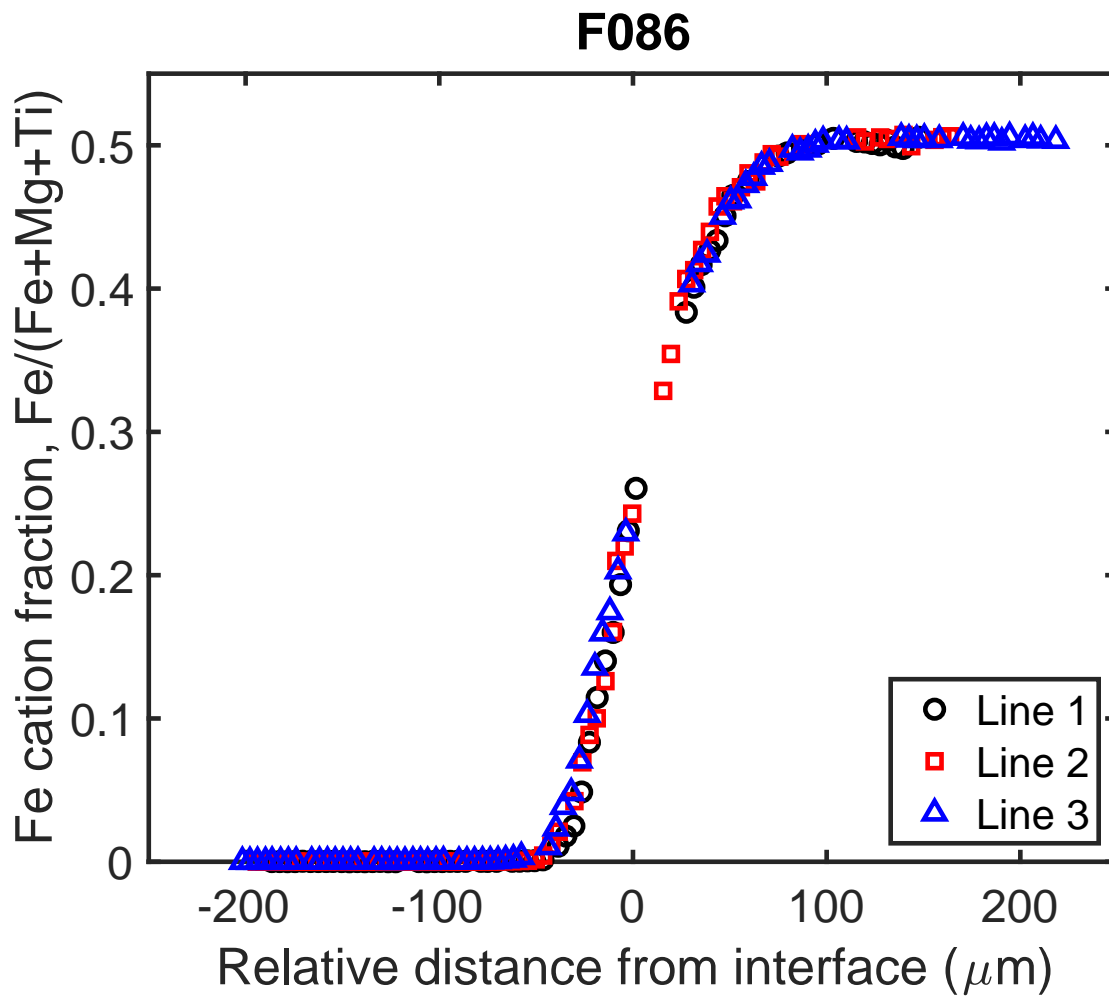Figure A.18: Electron microprobe analyses of experiment F118.

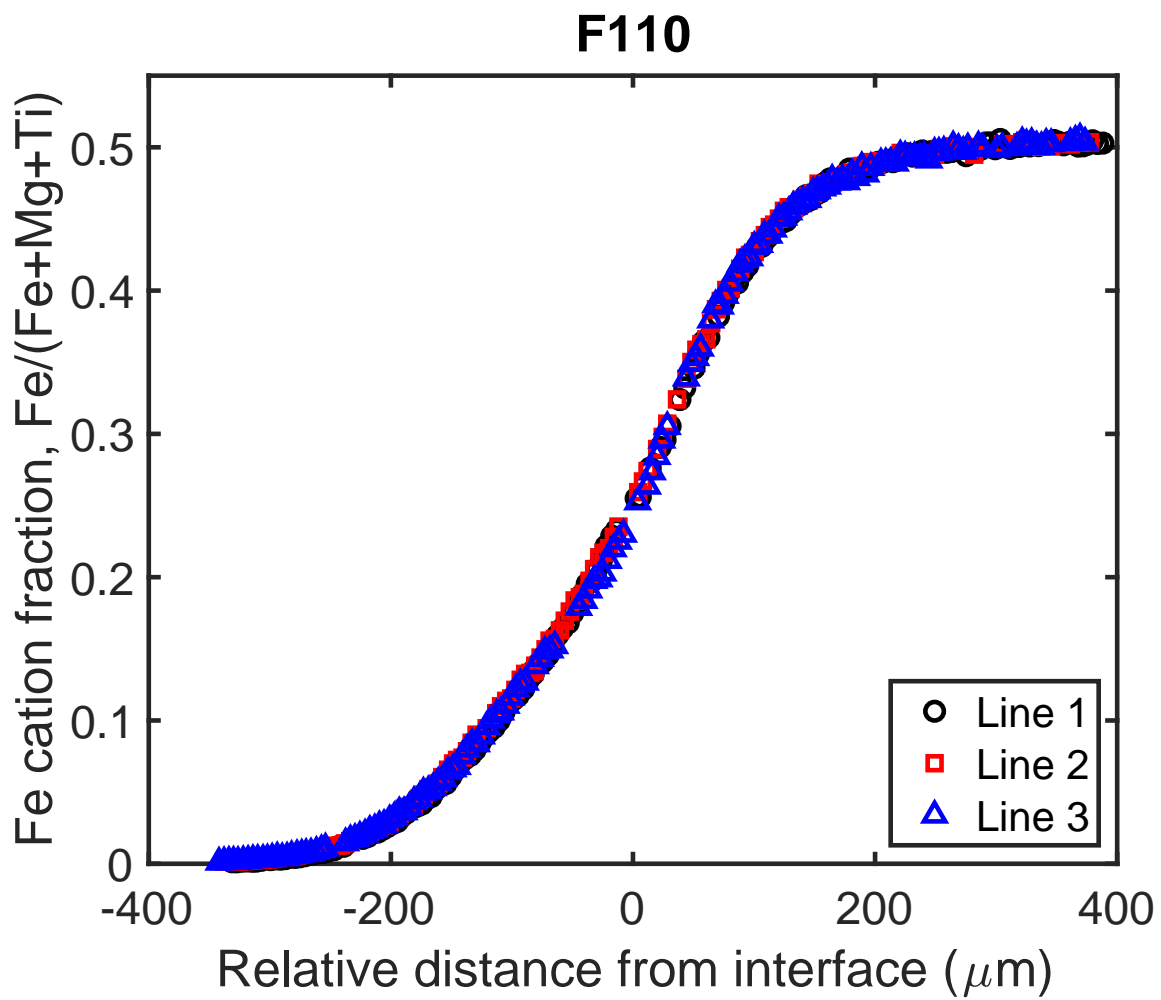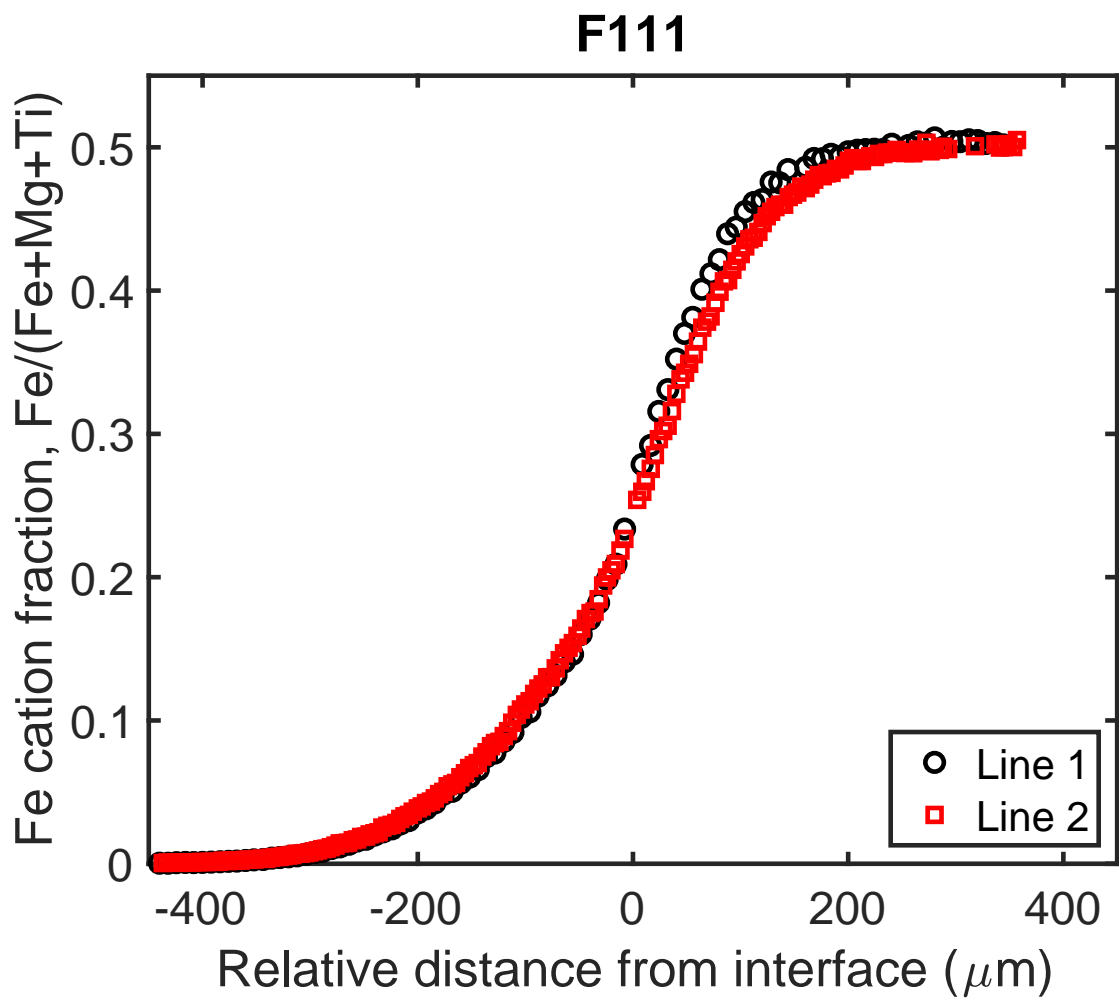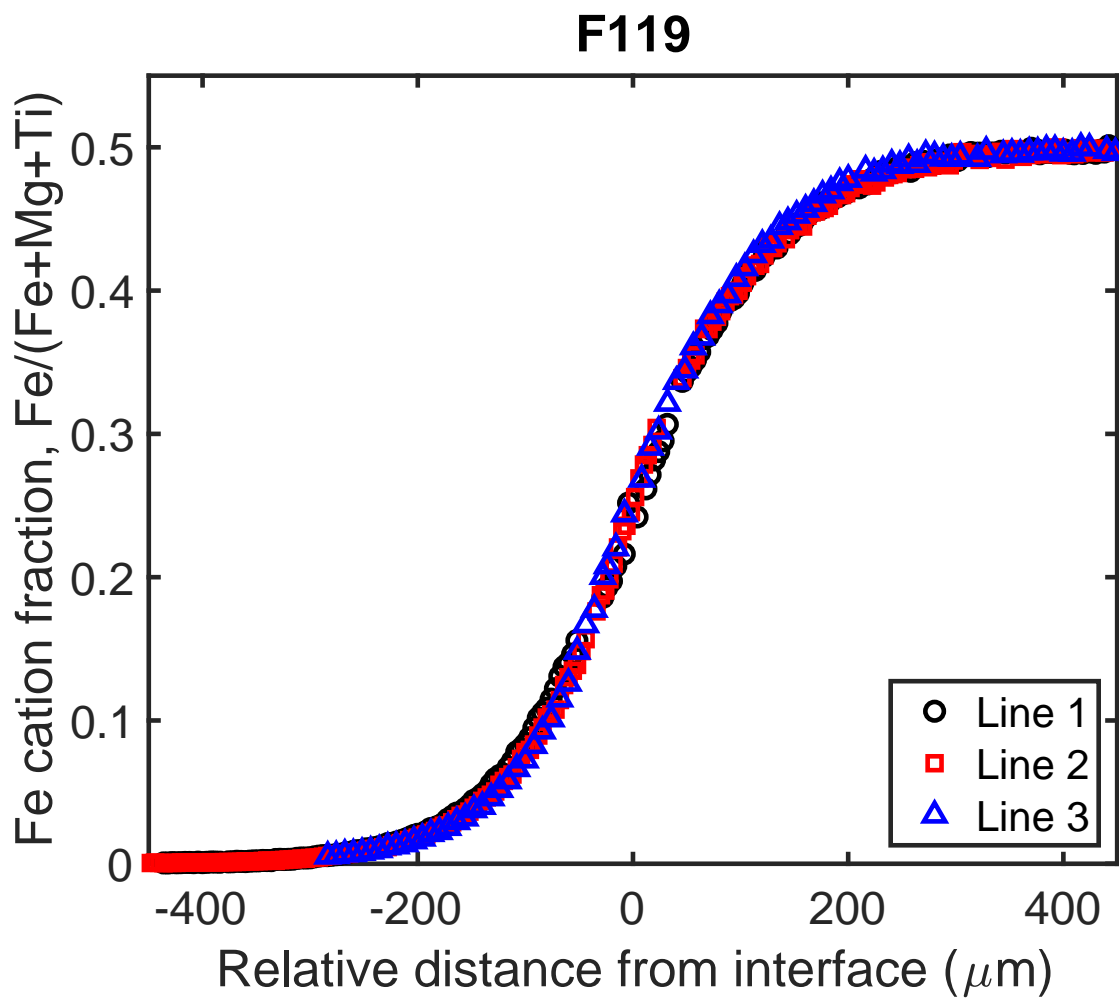Figure A.19: Electron microprobe analyses of experiment F119.
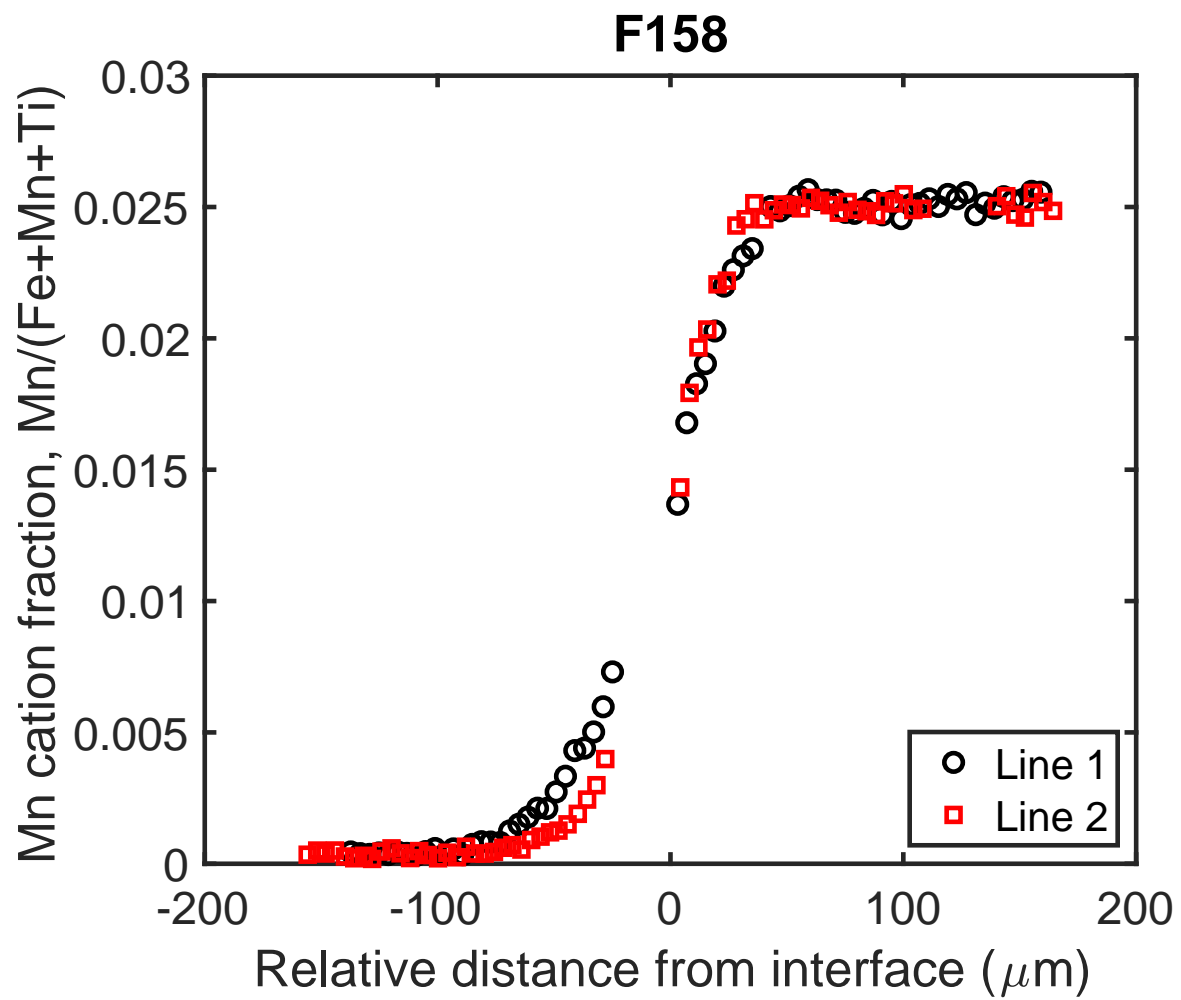
Figure A.20: Electron microprobe analyses of experiment F158.
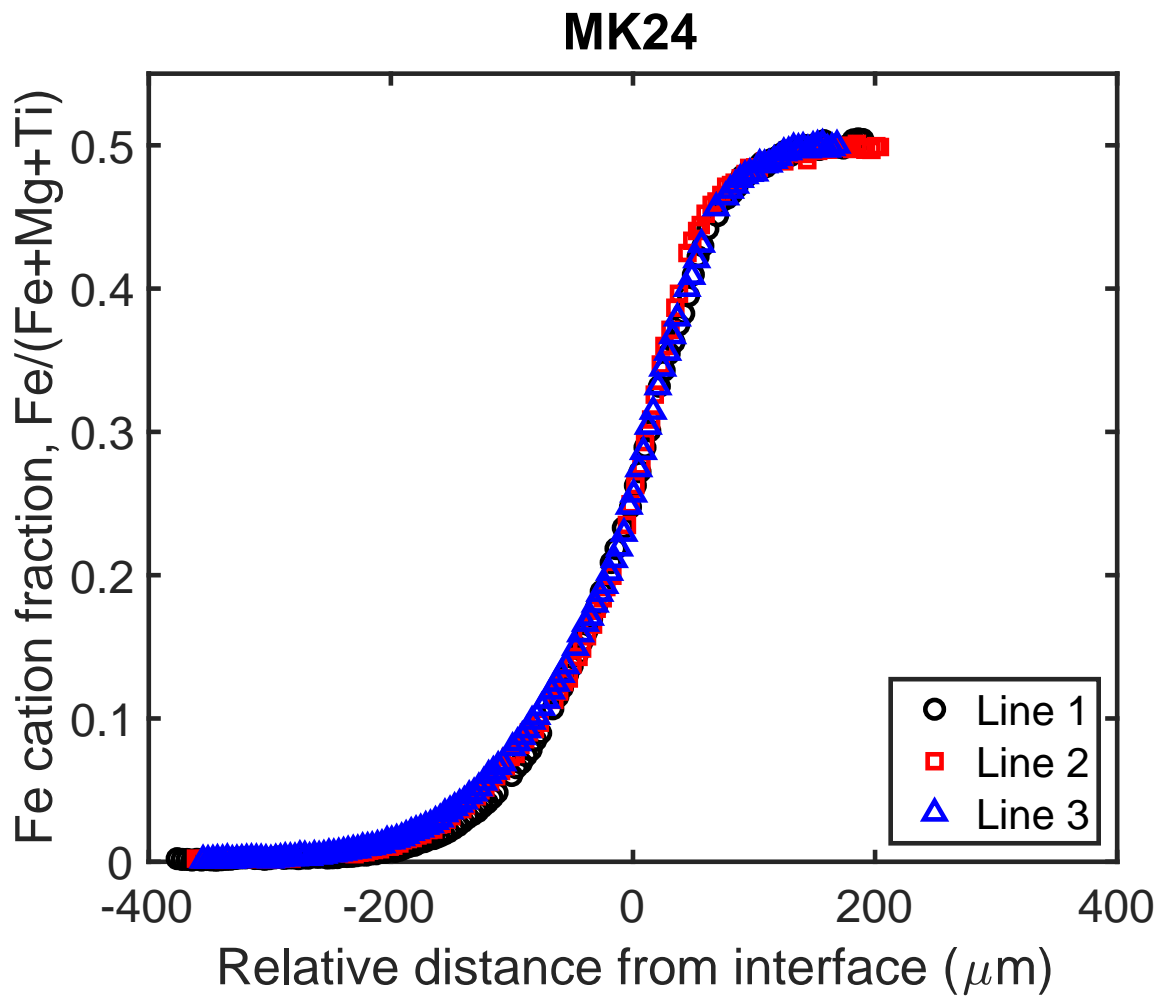
Figure A.21: Electron microprobe analyses of experiment MK24.

Appendix B

Appendix to Chapter 3

Purity of Starting Materials The brands and purities of the powders we used for our experimental starting material mixtures are reported below. For powders where the purity information was not readily available, the lot number has been included for reference.

- Al_2O_3, Alfa Aesar 99%

- $CaCO_3$, Johnson Matthey Electronics, Lot #H14B04

- $CaSiO_3$, Johnson Matthey Alfa Products, Lot #J24I

- $CaTiO_3$, Alfa Aesar, 99+%

- Cr_2O_3, Alfa Aesar 99.6%

- Fe_2O_3, Sigma-Aldrich, $\geq$99%

- Fe sponge, Alfa Aesar 99.9%

- K_2CO_3, Fisher Scientific, 99.9755%

- $Mg(OH)_2$, Johnson Matthey Electronics, Lot #K01A03. $Mg(OH)_2$ was dehydrated in an alumina crucible for more than 4 hours at 1000°C.

- MnO, Johnson Matthey catalog company, 99.5%

- Na_2CO_3, Johnson Matthey Alfa Products, Lot #K11G

- SiO_2, Fisher Scientific, Lot #917073A

- TiO_2, Sigma-Aldrich ≥99%

The Cambridge Isotopes [57]Fe spike material has a purity of 96.64% [57]Fe. To be conservative, we calculate the effect of contamination on the [56]Fe budget of our measured samples by assuming that the remaining 3.36% of the material is [56]Fe (though any impurity is likely comprised of [54]Fe and [58]Fe as well). Two samples, H056 wire and H055 olivine, have excess [57]Fe concentrations. We have calculated that the [57]Fe excess corresponds to a maximum 5% and 1.6% Fe contribution from the [57]Fe spike for H056 wire and H055 olivine, respectively. Considering the [57]Fe spike is at most 3.36% [56]Fe, the maximum [56]Fe that could be sourced from the [57]Fe spike is 0.17% and 0.05% of the sample Fe, respectively.

Additional Details Regarding Experimental Methods   To make the starting material pellets, we added approximately 50-75 mg of PVA solution to an aliquot (approximately 500 mg) of each starting material powder. (The PVA solution was made by heating a mixture of 200 grams of PVA powder and 1000 mL of deionized water until the solid was fully dissolved.) After allowing the starting material-PVA mixture to dry, the mixture was ground back to a powder with a mortar and pestle. The mixture was then separated into 75 mg aliquots for the individual pellets. For each aliquot, we loaded the 75 mg of powder into a stainless-steel die, applied 1.5 metric tons of pressure to the die assembly, and held the assembly at pressure for 2 minutes. The presence of PVA in the sample pellet could have promoted evaporative Fe loss

[177]

from our experimental samples, as the PVA degasses from the sample during the experiment. However, using the same pellet-making method, we have conducted experiments in our lab at $f_{O_2} = $ IW (not presented in this work) that did not experience Fe loss, suggesting the addition of PVA is not controlling the observed evaporative Fe loss.

The Re wire for each sample was made from 1.5 cm length of Re wire where approximately 0.5 cm was bent into a loop with which to hold the pellet. To fuse the pellets to Re metal loops we used an oxy-acetylene torch. The sample pellet was rested on the looped portion of the Re wire, then lowered into the torch flame for approximately 2 seconds until the bottom of the sample pellet had fused to the Re wire loop.

Determination of Evaporation Coefficients (α_{Fe}) for Hertz-Knudsen Equation

We used the Hertz-Knudsen Equation to calculate the evaporative flux of Fe from our Apollo 14 VLT and Apollo 14 Black samples, at both IW-1 and IW$+2$. The activity of FeO (a_{FeO}) for each liquid composition was calculated at the experimental temperature (1266°C) and oxygen fugacities using the rhyolite-MELTS code. The resulting activities are presented in Table B.3. In the range of oxygen fugacities we explored, the activity of FeO in each composition did not change.

As described in Section 3.4.1, P_{Fe}^{sample} is calculated using the activity of FeO in the starting composition and the oxygen fugacity of the experiment. For this calculation, we used the measured f_{O_2} of the 4-day experiments that had been analyzed on the electron microprobe (Table 3.2, experiments J040, H057, J007, and H037). The Fe loss in 4-day experimental samples analyzed on the microprobe is assumed to be identical for the 4-day experiment of similar composition and oxygen fugacity that we measured for iron isotopic compositions using the ICP-MS (experiments H056, H043, H055, H030, and J012). The calculated P_{Fe}^{sample} for each composition-oxygen fugacity condition is reported in Table B.3. For our calculation, we

[178]

have assumed that the gas flow in our furnaces removes any Fe from the ambient atmosphere. The combined gas flow of H_2 and CO_2 was 0.15 liters per minute for experiments J012, J017, J019, J040, H037, H038, H039, H042, H055, H056, and H057 and 0.30 liters per minute for experiments J007, J009, H030, and H031.

In solving for both the evaporative flux (J_{Fe}) and evaporation coefficient (α_{Fe}), we iterated α_{Fe} and used the calculated J_{Fe} for each iteration to estimate the evaporative loss associated with that particular α_{Fe} value. The calculated evaporative flux is multiplied by the surface area of our experimental sample, assuming a spherical geometry for a known sample volume, and the amount of Fe lost is compared to the initial abundance of Fe in the sample to derive a percent Fe lost via evaporation. This method allowed us to determine a range of α_{Fe} values that produced the best visual fit to our experimental data (Figure B.1). Because the experiments at IW-1 experience Fe loss through diffusion into the Re wire (4.1-6.5% Fe loss) as well as through evaporation (11.4-13.8% Fe loss), we focused on modeling only the amount of evaporative Fe loss. For the experiments at IW+2, almost all of the Fe loss was through evaporation (8-8.5% Fe loss) so we did not correct for the amount of Fe lost to the Re wire. The evaporation coefficients we used to calculate evaporative Fe loss that matches the estimated evaporative Fe loss from our samples are reported in Table B.3. The evaporation coefficients are similar for both starting compositions at a given oxygen fugacity, but have smaller values at lower oxygen fugacity (IW-1) than at higher oxygen fugacity (IW+2).

Estimated total Fe losses for shorter duration experiments (Table 3.2) are included in Figure B.1. However, we do not have separate estimates of evaporative loss and loss to the wire, because we did not measure the Fe isotopic compositions of these samples. A positive deviation from the calculated evaporative Fe loss curve indicates that additional Fe loss occurred, most likely by diffusion into the Re wire.

[179]
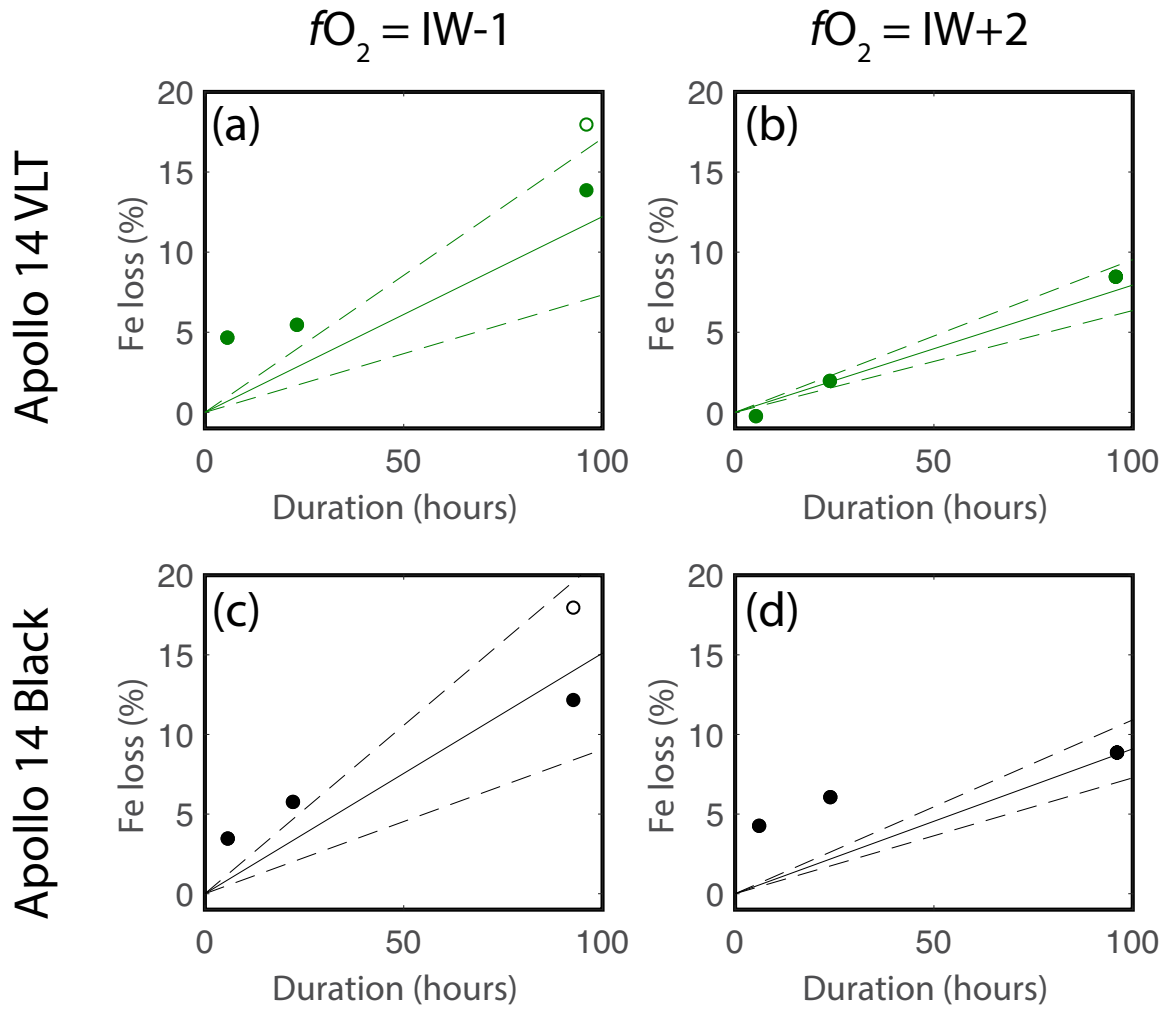
Figure B.1: Percent Fe loss versus run time for each experimental starting composition at two oxygen fugacities. In each plot, the lines represent the modeled evaporative Fe loss according to the Hertz-Knudsen calculations with variable coefficients of evaporation, with the solid line corresponding to the α_{Fe} reported in Table B.3 and the dashed lines bracketing the reported range of α_{Fe} for a given experimental composition and oxygen fugacity. Estimated values for total experimental Fe loss (Table 3.2) are plotted as circles for comparison to the calculated curves. The unfilled circles in panes (a) and (c) represent the total experimental Fe loss estimated for the 4-day experiments. This value was adjusted by subtracting the amount of Fe loss that occurred by diffusion into the Re wire, and the resulting evaporative Fe loss is plotted as a solid circle.

[180]

Table B.1: Iron isotopic compositions of geostandards and two Fe compounds used to mix the synthetic starting materials. Reported values are the weighted averages and weighted errors (95% confidence interval) of multiple measurements.

Sample	δ^{56}Fe (‰)	2σ	δ^{57}Fe (‰)	2σ
AGV-2-2	0.08	0.02	0.12	0.03
BCR-2-2	0.09	0.02	0.12	0.03
BIR-1-2	0.03	0.02	0.06	0.03
Fe Sponge	−0.46	0.04	−0.66	0.07
Fe_2O_3	0.26	0.04	0.38	0.07

Table B.2: Electron microprobe analyses of experimental Re wires in element weight percent. Blank entries for Fe indicate that the measured composition was below detection limit.

Experiment	Composition	Δ IW	Time (hr)	Fe	Re	Total	Distance from wire core (μm)	
J017	Apollo 14 VLT	-1.1	5.9		100.9	100.9	0	core
					100.0	100.0	58	
					100.4	100.4	117	
					100.0	100.0	129	rim
					100.5	100.5	0	core
					100.0	100.0	64	
					100.2	100.2	118	rim
J019	Apollo 14 VLT	-1.1	23.4		100.5	100.5	0	core
					100.2	100.2	42	
					100.3	100.3	102	
				3.6	96.6	100.2	118	
				7.1	92.1	99.2	120	
				6.2	92.8	99.0	131	rim
					100.9	100.9	0	core
				4.1	96.2	100.3	68	
				3.7	95.9	99.6	127	
				6.4	92.4	98.8	130	rim
J040	Apollo 14 VLT	-1.0	96.2		100.3	100.3	0	core
					100.4	100.4	34	
					100.5	100.5	71	
				0.2	100.3	100.5	86	
				3.8	95.5	99.3	104	
				3.9	95.4	99.3	115	rim

[182]

Experiment	Composition	Δ IW	Time (hr)	Fe	Re	Total	Distance from wire core (μm)	
H042	Apollo 14 Black	-1.0	6.0		101.6	101.6	0	core
					100.2	100.2	37	
					100.6	100.6	97	
				1.5	98.2	99.7	126	
				22.7	73.9	96.6	139	
				22.8	75.3	98.1	141	rim
H057	Apollo 14 Black	-1.0	92.9		100.1	100.1	0	core
					100.4	100.4	39	
					100.4	100.4	82	
				4.8	95.9	100.7	108	
				22.6	77.5	100.1	123	
				23.9	75.7	99.6	131	
				23.1	77.3	100.4	131	
				24.3	74.9	99.2	141	rim
H025	Apollo 14 Black	0.1	22.4		100.1	100.1	0	core
					99.6	99.6	52	
					100.4	100.4	103	
					100.8	100.8	103	rim
J009	Apollo 14 VLT	1.9	5.5		97.2	97.2	0	core
					97.7	97.7	38	
					97.4	97.4	66	
					97.2	97.2	108	rim
H031	Apollo 14 VLT	2.0	24.1		97.9	97.9	0	core
					98.1	98.1	50	
					98.0	98.0	81	rim
					97.2	97.2	0	core
					98.1	98.1	31	
					96.7	96.7	65	
					98.2	98.2	118	rim

Table B.3: Thermodynamic parameters from the Hertz-Knudsen evaporative flux calculation described in Section 3.4.1. Starting compositions are listed in Table 3.1, and experiment run conditions are listed in Table 3.2.

Composition	Apollo 14 VLT		Apollo 14 Black	
$f_{\mathbf{O}_2}$	**IW**-1	**IW**$+2$	**IW**-1	**IW**$+2$
a_{FeO} at $1266°$C	0.22	0.22	0.28	0.28
$P_{\text{Fe}}^{\text{sample}}$ (bar)	1.6×10^{-2}	5.7×10^{-4}	2.0×10^{-2}	6.5×10^{-4}
J_{Fe} (m^{-2}s^{-1})	$(6.0 \pm 2.4) \times 10^{-7}$	$(5.3 \pm 1.1) \times 10^{-7}$	$(7.4 \pm 3.0) \times 10^{-7}$	$(6.1 \pm 1.2) \times 10^{-7}$
α_{Fe}	$(2.5 \pm 1.0) \times 10^{-3}$	$(6.3 \pm 1.3) \times 10^{-2}$	$(2.5 \pm 1.0) \times 10^{-3}$	$(6.3 \pm 1.3) \times 10^{-2}$